Lean Duplex Stainless Steel (LDSS) Flat Oval Hollow Columns under Axial Compression – a Finite Element Study

A thesis submitted for the degree of

Doctor of Philosophy

by

Khwairakpam Sachidananda

Department of Civil Engineering

Indian Institute on Technology Guwahati

Guwahati – 781 039, India

DECLARATION

I, Khwairakpam Sachidananda, a PhD Scholar of Indian Institute of Technology Guwahati declare that the content of this thesis entitled 'Lean Duplex Stainless Steel (LDSS) Flat Oval Hollow Columns under Axial Compression – a Finite Element Study' submitted here is a partial fulfilment for the requirement of awarding the Degree for **Doctor of Philosophy** and submitted in Indian Institute of Technology Guwahati, India. This thesis is the documentation of the research work carried out by me at the institute in a period of July, 2011 to March, 2017 under the supervision of ***Konjengbam Darunkumar Singh***, Professor, Department of Civil Engineering, Indian Institute of Technology Guwahati, I certify that the content of this thesis is the original one and has not been used for awarding any other degree. Moreover the thesis content has not been published by any other person.

Date: **(Mr. Khwairakpam Sachidananda)**

Reg. No: 11610403

Place: IIT Guwahati

CERTIFICATE

This is to certify that the work content in the thesis entitled by '***Lean Duplex Stainless Steel (LDSS) Flat Oval Hollow Columns under Axial Compression – a Finite Element Study***' being submitted here by Mr**. Khwairakpam Sachidananda** to Indian Institute of Technology Guwahati, India for the award of degree of **Doctor of Philosophy** is a record of genuine research work carried out by the aspirant being a Phd scholar under my supervision and guidance.

The Thesis work, being shown is creditable of considering for the award of degree of **Doctor of Philosophy** in accordance with the regulation of the Institute.

(**Konjengbam Darunkumar Singh**)
Professor
Department of Civil Engineering
Indian Institute of Technology Guwahati

Date:

Place: IIT Guwahati

To the Lord

To my family members:

Khwairakpam Tomba Singh

Khwairakpam (*Ongbi*) Memcha Devi

Khwairakpam (*Ongbi*) Rita Chakpram

Khwairakpam Anandi

Khwairakpam Chinglemba

ABSTRACT

Construction industry has been witnessing an increasing use of stainless steel members, especially, when there is a demand for higher strength to weight ratio, good corrosion resistance, low maintenance cost, high ductility, impact resistance, fire resistance, durability, recyclability etc., despite their higher material cost as compared to carbon steel. However, it has now become possible to offer cost-effective stainless steel material, with the introduction of a relatively new class of stainless steel called Lean Duplex Stainless Steel (LDSS / LDX 2101 / EN 1.4162 / UNS 32101). LDSS offers relatively cheaper cost (as compared to austenitic stainless steel), higher strength, acceptable weldability and fracture toughness properties, improved high temperature properties, etc. It may be mentioned that, in a recently amended EN 1993-1-4 (2006; A1:2015), LDSS has been included. Thus, in this thesis, an attempt has been made to systematically investigate the structural behavior of aesthetically pleasing and relatively new LDSS flat oval (a composite section of flat and curve elements) hollow columns under pure compression.

Parametric study on the structural behaviour (e.g. deformation modes, load capacity) of fixed ended LDSS flat oval hollow section stub column, is presented, considering variation of l_f (flat length), r (curvature radius), t (thickness), keeping w (flat plate spacing) and h (height of column) constant, using the finite element (FE) analyses. Based on the study, an expression has been proposed for calculating the effective thickness of curve elements of slender ($w/t \geq 40$) sections, for reliable load capacity predictions when used with ASDM, AS/NZS 4673, and EN 1993-1-4 equations.

Applicability of DSM (Direct Strength Method) and CSM (Continuous Strength Method) have also been verified.

The FE study has been extended to analyse the structural behavior of fixed ended LDSS flat oval hollow slender columns, of stocky and slender section, under axial compression, by varying l_f, r , t, w and h. From the investigation, three key deformation mechanisms have been identified. Appropriateness of EN 1993-1-4, AS/NZS 4673, DSM and modified versions of AS/NZS 4673 and DSM for the design of LDSS flat oval hollow slender cross-section have been examined.

Additionally, the study of LDSS flat oval hollow stub columns, has been extended further by incorporating single square perforations. The effects of single square perforation in relation to perforation size and location (i.e. along transverse and longitudinal directions, on both the flat and curve elements) have been investigated. A design approach based on ASDM has been proposed (based on modified effective thickness) to address the inclusion of single square perforation for the estimation of design capacity of single square perforated flat oval LDSS hollow columns.

ACKNOWLEDGEMENT

My acknowledgement goes to all the persons who help me out in the course of my research work. Their company, advices and knowledge enable me to complete my work. I shall ever remain indebted to all of them. First of all I would to thank IIT Guwahti, Department of Civil Engineering for providing the required facilities to complete my research work.

I would like to express my sincere gratitude to my supervisor Prof. ***Konjengbam Darunkumar Singh,*** Department of Civil Engineering, IIT Guwahati for his constant effort, invaluable guidance, encouragement and kind help throughout the course of my research work. He always gives me the inspiration and motivation for my research work that help me in completing my thesis. I have experience and learn many things from his way of working, which will have a great impact in my future life.

I shall also be thankful to Prof. Sudip Talukdar, Dr. Arunasis Chakraborty and Dr. Karuna Kalita, my doctoral committee members, who has enlightened me giving valuable suggestion and remarks from time to time, which help me in getting the final touch of my research work.

I would like to express my special thanks to my friends Shanta, Sukumar, Kiran, Sonu, Sunderlal, Somorjit, Disco, Gishan, Patton, Narendra and senior Thoiba for giving me their companion and cherish my stay in Hostel of IIT Guwahati.

I am also thankful to all my family members – Khwairakpam Tomba (Father), Khwairakpam (ongbi) Memcha Devi (Mother), Khwairakpam (ongbi) Rita Chakpram (wife) and Khwairakpam Anandi (sister). I would like to contribute my thesis to my son – Khwairakpam Chinglemba, as I am lucky to have him as my son during the course of my PhD work. Their motivation and inspiration during my hard time shall be my unforgettable moments in my entire life. Their blessing has enabled me to reach this stage of my life.

Last but not the least, I express my thanks to Almighty God for his constant guidance and blessing and giving me the strength to complete my thesis work.

Khwairakpam Sachidananda

CONTENTS

LIST OF FIGURES

LIST OF TABLES

NOTATIONS

ASDM	Automotive Steel Design Manual
$ASDM_{(p)}$	Proposed ASDM for flat oval section
$ASDM_m$	Modified proposed ASDM (for perforation)
$ASDM_{mp}$	Modified proposed ASDM for perforation (with proposed thickness t_{ep} in curve section)
AISI	American Iron and Steel Institute
ASD	Allowable Stress Design
AS/NZS	Australian/ New Zealand Standard
$AS/NZS\ 4673_{(P)}$	Proposed AS/NZS 4673 (2001) for flat oval section
AS/NZS*	Modified AS/NZS Standard (Huang and Young, 2014b)
ASCE	American Society for Civil Engineers
A	Total/ Gross cross-section area
A_e	Effective cross-sectional area
A_{ec}	Effective area of curve element
A_{ef}	Effective area of flat element
A_g	Gross cross-sectional area
A_o	Equivalent area
A_p	Area of perforation

$A_{e(p)}$	Effective area for perforated section
B	Plate width
CSM	Continuous Strength Method
CHS	Circular Hollow Section
C_p	Correction factor
D	Diameter of circle
DSM	Direct Strength Method
DSM*	Modified DSM (Huang and Young, 2014b)
DL	Dead Load
E_{sh}	Strain-hardening slope
E	Young's modulus
E_o	Initial young's modulus of elasticity
$E_{o.2}$	Tangent stiffness at the 0.2% proof stress
EN	European standard
EWM	Effective width method
EHS	Elliptical Hollow Section
EN 1993-1-4$_{(p)}$	Proposed EN 1993-1-4 (2015) for flat oval section
FE	Finite Element
F_m	Mean value of fabrication factor
I	Second moment of inertia of cross-section
LDSS	Lean Duplex Stainless Steel
LRFD	Load Resistance Factor Design
LL	Live load
M_m	Mean ratio of yield strength to minimum specified value

NAS	North American Specification
NACA	National Advisory Committee for Aeronautics
N_e	Number of elements along the perforation edge
OHS	Oval Hollow Section
P	Load
P_u	Ultimate load
P_{up}	Ultimate load for perforated column
P_y	Yield load
P_{ne}	Nominal axial strength for flexural buckling
P_{nl}	Nominal axial strength for local buckling as well as interaction of local and flexural buckling
P_{crl}	Critical elastic local buckling load
P_{cre}	Critical elastic flexural buckling
P_{FE}	Ultimate load obtained from FE analysis
P_{CSM}	Design strength predicted by CSM
P_{EN}	Design strength predicted by EN 1993-1-4 (2015)
P_{ASCE}	Design strength predicted by ASCE 8-02 (2002)
$P_{AS/NZS}$	Design strength predicted by AS/NZS 4673 (2001)
P_{ASDM}	Design strength predicted by ASDM (2002)
P_{DSM}	Design strength predicted by DSM
P^*_{DSM}	Design strength predicted by modified DSM (Huang and Young, 2014b)
$P^*_{AS/NZS}$	Design strength predicted by modified AS/NZS (Huang and Young, 2014b)
$P_{ASDM(p)}$	Design strength predicted by Proposed ASDM (2002)

$P_{EN(p)}$	Design strength predicted by Proposed EN 1993-1-4 (2015)
$P_{AS/NZS(p)}$	Design strength predicted by Proposed AS/NZS 4673 (2001)
PHCs	Perforated hollow columns
RP	Reference Point
RHS	Rectangular Hollow Section
TRF	Thickness reduction factor
V_F	Coefficient of variation of fabrication
b	Length of the outer mesh
c-m	Perforation located at mid of curve element
d	Curve element diameter
f	Critical stress in compression element
f-m	Perforation located at mid of flat element
f_y	Yield stress
f_n	Stress in member (least of flexural, torsional, flexural-torsional buckling)
f_{csm}	Limit stress strength as per CSM
f_{yrs}	Reduced yield strength
h	Column height/length
h_e	Effective length of column
h_p	Location of perforation along longitudinal direction
h_{ph}	Position of perforation w.r.t. length of column (= h_p /h)
j	Coefficient of effective length of column
k	Plate buckling coefficient
l_s	Perforation length

l_c	Curve element arc length
l_{sc}	Arc length
l_f	Flat element length
l_{ef}	Effective length of flat element
l_{ec}	Effective length of curve element
l_{if}	Ineffective length in flat element
l_{ic}	Length of effective thickness of curve portion
n	Ramberg-Osgood hardening exponent between zero strain and $\varepsilon_{t0.2}$
$n'_{0.2,1.0}$	Ramberg-Osgood hardening exponent based on $\sigma_{0.2}$ and $\sigma_{1.0}$
r	Radius of curvature of curve element
r_y	Radius of gyration of gross section about minor axis of buckling
r_i	Internal corner radius
t	Thickness of section
t_e	Effective thickness of curve element
t_{ep}	Proposed effective thickness for curve element
w	Width between flat elements
w_o	Imperfection magnitude
α	Imperfection factor
β	Reliability Index
β_o	Target reliability Index
δ	Axial displacement
δ_u	Axial deformation at P_u

δ_{lat}	Lateral mid-length deflection
ΔA	Change in cross-sectional area
ΔP	Changes in load
ε	Strain
$\varepsilon_{t0.2}$	Total strain at 0.2% proof stress
$\varepsilon_{t1.0}$	Total strain at 1% proof stress
ε_{nom}	Engineering strain
ε_y	Strain at yield
ε_{csm}	Deformation capacity as per CSM
ε_{true}^{pl}	True plastic strain
ε_u	Strain at ultimate load(= δ_u /h)
ε_{lb}	failure strain (δ_u/h) of cross-section
λ	Non-dimensional slenderness ratio
$\bar{\lambda}_p$	Element or cross-section slenderness
$\bar{\lambda}_o$	Limiting slenderness
ρ	Reduction factor for local buckling
σ	Stress
σ_u	Ultimate stress
$\sigma_{0.2}$	0.2% proof stress
$\sigma_{1.0}$	1% proof stress
$\sigma_{0.01}$	0.01% proof stress
σ_{true}	True stress
σ_{nom}	Engineering stress

σ_{cr}	Critical stress
$\sigma_{cr,cs}$	Elastic buckling stress of full cross-section
Φ	Resistance factor
χ	Buckling reduction factor
Ψ_r	% reduction in load capacity due to perforation.

CHAPTER 1

1.1 BACKGROUND

As early as the late 19th century, 'carbon' steel became a popular construction material choice and began to influence the construction industry (TataSteelConstruction, 2017). Since then, a prevalent use of carbon steel especially as structural members can be seen till date. Amongst various reasons for its popularity with engineers and architects in the recent decades, mention can be made of e.g. low cost, easy availability, long experience, different strength grades, well developed design rules, etc. However, its inherent low corrosion resistance became an obvious major drawback, which can significantly subside its durability, notably for corrosive exposures. But with the invention of stainless steel, a significant appealing improvement over carbon steel, could be seen, e.g. higher strength to weight ratio, good corrosion resistance, low maintenance cost, high ductility, impact resistance, fire resistance, durability, recyclability (100% recyclable with no degradation) etc. Further, stainless steel can provide smooth, uniform and glossy finish, resulting in excellent aesthetic appearance. This led to a boost in the utilization of stainless steel as structural members, particularly in exposed architectural designs. From an economy perspective, it has been estimated that stainless steel can offer a cost-effective option as compared to carbon steel, if a

whole-life costing method is adopted. In spite of its attractive advantages, the use of stainless steel in the construction industry remains relatively limited as compared to carbon steel, primarily owing to the need of specialist expertise of its structural behavior (e.g. Mann, 1993; Gardner, 2005; Ashraf *et al.*, 2006a; Theofanous and Gardner, 2010). Predominantly, in the construction industry, stainless steels of the austenitic variety are commonly used. However, due to its high nickel content (~8-10% by mass), cost of austenitic variety remains high (~ 3-5 times that of carbon steel). With the advancement in stainless steel alloy development, a new breed of stainless steel named Lean Duplex Stainless Steel, LDSS (LDX 2101/ EN 1.4162/ UNS 32101) has been introduced offering striking benefits such as cheaper cost (nickel content = ~1.5% i.e. much lower as compared to austenitic stainless steel), higher strength, acceptable weldability and fracture toughness properties, improved high temperature properties, etc. (e.g. Theofanous and Gardner, 2009; Saliba and Gardner, 2013a). As a result, in the recent times, limited research efforts have begun to appear with a strong focus on the structural behaviour of LDSS members, more specifically, from the research groups of Gardner and Young, and their co-workers (e.g. Ashraf *et al.*, 2006b; Gardner and Ashraf, 2006; Chan and Gardner, 2008; Theofanous and Gardner, 2009; Zhu and Young, 2011, 2012; Huang and Young, 2014a, 2014b). Some of the examples of the application of LDSS structural members in the construction are shown in Figures 1.1-1.4. It is valuable to note that, recently EN 1993-1-4 (2006) incorporated LDSS in its amended version of EN 1993-1-4 :2006/A1:2015).

In the literature, several studies have been reported related to structural behavior of steel columns of both open and closed cross-sectional shapes (both carbon and stainless steels) e.g. I-section (Ashraf *et al*, 2006b; Saliba and Gardner, 2013b), Circular Hollow section (CHS) (Ashraf *et al.*, 2008), Square Hollow Section (SHS) (Theofanous and Gardner, 2009; Gardner, 2002); Rectangular Hollow Section (RHS) (Theofanous *et al.*, 2012), L, T, + (Patton and Singh, 2012, 2013) etc. Lately,

aesthetically pleasing cross sections such as Elliptical Hollow Section (EHS) (Silvestre, 2008) and Oval Hollow Section (OHS) (Gardner and Ministro, 2004), Flat oval hollow section (Zhu and Young, 2011, 2012) have gained research interest. In addition to their unique aesthetically pleasing shapes these cross sections (like ellipse, oval, flat oval etc.), furnish variant cross sectional properties with regard to both minor and major axes (Zhu and Young, 2011, 2012).

Studies on elliptical/oval hollow sections loaded with axial compression have been published as early as 1950s, primarily due to the requirements (seeking improved strength to weight ratios) of both aerospace and automobile industries e.g. Hutchinson (1968); Kemper and Chen (1969); Feinstein *et al*., (1971) reported on the elastic buckling of elliptical/oval hollow through analytical studies; Parks and Yu (1989) presented on both analytical and experimental studies on the interaction effects of curve and flat elements of stiffened flat oval (having both flat and curved elements connected through bolting) steel stub columns. For civil engineering applications (as structural elements), few researches have been reported on cold formed oval hollow steel sections e.g. Gardner and Ministro (2004); Theofanous *et al*., (2009a); Zhu and Young (2011, 2012); Silvestre and Gardner (2011). In this context, it is worthwhile to mention that, probably, Zhu and Young (2011, 2012) were the first to initiate work on cold formed flat oval hollow steel section (a single section made of two flat webs and two rounded semi-circular flange faces) columns under compressive load using both experimental and non-linear finite element buckling analyses, for potential application towards civil engineering structures. An extension of such studies has also been reported by Wang *et al*. (in Chinese) (2014) and Faxing *et al.*, (2015) on concrete-filled flat oval (with rounded ends) steel columns. In the construction industry, use of such oval / elliptical sections can be seen in places such as at Legends center, Canada, Electronics arts stairwell, Canada (Haque, 2011), Barajas airport, Spain; Heathrow airport, UK; Cork airport, Ireland; Zeeman building, University of Warwick, UK, Society bridge, Scotland (Chan *et*

al., 2010) indicating confidence amongst engineers and architects for such new sections. Examples of flat oval steel sections that are now available commercially are Form 220 and 370 flat oval from Ruukki (2017). However, it must be noted that the current steel design codes do not have exclusive provisions for flat oval hollow sections, possibly due to the lack of sufficient information on their structural performances.

Further, very often it become inevitable to provide cut-outs / opening or perforations in structural steel members, in order to facilitate inspection, piping, wiring, ducts etc. (e.g. Yu and Davis, 1971; Davis, 1972; Vann, 1971; Yu, 2000; Ortiz-Colberg, 1981; Shanmugan, 1997; Han *et al*., 2006; Shariati and Rokhi, 2008; Umbarkar *et al*., 2013, Kulatunga and Macdonald, 2013). Previous work mainly concentrated on plates, stiffened plates, circular columns etc., perforated with circular (Vann, 1971; Narayanan and Chow, 1984; Yang *et. al.*, 2008), square (Yao and Rasmussen, 2014), elliptical perforations (Forskitt *et. al*., 1991) etc. To the best of author's knowledge, only Umbarkar *et al.*, (2013), attempted to study the effect of circular perforation on LDSS circular stub columns using FE analyses.

Hence, an attempt has been made to systematically study the parametric effects of geometric dimensions (e.g. element radius, flat element length, thickness, length/height) on LDSS flat oval hollow columns, under the action of pure axial compression, using the commercial Finite Element (FE) software, Abaqus (2009). The study has also been extended to investigate the effects of square perforation with regard to size and location on the structural behaviour. The resulted research work is presented in a thesis consisting of six chapters.

1.2 OBJECTIVES

The main objective of the thesis is to investigate the structural behaviour of both unperforated and perforated LDSS flat oval hollow columns under pure axial compression, using finite element (FE) analyses. Additionally, the study also aims to compare the FE results with international design codes and methods. The key objectives of the present study are itemised below:

1. To study the effects of cross sectional parameters such as flat length, curvature radius, thickness on the structural behaviour of LDSS hollow stub columns, under axial compression.

2. To investigate the effects of geometric parameters viz., flat length, curvature radius, width between flat plates, thickness and height of column on the structural behaviour of LDSS hollow slender columns, under axial compression.

3. To assess the effects of location and size of single square perforation on the structural performance of perforated LDSS flat oval stub columns, under axial compression.

1.3 THESIS OUTLINE

The content of the thesis is divided into six chapters.

Chapter 1 briefly presents the background of the current research effort, including the key objectives of the work, and thesis outlines. In **Chapter 1**, special attention has been made on the promising stainless steel variety 'Lean Duplex Stainless Steel (LDSS)', and aesthetically pleasing steel cross-sectional shapes such as ellipse, oval and flat oval.

Literature review related to the present work is presented in **Chapter 2**. The literature review is broadly organised into two sub-headings *viz.*, unperforated and perforated steel hollow columns. Brief reviews on some of the popular international codes *viz.*, EN 1993-1-4 (2015), AS/NZS 4673 (2001), ASCE 8-02 (2002), and design methods viz., Direct Strength Method (DSM), and Continuous strength method (CSM) are also shown in **Chapter 2**. Also, reviews on the work related to LDSS and FE modelling of steel hollow sections are also presented.

In **Chapter 3,** a finite element study on the parametric effects of cross-sectional dimensions (e.g. curve element radius, flat element length, thickness) on LDSS flat oval stub columns under the action of pure axial compression is presented. Comparison of the FE results with those from design codes and design methods are also shown.

The previous study (Chapter 3) is extended for slender flat oval LDSS columns for both slender and stocky sections, using FE analyses, in **Chapter 4**. The effect of the various cross-sectional parameters *viz*., curve element radius, flat element length, thickness, width between flat elements, on the structural behaviour of slender flat oval LDSS columns are assessed as a function of column height or length. The FE results are then compared with those predicted by design codes and design methods.

The work presented in Chapter 3 on stub columns, is further extended in **Chapter 5**, by considering square perforations. In Chapter 5, investigation on the effect of square perforation with regard to size and location on the structural behaviour of flat oval LDSS stub hollow columns is presented.

In **Chapter 6** summarises the main conclusions obtained from the current research work on unperforated and perforated LDSS flat oval hollow columns. Some of the possible future scope of work are also highlighted in **Chapter 6**.

Sample design calculations for fixed ended LDSS flat oval hollow stub and slender columns are presented in **Appendices A-C**.

Figure 1.1: Qatar Airport, Doha (Metalresources, 2017)

Figure 1.2: Arco Malizia bridge, Siena (Constructalia, 2017)

Figure 1.3: Celtic Gateway, Wales (Wikimedia, 2017a)

Figure 1.4: Sant Fruitos Bridge, Spain (Wikimedia, 2017b)

CHAPTER 2

LITERATURE REVIEW

2.1 INTRODUCTION

A review of literature pertaining to unperforated and perforated steel hollow / tubular columns is presented in this chapter. A brief introduction on the usage of stainless steel in construction industry, with a key focus on the work related to Lean Duplex Stainless Steel (LDSS) columns is also presented. Summary of the international design specifications such as EN 1993-1-4: 2006+A1(2015) (also referred in this work as EN 1993-1-4 (2015) for convenience), AS/NZS 4673 (2001), ASCE 8-02 (2002) etc., which furnish guidelines for the design of stainless steel members are provided. In addition, applicable design methods for the design of steel members, such as Effective Width Method (EWM), Direct Strength Method (DSM), and Continuous Strength Method (CSM) are also reviewed. Further, primary finite element modelling parameters (*viz.*, non-linear material models, local and global imperfections, residual stress) associated for performing GMNIA (geometrically and materially nonlinear imperfect analysis) of thin-walled structures, with a particular attention to stainless steel material modelling are also highlighted. At the end of this chapter, summary drawn from the literature review are presented, to form a basis for the motivation of the current research effort.

2.2 STEEL HOLLOW / TUBULAR COLUMNS

As mentioned in Chapter 1, in the steel construction industry, tubular or closed steel sections / members have been getting attention and popular, especially for exposed architecture, owing to their aesthetic appeal and better torsional resistance as compared to open sections. Hence, these steel tubular sections have been used for a variety of structural applications such as beams, columns, braces etc. Although such tubular steel sections are generally used as 'unperforated' i.e. without any holes or cut-outs being made (especially if welded connections are being used), there may arise situations wherein 'perforations' may become obligatory to accommodate services such as piping, ducts, inspection holes etc. In the literature, studies on such steel tubular columns are mainly reported for square (e.g., Virdi, 1981, Gardner, 2002, Liu and Young, 2003, Gardner and Nethercot, 2004a, 2004b, 2004c, Zhou and Young, 2005, Theofanous and Gardner, 2009, Huang & Young, 2013), rectangular (e.g. Virdi, 1981, Talja and Salmi, 1995, Young and Liu, 2002, Ridley *et al*., 2003, Gardner and Nethercot, 2004b, Zhou and Young, 2005, Dabaon *et al*., 2009, Theofanous and Gardner, 2009), L- (e.g. Patton and Singh, 2012), T- (e.g. Patton and Singh, 2012) and circular (e.g. Hutchinson, 1968, Virdi, 1981, Young and Hartono, 2002, Bardi and Kyriakides, 2006, Ashraf *et al.* 2008b) sections. In addition to these traditional shapes, in the recent past, studies on innovative shapes such as elliptical (e.g. Tennyson *et al.* 1971; Feinstein *et al*. 1971; Zhu and Wilkinson, 2006; Ruiz-Teran and Gardner, 2008; Gardner *et al*., 2008; Silvestre, 2008; Chan *et al*., 2010), oval (e.g. Kempner and Chen, 1964; Kempner and Chen, 1966; Tvegraard, 1976; Gardner and Ministro, 2004; Theofanous *et al*., 2009a; 2009b; Gardner, 2010; Chan and Gardner, 2009a; 2009b) and flat-oval (i.e. consisting of both flat and curved elements) (e.g. Parks and Yu, 1987; 1989; Zhu and Young, 2011; 2012) have been found in the literature. These new tubular sectional shapes i.e. elliptical/oval etc. provide different flexural and torsional rigidities about the two principal axes; and have combined or mixed structural

properties of circular hollow section (CHS) and rectangular hollow section (RHS), and are liked by architects for their enhanced aesthetic appeal (Chan *et al.*, 2010; Theofanous *et al.*, 2009b). Hence, in the following sections, focussed reviews on literature of both unperforated and perforated steel columns of elliptical/oval hollow/tubular sections are presented, with a special attention towards flat-oval hollow sections.

2.2.1 **Unperforated columns**

The studies on oval sections were first initiated around 1950s and 1960s (Marguerre, 1951; Hutchinson, 1968; Feinstein *et al.*, 1971). The elastic critical buckling and post buckling analyses of oval hollow section under axial loading condition have been reported by Marguerre (1951) and Kempner (1962). The instability of thin oval hollow section showing sharp unloading behavior has been shown experimentally by Hutchinson (1968).

Marguerre (1951) presented an analytical approach for the structural stability of cylindrical shell of variable curvature, considering both compression and combination of compression and shear loadings. Based on the study, formulas have been proposed involving Fourier expressions by considering reciprocal of curvature radius.

Kempner and Chen (1964) analytically studied the post-buckling behaviour of OHS (Oval Hollow Section), and showed that higher aspect ratio of the OHS yielded more stable post-buckling behaviour (approaching a flat plate response) whilst, lower aspect ratio (thus approaching circular section), led to a relatively unstable behaviour at the post-buckling stage. It was also found that smaller the ratio of radius to thickness, resulted in less stable post-buckling behavior.

Hutchinson (1968) experimentally and analytically studied the buckling, initial post-buckling behavior and stability of thin elastic cylindrical shell of elliptical/oval

tubular sections under axial compression. Based on the study, it has been observed that the initial part of the post buckling deformation is sensitive to small geometric imperfections, and can result in buckling loads well below those predicted by considering perfect shell.

Kempner and Chen (1969) analytically studied the post buckling behavior of oval cylindrical shell under axial compression, using approximate energy analysis. It has been found that for a flatter oval section, a relatively higher load capacity as compared to classical load capacity was seen for 'far' post buckling region. Further, initial imperfection has been seen to have relatively lesser influence on the buckling behaviour as compared to circular cylinders.

Feinstein *et al.* (1971) experimentally investigated the stability of oval cylindrical shells under clamped boundaries. The study showed different buckling modes for circular and oval cylindrical shells. In the case of circular shells, buckling has been observed to occur instantaneously over the entire circumference of the shell leading to the sudden drop of load capacity of column. However, initiation of buckling at the region of minimum curvature has been seen for the case of oval section.

Tvergaard (1976) studied oval cylindrical shells under axial compression, and observed that post buckling behavior was affected by plastic yielding of the sections. The strong curved region has been seen to get weakened by material nonlinearity (due to plasticity) leading to stiffness drop of the corner region.

Parks and Yu (1987) experimentally studied the structural performance of flat oval hollow sections, containing combined sections of flat and curve parts. The combined section tests have shown that curve parts have more strength as compared to those of flat parts. A modified effective design method has been proposed for the design of such combined sections. The proposed design equation has been incorporated in ASDM (2002).

Gardner (2005) conducted experimental and finite element (FE or numerical) studies on high strength hot rolled oval hollow section under compression and bending, to assess the effect of cross-section slenderness by taking into account the effect of strain hardening and local buckling. A good agreement between FE and experimental ultimate loads has been observed, although deformations could not be well matched.

Zhu and Wilkinson (2007) studied numerically the local buckling of elliptical hollow section columns under compression. The elastic buckling, inelastic buckling (due to material nonlinearity) and the effects of geometric imperfection have been studied. The results of numerical analysis have been found to compare well with the experimental results. The equivalent diameter concepts of elliptical hollow section with the circular diameter have been presented.

Ruiz-Teran and Gardner (2008) performed analytical and numerical studies on the elastic buckling of elliptical hollow sections in compression and shown that the structural performance of the elliptical section lies in between those of circular and flat plates. Based on the study, cross-sectional classifications and formulas for the calculation of effective sectional properties for elliptical sections have been presented.

Silvestre (2008) presented buckling behavior of elliptical hollow columns under compression using Generalised Beam Theory (GBT). It has been shown that columns of short to intermediate lengths showed local buckling modes, whilst longer columns undergo both distortional and global buckling modes. Further, it has been reported that, length of local buckling modes decreases with increase in sectional thickness, however thickness is found to have minor effect on the global buckling modes.

Chan and Gardner (2008) experimentally and numerically studied the behavior of hot rolled carbon steel elliptical stub hollow column under axial compression. Based on the parametric study, relationships have been established between cross-section slenderness and compressive resistance. The relationship also showed that the Class 3 limit of 90 as suggested by EN 1993-1-4 (2006) can be safely adopted for elliptical section also.

Theofanous *et al.* (2009a) performed experimental as well as numerical work on cold-formed stainless steel oval shaped stub and slender hollow columns. Results of parametric study considering aspect ratio, cross-sectional and member slenderness have been shown. Based on the study, a Class 3 limit for stainless steel oval hollow section under compression has been proposed. The stainless steel oval hollow sections have been observed to exhibit superior load capacity in compression as compared to comparable carbon steel sections. Further, a new buckling curve for the design of slender stainless steel oval columns, has been proposed.

Chan and Gardner (2009a) investigated experimentally and numerically the structural flexural behavior of elliptical hollow columns. It has been found that the strengths predicted by European standard (EN 1993-1-1, 2005), American specification (AISC 360, 2005), and Australian Standard (AS 4100, 1998) are applicable for the design of elliptical hollow section column.

Chan and Gardner (2009b) investigated experimentally and numerically, the structural behaviour of cold-formed stainless steel oval hollow columns along with bending. Based on the study, design rules of cross-section slenderness limits on compression and bending and column buckling curve have been proposed for stainless steel oval hollow columns.

Silvestre and Gardner (2011) analysed elastic local post-buckling behavior of elliptical tubes under compression. Based on the analyses, three failure mechanisms *viz.*, local buckling mechanisms at short to intermediate length, distortional mechanisms at intermediate to moderately long column, and global failure mechanism at longer columns, have been observed. It is found that low to moderate aspect ratio ($a/b \leq 1.5$) can be loaded up to limit loads while those with moderate to higher aspect ratio ($a/b \geq 2$) has been found to have higher load capacity i.e. beyond limit loads. Further, it is also observed that accumulated stresses near the zone of minimum radius of curvature increases with increasing aspect ratio.

Nowzartash and Mohareb (2011) conducted thermo-mechanical numerical analysis for hot-rolled elliptical sections and estimated the cross-sectional effect on residual stress distribution. Based on the study, it has been seen that, yield strength has negligible effect of the residual stress at room temperature. Further, EN 1993-1-1 (2005) buckling curve 'b' has been reported to give good approximation for the EHS (Elliptical Hollow Section) buckling about major axis.

Zhu and Young (2011) performed experimental tests on cold-formed flat oval sections with semi-circular curve elements, under fixed support conditions. Based on the study, three failure modes *viz.*, local, flexural and interaction of local and flexural mechanisms, have been reported. The column strength of flat oval sections, have been compared with the design strength of AISI (2007), ASDM (2002), AS/NZS 4600 (2005) and EN 1993-1-3 (2006), and found that the codal predictions are conservative.

Zhu and Young (2012) presented numerical analyses of cold-formed flat oval (with semi-circular end sections) fixed ended columns. Based on the numerical study, three failure modes *viz.*, yielding, local, flexural and interaction of local and flexure, have been reported. The numerical results have been compared with those predicted

by AISI (2007), AS/NZS 4600 (2005), EN 1993-1-3 (2006) and Direct Strength Method (DSM). The design specifications are found to be applicable to flat oval sections for compact sections while they showed unconservative nature for slender section columns. The DSM, on the other hand, has been observed to be applicable for both compact and slender section columns.

Silvestre *et al.*, (2013) studied the structural behavior of semi-elliptical (combination of a flat part and a semi-elliptical part) hollow section column under compressive force, in terms of buckling pattern, ultimate strength and failure of columns. The local buckling was reported to be controlled by the flat part while the ultimate behavior depends on the pre-buckling stiffness of the semi-elliptical part. A design equation has been proposed to estimate the ultimate capacity of semi-elliptical section of columns.

McCann *et al*. (2016) studied numerically the local buckling behavior and ultimate strength of elliptical tubular compression members. It has been observed that behaviors of lower cross-sectional aspect ratio columns are similar with those of circular sections columns. Design curves have been proposed for Class 4 sections, considering local buckling mechanism.

2.2.2 Perforated columns

Jullien and Liman (1998) investigated experimentally and numerically the effects of perforations in cylindrical shell made of steel sheet under axial compression. Parametric studies on the effects of different perforation shapes (e.g. square, rectangular, circular) and dimensions (axial and circumferential) of the perforations have been studied. It has been found that square perforation reduces the local and global buckling load capacities of column. Further, square and rectangular perforations with identical perforation lengths, have been reported to produce

similar critical buckling load. Circular perforations with smaller diameters have been found to give negligible effect on the critical load capacity. Imperfection is found to have negligible effect for columns with large perforations, as compared to smaller perforations. For the parameters considered, perforation positions have been seen to have little influence on critical load.

Murakami *et al*. (1998) studied experimentally and numerically the effects of circular perforation on the ultimate strength of cylindrical column. It has been shown that presence of perforation reduced the column strength and changed the buckling deformation, as compared to that of unperforated columns. It is reasoned that, the decrease in ultimate load for perforated columns may be due to the interactive behavior of membrane buckling and local deformation around perforation.

Sivakumaran and Abdel-Rahman (1998) carried out experimental and numerical studies on both perforated and unperforated cold formed steel sections under compression, considering square, oval, rectangular and circular perforations. It has been observed that perforated column strengths are lower than that of unperforated columns. Further, perforation shapes are found to have little effect on the ultimate load. Also, it has been reported that perforations can have relatively more reduction in column capacity for stocky sections, as compared to slender sections.

Vartdal *et al*., (2006) performed experimental and numerical studies on simply supported cylindrical carbon steel column with rectangular perforation located at mid height of column under compression. The contact between the deformed perforation edges (at post-ultimate) has been found to have significant effect for small perforation in relation to that of larger perforation. Empirical formulation has been introduced that can predict the behavior of perforated column.

Shariati and Rokhi (2008) numerically and experimentally investigated the effects of elliptical cutouts on mild steel cylinder under axial compression. It has been

found that, changing the perforation position from mid-height towards the end increases the load capacity. Based on the study, empirical numerical equations have been developed for cylindrical shell with elliptical cutout.

Shariati and Rokhi (2010) investigated the performance of mild steel cylindrical shell column with elliptical perforation. The effect of perforations has been studied considering different sizes, angles and aspect ratio (length to diameter and diameter to thickness ratios) on buckling behaviour. Equations to predict buckling load of perforated columns have been developed. The load capacity has been observed to reduce as the location height of perforation and size increase. The load capacity has also been seen to increase with increase in height to width ratio of perforation, and perforation angles.

Ghazijahani *et al*., (2015) performed experiments on cylindrical mild steel tube with various perforations shapes (rectangular cutout with two semi-circular ends, elliptical, semi-oval, rectangular cutouts with fillet corners) near the support, subjected to compressive force. The occurrence of elephant foot was seen opposite to the side of cutout as the stress flow line deviated from the cutout portion and got concentrated on the surface opposite to the cutout. Samples with different cutout showed different buckling modes as the perforation influenced the buckling pattern. The initiation of buckling near perforation caused the instability of the column leading to the reduction of load capacity.

2.3 STAINLESS STEEL IN CONSTRUCTION

As highlighted in Chapter 1, historically, carbon steels have been used as reliable construction material. However, stainless steel constructions have also increased, due to their beneficial properties like corrosion-resistant, long lasting / durability, aesthetic appearance, etc. In addition, stainless steel is known to have good recyclability in comparison to carbon steel. Considering total life cycle cost, it has

been reported by Gardner *et al.* (2007) that stainless steel can be an economical option for construction, in spite of its higher initial cost. Hence, of late, several research efforts have been made on stainless steel members, both for open (e.g. Ashraf et al., 2006; Saliba and Gardner, 2013; Becque and Rasmussen, 2009; Patton and Singh, 2012, 2013; Cardoso and Rasmussen, 2013) and closed (e.g. Ashraf *et al*., 2008; Theofanous and Gardner, 2009; Zhu and Young, 2011, 2012; Silvestre and Gardner, 2011; McCann et al., 2016) sections. Some of the popular steel structures are Cala Galdana Bridge (Minorca, Spain) (Structurae, 2017), Hamad International Airport (Doha) (Hok, 2017), Arco Malizia (Siena, Italy) (Constructalia, 2017), Cloud Gate (The Bean, Chicago, US) (Juliaworld, 2017) etc. In the construction industry, various grades of stainless steel (e.g. Austentic, Ferritic, Martensitic, Duplex, LDSS, Super duplex etc.) are used (Ancon, 2017). Amongst, stainless steel varieties, LDSS has become a promising candidate for the construction industry, which can offset the high initial cost, commonly encountered for other types of stainless steel. And hence, several recent research efforts have been directed towards LDSS members for both open (I-section) and closed (square, circular, L-T, + etc.) members, under compression (e.g. Theofanous and Gardner, 2009; Patton and Singh, 2012, 2013; Umbarkar *et al.*, 2013; Huang and Young, 2013, 2014b; Anbarasu and Ashraf , 2017) , bending (e.g. Hassanein, 2011; Saliba and Gardner, 2013; Theofanous and Gardner, 2010) etc. However, as the current research is directed towards columns, only those literatures on LDSS columns are presented in the following section.

2.4 LDSS TUBULAR / HOLLOW COLUMNS

Theofanous and Gardner (2009) performed experiments on LDSS (EN 1.4162, a types of duplex material) square and rectangular column sections under axial compression. The experimental test gave details of the material properties, geometric and the imperfection of the sections. The experiment was performed both

on stub and slender column. The experimental study was extended to finite element analysis by studying a wide range of sections. Based on the study, the applicability of the Class classification of EN 1993-1-4 (2006) has been assessed. New class classification limit for class 3 section along with the new formula for effective width calculation of internal elements (taking into account local buckling effect) has been proposed. These proposed limitation and the effective width formula have been adopted in the new amended EN 1993-1-4 (2015).

Huang and Young (2012) studied the material properties of square and rectangular hollow lean duplex stainless steel column under axial compression. The initial local geometric imperfection and residual stresses were measured from test. Design strengths of American specification (ASCE 8-02, 2002), Australian/New Zealand standard (AS/NZS 4673, 2001) and European Code (EN 1993-1-4, 2006) were compared with the stub column test under axial compression and was reported to be conservative for cold-formed LDSS stub column. Out of these codes, European code has been found to prove the most conservative values when compared with the test results.

Umbarkar *et al.* (2013) conducted numerical study on the effects of single circular perforation on cylindrical LDSS stub column under axial compression. The effects of hole sizes, column thickness, eccentricity of hole from the edge of column have been assessed parametrically. The buckling load capacity has been found to increase with increase in column thickness. Further, it has been observed that the lowest column strength occurred when the perforation is located at mid-height. For smaller size perforations no significant effect on the buckling load has been seen, however, as the perforation size increases, the load capacity has been observed to reduce.

Patton and Singh (2012, 2013) investigated through FE analyses, the structural behavior of L, T and + Shaped LDSS hollow stub and slender columns under pure compression. It has been shown that predictions made by EN 1993-1-4 (2006), and

AS/NZS 4673 (2001) are found to be applicable, for the non-rectangular shaped LDSS columns.

Huang and Young (2014a) performed experimental investigation on LDSS stainless steel hollow square and rectangular section members under combined action of compression and minor axis bending. Failure modes have been observed in terms of local buckling, flexural buckling and interaction of local and flexural buckling. Comparison of the experimental results with ASCE 8-02 (2002), AS/NZS 4673 (2001) and EN 1993-1-4 (2006)) have shown that all the design codes are reliable but EN 1993-1-4 (2006) results provide the most conservative predictions.

Huang and Young (2014b) investigated numerically and experimentally the structural behavior of pin ended LDSS square and rectangular hollow section columns under axial compression. Based on the study, design modifications have been proposed for AS/NZS 4673 (2001), EN 1993-1-4 (2006) and DSM for LDSS hollow columns.

Huang and Young (2015) performed numerical analysis for studying the structural performance of the cold-formed LDSS members under combined compression and bending. The numerical results have been compared with the design strengths of ASCE 8-02 (2002), AS/NZS 4673 (2001) and EN 1993-1-4 (2006) and found that the codal predictions are conservative. Further, modified AS/NZS 4673 (2001) and DSM (AISI S100, 2007) have been proposed for the design of cold-formed LDSS steel structural members under combined action of compression and bending.

Anbarasu and Ashraf (2017) conducted numerical studies to investigate the interaction effects of local-flexural buckling of LDSS square and rectangular hollow columns under compression. Based on the study, it has been found that design strength of AS/NZS 4673 (2001), EN 1993-1-4 (2015), ASCE (2002) and DSM

(AISI, 2007) are unconservative. The modified design strength of DSM, AS/NZS, EN 1993-1-4 by Huang and Young (2014b) were also shown to be unconservative. Modification to the standards codes of AS/NZS, EN 1993-1-4, DSM has been proposed for the LDSS column with interaction effect of local-flexural buckling which gave the conservative result.

2.5 DESIGN STANDARDS FOR STEEL COLUMN

Design guidelines or specifications (available for various materials such as carbon, stainless steel etc.) help in the design of safe structures. Such design guidelines are country specific and available for different countries such as United States, Japan, Canada, Australia, New Zealand, India etc. In this section, widely used international codes in the literature, which have specific stainless steel guidelines, such as American (ASCE 8-02, 2002), Australian/New Zealand (AS/NZS 4673, 2001) and European (EN 1993-1-4, 2015) would be presented. All the three codes mentioned above have different criteria for the analysis of column strengths. It may be worthwhile to mention that to the best of author's knowledge, no design standards exist for the design of flat oval hollow sections.

2.5.1 American Standards

The first American code for the specification of the design of cold-formed stainless steel structural members was published in 1968 based on the researches contribution made by Johnson and Winter in 1966 (CFS, 2015), for austenitic stainless steel. This specification covered cold-formed to structural shapes made from annealed and strain-flattened light-gauge steel. Hard tempered steel works came to be included in the revised version in 1974 by AISI (1974). Based on both Load and Resistance Factor Design (LRFD) and Allowable Stress Design (ASD) methods, the ASCE standard AISI/ASCE-8-90 was published in 1990, with the

LRFD method being mainly based on Austenitic and Ferritic stainless steel results. In the following year, i.e. 1991, ANSI/ ASCE-8 Structural Stainless Steel Design Standard was published with key contributions from Lin *et al.* (1988) from University of Missouri-Rolla. Later, 'Specification for the design of cold formed stainless steel structural members' was introduced as SEI/ASCE 8-02 (2002). ASCE 8-02 (2002) have design provisions for the design of members subjected to tension, compression, flexure and combined axial- bending loadings. Further development in cold formed steel design, led to North American Specification for the Design of Cold-Formed Steel Structural Members' (NAS, 2007), encompassing ASD, LRFD, Limit State Design (LSD) and Direct Strength Method (DSM).

In addition to the above mentioned specifications, a manual known as Automotive Steel Design Manual (ASDM) of American Iron and Steel Institute (AISI) and Auto/Steel Partnership was introduced in 1986, for the automotive steel industries. Later version e.g. ASDM (2002) included design treatments for combined sections (i.e. sections composed of both flat and curve elements). The difference of this design manual from the other design standards (such as EN 1993-1-4, 2015, AS/NZS 4673, 2001) is the consideration of effective area for both the curve and flat elements, whilst it is only for the flat elements in the other standards. The basis of this approach is mainly from the work of Parks and Yu (1987), *via* a project sponsored by AISI.

2.5.2 Australia/ New Zealand Standards

In 2001, the first Australian/New Zealand design code for stainless steel structures (AS/NZS 4673, 2001) was introduced. It is based on the ASCE and AISI specifications for the structural stainless steel members (Baddoo, 2003). The AS/NZS 4673 (2001) have covers several types of stainless steels such as austenitic (304, 316, 304L, 316L), ferritic steel (409 and 430) and duplex material (S31803 or

EN 1.4462). The design calculation of effective width (considering only effective flat plate) is similar to that of ASCE 8-02 calculation. In 2005, AS/NZS 4600 (2005) was introduced by the joint standards of Australia and New Zealand Committee BD-082 for cold formed steel structures. Direct Strength Method (DSM) has been introduced as an alternative method to effective width method in AS/NZS 4600 (2005)

2.5.3 European Standards

The design of steel structures has been dealt in Eurocode 3, *via* limit state design philosophy. Eurocode 3 (EN 1993-1-4, 1996) pre-standard was introduced in 1996 by European Standards organization (CEN) with the supplementary guidelines for stainless steel. The standard EN 1993-1-4 (2006), is based on this pre-standard. Although, EN 1993-1-4 (2006) provides guidelines for the design of stainless steel structures (in combination with EN 1993-1-1 (2005) and EN 1993-1-3 (2006)) but the LDSS (Lean Duplex Stainless Steel) material is not included. Recently, amendment has been made to EN 1993-1-4 (2006) (see EN 1993-1-4, 2006; A1:2015) with the inclusion of four grades of lean duplex stainless steels i.e. EN 1.4062, EN 1.4162, EN 1.4482, EN 1.4662. The newly amended i.e. EN 1993-1-4 (2006; A1:2015) has made certain changes such as class classification limits i.e. the new class limits (based on flat element length, l_f) are 1) $l_f / t\varepsilon \leq 33$ for Class 1, 2) $l_f / t\varepsilon \leq 35$ for Class 2 and $l_f / t\varepsilon \leq 37$ for Class 3. The expression for reduction factor (ρ) for the Class 4 section (Clause 5.2.3 of EN 1993-1-4:2006+A1:2015) has also been changed. However, the buckling curve equation (Clause 5.4.2.1) remains unchanged.

2.6 DESIGN METHODS

In the literature, three main design approaches *viz.*, Effective Width Method (EWM), Direct Strength Method (DSM) and Continuous Strength Method (CSM) are reported for the design of thin walled structures. The three methods are briefly discussed here.

2.6.1 Effective Width Method

Effective width method (EWM) is also used in the design standards / specifications *viz.*, American standards, Australian/ New Zealand standards, European standards, by considering the local and distortional deformations. EWM was first proposed by Von Karman in 1932 (Lind *et al*., 1971), by assuming an equivalent distribution of stress over an effective area. This method was later applied to cold formed members after suitable calibration by Winter (1948). The von Karman equation was found to be suited especially for thin plates, but overestimated for stockier sections. Hence, an alternative equation to von Karman equation was proposed by Winter (1948), based on a series of experiments, to accommodate the progression from slender to stocky sections. Since then, several versions of Winter's equation came to be established to take care of local buckling, distortional buckling either with stiffener or without stiffener, stress gardient (Lind *et al*., 1971; Bambach and Rasmussen, 2004).

Although, EWM is relatively simple, for complex sections where interaction amongst several elements can be expected (e.g. sections consisting of flat and curve elements), deriving expressions for EWM became challenging. In 1983, Narayanan and Chow (1983) derived the equations of effective width for different boundary conditions using energy methods. for uniaxially loaded rectangular plate. Parks and Yu (1987, 1989) developed empirical equations for stiffened and unstiffened

combined sections consisting of flat and semi-circular sections. These empirical equations have been adopted in ASDM (2002). Some of the drawbacks of FEM include inability to treat explicitly inter-element equilibrium and compatibility for buckling behavior, necessity of laborious trial and error calculations in case of members with edge or intermediate stiffeners, etc. Hence, to circumvent these shortcomings of EWM, new design methods like Direct Strength Method (DSM) and Continuous Strength Method (CSM) have been proposed (Theofanous and Gardner, 2011).

2.6.2 Direct Strength Method (DSM)

In Direct Strength Method (DSM) the accurate prediction of member elastic stability forms the main theme (e.g. Schafer and Pekoz, 1998, Hancock *et al.*, 1994, Schafer, 2002, 2006, 2008). DSM has been featured in Appendix 1 of North American Specification for the design of cold-formed steel structural members in 2004 (Schafer, 2006). DSM has been also adopted in Australia/New Zealand (AS/NZS 4600, 2005) code. Key considerations of DSM include estimation of elastic instabilities for the gross section (unlike EWM). In this method elastic instabilities such as local, distortional and global flexure or flexural-torsional modes have been taken into account along with the interaction between the modes. Application of DSM for beams, columns, perforated channel sections etc. have been reported (e.g. Schafer and Pekoz, 1998, Moen and Schafer, 2011, Pham and Handcock, 2012, Pham *et al*., 2014). DSM has been extended for stainless steel by Becque *et al.* (2008). Zhu and Young (2012) applied DSM for flat oval steel section in both stub and slender columns and found to be reliable. Huang and Young (2014b) have investigated the LDSS square and rectangular cold-formed stainless steel section and found that the current DSM to be conservative and hence modified DSM have been proposed for cold-formed lean duplex stainless steel columns (see Huang and Young, 2014a, 2014b). Moen and Schafer (2011) derived DSM

equations for perforated cold-formed open steel section columns. Yuan *et al.* (2014) demonstrated that DSM is capable of predicting the strength for built-up sections of stainless steel and found to be capable to predict the result of the experiment result. Recently, Anbarasu and Ashraf (2017) proposed a modified DSM for the prediction of interaction failure of local-flexural buckling for cold-formed lean duplex stainless steel hollow columns. Although a very widely popular alternative to EWM, DSM suffers from its limitation to limit the material stress to yield stress (i.e. $\sigma_{0.2}$), and hence cannot effectively address the gain in strength through strain hardening, especially for stocky sections.

2.6.3 Continuous Strength Method (CSM)

The Continuous Strength Method (CSM) was first proposed by Gardner (2008). CSM is a deformation based design following continuous relationship between cross-sectional slenderness and cross-sectional deformation capacity together with strain hardening (Gardner 2008; Afshan and Gardner, 2013). CSM provides a continuous relationship between the normalized cross-section deformation capacity and the cross-section slenderness, through a base curve, which relates the level of strain in a cross section to the material stress level. CSM is now published as a NCCI (2013) i.e Non-Contradictory Complementary Information and provides supplementary guidance to Eurocodes for structural design (REF, 2014). This method is being used by Ancon, an international stainless steel producer (REF, 2014) due to the enhanced member strength predicted by CSM. Recent studies by Gardner (2016), Ahmed *et al.*, (2016), Zhao *et al*. (2017) have extended the applicability of CSM for slender sections.

2.7 FE ANALYSIS OF THIN-WALLED LDSS COLUMNS

Researchers and engineers have often employed numerical modelling procedures (such as FE Analysis) to analyse thin-walled elements or members made of metals

such as steels, to assess useful structural information *viz.*, load capacity, deformation pattern, failure mechanisms etc (see e.g. Theofanous and Gardner, 2009; Patton and Singh, 2012). One of the main reasons for resorting to numerical simulation is the expensive nature (due to costs of materials, involvement of technical staffs, fabrication of special test arrangements etc.) of experimental tests to generate large amount of data. On the other hand, FE analysis can conveniently generate and explore a much larger parametric space, when suitably calibrated or validated against reliable experimental data. Such validated or calibrated FE modelling procedures can be used as stand alone or in combination with available experimental data to provide reasonably reliable structural behaviour information. Also, variation of parameters can be done inexpensively, which hitherto would be difficult in experimental regimes (see e.g. Ashraf *et. al.*, 2006b, Ellobody *et. al.*, 2014). In the following sections, some important considerations such as FE elements, material modelling, imperfection, residual stress, that can significantly influence the accuracy and reliability of FE models are mentioned briefly.

2.7.1 Element type

In the literature, the FE modeling of thin metal structures are generally achieved with the use of shell FE elements, due to relative thinness of the sections. For modelling of thin walled members e.g. steel hollow / tubular members, the conventional shell element type i.e. S4R element found in Abaqus (2009) (four-noded doubly curved shell element with reduced integration; having six degrees of freedom per node, i.e., three rotations and three translations) has been used by various researchers under different loading conditions such as compression (Thaofanous and Gardner, 2009; Chan and Gardner, 2008; Theofanous *et al*., 2009a; Ellobody and Young, 2005; Zhu and Young, 2012) and bending. (Chan and Gardner, 2008; Niu *et al.*, 2015; Thaofanous and Gardner, 2010). S4R element has been reported to give accurate results when compared to experimental studies.

Further, in most studies, the aspect ratio of the element has been maintained nearly at ~1, in order to provide reliable FE results.

2.7.2 LDSS Material modelling

Accurate material modelling plays an important role in predicting reliable strength of thin walled steel members. According to the types of steel materials (e.g. carbon, stainless steel etc.), different material models exist. Precise representation and good understanding of material modelling are needed to predict the structural behavior of the member during various stages of loading. In the literature, various material models have been proposed by researchers, as early as 1940s (e.g. Ramberg-Osgood, 1943; Hill, 1944). For stainless steel, researchers like Mirambell and Real, 2000; Rasmussen, 2003; Gardner and Ashraf, 2006 have proposed several material modelling concepts. Out of the proposed material models for stainless steel, Ramberg-Osgood, 1943 model has generally been accepted to be valid till attainment of yield stress, and for stress levels beyond yield, different models have been put forward by Rassmussen (2003); Gardner and Ashraf (2006) etc.

The Ramberg-Osgood model (1943) is a simple formula defined in Equation 2.1, describing the stress-strain curve in terms of three parameters, namely, Young's modulus (E) and two secant yield strengths. The NACA Technical Note No. 840 (NACA 840) indicated applicability of this model for aluminum-alloy, stainless-steel and carbons steel. This model is especially useful for metals that harden with plastic deformation i.e., smooth elastic-plastic transition. Considering the stress at 0.2% plastic strain as 0.2% ($\sigma_{0.2}$ proof stress, the Ramberg-Osgood expression is given by Equation 2.1.

$$\varepsilon = \frac{\sigma}{E} + k\left(\frac{\sigma}{\sigma_{0.2}}\right)^{n} \tag{2.1}$$

where σ and ε are the stress and strains respectively. The constant *n* is the strain hardening exponent and defines the degree of roundness of the curve. *k* and *n* are material nonlinearity indices of the stress-strain behavior. The parameter (*n*) has been found out by using the 0.01% and 0.2% proof stresses (i.e. $\sigma_{0.01}$ and $\sigma_{0.2}$). The value of $k = 0.002$ has been reported to give reasonably good predictions of stress-strain behavior for stainless steel material up to the 0.2% proof stress ($\sigma_{0.2}$), The model has been reported to exaggerate the corresponding stress beyond 0.2% proof stress (see e.g. Rasmussen, 2003, Patton and Singh, 2012). The extrapolation of this model beyond $\sigma_{0.2}$ has been found to be inaccurate for alloys with pronounced strain hardening.

To estimate the material model beyond the yield stress (or $\sigma_{0.2}$), Rasmussen (2003) suggested a material model that is valid for the full strain range. Rasmussen (2003) adopted Mirambell and Real's (2000) modified Ramberg-Osgood model for stresses beyond the 0.2% proof stress to develop the full stress strain (see Equation 2.2).

$$\varepsilon = \frac{(\sigma - \sigma_{0.2})}{E_{0.2}} + \varepsilon_u \times \left(\frac{\sigma - \sigma_{0.2}}{\sigma_u - \sigma_{0.2}} \right)^m + \varepsilon_{t0.2} \tag{2.2}$$

where, σ_u, ε_u, m and $E_{0.2}$ are the ultimate tensile strength, ultimate strain, additional strain hardening exponent and the tangent modulus of the stress strain curve at the 0.2% proof stress respectively. $E_{0.2}$ is defined in Equation 2.3.

$$E_{0.2} = \frac{\sigma_{0.2} E}{\sigma_{0.2} + 0.002nE} \tag{2.3}$$

The strain hardening exponent, *m* proposed by Rasmussen (2003) is given as

$$m = 1 + 3.5 \frac{\sigma_{0.2}}{\sigma_u} \tag{2.4}$$

The ultimate tensile strength (σ_u) and ultimate strain (ε_u) are determined using Equations 2.5 and 2.6 in terms of $\sigma_{0.2}$, E and n.

$$\frac{\sigma_{0.2}}{\sigma_u} = \frac{0.2 + 185\left(\frac{\sigma_{0.2}}{E}\right)}{1 - 0.0375(n-5)} \tag{2.5}$$

$$\varepsilon_u = 1 - \frac{\sigma_{0.2}}{\sigma_u} \tag{2.6}$$

The full-range stress-strain curve is then given by Equation 2.7.

$$\varepsilon = \begin{cases} \frac{\sigma}{E} + K\left(\frac{\sigma}{\sigma_{0.2}}\right)^n & \text{for } \sigma \le \sigma_{0.2} \\ \frac{(\sigma - \sigma_{0.2})}{E_{0.2}} + \varepsilon_u \times \left(\frac{\sigma - \sigma_{0.2}}{\sigma_u - \sigma_{0.2}}\right)^m + \varepsilon_{t0.2} & \text{for } \sigma > \sigma_{0.2} \end{cases} \tag{2.7}$$

Rasmussen (2003) model has been adopted as a guideline for material modelling of stainless steel in EN 1993-1-4 (2006/A1:2015).

Gardner and Ashraf (2006) mentioned that the two stage model as proposed by Rasmussen (2003) and Mirambell and Real's (2000), are applicable only to tensile stress-strain behavior as these methods depend on ultimate stress (σ_u) and strain (ε_u). However, it has been suggested that as necking phenomenon is absent during compression, Gardner (2002) proposed for the use of 1% proof stress ($\sigma_{0.1}$) and strain ($\varepsilon_{t1.0}$) in lieu of ultimate stress (σ_u) and strain (ε_u). The proposed model by Gardner and Ashraf (2006) is given in Equation 2.8 for stress level greater than σ_u.

$$\varepsilon = \left(\frac{\sigma - \sigma_{0.2}}{E_{0.2}}\right) + \left(\varepsilon_{t1.0} - \varepsilon_{t0.2} - \frac{\sigma_{1.0} - \sigma_{0.2}}{E_{0.2}}\right) x \left(\frac{\sigma - \sigma_{0.2}}{\sigma_{1.0} - \sigma_{0.2}}\right)^{n'0.2,1.0} + \varepsilon_{t0.2} \tag{2.8}$$

where $\varepsilon_{t0.2}$ and $\varepsilon_{t1.0}$ are total strains at $\sigma_{0.2}$ and $\sigma_{1.0}$, respectively; and $n'_{0.2,1.0}$ is the strain hardening exponent. Equation 2.8 has been found to give excellent agreement with measured stress–strain curves in both tension and compression (e.g.

Ashraf *et al*., 2006). Till date, Gardner and Ashraf (2006) model has been generally accepted as the most accurate material model for LDSS.

2.7.3 Initial imperfections

The term geometric imperfection generally refers to the alteration of the shape from the perfect geometry. Generally, geometric imperfection comes in forms of denting, undulation in plates, bowing, warping and twisting while manufacturing, transporting or fabrication. The imperfection that occurred on the surface are termed as local imperfection and the one along the whole member in any direction (e.g. bowing, warping and twisting) is termed as global imperfection. The magnitude of geometric imperfection greatly affects the structural behavior (load carrying capacity, deformation, post buckling) of structures. Experimentally, imperfections can be measured in situ by using techniques and instruments like theodolite (Yuan *et al*., 2014; Young and Liu, 2002), feeler gauges and a straight edge (Gardner and Nethercot, 2004c); laser set up (Becque and Rasmussen, 2009) etc.

Studies on local imperfections have been reported by Dawson and Walker (1972); Sun and Butterworth (1998); Gardner (2002); Gardner and Nethercot (2004a), Theofanous and Gardner (2009); Theofanous *et al*., (2009a) etc. for square, rectangular, circular, oval hollow sections etc. For square and rectangular hollow sections, Gardner (2002) proposed the following expression for imperfection magnitude (w_o) (Equation 2.9):

$$w_o = 0.023\left(\frac{\sigma_{0.2}}{\sigma_{cr}}\right)t \qquad (2.9)$$

where, σ_{cr} is the elastic critical buckling stress determined from the buckling analysis, and t is the thickness. For the case of oval / elliptical hollow sections, Gardner (2002); Theofanous *et al*., (2009a); Chan and Gardner (2008) suggested for the expression given below (Equation 2.10):

$w_o = t/100$ (2.10)

For circular hollow sections, Gardner and Nethercot (2004a) suggested slightly higher value of $w_o = 0.2t$.

The global buckling is taken as out-of-straightness of a member from its straight perfect line. Usually initial out-of-straightness is normally expressed as a fraction of length of member. Gardner and Nethercot, 2004a recommend a global imperfection magnitude of $h/2000$ based on the study of square and rectangle section. Theofanous and Gardner (2009) conducted both the experimental and numerical analysis, in which for global buckling imperfection amplitudes four fractions of buckling length i.e. $h/500$, $h/1000$, $h/1500$ and $h/2000$ have been taken into account. Based on the study, it has been seen that that $h/1500$ provides the most accurate result for comparison of FE results with those of experimental results. For flat oval hollow sections, Zhu and Young (2012) have found that a global imperfection value of $h/1500$ in FE models has been able to predict the experimental results. Similar magnitude of $h/1500$ has also be used by Patton and Singh (2013) for the numerical analysis of slender L-, T-, + cross section columns

2.7.4 Residual Stress

Residual stresses are stresses that are induced in the absence of any external load or force. Residual stresses may arise from different mechanisms like inelastic (plastic) deformations, temperature gradients or structural changes while welding, etc. In the literature, the effect of residual stress has been reported to have less significant effect on the structural behavior under compression (Gardner and Nethercot, 2004a; ; Ellobody and Young, 2005; Theofanous *et al.*, 2009; Gardner *et al.*, 2011; Huang and Young, 2014b).

2.8 SUMMARY

This chapter gives a review of research activities that have been reported on unperforated and perforated hollow steel members. A brief introduction on stainless steel members with a special focus on the relatively new and promising material 'LDSS' has also be presented. Design methods (e.g. EWM, DSM, CSM), manual (e.g. ASDM) and codes / specifications (EN 1993-1-4, 2006; AS/NZS 4673; 2001, ASCE 8-02; 2002) that are relevant for the steel design have been summarised. In addition, key FE modelling parameters viz., non-linear material models, local and global imperfections, residual stress) associated for performing GMNIA (geometrically and materially nonlinear imperfect analysis) of thin-walled structures, have been discussed.

Based on the literature review, it has been seen that, several studies have been made on both carbon and stainless steel tubular sections (e.g. circle, oval, ellipse, square, rectangle, L, T, + etc.) subjected to compressive load. However, the studies on LDSS flat oval hollow tubular sections have not been reported.

CHAPTER 3

NUMERICAL STUDY OF FIXED ENDED LEAN DUPLEX STAINLESS STEEL (LDSS) FLAT OVAL HOLLOW STUB COLUMNS UNDER PURE AXIAL COMPRESSION

3.1 INTRODUCTION

In Chapter 2, it has been highlighted that limited experimental studies on the structural behaviour of LDSS hollow columns have been reported in the literature, more specifically, from the research groups of Gardner and Young, and their co-workers (e.g. Theofanous and Gardner, 2009; Huang and Young, 2012, 2014a, 2014b, 2015). Understandably, such inherent limitations are influenced by costs, time, technical workforce, testing frame capacity (load as well as size), loading actuator capacity, measurement devices, data acquisition systems etc. (e.g. Ellobody *et al.*, 2014), making it practically difficult (if not impossible) to generate experimentally, comprehensive data encompassing a wide range of parameters of interests such as cross-sectional dimensions, cross-sectional shapes, lengths etc. Hence, in the literature (e.g. Gardner and Nethercot, 2004a; Ashraf *et al*., 2006b;

Hassanein, 2011; Zhu and Young, 2012; Patton and Singh, 2013; Huang and Young, 2014b) several numerical techniques such as finite element (FE) modelling procedures were adopted to compensate the shortage of experimental data and broaden the data matrix. FE modelling has now become a useful and efficient analysis tool for studying the behaviour of metal structures, when validated (or calibrated) against available test results. In addition, such validated FE modelling procedures (through use of appropriate input parameters such as FE mesh, boundary conditions, constitutive models etc.) can be effectively used to gain significant insight e.g. stresses, strains, deformations at desired specimen locations which hitherto would be difficult to assess through instrumentation (e.g. Ellobody *et al.*, 2014). In this chapter, an attempt has been made to systematically study the parametric effects of cross-sectional dimensions (e.g. element radius, flat element length, thickness) on LDSS flat oval stub columns under the action of pure axial compression, using the commercial Finite Element (FE) software, Abaqus (2009). Initially, the FE modelling approach followed in this study has been validated with experimental data reported by Theofanous and Gardner (2009) for LDSS (Grade EN 1.4162) hollow-section column for similar loading and end conditions. The FE parametric results are then compared with EN 1993-1-4 (2015), ASCE 8-02 (2002), AS/NZS 4673 (2001) and ASDM (2002), to check their applicability for flat oval LDSS stub columns. The suitability of promising design methods such as the DSM (Schafer, 2002; NAS, 2007) and the CSM (Gardner, 2008; Afshan and Gardner, 2013) for the design of LDSS flat oval section stub columns has also been assessed on the basis of the FE results reported herein.

3.2 FINITE ELEMENT (FE) MODELLING

3.2.1 General

Parametric study of the structural performance of fixed ended flat oval stub hollow columns has been performed with ABAQUS (2009) considering different values of r (curvature radius), l_f (flat length) and t (thickness) of flat oval cross-section,

keeping the width between flat elements constant (w = 300 mm). FE analyses considered both the local imperfection and material nonlinearity aspects. Current FE modelling approach has been validated by comparing with an experimental study on a square LDSS stub column under axial compression (Theofanous and Gardner, 2009). The following sub-sections discuss the main modelling parameters considered in this study.

3.2.2 Geometry and boundary conditions

The FE modelling approach followed the same procedure as those published in the literature for fixed-ended hollow steel columns (Theofanous and Gardner, 2009; Patton and Singh, 2012; Ashraf *et al*., 2006b; Gardner and Ministro, 2004). Typical cross-section and boundary conditions are presented schematically in Figures 3.1 and 3.2. Height (h) of the stub column is taken as 900 mm. Flat length (l_f), curvature radius (r) and thickness (t) are varied in the range 300-700 mm, 150-750 mm, and 3-20 mm respectively, to encompass a wide range of cross-sectional slenderness ratios. Bottom part of the column was fixed while allowing the top loaded part to undergo free vertical translation (i.e. along the column length direction, axially). Reference points (RP-1 and RP-2) were provided to define the boundary conditions by constraining column ends through kinematic coupling (available in Abaqus, 2009), as shown in Figure 3.2. Except for the vertical translation, all degree of freedom were restrained at the loaded end. Using displacement control, a centrally concentrated normal displacement was applied statically through the reference node (RP-2) to apply uniform displacement at the top surface of the columns.

3.2.3 Finite element mesh

Four-noded doubly curved shell (S4R) element with reduced integration (Abaqus, 2009) having six degrees (3 rotations and 3 translations) of freedom per node has been utilised to discretise the models (Patton and Singh, 2012) as it was shown to accurately model several types of hollow columns with cross-sections such as

square (Theofanous and Gardner, 2009; Patton and Singh, 2012), oval (Zhu and Young, 2012) etc. FE element size has been kept at ~11.5 mm x 11.5 mm for the FE models following mesh convergence study (by performing linear elastic eigen value buckling analysis). The number of S4R elements used in the analyses for various models ranges from ~ 1000 to 11,000. A typical FE mesh is shown in Figure 3.2.

3.2.4 Local geometric imperfection

The buckling mode shapes of the columns were found out by linear elastic eigen buckling analyses, using the Lanczos method (Abaqus, 2009). Modified Riks method (Riks, 1972, 1979) was employed to capture the full load–deformation response accurately. The first (i.e. lowest) local buckling mode shape was utilized to perturb the geometry of the columns, by scaling with the local imperfection amplitude of 1% of plate thickness (i.e. *t*/100) as recommended in the literature (Theofanous *et al*., 2009a; Chan and Gardner, 2008).

3.2.5 Material modelling

According to EN 10088-4 (2009), the minimum specified material properties of LDSS Grade EN 1.4162 are 0.2% proof stress ($\sigma_{0.2}$) of 530 MPa and ultimate stress (σ_u) of 700-900 MPa. The material properties given in Table 3.1 (Theofanous and Gardner, 2009) is used in deriving stress strain of LDSS material as suggested by Gardner and Ashraf, 2006 (modified version of original Ramberg–Osgood, 1943; Rasmussen, 2003). Poisson's ratio was taken as 0.3. The LDSS stress (σ) - strain (ε) (Figure 3.3) consisting of two parts *viz.*, (a) up to 0.2% proof stress ($\sigma_{0.2}$), where Ramberg-Osgood model (Ramberg and Osgood, 1943) is considered and (b) from $\sigma_{0.2}$ to $\sigma_{1.0}$, Gardner and Ashraf model (Gardner and Ashraf, 2006) is used as shown in Equation 3.1.

$$\varepsilon = \left(\frac{\sigma - \sigma_{0.2}}{E_{0.2}}\right) + \left(\varepsilon_{t1.0} - \varepsilon_{t0.2} - \frac{\sigma_{1.0} - \sigma_{0.2}}{E_{0.2}}\right) x \left(\frac{\sigma - \sigma_{0.2}}{\sigma_{1.0} - \sigma_{0.2}}\right)^{n'0.2,1.0} + \varepsilon_{t0.2} \qquad (3.1)$$

where $\epsilon_{t0.2}$ and $\epsilon_{t1.0}$ are total strains at $\sigma_{0.2}$ and $\sigma_{1.0}$, respectively; and $n'_{0.2,1.0}$ is the strain hardening exponent. Equation 3.1 has been found to give excellent agreement with the measured stress–strain in both tension and compression (e.g. Theofanous and Gardner, 2009; Patton and Singh, 2012). Further, similar material properties were considered for both the flat and curve regions. However, it may be noted that, strength enhancement can take place in the corner region, due to work hardening, during cold forming of stainless steel hollow sections (Theofanous *et al.*, 2009a; Ashraf *et al.*, 2005). Hence, the present FE idealisation is likely to provide a conservative estimate of the actual experimental values. In this study, the effects of residual stresses are not accounted for to simplify the modelling process, as done in similar studies (Theofanous *et al*., 2009a; Gardner *et al*., 2011). Further, Huang and Young (2014b) reported that the difference between FE results, with and without the inclusion of measured membrane residual stresses is ~1%, in their study on cold formed LDSS columns. Similar type of conclusion has also been made by Ellobody and Young (2005) in their FE study of cold formed high strength stainless steel columns.

3.2.6 Validation of finite element model

A result of the experimental investigation by Theofanous and Gardner (2009) on LDSS (Grade EN 1.4162) square hollow column-80x80x4-SC2 has been used to verify the developed FE modelling approach in this study. The material properties and column dimensions of the square model are shown in Tables 3.1 and 3.2. The material model shown in Figure 3.3 was used as input parameters to Abaqus (2009), by converting into true stress (σ_{true}) and true plastic strains $\left(\varepsilon_{true}^{pl}\right)$ using the following Equations 3.2- 3.3.

$$\sigma_{true} = \sigma_{nom}(1+\varepsilon_{nom}) \tag{3.2}$$

$$\varepsilon_{true}^{pl} = \ln(1+\varepsilon_{nom}) - \frac{\sigma_{true}}{E_o} \tag{3.3}$$

where E_o is the Young's modulus; σ_{nom} and ε_{nom} are the engineering stress and strain respectively.

Variation of load (P)-axial displacement (δ) plots of the experimental (Theofanous and Gardner, 2009) and the present FE analysis of stub column has been plotted in Figure 3.4 where the ultimate load (P_u) and deformation at P_u (i.e. δ_u) are in good agreement between the experimental and FE results. Further in Figure 3.4, the effect of imperfection magnitudes (t/10, t/100, t/1000) are also plotted. And it can be seen that local buckling imperfection value of t/100 is found to give the best result. This verification ensures the accuracy of simulating stub columns with a good degree of confidence, and is then used in the subsequent study for fixed-ended flat oval stub columns.

3.3 Parametric study of LDSS flat oval hollow stub columns

Parametric study of the flat oval LDSS columns has been performed by varying flat length (l_f = 300 to 700 mm), thickness (t = 3 to 20 mm), curvature radius (r =150 to 750 mm), keeping both h (height) and w (width between flat plate elements) as constants i.e. h and w are taken as 900 mm and 300 mm respectively. A total of around 78 FE flat oval column models has been analysed with special focus on the ultimate load (P_u) and failure modes. The specimens are labelled with complete details of its cross-section like l300w300r150t5 where l300, w300, r150 and t5, refer to flat length of 300 mm, width between flat elements of 300 mm, curvature radius of 150 mm at the curve face and specimen thickness of 5 mm, respectively. The structural performance of the flat oval sections is also checked against some international design codes / rules.

3.3.1 Codal design considerations

Many design codes and manual are available for the design of cold formed stainless steel such as European (EN 1993-1-4, 2015) Code, American Society for Civil Engineers (ASCE 8-02, 2002) Standard, Australian/New Zealand Standard

(AS/NZS 4673, 2001), Automotive Steel Design Manual (ASDM, 2002) etc. (hereafter referred to as 'codal'), but none have design provisions for structural flat oval hollow columns. However, it may be worth mentioning that ASDM (2002) provides design guidance i.e. consideration of effective areas, for elemental local buckling interaction of curve and flat panels, for general mechanical engineering applications. The calculations of effective width/length (and hence effective area) are necessary for slender flat plates (EN 1993-1-4, 2015; ASCE-8-02, 2002; AS/NZS 4673, 2001; ASDM, 2002). ASCE 8-02 (2002) and AS/NZS 4673 (2001) specifications are similar, with flat plate buckling coefficient k taken as 4 (Zhu and Young, 2012). Zhu and Young (2011, 2012) considered semicircular curve portion of the section to be fully effective (i.e. gross area of the semicircular curved section is considered for load calculation) as the local buckling resistance of portions is relatively higher than that of the flat plates; whilst only effective area has been considered for the flat portions as per the provisions of the code (see Figure 3.5a for the schematic representation of the effective length, l_{ef}). Similar assumptions are made for the present study.

Considering the importance of curve portion in flat oval section, the curve sections can be divided into two groups i.e. fully effective (compact) and ineffective (slender) curve portions based on w/t ($w = D$ as D is diameter of circle) ratio. It may be noted that semi-circle element with $w/t < 40$ has been considered as fully effective as per AS/NZS 4600 (2005) (Zhu and Young, 2012). Thus, for parametric comparison, the flat oval hollow sections have been grouped into two categories with $w/t < 40$ (compact curve section) and $w/t \geq 40$ (slender curve section) (Zhu and Young, 2012).

The effective area calculations as per EN 1993-1-4 (2015), ASCE 8-02 (2002), AS/NZS 4673, (2001) and ASDM (2002) are briefly described below:

a) The present study of flat oval cross-sections comprises of Class 2 ($l_f/t\varepsilon \leq 35$), Class 3 ($l_f/t\varepsilon \leq 37$) and Class 4 ($l_f/t\varepsilon > 37$) sections as per EN 1993-1-4 (2015),

depending on the value of cross-section slenderness (l_f /$t\varepsilon$, where l_f is the flat element length, t is the plate thickness and $\varepsilon = \left(\frac{235}{f_y}\frac{E}{210000}\right)^{0.5}$, f_y is the material yield stress). For Class 2 and 3 sections, no deductions in material cross-sectional area are made (i.e. gross area, A_g is considered to be wholly effective) in the calculation of axial compressive strength. For Class 4 section, effective area (A_e) of cross-section is considered to take into account of the effect of local buckling. As per EN 1993-1-4 (2015), the effective width (l_{ef}) for Class 4 (i.e. for slender cross-sections) plated structural element, is based on a reduction factor (ρ; $\rho = l_{ef}/l_f$) parameter given by Equation 3.4,

$$\rho = \frac{0.772}{\bar{\lambda}_P} - \frac{0.079}{\bar{\lambda}_p^{\,2}} \text{ ; where } \bar{\lambda}_P = \frac{l_f/t}{28.4\varepsilon\sqrt{k}} \tag{3.4}$$

The effective area for Class 4 flat oval section is calculated using Equation 3.5.

$$A_e = A_g - 2\,(l_f - l_{ef})t \tag{3.5}$$

The cross-sectional resistance as per EN 1993-1-4 (2015) is then given by Equation 3.6.

$$P_{EN} = f_y A \tag{3.6}$$

where, A may be A_g or A_e depending on class type of the section under consideration.

b) As per ASCE 8-02 (2002) and AS/NZS 4673 (2001), the member capacity is calculated based on the effective width given by Equations 3.7-3.9. The effective width (l_{ef}) is dependent on the value of cross-sectional slenderness ratio, λ.

$$\text{For } \lambda \leq 0.673,\ l_{ef} = l_f \tag{3.7}$$

$$\text{For } \lambda > 0.673,\ l_{ef} = \rho l_f, \tag{3.8}$$

where, $\rho = \dfrac{\left(1-\dfrac{0.22}{\lambda}\right)}{\lambda} \leq 1.0$; $\lambda = \left(\dfrac{1.052}{\sqrt{k}}\right)\left(\dfrac{l_f}{t}\right)\left(\sqrt{\dfrac{f}{E}}\right)$

where f ($= \sigma_{cr}$) is the critical stress for unstiffened compression element. The value of k is conservatively taken as 4.0. The member capacity is then computed as per Equation 3.9.

P_{ASCE} or $P_{AS/NZS} = f_y A_e$; where A_e is calculated based on Equation 3.5. (3.9)

c) In the case of ASDM (2002), the total effective area is calculated as a sum of the effective areas of flat and curved sections (see Figure 3.5b). The effective width of flat (l_{ef}) and curved (l_{ec}) elements are determined as a function of cross-sectional slenderness ratio (λ) using Equations 3.7 and 3.8 (ASCE 8-02, 2002; AS/NZS 4673, 2001; Zhu and Young, 2011). However, as f_y > 552 MPa, a reduced yield strength (f_{yrs}) be substituted for limiting value of f (ASDM, 2002) as given by Equation 3.10.

$$f_{yrs} = f = \left(1-0.2\sqrt{\frac{l_f}{t}}\sqrt{\frac{f_y}{E}}\right)f_y \tag{3.10}$$

Further, for the curve portion instead of completely neglecting the central portion as done for flat elements, an effective thickness (t_e) has been considered (Equation 3.11).

$$t_e = \left(\frac{A_o}{A}\right)\left(\frac{f_y}{f}\right)t \tag{3.11}$$

where, A_o denotes the equivalent area in compression element respectively (see Equations (3.12-3.14))

$A_o = A$; for $\dfrac{D}{t} \leq 0.114\dfrac{E}{f_y}$ (3.12)

$$A_o = \left(\frac{2}{3} + \frac{0.038 \frac{E}{f_y}}{\frac{D}{t}} \right) A; \quad \text{for} \quad 0.114 \frac{E}{f_y} < \frac{D}{t} \leq 0.448 \frac{E}{f_y} \tag{3.13}$$

$$A_o = \left(\frac{0.336 \frac{E}{F_y}}{\frac{D}{t}} \right) A; \quad \text{for} \quad \frac{D}{t} \geq 0.448 \frac{E}{F_y} \tag{3.14}$$

where, D = diameter of the curve element.

Then, the effective area for the curve (A_{ec}) and flat (A_{ef}) portions are calculated as per Equations (3.15-3.16). The total effective area of the flat oval section (A_e) as per ASDM (2002) is then given by Equation 3.17.

$$A_{ec} = 2(l_c - l_{ec})t_e + 2tl_{ec} \tag{3.15}$$

$$A_{ef} = 2tl_{ef} \tag{3.16}$$

$$A_e = A_{ec} + A_{ef} \tag{3.17}$$

where, l_c is the arc length of the curve element.

The member capacity of ASDM (2002) is calculated as per Equation 3.18.

$$P_{ASDM} = f_y A_e \tag{3.18}$$

In ASDM, the ineffective portion of the curve element is assumed to carry critical buckling stress (unlike a flat element) of a circular cylinder with equivalent radius and thickness (ASDM, 2002; Zhu and Young, 2012).

3.3.2 Direct strength method

The Direct Strength Method (DSM) was proposed by Schafer and Pekoz (1998) for the design of cold formed steel members undergoing local, global and distortional buckling. DSM does not rely on effective width but it requires the estimation of elastic buckling load in local, global and distortional buckling modes. The elastic buckling load can be determined by using existing numerical (Schafer and Adany,

2006) or FEM (finite element method) (Abaqus, 2009). The design procedure of DSM has been given in detail in Appendix 1 of NAS (2007). In DSM, the slenderness ratio of the full cross-section is employed instead of the most slender constituent elements. The column design equations of DSM for cold formed steel (NAS 2007) are shown in Equations (3.19-3.21). The nominal axial strength, P_{DSM} is given by Equation 3.19 (as distortional buckling is not considered for flat oval being a closed section (Zhu and Young, 2012))

$$p_{DSM} = \min(.P_{ne}, P_{nl}) \tag{3.19}$$

where,

$$p_{ne} = \begin{cases} (0.658^{\lambda_c^2})P_y & \text{for} \quad \lambda_c \leq 1.5 \\ \left(\frac{0.877}{\lambda_c^2}\right)P_y & \text{for} \quad \lambda_c \leq 1.5 \end{cases} \tag{3.20}$$

$$P_{nl} = \begin{cases} P_{ne} & \text{for} \quad \lambda_l \leq 0.776 \\ \left[1 - 0.15\left(\frac{P_{crl}}{P_{ne}}\right)^{0.4}\right]\left(\frac{P_{crl}}{P_{ne}}\right)^{0.4} P_{ne} & \text{for} \quad \lambda_l > 0.776 \end{cases} \tag{3.21}$$

Here, $P_y = f_y A$; $\lambda_c = \sqrt{P_y / P_{cre}}$; $\lambda_l = \sqrt{P_{ne} / P_{crl}}$, where P_{cre} $(= \pi^2 EA/(h_e/r_y)^2)$, P_{crl}, r_y, h_e, P_{ne} and P_{nl} are the critical elastic buckling load in flexural buckling, critical elastic local buckling load, radius of gyration of gross cross-section about the minor axis of buckling, effective height of column, nominal axial strength for flexural buckling and nominal axial strength for local buckling as well as interaction of local and overall/global buckling respectively.

3.3.3 Continuous strength method

The Continuous Strength Method (CSM) was proposed by Gardner (Gardner, 2008; Afshan and Gardner, 2013) based on the relationship between cross-section slenderness and local buckling along with strain hardening effect. In this method, a 'base' curve has been derived based on a calibration done against several stub column experimental data. The base curve relates between cross-section's

slenderness (denoted by $\bar{\lambda}_p$) and normalised strain capacity ($\varepsilon_{csm}/\varepsilon_y$), where ε_{csm} and ε_y denote the deformation/strain capacity (obtained by subtracting the plastic strain corresponding to 0.2% proof stress from the actual local buckling strain, ε_{lb}; $\varepsilon_{lb} = \delta_u/h$, δ_u and h are the deformation corresponding to ultimate load and column length respectively), and strain at yield ($\varepsilon_y = f_y/E$) respectively. The expressions for the base curve, showing relationship between $\varepsilon_{csm}/\varepsilon_y$ and $\bar{\lambda}_p$ is given by Equation 3.22.

$$\frac{\varepsilon_{csm}}{\varepsilon_y} = \frac{0.25}{\bar{\lambda}_p^{3.6}} \text{ but } \frac{\varepsilon_{csm}}{\varepsilon_y} \leq \min\left(15, \frac{0.1\varepsilon_u}{\varepsilon_y}\right); \ \bar{\lambda}_p \leq 0.68 \tag{3.22}$$

where, ε_u is the ultimate tensile strain.

The column member capacity according to CSM (Afshan and Gardner, 2013) is calculated as per Equations 3.23-3.29.

$$f_{csm} = f_y + E_{sh}\varepsilon_y\left(\frac{\varepsilon_{csm}}{\varepsilon_y} - 1\right) \tag{3.23}$$

$$P_{csm} = f_{csm}A \tag{3.24}$$

where f_{csm}, ε_{csm} and ε_y (= f_y/E) denote the limiting stress determined from the strain hardening material model, the strain at ultimate load and yield, respectively. The load capacity as per CSM (Afshan and Gardner, 2013) is determined based on the gross sectional area (A). The strain ratio, $\varepsilon_{csm}/\varepsilon_y$ shows the deformation capacity of the cross-section and is given by Equation 3.22.

The strain- hardening slope (E_{sh}) is given by Equation 3.25.

$$E_{sh} = \frac{f_u - f_y}{0.16\varepsilon_u - \varepsilon_y} \tag{3.25}$$

where, f_u is the ultimate tensile stress. The cross-sectional slenderness ($\bar{\lambda}_p$) is calculated as shown in Equation 3.26.

$\bar{\lambda}_p = \sqrt{\frac{f_y}{\sigma_{cr,cs}}}$, based on the centreline dimensions. (3.26)

where $\sigma_{cr,cs}$ is the elastic buckling stress of the full cross-section (can be determined either through elastic buckling analyses using finite strip method (such as CUFSM (Schafer and Adany, 2006)) or finite element method (such as Abaqus, 2009). The two upper bounds i.e. 15 and $0.1\varepsilon_u / \varepsilon_y$ (see Equation 3.22 are based on the predicted cross-section deformation capacity; the upper limit of 15 corresponds to the material ductility requirement in EN 1993-1-1 (2005) and the second limit of $0.1\varepsilon_u / \varepsilon_y$, ensures no significant over-predictions of the cross-sectional resistance (Afshan and Gardner, 2013). The base curve is allowed to pass through point (0.68,1) as it is the identified limit between slender and non-slender section (Afshan and Gardner, 2013). Beyond this point it is mention not to have any significant benefit for strain hardening.

Depending on the load capacity of column i.e. either $P_u \geq P_y$ or $P_u < P_y$, the slenderness ratio ($\varepsilon_{csm}/\varepsilon_y$) have been defined by the following Equations 3.27-3.29, in accordance with the cross-sectional slenderness $\bar{\lambda}_p$.

For cross-section slenderness, $\bar{\lambda}_p \leq 0.68$

$$\frac{\varepsilon_{csm}}{\varepsilon_y} = \frac{\varepsilon_{lb} - 0.002}{\varepsilon_y} = \frac{\delta_u / h - 0.002}{\varepsilon_y} \quad \text{for } P_u \geq P_y \qquad (3.27)$$

$$\frac{\varepsilon_{csm}}{\varepsilon_y} = \frac{P_u}{P_y} \quad \text{for } P_u < P_y \qquad (3.28)$$

In case $\bar{\lambda}_p > 0.68$,

$$\frac{\varepsilon_{csm}}{\varepsilon_y} = \frac{P_u}{P_y} \qquad (3.29)$$

Continuous Strength Method (CSM) has been applied for the strength calculation of stub hollow columns consisting of either flat (e.g. square section) or curve (e.g. circular section) sections (Gardner and Theofanous, 2008; Theofanous and Gardner, 2011; Huang and Young, 2013) but so far, its applicability for combined sections with flat and curve portions together has not been reported.

3.3.4 Modified DSM (Huang and Young, 2014b)

The original Direct Strength Method (DSM; see Section 3.3.2) was reported to give conservative results for both slender and non-slender sections by Huang and Young (2014b). Hence, Huang and Young (2014b) proposed a modification to the original DSM (hereafter referred to as modified DSM or DSM*) for the design of LDSS members, based on their experimental study on LDSS square and rectangular sections. The modified DSM method (DSM*) has been briefly presented, below.

The modified nominal axial strength, P^*_{DSM} is given in Equations 3.30-3.32.

$$p^*_{DSM} = \min(P_{ne}, P_{nl}) \quad (3.30)$$

where,

$$p_{ne} = \begin{cases} (0.87^{\lambda_c^2})P_y & \text{for } \lambda_c \le 1 \\ \left(\frac{0.877}{\lambda_c^2}\right)P_y & \text{for } \lambda_c \le 1 \end{cases} \quad (3.31)$$

$$P_{nl} = \begin{cases} P_{ne} & \text{for } \lambda_l \le 0.769 \\ \left[1 - 0.16\left(\frac{P_{crl}}{P_{ne}}\right)^{0.4}\right]\left(\frac{P_{crl}}{P_{ne}}\right)^{0.4} P_{ne} & \text{for } \lambda_l > 0.769 \end{cases} \quad (3.32)$$

A comparison of DSM (Equations 3.20 and 3.21) and DSM* (Equations 3.32 and 3.33), shows that the difference between the DSM and DSM* expressions are in the values of coefficients of P_y and P_{ne}; and on the limits of λ_l and λ_c. It may be noted that DSM* expressions have not been checked for their applicability for flat oval LDSS sections.

3.3.5 Reliability analysis

The results of the present FE analyses on flat-oval hollow stub columns have been compared with those predicted by various international standards or codes (e.g. EN 1993-1-4, 2015; ASCE 8-02, 2002; AS/NZS 4673, 2001), design manual (e.g. ASDM, 2002), and design methods (e.g. DSM (Schafer, 2002) and DSM* (Huang and Young, 2014b) and CSM (Afshan and Gardner, 2013)), in order to assess their applicability. Based on the comparison, reliability analysis has been performed following the method provided in the commentary of the ASCE Specification (ASCE 8-02, 2002) for cold formed steel structures, in order to evaluate the reliability of using the aforementioned design codes/methods/manual for the design of flat-oval stub columns. In the reliability analyses, the resistance factor (Φ) of 0.91, 0.85, 0.85 are used for the EN 1993-1-4 (2015), ASCE 8-02 (2002) and AS/NZS 4673 (2001) specifications, respectively, have been used to find the reliability index (β). The resistance factors for DSM (Schafer, 2002; NAS, 2007), DSM* (Huang and Young, 2014b) and CSM (Afshan and Schafer, 2013) have been taken as 0.80, as specified by the NAS (2007) for sections that are not pre-qualified (Zhu and Young, 2012). For ASDM (2002), the same resistance factor as that of ASCE 8-02, 2002 i.e. 0.85 has been adopted as in the work of Zhu and Young (2011). The load combinations of 1.35DL+1.5LL, 1.2DL+1.6LL and 1.25DL+1.5LL (where LL and DL are the live and dead loads) have been used for the reliability analysis following EN 1993-1-4 (2015), ASCE 8-02 (2002) and AS/NZS 4673 (2001). The ratio of DL/LL is taken as 0.2 as per NAS (2007). The statistical values of M_m, F_m, V_M and V_F (i.e. mean, coefficients of variation (COV) of material and fabrication, respectively) are taken as 1.10, 1.0, 0.10 and 0.05 according to the ASCE specification (ASCE 8-02, 2002). In the case of DSM, DSM* and CSM, the load combination factors as per ASCE 8-02 (2002) i.e. 1.2DL+1.6LL, has been considered. For the case of ASDM (2002) also, following Zhu and Young (2011), the load combination has been taken as 1.2DL+1.6LL, which is similar to that given by ASCE 8-02 (2002). In order to take into account of

the influence of the number of data, a correction factor (C_p) given in Equation F1.1-3 of NAS (2007) specification has been considered. From NAS (2007), a target reliability index (β_o) value of 2.5 is used for the reliability analyses. This value defines the lower limit for a design to be considered reliable.

3.4 RESULTS AND DISCUSSION

3.4.1 Deformed shapes

Von-Mises stress contours superimposed on deformed shapes for *l*300*w*300*r*300*t*3 and *l*300*w*300*r*300*t*20 specimens (i.e. l_f = 300 mm, w = 300 mm, r = 300 mm) corresponding to δ_u (axial deformation/shortening corresponding to ultimate load, P_u) and 1.5δ_u (i.e. 1.5 times the axial deformations at P_u); for Class 4 (t = 3 mm; slender cross-section) and Class 3 (t = 20 mm; stocky cross-section) sections are shown in Figure 3.6. In Figure 3.6, the values of von-Mises stress ≥ 657 MPa (i.e. $\sigma_{0.2}$) are colored in grey, in order to identify areas which have crossed the yield stress. This method is followed in all the subsequent such contour plots. Also, in order to have consistensy in the stress contour plots, only von-Mises stress (hereafter refererred as 'stress') are plotted. It can be seen from Figure 3.6 that at P_u, the von-Mises stress for Class 3 section (*l*300*w*300*r*300*t*20) has exceeded the yield stress, indicating that it is fully yielded without any signs of surface buckling (Figure 3.6c), whereas in the case of thinner section i.e. Class 4 (*l*300*w*300*r*300*t*3) section, initiation of local buckling is visible on the flat surfaces (or elements) with very small areas at the junction of flat and curve surfaces showing signs of yielding (Figure 3.6a). Although initiation of buckling is not readily seen at P_u, for thin sections, evidences of non-uniform distribution of stresses can be seen on the curve surfaces (see Figure 3.6a). At post P_u i.e. when the axial deformation has reached 1.5δ_u, local buckling can be seen at two locations, on the flat surface and with centrally located region on curve surfaces being slightly distressed (i.e. stress dropping below yield stress) for Class 3 section (Figure 3.6b); on the other hand, for Class 4 section, buckling on both the flat and curve surfaces can be observed along

with extended areas of yielded zones, especially corner region and central portion of the curve surfaces (Figure 3.6b). From Figures 3.6a and 3.6b, it can also be seen that as compared to the flat surfaces, relatively more surface areas (i.e. effective in taking load) of higher stress is observed on curve surface. Presence of effective areas (i.e. relatively effective in carrying load) on the sides (shown by relatively higher stress regions on the sides of the flat surface) and ineffective areas in the central portion of the flat surface can also be seen in Figure 3.6a, whereas in the case of Class 3 (Figure 3.6c), all areas are effective in taking the load. Further, evidence of interaction between the flat and curve elements can be seen for thin section (see yielded zones at the junction of flat and elements in Figures 3.6a and 3.6b), whereas such interaction appears to be absent for the thicker section (Figure 3.6d) even at post P_u (i.e. even at $1.5\delta_u$).

3.4.2 Variation of buckling loads

3.4.2.1 Effect of curvature radius *(r)*

Variation of load (P) with axial shortening/deformation (δ) for the thin (t = 3 mm) and thick (t = 20 mm) section stub columns, for r = 150, 300 and 750 mm (l_f = 300 mm) are shown in Figures 3.7 and 3.8 respectively. For the case of thin section i.e. t = 3 mm (Figure 3.7), it can be seen that as the value of r increases there is a drop in the values of P_u. For the semicircular section (i.e. r = 150 mm or r/w = 0.5), post P_u, snap-through buckling pattern can be seen, where at P_u (T1), initiation of bucking can be seen on the flat face (i.e. not on the surface) with the appearance of a small yielded portion located at the junction of plate and surfaces around mid-height. Following the drop in P_u due to buckling at the mid-height of the flat portion (T2), a somewhat stable load profile can be seen till around T3 (T3 corresponds to the second peak), and this may be related to the redistribution of the load towards the curve portions. At post P_u (i.e. T2 and T3), an increase in the spread of high stress or yielded region can be observed on the surfaces, indicating a major portion of the load is carried by the curve section, due to enhanced stiffness of the curve

section. Post T3 drop in P, may then be related to the enhanced buckling of the flat portions at column mid-height, with stress relaxation and redistribution in the curve portions (see T4).

On the other hand, for larger values of r (or flatter curve sections), a snap-back buckling pattern is observed, where at P_u, initiation of buckling can be seen both on the flat and curve sections (S1), with the occurrence of a very small yielded portion located at the mid-height of the curve section. However, it can be seen from S2, that snap-back buckling has taken place due to the occurrence of buckling at the mid-height (with sudden relaxation of stress on either sides of the mid-height region) of the curve portion. Beyond S2, P increases till around S3 (S3 corresponds to the second peak), and this occurs mainly because of the increase in yielded zone (indicating more load being taken up) near the mid-height column of the curve portion. Again it must be noted that the spread of this yielded zone towards the curve portion is constrained due to the relatively sharp junction corner, hence confined to the junction areas.

At post P_u, the yielded region on the curve surface is increased and spread to the junction between flat and curve surfaces (S2 and S3). Also, it is seen that deformation at P_u (i.e. δ_u) decreases with reducing r/w value, suggesting that semicircular section provided improved ductility at P_u, as compared to other flatter sections. In contrast to semi-circular curve sections, post P_u yielded region is confined to a relatively smaller region at mid-height, indicative of lesser load bearing capacity of the flatter sections. The drop in P beyond S3, may be associated with the buckling of the flat portions (see S4) of the column, with the yielded zone being increased on both the curve and flat portions.

Further, for the thin section under consideration (t = 3 mm), there is an indication of the tendency to spread the buckling from flat elements on to the curve elements, at lower r values e.g. r = 150 mm (T1, T2 and T3), although such spread appears to be absent for larger r values (say r = 750 mm; S1, S2, S3). Such spreading phenomena

for small values of *r/t* have been reported by Parks and Yu (1989) in their stiffened flat-oval experimental tests. This may be because, when the radius of the curve portion is small and the flat length is sufficiently long, buckling of the flat element would have occurred earlier, and the chance of spreading the flat buckling would be sufficiently improved when a smooth corner junction / transition of the flat and elements is present. When the radius of the curve portion is large, there would be a relatively sharp corner at the junction of the flat and curve elements, which would arrest the flat element buckling from crossing over to the curve elements.

In the case of, thicker section (t = 20 mm) (see Figure 3.8), it can be seen that both the semi-circular and flatter curve sections have completely yielded at P_u (T1 and S1), although the value of P_u is significantly larger for semi-circular curve section, as compared to that of flatter curve sections. Further, the change in P_u for flatter curve sections (i.e. $r \geq 300$ mm) is found not to be very significant. At post P_u, the rate of decrease in P with deformation is higher for semicircular section (indicated by the appearance of buckling and reduction of stress below yield stress on flat surfaces) as compared to flatter sections where the post P_u load behavior is relatively flatter for comparable axial deformation, i.e. post buckling strength is relatively higher in the case of flatter curve sections (or higher *r/w* values). Again, appearance of buckling can be seen on the flat surfaces without any signs of stress reduction. This may be due to relatively higher strength (or stiffness) mismatch between the flat and semicircular sections as compared to the mismatch between flat and flatter curve sections. Further, the reduction in P_u with increasing r or *r/w* can be related to the reduction in the effective cross-sectional area, due to the reduction in the curvature length. The behaviour of δ_u is found to be different in the case of thick section, wherein semicircular section gave the least value of δ_u, with δ_u remaining almost stable for higher values of *r/w*. As in the case of thin sections (Figure 3.7) as discussed above, at post P_u, evidence of the tendency to spread flat element buckling on to the curve portions can be seen (see Figure 3.8; T2) for the lower r value, whereas such tendency appears to be prevented (see Figure 3.8; S2)

due to the sharp corner junction of the curve and flat portions. Moreover, from Figures 3.7 and 3.8, it appears that, for lower values of r, buckling of the flat portion controls the stub column strength whereas, for larger r values the strength is mainly decided by the buckling of the curve portion, for both thin and thick sections.

Variation of P_u with r/w is plotted in Figure 3.9, for different thicknesses, with t ranging from 3-20 mm for a fixed flat length, l_f = 300 mm. A value of r/w = 0.5 indicates the section is flat oval (with semicircular curve section), whereas a value of $r/w = \infty$, represents a square (with infinite radius of curvature for the curve sections) section. It can be observed that for the values of t (t > 3 mm), semicircular curve section (i.e. r/w = 0.5) produces the highest value of P_u; for larger values of r, i.e. $r/w \geq 0.5$, a sharp drop in the values of P_u can be seen, the drop being relatively larger for higher values of t. In the case of the thinnest section (t = 3 mm) considered, a relatively smoother (or linear) drop is seen in P_u. As r/w increases, P_u values converge to those of square sections ($r/w = \infty$). These observed behaviour of P_u are consistent with the variation of effective area, A_e (computed as per EN 1993-1-4, 2015) shown in Figure 3.10. As mentioned in Section 3.3.1, EN 1993-1-4 (2015) is silent on the estimation of A_e for flat oval sections, and hence, full area is taken for the curve portions, whereas effective area is taken for the flat portions. In Figure 3.10, it can be seen that, semicircular section produced the highest value of A_e available for resisting the load, and for flatter sections, although a decrease in the values of A_e can be seen with increasing r/w (r/w > 0.5), the slope of decrement is relatively mild. Whilst the relatively sharp drop in A_e (from semicircular section value) is clearly visible in Figure 3.10, for the thinnest section considered (t = 3 mm), such behaviour is not seen in P_u (see Figure 3.9), this may be because, for the thin section (with semicircular curve portions), the assumption of the gross semicircular portion being effective may not be strictly valid.

In Figure 3.11, variation of normalized P_u i.e. P_u/A_gf_y (where A_gf_y is the material gross yield capacity) with r/w is shown. It can be seen that for all the values of r/w, sections with $t \geq 12.5$ mm have $P_u/A_gf_y > 1$, suggesting that corresponding sections have yielded when P_u is reached, whilst for $t \leq 12.5$ mm, $P_u/A_gf_y < 1$, indicating that buckling has occurred before reaching the gross yield load. The increase of P_u beyond gross yield for thicker sections can be related to strain hardening effect. The decrease in P_u/A_gf_y for thinner sections ($t \leq 12.5$ mm) with increasing values of r/w, may be associated with the earlier occurrence of buckling due to reduced stiffness for flatter sections as compared to sections with lower radius of curvature for the curve portions. However for the thicker sections ($t \geq 12.5$ mm), the behaviour of P_u/A_gf_y for increasing value of r/w is almost flat (i.e. not much significant change is observed), and this may be because, as the section is quite thick enough to get affected by the curvature reduction due to increasing values of r/w.

3.4.2.2 Effect of flat length (l_f)

In the previous plots (Figure 3.9), it has been found that the maximum value of load capacity (P_u) is obtained when semicircular sections are used (keeping flat length, l_f constant) on the sides of flat plate portions, hence in order to ascertain the effects of length of the flat portion, results are presented keeping $r/w = 0.5$ or $r = 150$ mm, for various values of $l_f = 300 – 700$ mm. Figures 3.12 and 3.13 show the variation of P with δ for thin ($t = 3$ mm) and thick ($t = 20$ mm) sections respectively, for $l_f = 300$, 400 and 600 mm. It can be seen from Figure 3.12 that for the thin section, snap through buckling behaviour is observed (mentioned in Section 3.4.2.1), without significant variation in the pattern and values of P_u. As stated before (see Figure 3.7), at P_u, buckling of the flat is initiated, as also in Figure 3.12, with most of the post P_u load being carried (identified by relatively higher stressed region) by the semicircular portions (S2, S3 and S4). The spread of flat section buckling on to the curve section can be seen for values of $l_f = 300$ to 600 mm (S2, S3, and S4), indicating that for the thin sections, flat section buckling controls the column

strength. Of course, when l_f becomes zero (or the section becomes circular), the contribution of the flat section buckling would get diminished (along with the reduction in A_e contribution in resisting load). The value of δ_u remains almost unaffected for increasing values of l_f.

However, for the thick sections, such type of snap through buckling is absent (see Figure 3.13), and P_u is found to increase with increasing values of l_f. A decrease in the value of δ_u is observed for increasing values of l_f. At P_u, for the shorter value of l_f (= 300 mm), the section is fully stressed beyond the yield stress, without visible sign of buckling, whereas, for the longer flat length (l_f = 600 mm), initiation of buckling can be observed at the mid-height of the column on flat portion, with some portion at the ends of the curve portion being stressed below the yield stress. This behaviour may be related to the cross-section being relatively slender in the case of longer l_f values. Improvement in the value of δ_u for lower values of l_f, may again be related to the cross-section being relatively stockier with larger portion of the cross-section being stressed beyond the yield stress. In order to assess the effect of flat length on P_u, variation of P_u with l_f/w is plotted in Figure 3.14, for t = 4-20 mm (r/w = 0.5). The variation of P_u with l_f/w in Figure 3.14 also agrees with the variation of A_e with l_f/w as shown in Figure 3.15, i.e. the rate of increase of A_e for lower thicknesses is not very significant, as compared to thicker sections. For the case of circular section, when l_f becomes zero, the effective area, A_e for thin section (Class 4 as per EN 1993-1-4, 2015) has been calculated as per Equation 3.33 (Trahair *et al*., 2008).

$$A_e = \sqrt{\frac{90}{d/(t\varepsilon^2)}} A_g \tag{3.33}$$

where, d is diameter of the circular section and A_g is the gross cross-section area.

The value of l_f/w = 0, indicates that the sections considered are circular with radius equal to 150 mm. It can be observed from Figure 3.14 that for the thinner sections (e.g. $t \leq 5$ mm), there is no significant variation on the values of P_u, when l_f/w is

increased from 0 to 2.33 (i.e. l_f = 700 mm). However, as the thickness is increased, an increase in the value of P_u can be seen as l_f/w increases, with the slope of increment getting relatively higher as the thickness increases. This behaviour is consistent with the changes in A_e (see Figure 3.15). Also, it is seen that the rate of increase in P_u is relatively higher at lower values of l_f/w ($\leq$ 1), indicating that the contribution of flat length at higher thickness, increases at a higher proportion, which at later higher values of l_f/w slows down (the slope of increase getting flatterer). This may be because, at lower values of l_f/w, the cross-section is relatively stockier, thus relatively higher value of A_e is available for load resistance, and however, as the value of l_f increases, A_e decreases, as the cross-section become slender.

Variation of P_u/A_gf_y with l_f/w is shown in Figure 3.16. It is seen from Figure 3.16 that as l_f/w is increased there is a drop in the values of P_u/A_gf_y for all the thicknesses analysed. For circular section with l_f/w = 0, $P_u/A_gf_y \geq 1$ (due to strain hardening), for all the thicknesses, indicating that P_u has exceeded the yield load, however, as l_f/w increases, even for the thickest section (t = 20 mm) analysed, P_u continue to drop and P_u/A_gf_y becomes lesser than 1, suggesting that buckling has occurred below the gross yield load (indicated by lower stress below the yield stress at the portions near the column ends (T2)). For the thinner sections (e.g. t = 3 mm), P_u values are well below the gross yield load (i.e. $P_u/A_gf_y \leq 1$) and local bucking precedes the attainment of yield load (S1 and S2).

3.4.2.3 Effect of change in cross-sectional area on strength

The increase in column strength per unit increase in cross-sectional area ($\Delta P/\Delta A$, where ΔP and ΔA are the changes in load and cross-sectional area respectively), as a result of increase in t (3-20 mm), for r = 150-750 mm; l_f = 300-600 mm; increase in l_f (300-600 mm) for t = 4-20 mm, are presented in Tables 3.3a, 3.3b and 3.3c respectively. In Table 3.3d, the variation of $\Delta P/\Delta A$ for increasing r (=150-750 mm) and t (=4-17.5 mm), is shown. Table 3.3d indicates the decrease (shown by -ve

sign) in strength due to decrease in curve length (as as result of increasing r). It can be seen that $\Delta P/\Delta A$ increment owing to ~ 566% increase in t (from t = 3 mm) are ~ 87%, 93%, 95% and 97% for r = 150 mm, 300mm, 450 mm, and 750 mm respectively (w = l_f = 300 mm) (see Table 3.3a). The useful effect of increasing thickness for flatter section (i.e. higher values of r) is readily seen, i.e. the enhancement of column strength per unit increase in cross-sectional area due to increase in t, increases as the curve curvature increases or become flatter. This may be related to some portion of the cross-section becoming ineffective at lower t values, thus resulting in lower load capacity, while at higher values of t (or as the section become stocky, leading to gross section become effective), the strength gain is directly proportional to the increase in cross-sectional area.

In Table 3.3b, it is observed that the change in $\Delta P/\Delta A$ due to increasing thickness of ~566% from t = 3 mm, along with change in flat length are of the order ~ 87%, 82 %, 78% and 71 % for l_f = 300 mm, 400 mm, 500 mm, and 600 mm respectively (w = 300 mm and r = 150 mm). This points out that there is no advantage in increasing thickness for longer flat length, as the change $\Delta P/\Delta A$ owing to the increase in thickness) decreases with increasing flat length. This may be because thinner sections become ineffective at higher values of flat length (i.e. cross-section becomes more slender), while at higher thickness, $\Delta P/\Delta A$ would be expected to remain unchanged, as load increment would be proportional to the increase in area when the gross cross-section becomes effective.

In Table 3.3c, for 133% increase in l_f (i.e. 300- 700 mm), increments of $\Delta P/\Delta A$ are found to be ~ 13% 19%, 22% and 24% for t = 4 mm, 12.5 mm, 17.5 mm, and 20 mm respectively (w = 300 mm and r = 150 mm). This indicates that the value of $\Delta P/\Delta A$ due to the increase in flat length increases with increasing thickness, and hence it is advantageous to increase flat length for higher thickness. The contribution of flat length in resisting load is enhanced when the section become stockier.

The change of $\Delta P/\Delta A$ due to the decrease in cross-sectional area as a result of 400 % increase in r (150 mm to 750 mm) are seen to be ~ 70%, 66%, 51% and 48% respectively, for t = 4 mm, 7.5 mm, 15 mm and 17.5 mm respectively ($w = l_f$ = 300 mm) in Table 3.3d. It can be noticed that the decrement in $\Delta P/\Delta A$ as a result of increasing r, decreases with increasing thickness, indicating that for higher thickness, increase in r is beneficial. Again, this may be due to relatively significant contribution of flatter curves (i.e. higher r values) in decreasing the load capacity at lower value of t due to the enhance ineffectiveness in cross-section.

3.4.3 Comparison of FE and design strength results

Comparison of FE and codal/manual (ASCE 8-02, AS/NZS 4673, EN 1993-1-4 and ASDM) values of P_u for different r values are shown in Figure 3.17, for t = 4, 12.5 and 20 mm (l_f = 300 mm). In Figure 3.18, comparison between FE and codal predictions of P_u are plotted for two values of r (r = 150 mm and r = 750 mm), as a function of two sets of thicknesses i.e. (a) t = 3-7.5 mm and (b) t = 10-20 mm. It can be seen from Figure 3.18 that for the thinner sections ($t \leq 7.5$ mm; Figures 3.18a,c), FE predicted lower values of P_u; whereas for the higher values of t ($t > 7.5$ mm; Figures 3.18b,d), an increasing over prediction of FE values can be seen as compared to the codal predictions. This variation appears to hold true for all the ranges of r (see Figure 3.17). Thus it can be inferred that for thinner sections (for a constant flat length), codal predictions are unconservative, whereas it is conservative for thicker sections. Further, the predictions made by ASCE 8-02, AS/NZS 4673, EN 1993-1-4 and ASDM are very similar, although their differences narrows down at higher thickness values (e.g. at t = 20 mm; see Figure 3.17). Similar comparisons of FE and codal P_u predictions are plotted in Figure 3.19 for different values of l_f, for t = 4, 12.5 and 20 mm, keeping r constant at 150 mm (i.e. semicircular section). Again, the comparisons of P_u are shown for two sets of thicknesses i.e. (a) t = 3-7.5 mm (Figure 3.20a) and (b) t = 10-20 mm (Figure 3.20b). Like the previous observation for constant l_f (i.e. varying r), in the case of

constant r (i.e. varying l_f), it can be seen that, FE predictions are lower for thinner sections, and similar or higher for thicker sections, as compared to that of codal predictions. This behaviour is true for both lower (l_f = 300 mm; see Fig 3.18a and b) and higher (l_f = 600 mm; see Fig 3.20a and b) values of l_f. In Figure 3.19, it is observed that predictions made by ASCE 8-02, AS/NZS 4673, EN 1993-1-4 and ASDM are very close at lower thickness (e.g. t = 4 mm), whereas EN 1993-1-4 predicted lower P_u as the thickness increases in comparison to that of ASCE 8-02, AS/NZS 4673 and ASDM.

Higher values of P_u predicted by FE as compared to codal values at higher thicknesses, may be related to increased effective area and strain hardening effect (for stockier sections, it is seen that buckling load is higher than that of gross yield load). It may be noted that the effect of strain hardening effect is not considered in the predictions made by ASCE 8-02, AS/NZS 4673, EN 1993-1-4 and ASDM. However at lower values of thicknesses, in the calculation of codal predictions of P_u, it was assumed that the whole gross cross-section of the curve portions as totally effective (see Section 3.3; Figure 3.5) for ASCE 8-02, AS/NZS 4673, EN 1993-1-4, whilst an effective cross-section was considered for ASDM predictions, and hence it is unlikely that such assumptions may accurately show the interactions of curve and flat portions being modelled by the present non-linear FE models.

The column strengths calculated by FE (P_{FE}) analysis have been compared with the values calculated on the basis of the design codes of ASCE 8-02 specifications (P_{ASCE}), AS/NZS 4673 standard ($P_{AS/NZS}$), EN 1993-1-4 (P_{EN}), ASDM (P_{ASDM}) and DSM (P_{DSM}) in Table 3.4. The comparisons are plotted in the form of normalised load ratios *viz.*, P_{FE}/P_{ASCE}, $P_{FE}/P_{AS/NZS}$, P_{FE}/P_{EN}, P_{FE}/P_{ASDM} and P_{FE}/P_{DSM}. It can be seen from Table 3.4 that, the values of mean; COV and reliability index (β) are 1.01, 1.01, 1.04, 1.06, 1.15, 1.16; 0.19, 0.19, 0.17, 0.15. 0.12, 0.12; and 2.23, 2.06, 2.06, 2.59, 3.27, and 3.31 respectively, for P_{FE}/P_{ASCE}, $P_{FE}/P_{AS/NZS}$, P_{FE}/P_{EN}, P_{FE}/P_{ASDM}, P_{FE}/P_{DSM} and P_{FE}/P^*_{DSM}. The value of β provided by ASDM

($\beta = 2.59$), DSM ($\beta = 3.27$) and DSM* ($\beta = 3.31$) are found to be greater than 2.5 (target value), whilst ASCE 8-02, AS/NZS 4673, EN 1993-1-4 provided values which are lesser than 2.5, suggesting that ASDM, DSM and DSM* design rules are applicable for the design of flat oval sections. Thus it can be seen that predictions made by the modified DSM (or DSM* proposed by Huang and Young, 2012) gave a slightly higher value of reliability index. Comparison of FE and design strengths for DSM and DSM* are plotted as a variation of P_u/P_{ne} with λ_l in Figure 3.21 and 3.22 respectively. From Figure 3.21 and 3.22, the applicability of DSM and DSM* for flat-oval LDSS (both stocky and slender sections) sections can be seen, except for a very few specimens. For $\lambda_l \leq$ ~0.776 (0.769 for the case of DSM*) (i.e. when the cross-section is stockier) $P_u/P_{ne} \geq 1.0$, indicating the effect of strain hardening for stockier sections. For intermediate cross-sectional slenderness values (~0.776 $\leq \lambda_l \leq \sim$ 1.2 or ~0.769 $\leq \lambda_l \leq \sim$ 1.2), FE values are well predicted by DSM (and DSM*), but as λ_l increases (say $\geq \sim$ 1.2) the predictions made by DSM tends to be on the conservative side (~20% at λ_l = 2.8). The present results agrees with the conclusions made by Zhu and Young (2012) based on the FE analyses of ~100 cold formed flat oval (semi-circular section being used) carbon steel sections (considering both slender and compact/stocky sections), wherein it was obtained that β values for AS/NZS 4673, EN 1993-1-4 and DSM are 2.03, 1.79 and 2.9 respectively, suggesting that only DSM is reliable. However, when compared with the experimental results of 'compact' sections (w/t < 40), Zhu and Young (2012) obtained β values of the order 2.63, 2.70, and 3.0 for AS/NZS 4673, EN 1993-1-4 and DSM respectively, suggesting that all the compared codal designs are applicable, with DSM being the most reliable.

A comparison of FE and design strengths are shown separately in Tables 3.5 and 3.6 respectively for flat oval section, w/t < 40 and $w/t \geq 40$ sections. It can be seen that, for stocky curve sections (w/t < 40), ASCE 8-02, AS/NZS 4673, EN 1993-1-4, ASDM and DSM provided conservative results with β = 3.12, 2.93, 2.88, 3.19, 3.40

(i.e. > the target value of 2.5), respectively, indicating that predictions by ASCE 8-02, AS/NZS 4673, EN 1993-1-4, ASDM and DSM are conservative (see Table 3.5). However, for the case of slender curve sections ($w/t \geq 40$) (see Table 3.6), it appears that only DSM is found to be reliable (with $\beta = 3.04$).

3.4.4 Continuous strength method

In order to assess the applicability of CSM on flat oval sections, variation of $\varepsilon_{csm}/\varepsilon_y$ vs $\bar{\lambda}_p$ is compared between CSM and FE results in Figure 3.23. Figures 3.24 and 3.25 show the comparison of FE and CSM in terms of stress (f, where $f = P_u/A$ for FE and $f = f_{CSM}$ (Equation 3.23)) and P_{FE}/P_{CSM} (where P_{FE} and P_{CSM} are load capacity predictions from FE and CSM, respectively). It may be noted that CSM is applicable only for $\bar{\lambda}_p \leq 0.68$, and hence FE results for $\bar{\lambda}_p > 0.68$ are not used for direct comparison with CSM, as they are not likely to get affected by strain hardening phenomena (the cross-sections being slender). From Figure 3.24, it can be seen that the average stress predicted by FE is higher than those of CSM (for $\bar{\lambda}_p \leq 6.8$ where CSM is applicable). The strength enhancement due to strain hardening effect is readily visible i.e. $f \geq 657$ MPa (i.e. f_y). The column strength predicted by FE is found to be ~ 9-19% higher than those of CSM (Figure 3.25). The present finding also agrees (although on higher side) with Huang and Young (2013) where 10% higher mean value in the case of FE as compared to that of CSM prediction, was reported, suggesting that CSM for stainless steel is able to conservatively predict LDSS stub column strength. Again, for the selected FE results corresponding to $\bar{\lambda}_p \leq 6.8$, comparisons have been made of predictions from various codes *viz.*, ASCE 8-02, AS/NZS 4673, EN 1993-1-4, ASDM, DSM and CSM in Table 3.7. From Table 3.7, it can be observed that β values for ASCE 8-02, AS/NZS 4673, EN 1993-1-4, ASDM, DSM and CSM are 3.59, 3.38, 3.20, 3.62, 3.84 and 3.69 respectively, suggesting that all the design methods are applicable for flat oval LDSS stub sections. However, comparison of the mean values suggest that

the predictions made by CSM is relatively closer to FE results i.e. P_{FE}/P_{CSM} = 1.16 is relatively lower than 1.21, 1.21, 1.22, 1.22 and 1.22 obtained in the case of ASCE 8-02, AS/NZS 4673, EN 1993-1-4, ASDM and DSM respectively.

3.4.5 Proposed modifications to EN 1993-1-4, AS/NZS 4673 and ASDM for flat oval section

As discussed above in Section 3.4.3 (also see Table 3.6), for flat oval sections, $w/t \geq 40$, the predictions made by ASCE 8-02, AS/NZS 4673, EN 1993-1-4 and ASDM are found to be unreliable with $\beta < 2.5$. Hence, following the approach adopted by ASDM for combined curve and flat sections (see Parks and Yu, 1987), further modification to the effective thickness (t_e see Section 3.3.1) in order to arrive at suitable effective area values, so that the predictions become reliable. This has been attempted by incorporating a thickness reduction factor (TRF) to the expression of t_e as shown in Equation 3.34.

$$t_e = TRF\left(\frac{A_o}{A}\right)\left(\frac{F_y}{f}\right)t \tag{3.34}$$

In order to arrive at an optimal value of TRF, the value of TRF has been varied from 0.3-1.0, and corresponding β value has been estimated for EN 1993-1-4(2015), AS/NZS 4673(2001) and ASDM (2002) predictions of load capacity. The computed variation of β with TRF is plotted in Figure 3.26 (see also Table 3.8). It can be observed that, values of TRF in the range ~0.5-0.6 is able to provide the required target value of β_o (i.e. 2.5). Hence, a conservative value of TRF = 0.5 has been deduced for further modification to t_e. The proposed expression for t_e (or t_{ep}) thus becomes

$$t_{ep} = 0.5\left(\frac{A_o}{A}\right)\left(\frac{F_y}{f}\right)t \tag{3.35}$$

The new expression for the effective area of the curve portion (A_{ec}) is then given by Equation 3.36.

$$A_{ec} = 2(l_c - l_{ec})t_{ep} + 2tl_{ec} \quad (3.36)$$

Following the procedures outlined in Section 3.3.1 in conjunction with Equation 3.36 (see Figure 3.5(b)), the results of (proposed) modified EN 1993-1-4(2015), AS/NZS 4673(2001) and ASDM (2002) predictions of load capacity are then compared with those of FE flat oval section ($w/t \geq 40$) in Table 3.9 and Figure 3.27. In Table 3.9, $P_{AS/NZS(p)}$, $P_{EN(p)}$, and $P_{ASDM(p)}$ corresponds to the load capacity predicted by the proposed EN 1993-1-4(2015), AS/NZS 4673(2001) and ASDM (2002) expressions, respectively. It can be readily seen that, with the adoption of the proposed effective thickness expression (see Equation 3.35), the value of β has exceeded the target value of 2.5 (i.e. β = 2.77, 2.66 and 2.98 for the proposed EN 1993-1-4(2015), AS/NZS 4673(2001) and ASDM (2002) expressions). Figure 3.27 shows some comparison of FE and (proposed) modified EN 1993-1-4(2015), AS/NZS 4673(2001) and ASDM (i.e. EN 1993-1-4$_{(p)}$, AS/NZS 4673$_{(p)}$, ASDM$_{(P)}$ predictions), for increasing values of section thickness (t), for r = 150 and 450 (see Figure 3.27 a,b)and l_f = 500 and 600 (see Figure 3.27 c,d). Again, conservativeness of the proposed predictions can be seen.

3.5 CONCLUSION

Parametric study of the structural behaviour of fixed ended LDSS flat oval section stub column, by varying l_f (flat length), r (curvature radius), t (thickness), keeping w (flat plate spacing) and h (height of column) constant at 300 and 900 mm respectively, using the commercial finite element software, Abaqus, is presented. Based on the FE analyses, the following conclusions have been obtained:

1) Flat oval sections with semicircular elements on either sides of the flat elements (i.e. r/w = 0.5) provided the maximum column strength (P_u) of the stub columns, for $r/w \geq 0.5$ (or flatter sections) the rate of decrement in P_u is seen to be small.

2) For thin sections with lower values of r (e.g. for semicircular sections i.e. r/w = 0.5), initiation of buckling has been seen on the flat elements, with snap through

buckling pattern; for higher values of r (i.e. $r/w \geq 0.5$), it is seen that snap back buckling has been observed. Deformation at P_u (i.e. δ_u) has been found to decrease with increasing values of r, for thin sections.

3) For thick sections (e.g. 20 mm), such snap buckling phenomenon is found to be absent for all the values of r analysed. Further, post buckling strength of columns with semicircular sections appears to be relatively lower than those of flatter curve sections. In the case of thick section, value of δ_u has been seen to be the smallest for the semicircular curve section, however for flatter curve sections, there is no significant change.

4) For thinner sections (e.g. $t \leq 5$ mm), there is no significant variation on the values of P_u, when l_f/w is increased from 0 to 2.33 (i.e. $l_f = 700$ mm). However, as the thickness is increased, an increase in the value of P_u can be seen with increasing l_f/w, with the slope of increment getting relatively higher as the thickness increases. The value of δ_u remains almost unaffected for increasing values of l_f, for thin sections, whereas, for thick section, it decreases with increasing values of l_f.

5) Strength gain per unit increase in area by 1) increasing t, increases with increasing r and de-creases with increasing l_f ; 2) increasing l_f, increases with increasing t ; while the decrease in strength per unit decrease in area by increasing r decreases with increasing t. Increase in load capacity per unit material area increment as a result of increase of ~ 566% increase in t (from $t = 3$ mm) is ~≥ 87% for all radii of curvatures considered, while it is ~≥ 71% for increase in flat length, which shows that the increase in thickness has more positive effect on column strength.

6) The FE results have been compared with ASCE 8-02, AS/NZS 4673, EN 1993-1-4, DSM, Modified DSM or DSM* (Huang and Young, 2014b) and CSM predictions, and it has been found that ASDM, DSM, DSM* and CSM are reliable for the design of flat oval LDSS columns, whilst ASCE 8-02, AS/NZS 4673, and

EN 1993-1-4 are not, although, predictions made by ASCE 8-02, AS/NZS 4673, and EN 1993-1-4 are observed to be reliable for flat oval sections with $w/t < 40$.

7) An expression has been proposed for calculating the effective thickness of curve elements of flat oval LDSS sections with $w/t \geq 40$, which can provide reliable load capacity predictions when used with ASCE 8-02, AS/NZS 4673, and EN 1993-1-4 equations.

Table 3.1

Compressive flat material properties (Theofanous and Gardner, 2009).

Cross-section	E (MPa)	$\sigma_{0.2}$ (MPa)	$\sigma_{1.0}$ (MPa)	Compound R-O coefficients	
				n	$n'_{0.2,1.0}$
80x80x4-SC2	197200	657	770	4.7	2.6

Table 3.2

Stub column dimensions (Theofanous and Gardner, 2009).

Specimen	L (mm)	B (mm)	h (mm)	t (mm)	r_i (mm)
80x80x4-SC2	332.2	80	80	3.81	3.6

L = Length, B = Width, h = height, t = thickness, r_i = internal corner radius

Table 3.3

Comparison of change in strength per unit change in cross-section area ($\Delta P/\Delta A$): a) increasing t for various values of r, b) increasing t for various values of l_f, c) increasing l_f for various values of t, and d) by increasing r for various values of t.

(a) Increase in t	(Δ P/ΔA)	(b) Increase in t	(Δ P/ΔA)
$l300w300r150t3$ to $l300w300r150t20$	+87.07%	$l300w300r150t3$ to $l300w300r150t20$	+87.07%
$l300w300r300t3$ to $l300w300r300t20$	+93.39%	$l400w300r150t3$ to $l400w300r150t20$	+82.21%
$l300w300r450t3$ to $l300w300r450t20$	+95.47%	$l500w300r150t3$ to $l500w300r150t20$	+78.27%
$l300w300r750t3$ to $l300w300r750t20$	+97.16%	l600$w300r150t3$ to l600$w300r150t20$	+71.56%

(c) Increase in l_f	(Δ P/ΔA)	(d) Increase in r	(Δ P/ΔA)
*l*300*w*300*r*150*t*4 to *l*700*w*300*r*150*t*4	+13.17%	*l*300*w*300*r*150*t*4 to *l*300*w*300*r*750*t*4	-69.98%
*l*300*w*300*r*150*t*12.5 to 700*w*300*r*150*t*12.5	+18.93%	*l*300*w*300*r*150*t*7.5 to *l*300*w*300*r*750*t*7.5	-66.32%
*l*300*w*300*r*150*t*17.5 to 700*w*300*r*150*t*17.5	+22.12 %	*l*300*w*300*r*150*t*15 to *l*300*w*300*r*750*t*15	-51.30%
*l*300*w*300*r*150*t*20 to *l*700*w*300*r*150*t*20	+24.55%	*l*300*w*300*r*150*t*17.5 to *l*300*w*300*r*750*t*17.5	-47.60%

Table 3.4

Comparison of design strengths with FE strength.

Specimen	$\frac{P_{FE}}{p_{ASCE}}$	$\frac{P_{FE}}{p_{AS/NZS}}$	$\frac{P_{FE}}{p_{EN}}$	$\frac{P_{FE}}{p_{ASDM}}$	$\frac{P_{FE}}{p_{DSM}}$	$\frac{P_{FE}}{p^{*}_{DSM}}$
*l*300*w*300*r*150*t*7.5	0.97	0.97	1.01	0.98	1.15	1.16
*l*300*w*300*r*150*t*10	0.94	0.94	0.97	0.93	1.00	1.02
*l*300*w*300*r*150*t*12.5	1.05	1.05	1.07	1.05	1.05	1.07
*l*300*w*300*r*150*t*15	1.12	1.12	1.13	1.13	1.12	1.13
*l*300*w*300*r*150*t*17.5	1.15	1.15	1.15	1.15	1.15	1.15
*l*300*w*300*r*150*t*20	1.20	1.20	1.20	1.20	1.19	1.20
*l*300*w*300*r*300*t*7.5	1.06	1.06	1.12	1.09	1.07	1.09
*l*300*w*300*r*300*t*10	1.14	1.14	1.20	1.15	1.06	1.08
*l*300*w*300*r*300*t*12.5	1.20	1.20	1.23	1.19	1.19	1.19
*l*300*w*300*r*300*t*15	1.23	1.23	1.23	1.23	1.25	1.25
*l*300*w*300*r*300*t*17.5	1.24	1.24	1.25	1.25	1.27	1.27
*l*300*w*300*r*300*t*20	1.25	1.25	1.26	1.26	1.28	1.28
*l*300*w*300*r*450*t*7.5	1.02	1.02	1.09	1.06	1.03	1.04
*l*300*w*300*r*450*t*10	1.14	1.14	1.20	1.15	1.06	1.08
*l*300*w*300*r*450*t*12.5	1.17	1.17	1.21	1.17	1.17	1.17
*l*300*w*300*r*450*t*15	1.21	1.21	1.22	1.22	1.24	1.24
*l*300*w*300*r*450*t*17.5	1.25	1.25	1.26	1.25	1.28	1.28
*l*300*w*300*r*450*t*20	1.26	1.26	1.26	1.26	1.29	1.29
*l*300*w*300*r*600*t*7.5	0.98	0.98	1.04	1.02	0.99	1.01
*l*300*w*300*r*600*t*10	1.11	1.11	1.16	1.12	1.03	1.05
*l*300*w*300*r*600*t*12.5	1.16	1.16	1.20	1.16	1.16	1.16
*l*300*w*300*r*600*t*15	1.21	1.21	1.22	1.22	1.24	1.24
*l*300*w*300*r*600*t*17.5	1.24	1.24	1.24	1.24	1.27	1.27
*l*300*w*300*r*600*t*20	1.26	1.26	1.26	1.26	1.29	1.30

*l*300*w*300*r*750*t*7.5	0.94	0.94	1.00	0.98	0.96	0.98
*l*300*w*300*r*750*t*10	1.12	1.12	1.18	1.14	1.07	1.09
*l*300*w*300*r*750*t*12.5	1.17	1.17	1.20	1.17	1.16	1.17
*l*300*w*300*r*750*t*15	1.20	1.20	1.20	1.20	1.23	1.23
*l*300*w*300*r*750*t*17.5	1.25	1.25	1.25	1.25	1.28	1.28
*l*300*w*300*r*750*t*20	1.25	1.25	1.26	1.26	1.29	1.30
*l*400*w*300*r*150*t*7.5	1.05	1.05	1.11	1.35	1.30	1.32
*l*400*w*300*r*150*t*10	0.91	0.91	0.96	1.13	1.02	1.03
*l*400*w*300*r*150*t*12.5	0.98	0.98	1.03	1.19	1.02	1.04
*l*400*w*300*r*150*t*15	1.06	1.06	1.10	1.28	1.05	1.07
*l*400*w*300*r*150*t*17.5	1.09	1.09	1.11	1.29	1.08	1.08
*l*400*w*300*r*150*t*20	1.12	1.12	1.13	1.33	1.12	1.13
*l*500*w*300*r*150*t*7.5	0.86	0.86	0.92	0.87	1.08	1.09
*l*500*w*300*r*150*t*10	0.92	0.92	0.98	0.91	1.04	1.05
*l*500*w*300*r*150*t*12.5	0.96	0.96	1.03	0.96	1.01	1.03
*l*500*w*300*r*150*t*15	1.03	1.03	1.10	1.03	1.03	1.05
*l*500*w*300*r*150*t*17.5	1.10	1.10	1.16	1.10	1.06	1.08
*l*500*w*300*r*150*t*20	1.10	1.10	1.14	1.10	1.07	1.07
*l*600*w*300*r*150*t*7.5	1.00	1.00	1.07	1.00	1.24	1.26
*l*600*w*300*r*150*t*10	1.05	1.05	1.13	1.03	1.17	1.19
*l*600*w*300*r*150*t*12.5	1.07	1.07	1.15	1.06	1.13	1.14
*l*600*w*300*r*150*t*15	1.06	1.06	1.14	1.05	1.07	1.08
*l*600*w*300*r*150*t*17.5	1.33	1.33	1.15	1.07	1.05	1.07
*l*600*w*300*r*150*t*20	1.29	1.29	1.14	1.07	1.03	1.05
*l*700*w*300*r*150*t*7.5	1.02	1.02	1.11	1.04	1.30	1.31
*l*700*w*300*r*150*t*10	1.06	1.06	1.17	1.07	1.22	1.24
*l*700*w*300*r*150*t*12.5	1.07	1.07	1.19	1.08	1.16	1.17
*l*700*w*300*r*150*t*15	1.05	1.05	1.17	1.06	1.09	1.10
*l*700*w*300*r*150*t*17.5	1.05	1.05	1.17	1.07	1.06	1.07
*l*700*w*300*r*150*t*20	1.04	1.04	1.15	1.06	1.02	1.04
*l*300*w*300*r*150*t*3	0.68	0.68	0.70	0.79	1.24	1.24
*l*300*w*300*r*150*t*4	0.74	0.74	0.77	0.82	1.16	1.17
*l*300*w*300*r*150*t*5	0.87	0.87	0.91	0.94	1.23	1.24
*l*300*w*300*r*300*t*3	0.80	0.80	0.84	0.93	1.19	1.19
*l*300*w*300*r*300*t*4	0.91	0.91	0.96	1.01	1.23	1.24
*l*300*w*300*r*300*t*5	0.98	0.98	1.04	1.06	1.15	1.17
*l*300*w*300*r*450*t*3	0.66	0.66	0.69	0.77	0.97	0.98
*l*300*w*300*r*450*t*4	0.81	0.81	0.85	0.91	1.04	1.05
*l*300*w*300*r*450*t*5	0.94	0.94	1.00	1.03	1.10	1.11
*l*300*w*300*r*600*t*5	0.91	0.91	0.96	0.99	1.06	1.07
*l*300*w*300*r*750*t*3	0.50	0.50	0.52	0.59	0.74	0.74
*l*300*w*300*r*750*t*4	0.61	0.61	0.64	0.69	0.78	0.78
*l*300*w*300*r*750*t*5	0.69	0.69	0.74	0.84	0.81	0.82
*l*400*w*300*r*150*t*3	0.69	0.69	0.70	1.05	1.43	1.43

*l*400*w*300*r*150*t*4	0.75	0.75	0.78	1.08	1.23	1.23
*l*400*w*300*r*150*t*5	0.80	0.80	0.84	1.12	1.18	1.19
*l*500*w*300*r*150*t*3	0.69	0.69	0.72	0.80	1.36	1.36
*l*500*w*300*r*150*t*4	0.77	0.77	0.80	0.84	1.29	1.29
*l*500*w*300*r*150*t*5	0.81	0.81	0.85	0.86	1.21	1.22
*l*600*w*300*r*150*t*3	0.70	0.70	0.73	0.80	1.36	1.37
*l*600*w*300*r*150*t*4	0.77	0.77	0.80	0.84	1.27	1.28
*l*600*w*300*r*150*t*5	0.91	0.91	0.97	0.97	1.35	1.36
*l*700*w*300*r*150*t*4	0.87	0.87	0.91	0.95	1.46	1.46
*l*700*w*300*r*150*t*5	0.94	0.94	1.00	1.00	1.42	1.43
Mean	1.01	1.01	1.04	1.06	1.15	1.16
COV	0.19	0.19	0.17	0.15	0.12	0.12
Reliability index, β	2.23	2.06	2.06	2.59	3.27	3.31

Table 3.5

Comparison of design strengths with FE strength (w/t < 40).

Specimen	$\frac{P_{FE}}{p_{ASCE}}$	$\frac{P_{FE}}{p_{AS/NZS}}$	$\frac{P_{FE}}{p_{EN}}$	$\frac{P_{FE}}{p_{ASDM}}$	$\frac{P_{FE}}{p_{DSM}}$
*l*300*w*300*r*150*t*10	0.94	0.94	0.97	0.93	1.00
*l*300*w*300*r*150*t*12.5	1.05	1.05	1.07	1.05	1.05
*l*300*w*300*r*150*t*15	1.12	1.12	1.13	1.13	1.12
*l*300*w*300*r*150*t*17.5	1.15	1.15	1.15	1.15	1.15
*l*300*w*300*r*150*t*20	1.20	1.20	1.20	1.20	1.19
*l*300*w*300*r*300*t*10	1.14	1.14	1.20	1.15	1.06
*l*300*w*300*r*300*t*12.5	1.20	1.20	1.23	1.19	1.19
*l*300*w*300*r*300*t*15	1.23	1.23	1.23	1.23	1.25
*l*300*w*300*r*300*t*17.5	1.24	1.24	1.25	1.25	1.27
*l*300*w*300*r*300*t*20	1.25	1.25	1.26	1.26	1.28
*l*300*w*300*r*450*t*10	1.14	1.14	1.20	1.15	1.06
*l*300*w*300*r*450*t*12.5	1.17	1.17	1.21	1.17	1.17
*l*300*w*300*r*450*t*15	1.21	1.21	1.22	1.22	1.24
*l*300*w*300*r*450*t*17.5	1.25	1.25	1.26	1.25	1.28
*l*300*w*300*r*450*t*20	1.26	1.26	1.26	1.26	1.29
*l*300*w*300*r*600*t*10	1.11	1.11	1.16	1.12	1.03
*l*300*w*300*r*600*t*12.5	1.16	1.16	1.20	1.16	1.16
*l*300*w*300*r*600*t*15	1.21	1.21	1.22	1.22	1.24
*l*300*w*300*r*600*t*17.5	1.24	1.24	1.24	1.24	1.27
*l*300*w*300*r*600*t*20	1.26	1.26	1.26	1.26	1.29

*l*300*w*300*r*750*t*10	1.12	1.12	1.18	1.14	1.07
*l*300*w*300*r*750*t*12.5	1.17	1.17	1.20	1.17	1.16
*l*300*w*300*r*750*t*15	1.20	1.20	1.20	1.20	1.23
*l*300*w*300*r*750*t*17.5	1.25	1.25	1.25	1.25	1.28
*l*300*w*300*r*750*t*20	1.25	1.25	1.26	1.26	1.29
*l*400*w*300*r*150*t*10	0.91	0.91	0.96	1.13	1.02
*l*400*w*300*r*150*t*12.5	0.98	0.98	1.03	1.19	1.02
*l*400*w*300*r*150*t*15	1.06	1.06	1.10	1.28	1.05
*l*400*w*300*r*150*t*17.5	1.09	1.09	1.11	1.29	1.08
*l*400*w*300*r*150*t*20	1.12	1.12	1.13	1.33	1.12
*l*500*w*300*r*150*t*10	0.92	0.92	0.98	0.91	1.04
*l*500*w*300*r*150*t*12.5	0.96	0.96	1.03	0.96	1.01
*l*500*w*300*r*150*t*15	1.03	1.03	1.10	1.03	1.03
*l*500*w*300*r*150*t*17.5	1.10	1.10	1.16	1.10	1.06
*l*500*w*300*r*150*t*20	1.10	1.10	1.14	1.10	1.07
*l*600*w*300*r*150*t*10	1.05	1.05	1.13	1.03	1.17
*l*600*w*300*r*150*t*12.5	1.07	1.07	1.15	1.06	1.13
*l*600*w*300*r*150*t*15	1.06	1.06	1.14	1.05	1.07
*l*600*w*300*r*150*t*17.5	1.33	1.33	1.15	1.07	1.05
*l*600*w*300*r*150*t*20	1.29	1.29	1.14	1.07	1.03
*l*700*w*300*r*150*t*10	1.06	1.06	1.17	1.07	1.22
*l*700*w*300*r*150*t*12.5	1.07	1.07	1.19	1.08	1.16
*l*700*w*300*r*150*t*15	1.05	1.05	1.17	1.06	1.09
*l*700*w*300*r*150*t*17.5	1.05	1.05	1.17	1.07	1.06
*l*700*w*300*r*150*t*20	1.04	1.04	1.15	1.06	1.02
Mean	1.13	1.13	1.16	1.15	1.14
COV	0.09	0.09	0.07	0.09	0.09
Reliability index, β	3.12	2.93	2.88	3.19	3.40

Table 3.6

Comparison of design strengths with FE strength ($w/t \geq 40$).

Specimen	$\frac{P_{FE}}{p_{ASCE}}$	$\frac{P_{FE}}{p_{AS/NZS}}$	$\frac{P_{FE}}{p_{EN}}$	$\frac{P_{FE}}{p_{ASDM}}$	$\frac{P_{FE}}{p_{DSM}}$
*l*300*w*300*r*150*t*3	0.68	0.68	0.70	0.79	1.24
*l*300*w*300*r*150*t*4	0.74	0.74	0.77	0.82	1.16
*l*300*w*300*r*150*t*5	0.87	0.87	0.91	0.94	1.23
*l*300*w*300*r*150*t*7.5	0.97	0.97	1.01	0.98	1.15
*l*300*w*300*r*300*t*3	0.80	0.80	0.84	0.93	1.19

*l*300*w*300*r*300*t*4	0.91	0.91	0.96	1.01	1.23
*l*300*w*300*r*300*t*5	0.98	0.98	1.04	1.06	1.15
*l*300*w*300*r*300*t*7.5	1.06	1.06	1.12	1.09	1.07
*l*300*w*300*r*450*t*3	0.66	0.66	0.69	0.77	0.97
*l*300*w*300*r*450*t*4	0.81	0.81	0.85	0.91	1.04
*l*300*w*300*r*450*t*5	0.94	0.94	1.00	1.03	1.10
*l*300*w*300*r*450*t*7.5	1.02	1.02	1.09	1.06	1.03
*l*300*w*300*r*600*t*5	0.91	0.91	0.96	0.99	1.06
*l*300*w*300*r*600*t*7.5	0.98	0.98	1.04	1.02	0.99
*l*300*w*300*r*750*t*3	0.50	0.50	0.52	0.59	0.74
*l*300*w*300*r*750*t*4	0.61	0.61	0.64	0.69	0.78
*l*300*w*300*r*750*t*5	0.69	0.69	0.74	0.84	0.81
*l*300*w*300*r*750*t*7.5	0.94	0.94	1.00	0.98	0.96
*l*400*w*300*r*150*t*3	0.69	0.69	0.70	1.05	1.43
*l*400*w*300*r*150*t*4	0.75	0.75	0.78	1.08	1.23
*l*400*w*300*r*150*t*5	0.80	0.80	0.84	1.12	1.18
*l*400*w*300*r*150*t*7.5	1.05	1.05	1.11	1.35	1.30
*l*500*w*300*r*150*t*3	0.69	0.69	0.72	0.80	1.36
*l*500*w*300*r*150*t*4	0.77	0.77	0.80	0.84	1.29
*l*500*w*300*r*150*t*5	0.81	0.81	0.85	0.86	1.21
*l*500*w*300*r*150*t*7.5	0.86	0.86	0.92	0.87	1.08
*l*600*w*300*r*150*t*3	0.70	0.70	0.73	0.80	1.36
*l*600*w*300*r*150*t*4	0.77	0.77	0.80	0.84	1.27
*l*600*w*300*r*150*t*5	0.91	0.91	0.97	0.97	1.35
*l*600*w*300*r*150*t*7.5	1.00	1.00	1.07	1.00	1.24
*l*700*w*300*r*150*t*4	0.87	0.87	0.91	0.95	1.46
*l*700*w*300*r*150*t*5	0.94	0.94	1.00	1.00	1.42
*l*700*w*300*r*150*t*7.5	1.02	1.02	1.11	1.04	1.30
Mean	0.84	0.84	0.88	0.94	1.16
COV	0.17	0.17	0.18	0.15	0.16
Reliability index, β	1.67	1.50	1.44	2.14	3.04

Table 3.7

Comparison of design strengths with FE strengths ($\bar{\lambda}_p \leq 0.68$).

Specimen	$\frac{P_{FE}}{p_{ASCE}}$	$\frac{P_{FE}}{p_{AS/NZS}}$	$\frac{P_{FE}}{p_{EN}}$	$\frac{P_{FE}}{p_{ASDM}}$	$\frac{P_{FE}}{p_{DSM}}$	$\frac{P_{FE}}{p_{CSM}}$
*l*300*w*300*r*150*t*15	1.12	1.12	1.13	1.13	1.12	1.09
*l*300*w*300*r*150*t*17.5	1.15	1.15	1.15	1.15	1.15	1.10
*l*300*w*300*r*150*t*20	1.20	1.20	1.20	1.20	1.19	1.13

*l*300*w*300*r*300*t*12.5	1.20	1.20	1.23	1.19	1.19	1.15
*l*300*w*300*r*300*t*15	1.23	1.23	1.23	1.23	1.25	1.19
*l*300*w*300*r*300*t*17.5	1.24	1.24	1.25	1.25	1.27	1.19
*l*300*w*300*r*300*t*20	1.25	1.25	1.26	1.26	1.28	1.17
*l*300*w*300*r*450*t*12.5	1.17	1.17	1.21	1.17	1.17	1.13
*l*300*w*300*r*450*t*15	1.21	1.21	1.22	1.22	1.24	1.18
*l*300*w*300*r*450*t*17.5	1.25	1.25	1.26	1.25	1.28	1.20
*l*300*w*300*r*450*t*20	1.26	1.26	1.26	1.26	1.29	1.18
*l*300*w*300*r*600*t*12.5	1.16	1.16	1.20	1.16	1.16	1.12
*l*300*w*300*r*600*t*15	1.21	1.21	1.22	1.22	1.24	1.18
*l*300*w*300*r*600*t*17.5	1.24	1.24	1.24	1.24	1.27	1.19
*l*300*w*300*r*600*t*20	1.26	1.26	1.26	1.26	1.29	1.19
*l*300*w*300*r*750*t*12.5	1.17	1.17	1.20	1.17	1.16	1.13
*l*300*w*300*r*750*t*15	1.20	1.20	1.20	1.20	1.23	1.17
*l*300*w*300*r*750*t*17.5	1.25	1.25	1.25	1.25	1.28	1.20
*l*300*w*300*r*750*t*20	1.25	1.25	1.26	1.26	1.29	1.19
*l*400*w*300*r*150*t*20	1.12	1.12	1.13	1.33	1.12	1.09
Mean	1.21	1.21	1.22	1.22	1.22	1.16
COV	0.04	0.04	0.03	0.04	0.05	0.03
Reliability index, β	3.59	3.38	3.20	3.62	3.84	3.69

Table 3.8

Variation of reliability index (β) with curve thickness reduction factor (TRF).

No. of sample	Curve thickness reduction factor, TRF	β (EN 1993-1-4$_{(P)}$)	β (AS/NZS 4673$_{(P)}$)	β (ASDM$_{(P)}$)
33	0.30	3.19	3.09	3.37
33	0.40	3.00	2.88	3.16
33	0.50	2.77	2.66	2.98
33	0.60	2.55	2.45	2.81
33	0.65	2.40	2.38	2.70
33	0.70	2.30	2.27	2.58
33	0.80	2.13	2.08	2.39
33	0.90	1.91	1.89	2.19
33	1.00	1.73	1.73	2.03

Table 3.9

Comparison of design strengths with FE strengths ($w/t \geq 40$).

Specimen	Current codes			Proposed modified codes		
	$\frac{P_{FEA}}{P_{EN}}$	$\frac{P_{FEA}}{P_{AS/NZS}}$	$\frac{P_{FEA}}{P_{ASDM}}$	$\frac{P_{FEA}}{P_{EN(p)}}$	$\frac{P_{FEA}}{p_{AS/NZS(p)}}$	$\frac{P_{FEA}}{P_{ASDM(p)}}$
l300w300r150t3	0.70	0.68	0.79	1.21	1.13	1.13
l300w300r150t4	0.77	0.74	0.82	1.20	1.11	1.11
l300w300r150t5	0.91	0.87	0.94	1.32	1.22	1.22
l300w300r150t7.5	1.01	0.97	0.98	1.26	1.18	1.18
l300w300r300t3	0.84	0.80	0.93	1.18	1.09	1.18
l300w300r300t4	0.96	0.91	1.01	1.25	1.15	1.21
l300w300r300t5	1.04	0.98	1.06	1.37	1.25	1.22
l300w300r300t7.5	1.12	1.06	1.09	1.29	1.19	1.17
l300w300r450t3	0.69	0.66	0.77	0.96	0.89	0.96
l300w300r450t4	0.85	0.81	0.91	1.11	1.02	1.07
l300w300r450t5	1.00	0.94	1.03	1.23	1.13	1.16
l300w300r450t7.5	1.09	1.02	1.06	1.24	1.15	1.12
l300w300r600t5	0.96	0.91	0.99	1.18	1.08	1.12
l300w300r600t7.5	1.04	0.98	1.02	1.16	1.07	1.08
l300w300r750t3	0.52	0.50	0.59	0.72	0.67	0.72
l300w300r750t4	0.64	0.61	0.69	0.83	0.76	0.80
l300w300r750t5	0.74	0.69	0.84	0.99	0.91	0.94
l300w300r750t7.5	1.00	0.94	0.98	1.11	1.03	1.03
l400w300r150t3	0.70	0.69	1.05	1.21	1.12	1.12
l400w300r150t4	0.78	0.75	1.08	1.21	1.11	1.11
l400w300r150t5	0.84	0.80	1.12	1.21	1.11	1.11
l400w300r150t7.5	1.11	1.05	1.35	1.38	1.27	1.27
l500w300r150t3	0.72	0.69	0.80	1.24	1.14	1.14
l500w300r150t4	0.80	0.77	0.84	1.25	1.14	1.14
l500w300r150t5	0.85	0.81	0.86	1.22	1.12	1.12
l500w300r150t7.5	0.92	0.86	0.87	1.14	1.05	1.05
l600w300r150t3	0.73	0.70	0.80	1.25	1.15	1.15
l600w300r150t4	0.80	0.77	0.84	1.25	1.14	1.14
l600w300r150t5	0.97	0.91	0.97	1.39	1.26	1.26
l600w300r150t7.5	1.07	1.00	1.00	1.33	1.21	1.21
l700w300r150t4	0.91	0.87	0.95	1.42	1.29	1.29
l700w300r150t5	1.00	0.94	1.00	1.43	1.30	1.30
l700w300r150t7.5	1.11	1.02	1.04	1.38	1.25	1.25

Mean (P_m)	0.88	0.84	0.94	1.21	1.11	1.12
COV (V_p)	0.18	0.17	0.15	0.13	0.13	0.11
Resistance factor (Φ_o)	0.91	0.85	0.85	0.91	0.85	0.85
Reliability index, β	1.44	1.50	2.14	2.77	2.66	2.98

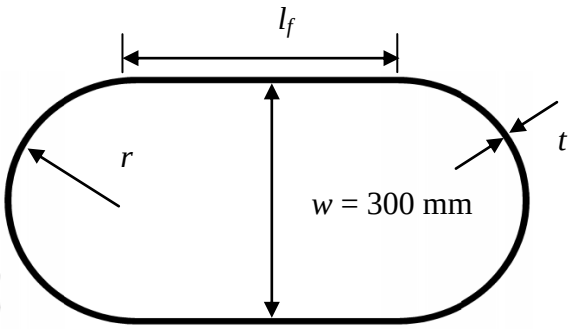

Figure 3.1: Flat oval hollow section.

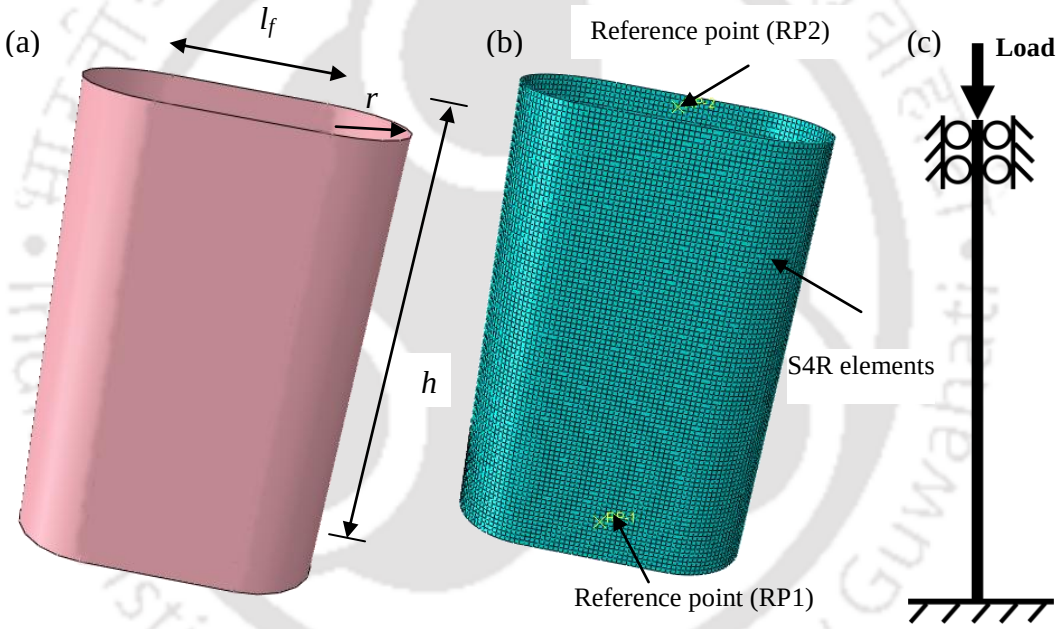

Figure 3.2: Typical FE (a) geometry, (b) FE mesh and (c) boundary conditions of LDSS flat oval hollow column.

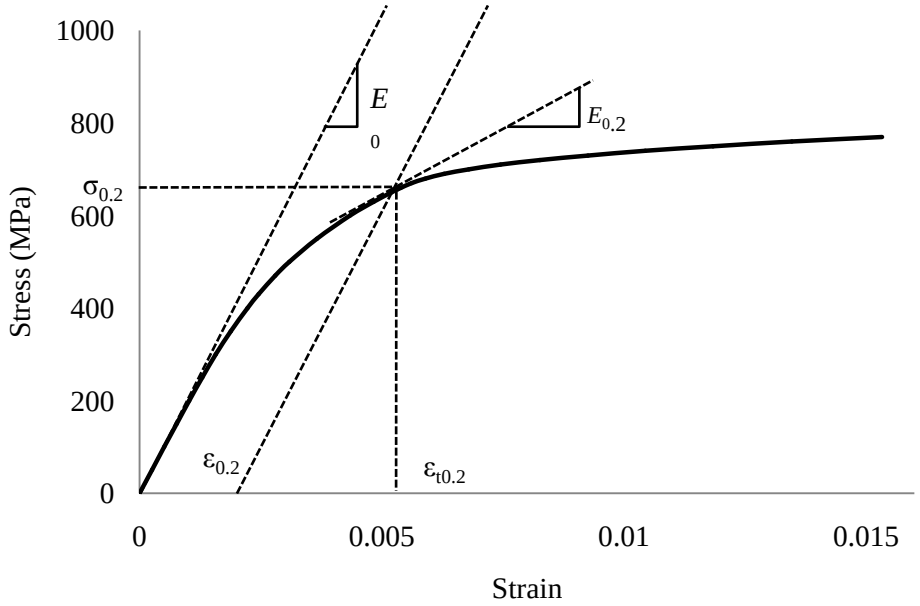

Figure 3.3: Experimental stress-strain curve of LDSS material Grade EN 1.4162 (Theofanous & Gardner, 2009).

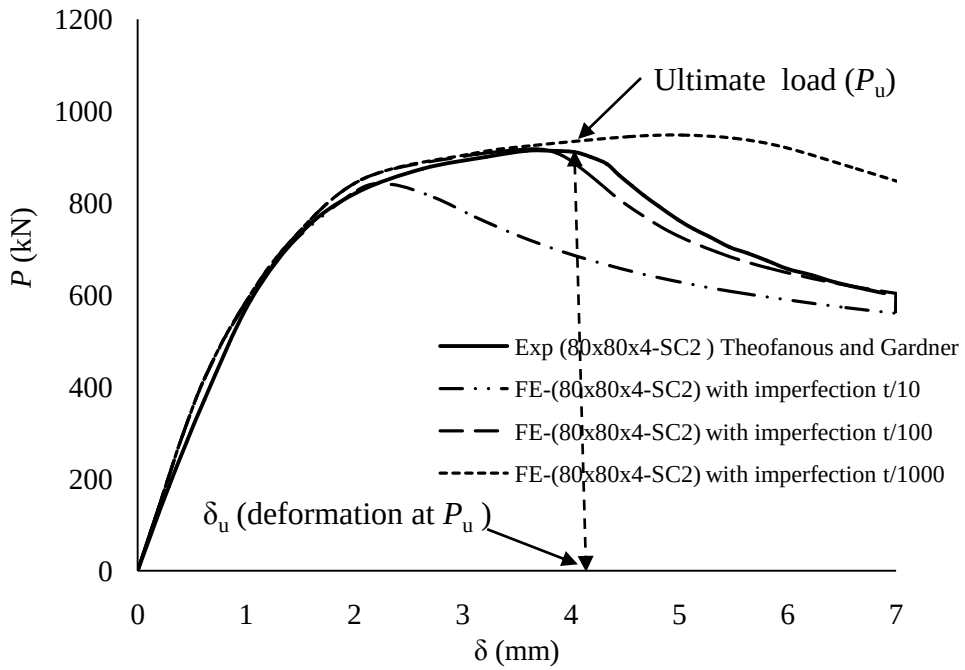

Figure 3.4: Variation of load (P) with axial displacement (δ) (SHC 80 x 80 x 4-SC2).

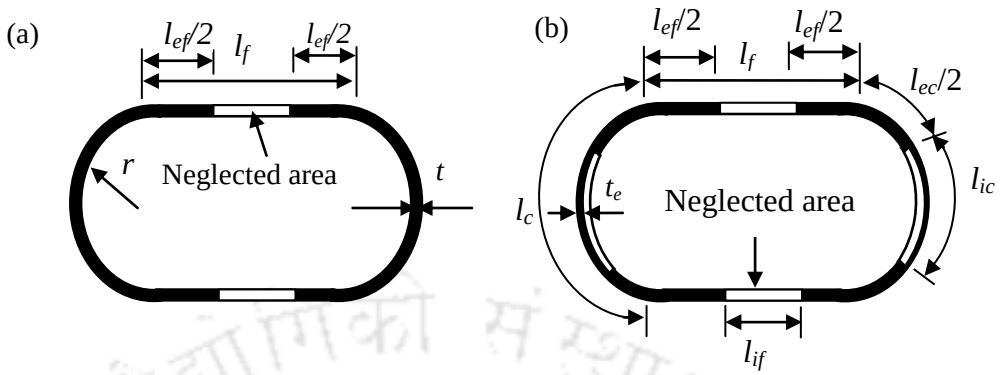

Figure 3.5: Schematic representation of effective length (l_{ef}): (a) EN 1993-1-4, ASCE 8-02, AS/NZS 4673, (b) ASDM.

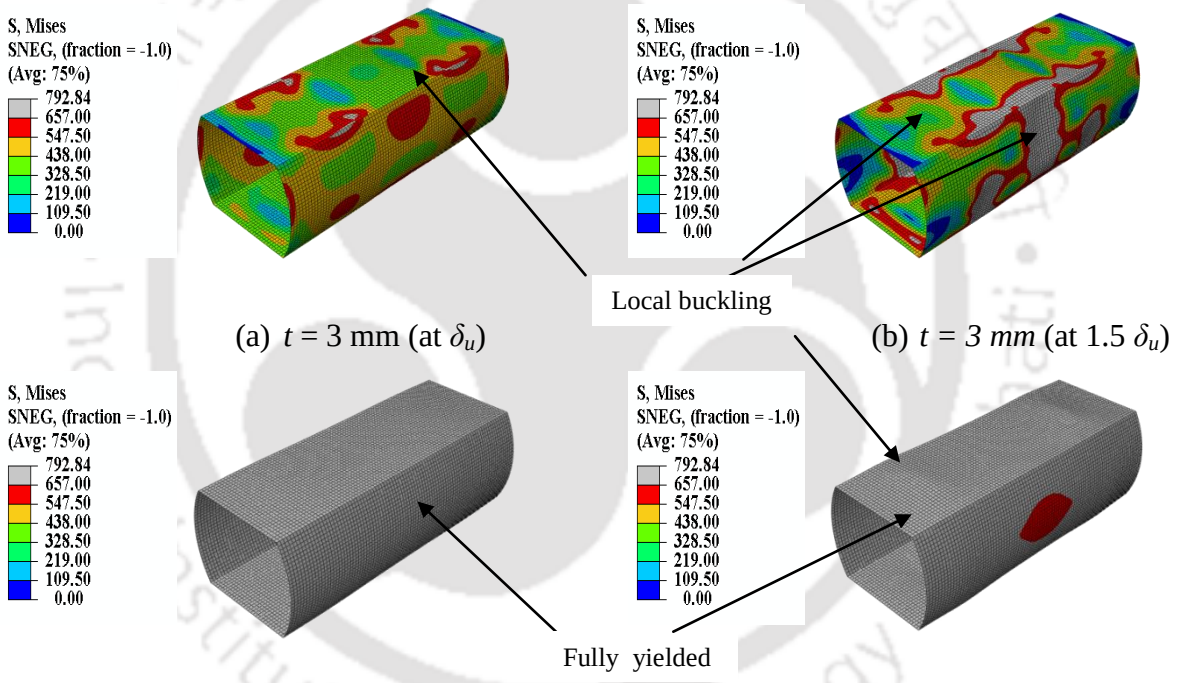

(a) t = 3 mm (at δ_u)

(b) t = *3 mm* (at 1.5 δ_u)

(c) t = 20 mm (at δ_u)

(d) t = 20 mm (at 1.5 δ_u)

Figure 3.6: Typical Von-Mises stress (superimposed on deformed shape): i) t = 3 mm (a, b), and ii) t = 20 mm (c, d) at ultimate load displacement (δ_u) and 1.5 δ_u (l_f = 300 mm; r = 300 mm).

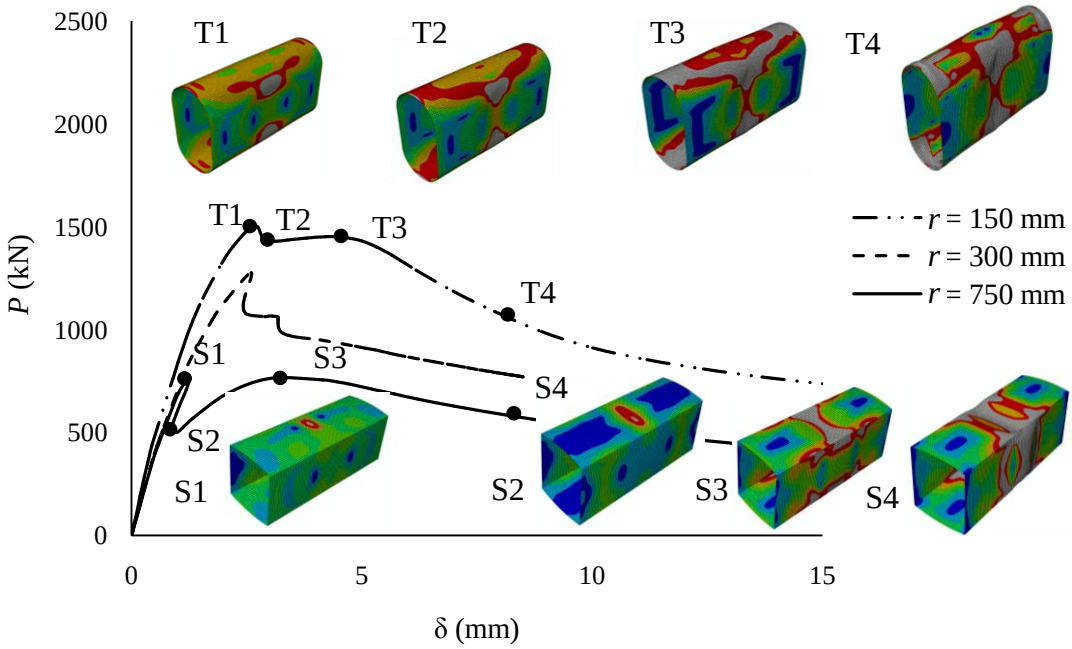

Figure 3.7: Variation of P with δ for t = 3.0 mm (l_f = 300 mm, w = 300 mm).

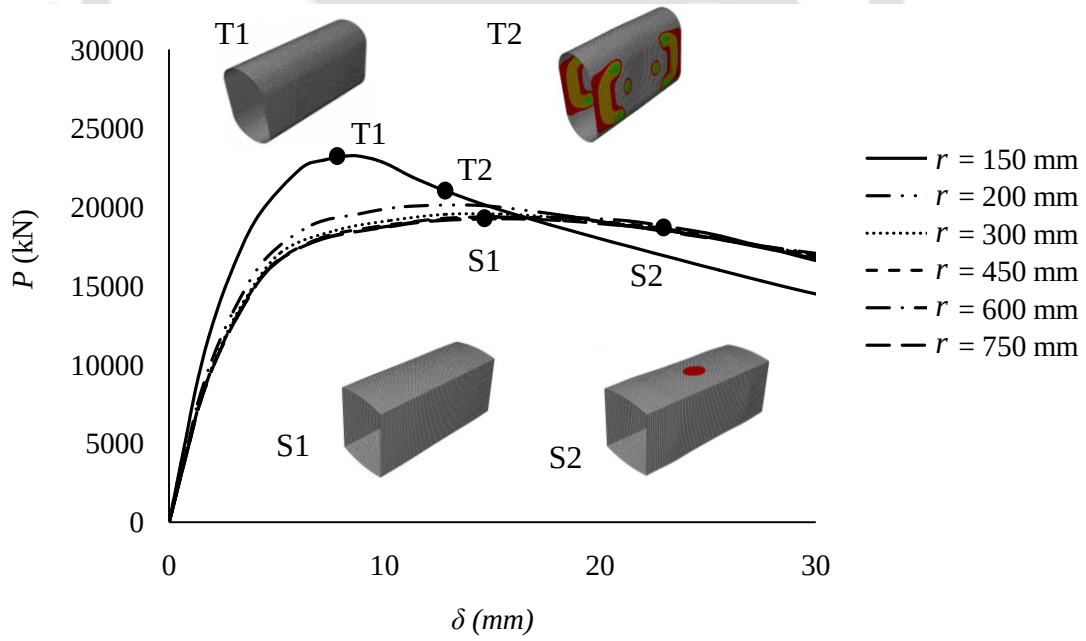

Figure 3.8: Variation of P with δ for t = 20.0 mm (l_f = 300 mm, w = 300 mm).

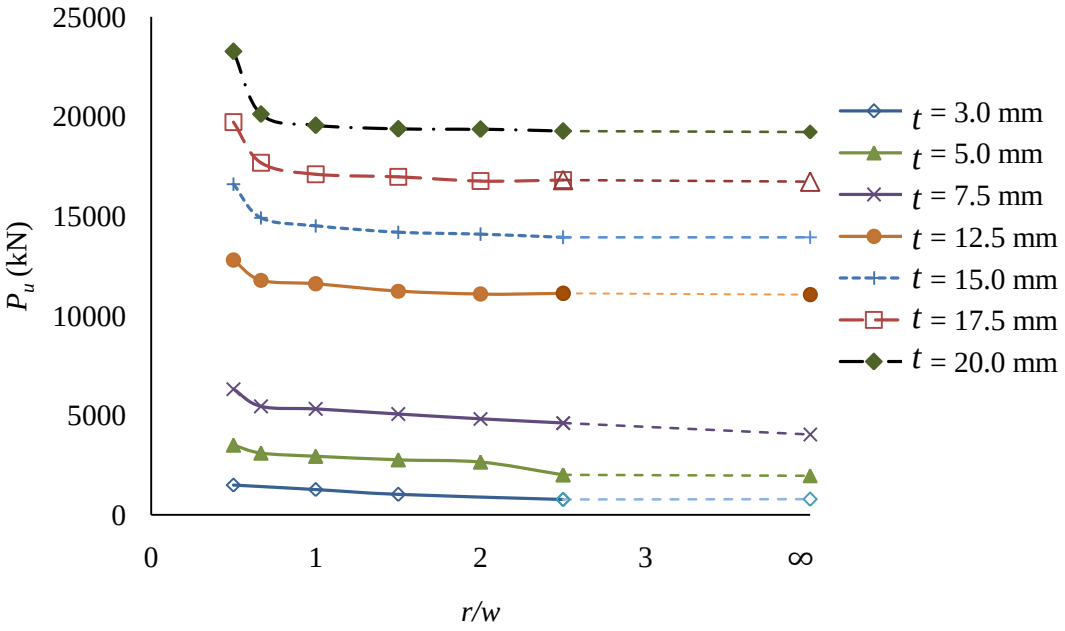

Figure 3.9: Variation of P_u with r/w (l_f = 300 mm, w = 300 mm).

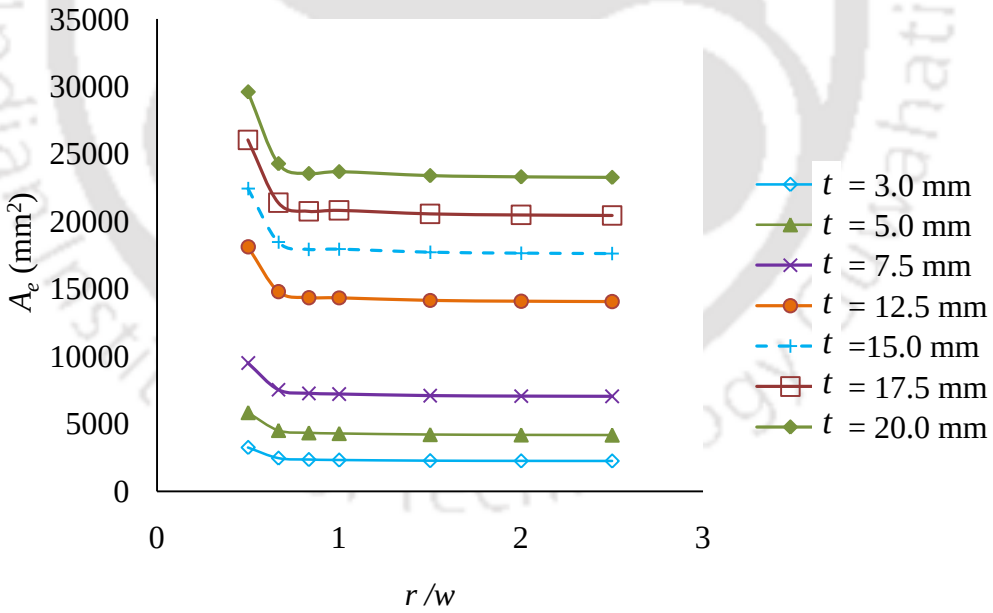

Figure 3.10: Variation of A_e with r/w (l_f = 300 mm, w = 300 mm).

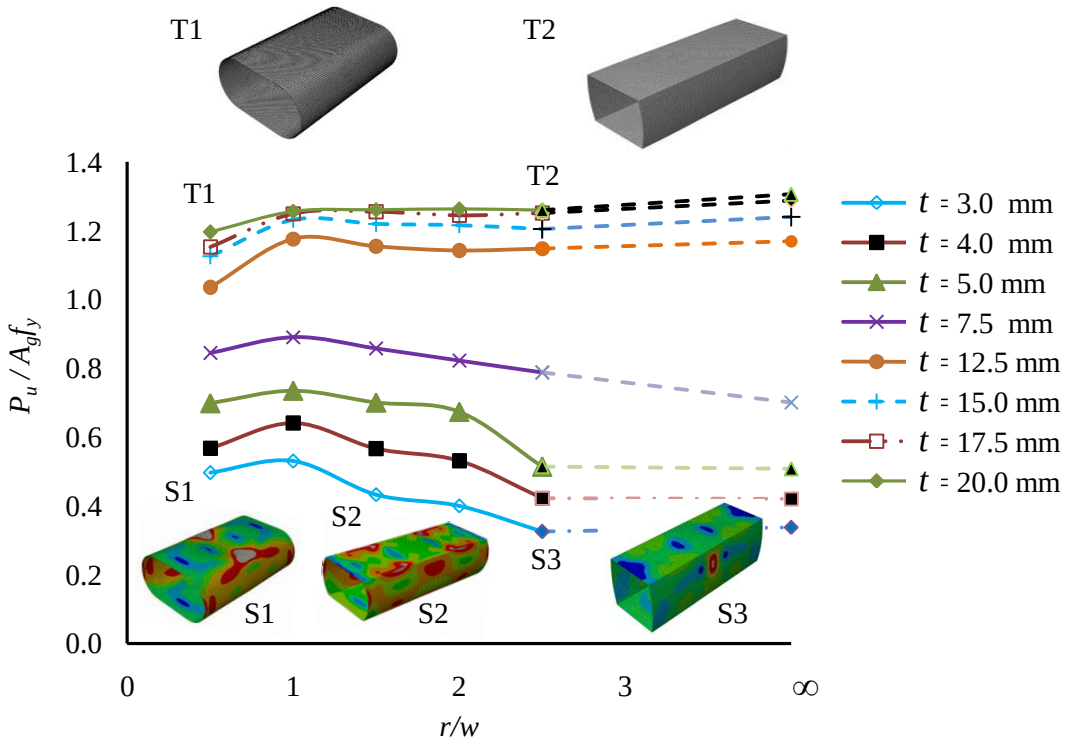

Figure 3.11: Variation of $P_u/A_g f_y$ with r/w (l_f = 300 mm, w = 300 mm).

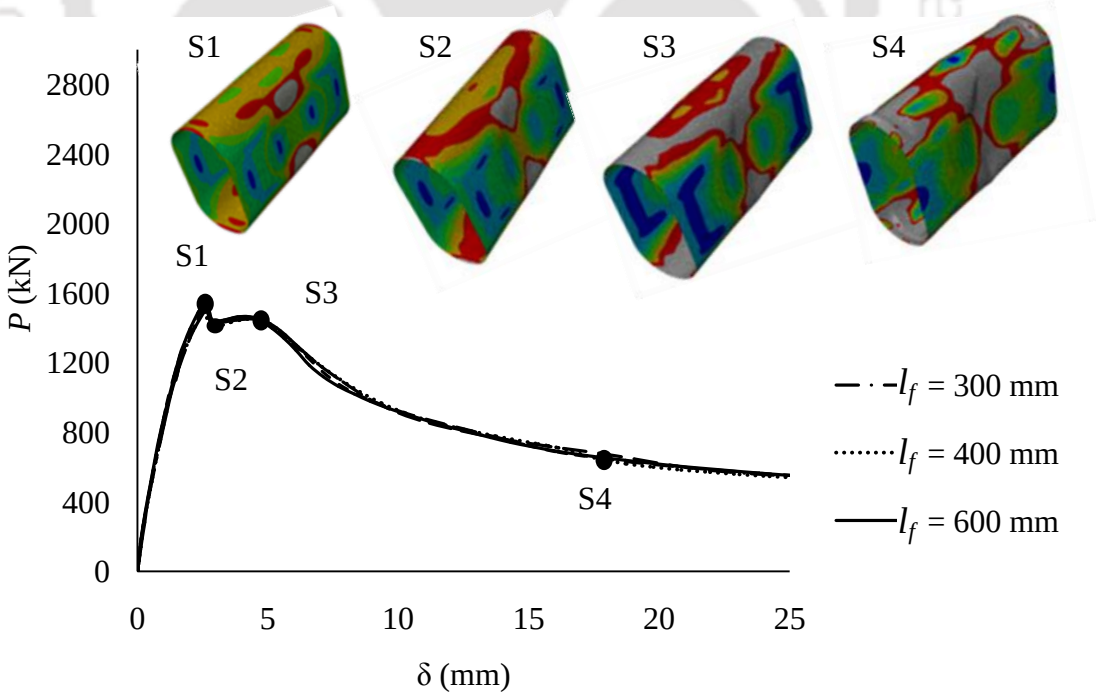

Figure 3.12: Variation of P with δ for t = 3 mm (r = 150 mm, w = 300 mm).

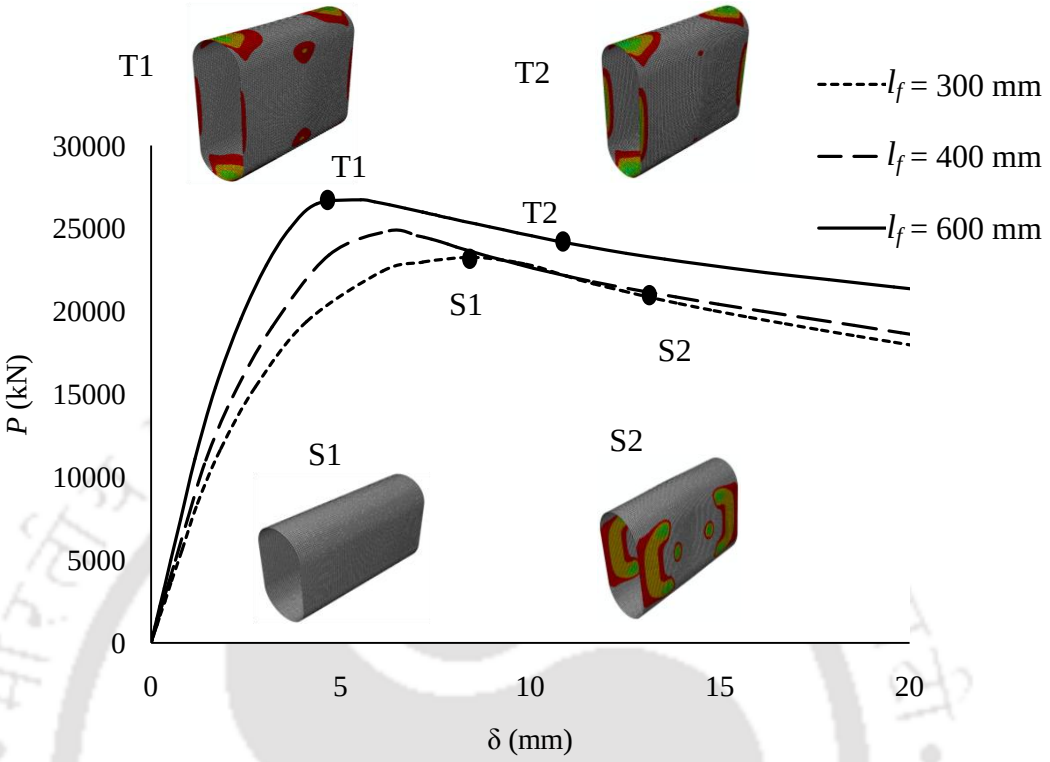

Figure 3.13: Variation of P with δ for t = 20 mm (r = 150 mm, w = 300 mm).

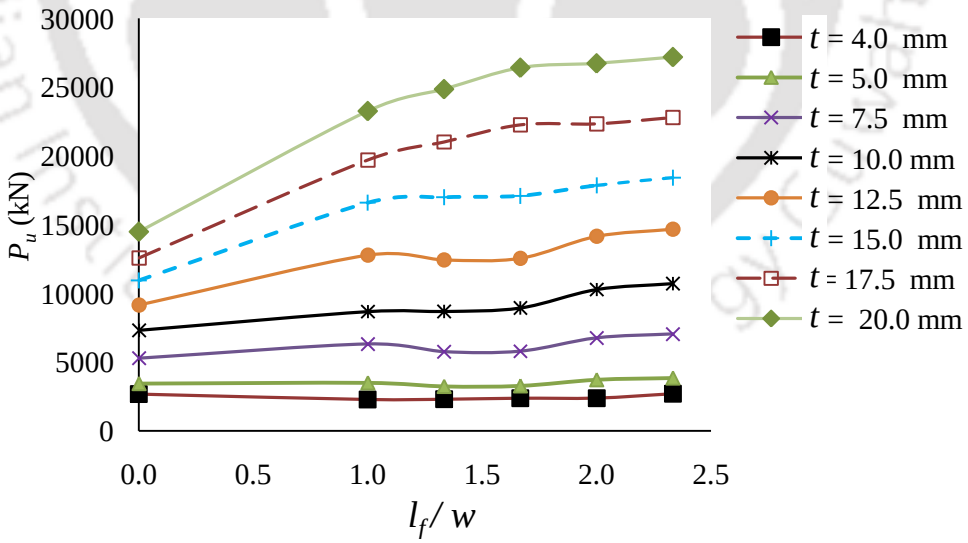

Figure 3.14: Variation of P_u with l_f/w (r = 150 mm, w = 300 mm).

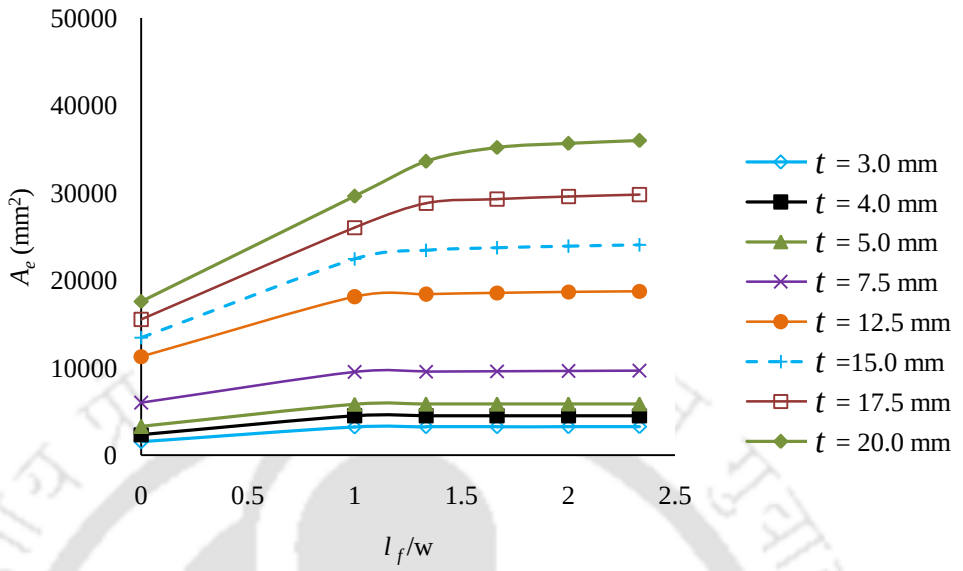

Figure 3.15: Variation of A_e with l_f/w as per EN 1993-1-4 (w = 300 mm, r = 150 mm).

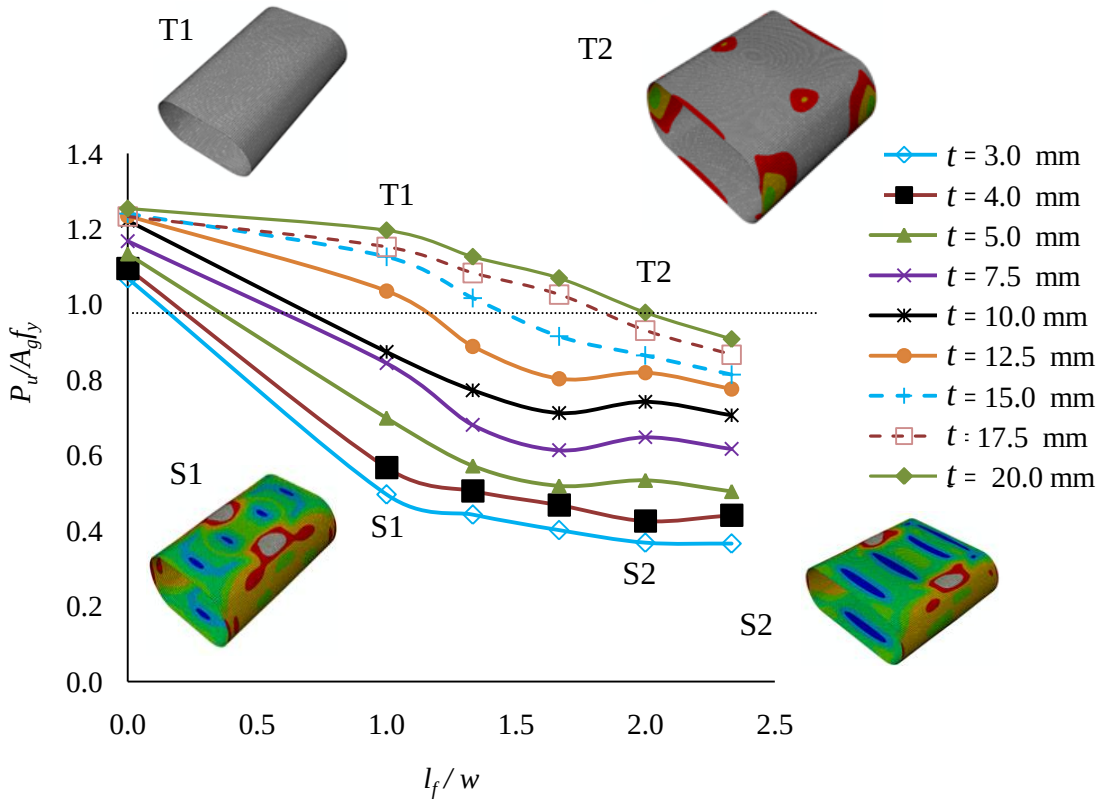

Figure 3.16: Variation of P_u/A_gf_y with l_f/w (r = 150 mm, w = 300 mm).

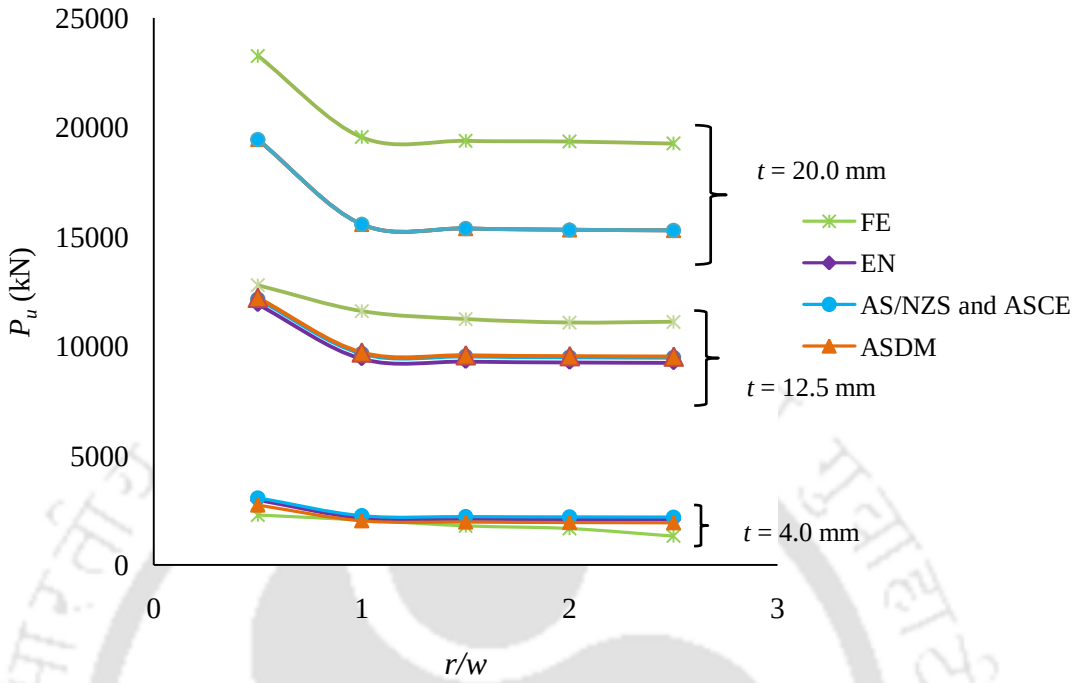

Figure 3.17: Comparison of FE and codal predictions of P_u (l_f = 300 mm, w = 300 mm).

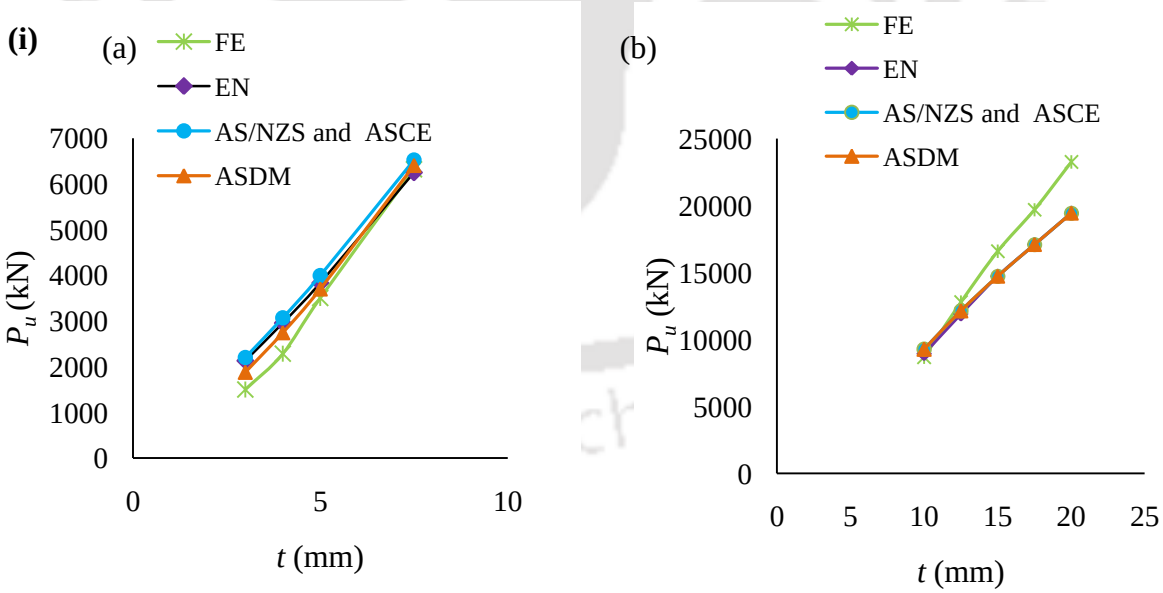

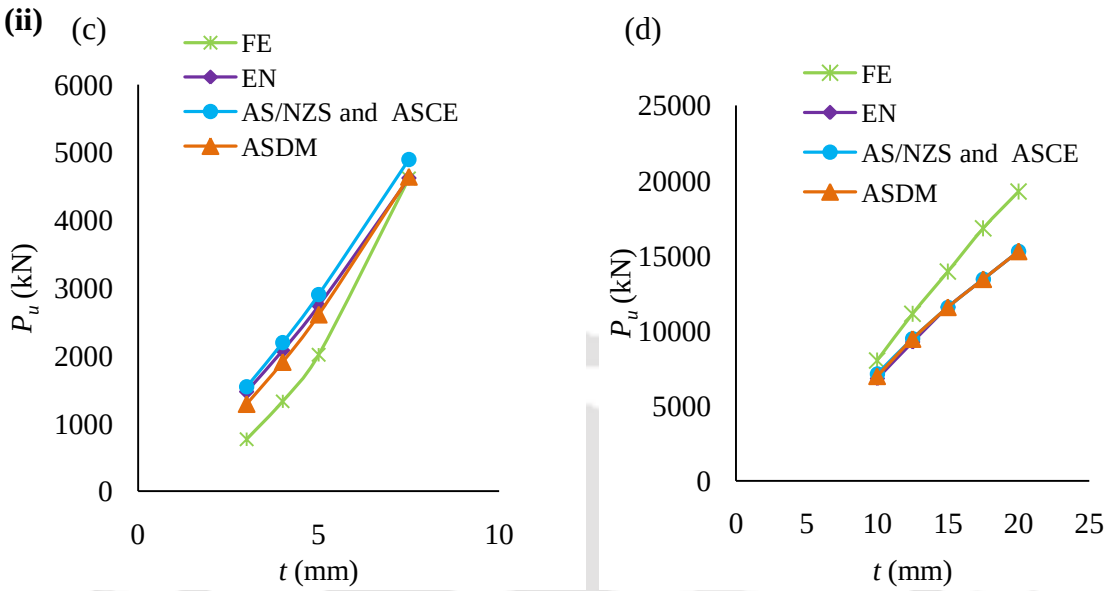

Figure 3.18: Comparison of FE and codal predictions of P_u: i) r = 150 mm [a) t = 3-7.5 mm; b) t = 10-20 mm] and ii) r = 750 mm [a) t = 3-7.5 mm; b) t = 10-20 mm] (w = 300 mm and l_f = 300 mm).

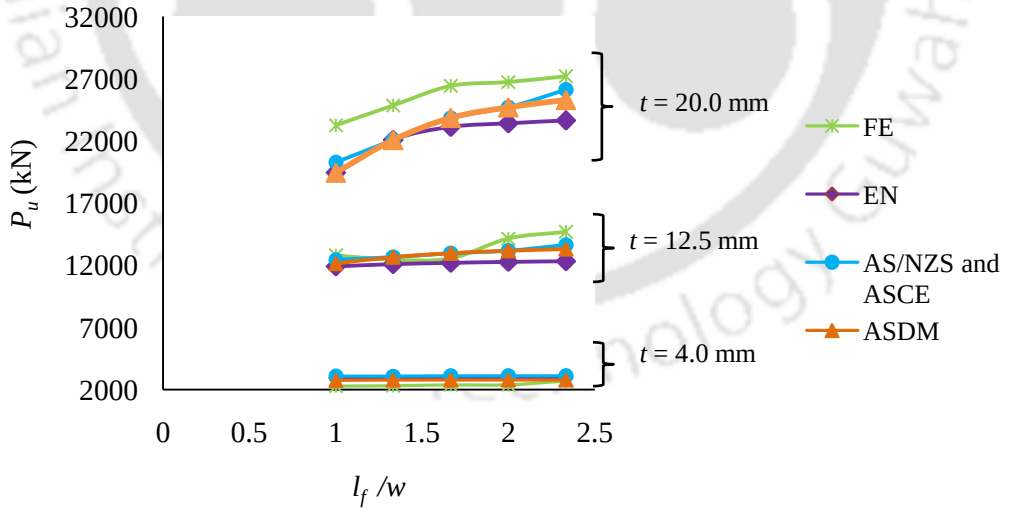

Figure 3.19: Comparison of FE and codals predictions of P_u (r = 150 mm, w = 300 mm).

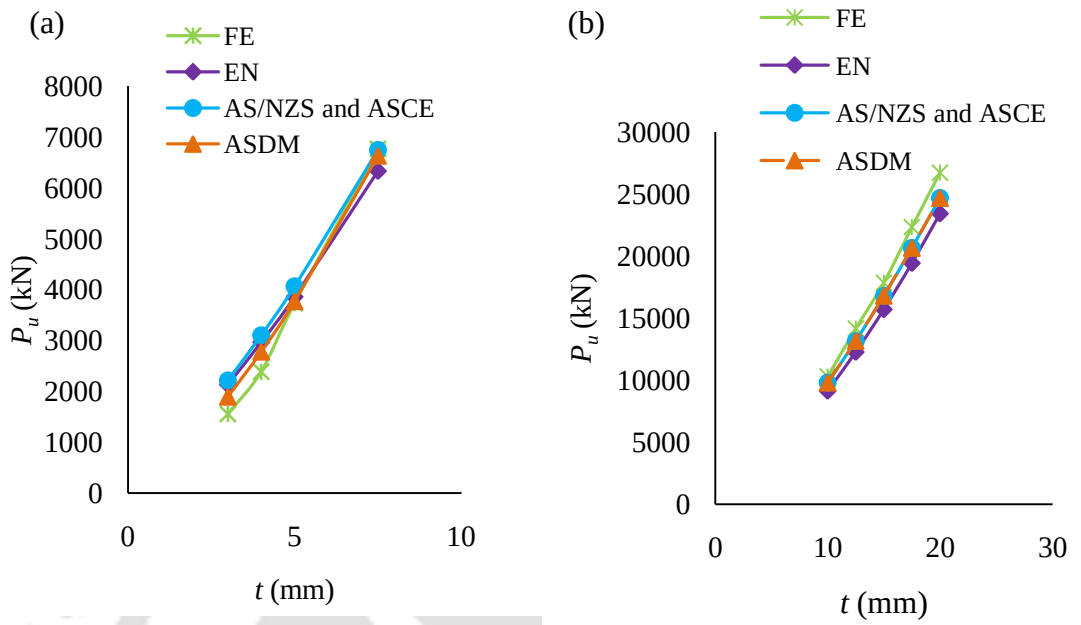

Figure 3.20: Comparison of FE and codal predictions of P_u: a) t = 3-7.5 mm; b) t = 10-20 mm (w = 300 mm and r = 150 mm, l_f = 600 mm).

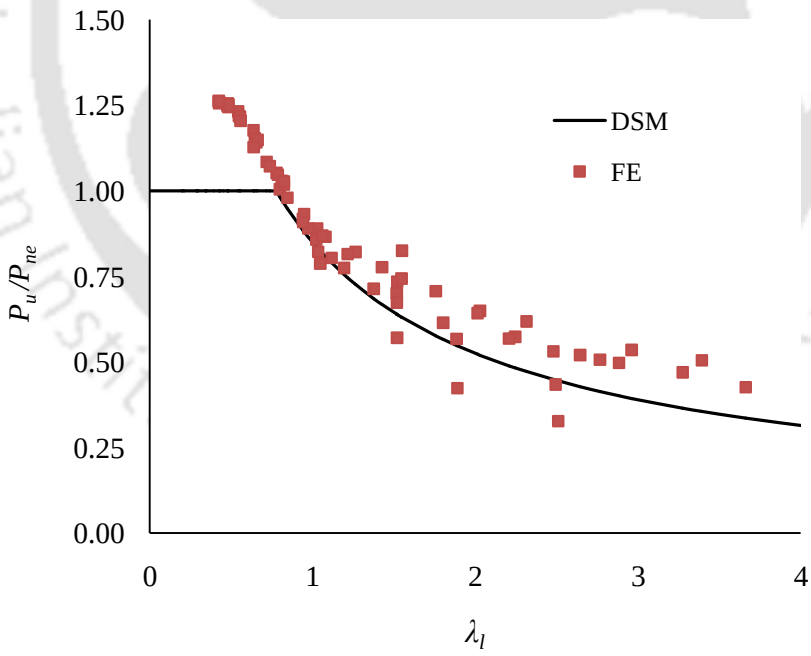

Figure 3.21: Comparison of FE and DSM results.

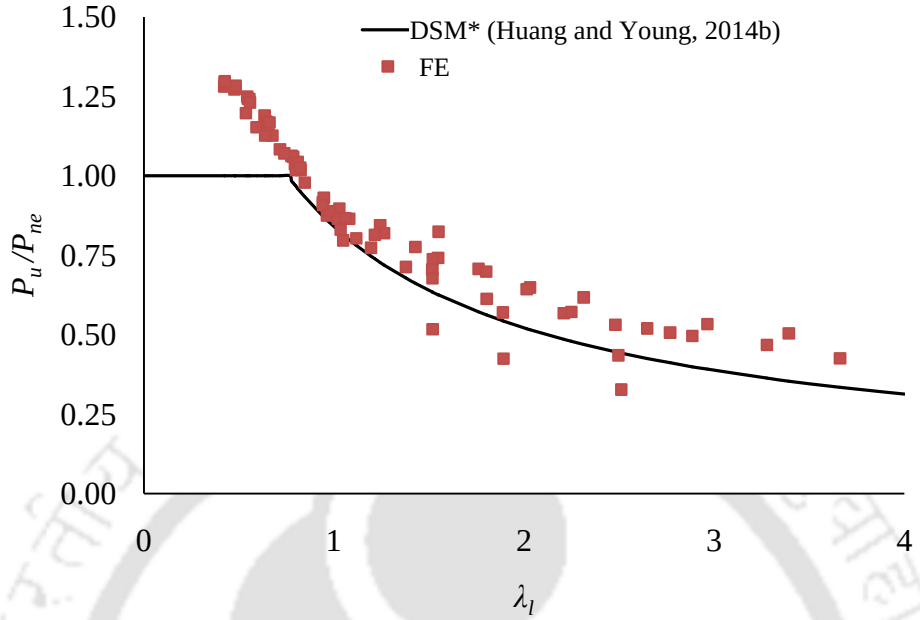

Figure 3.22: Comparison of FE and DSM* (Huang and Young, 2014b) results.

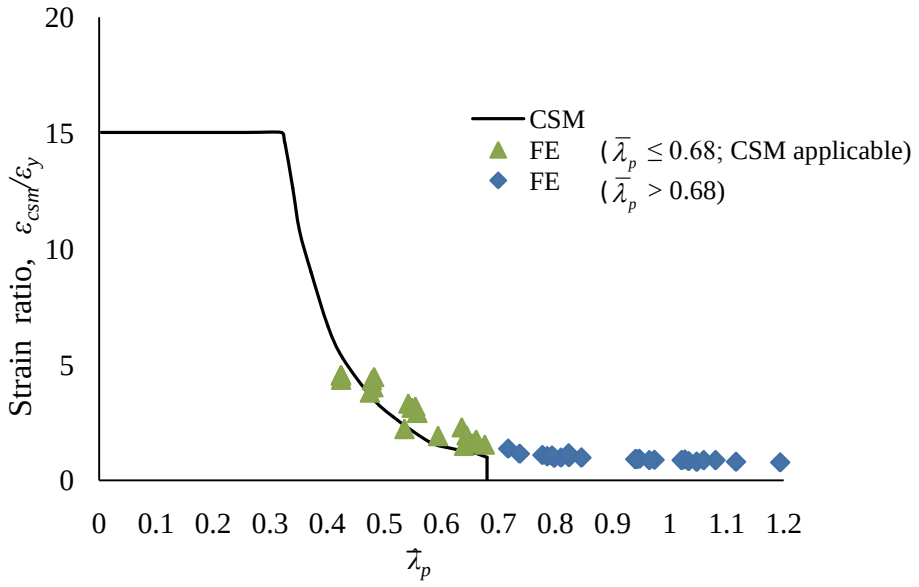

Figure 3.23: Comparison of FE and CSM strain ratios ($\varepsilon_{csm}/\varepsilon_y$).

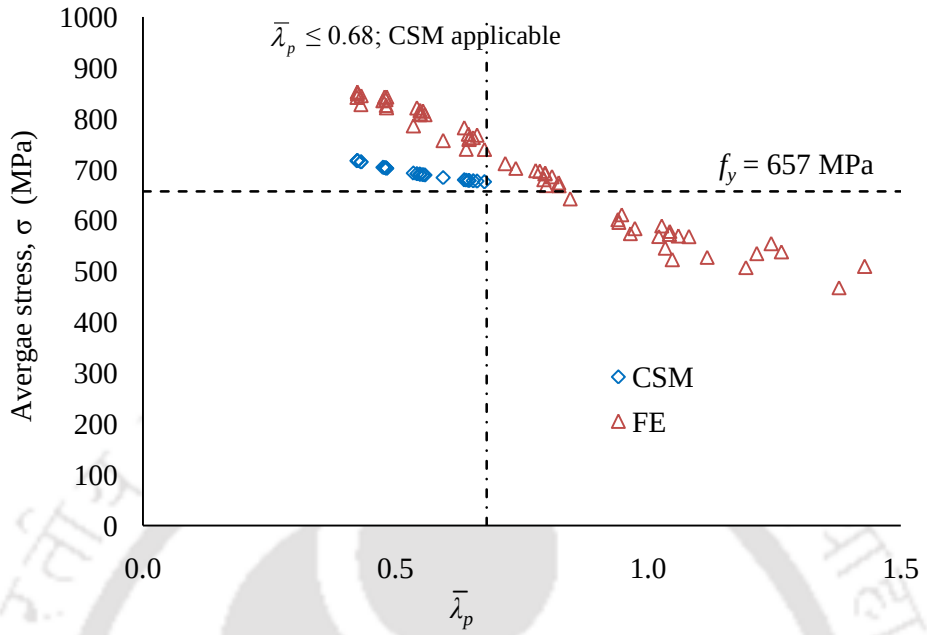

Figure 3.24: Comparison of FE and CSM average stress (σ).

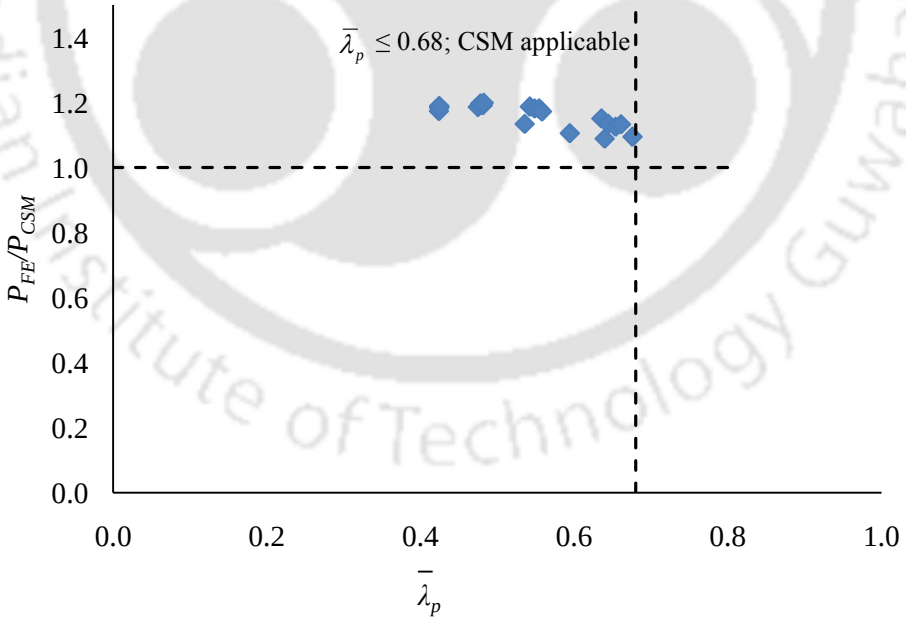

Figure 3.25: Variation of P_{FE}/P_{CSM} with $\bar{\lambda}_p$.

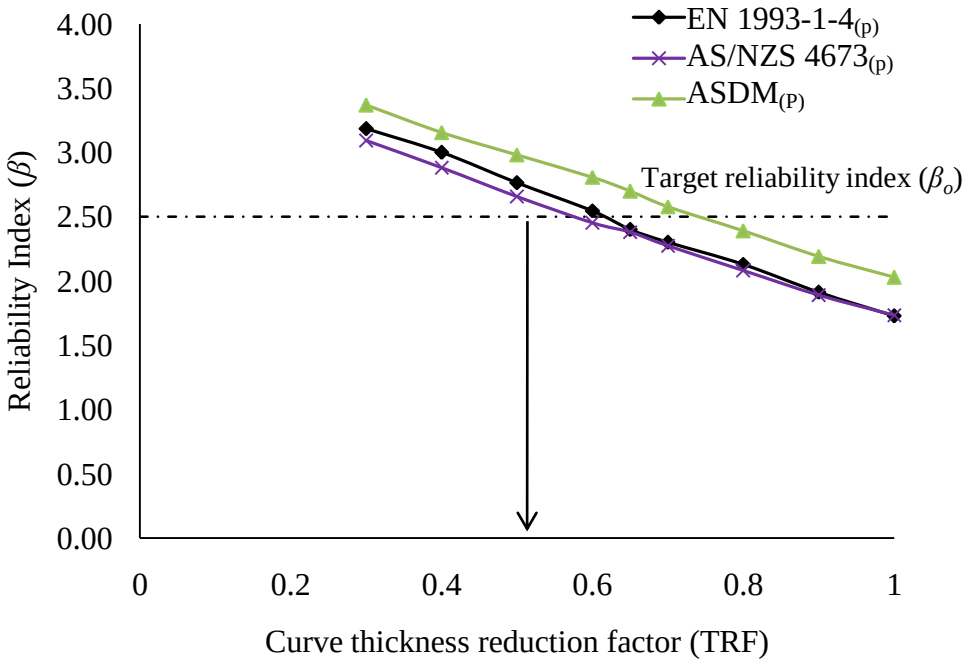

Figure 3.26: Reliability index (β) vs TRF (curve thickness reduction factor) for (proposed) modified design codes.

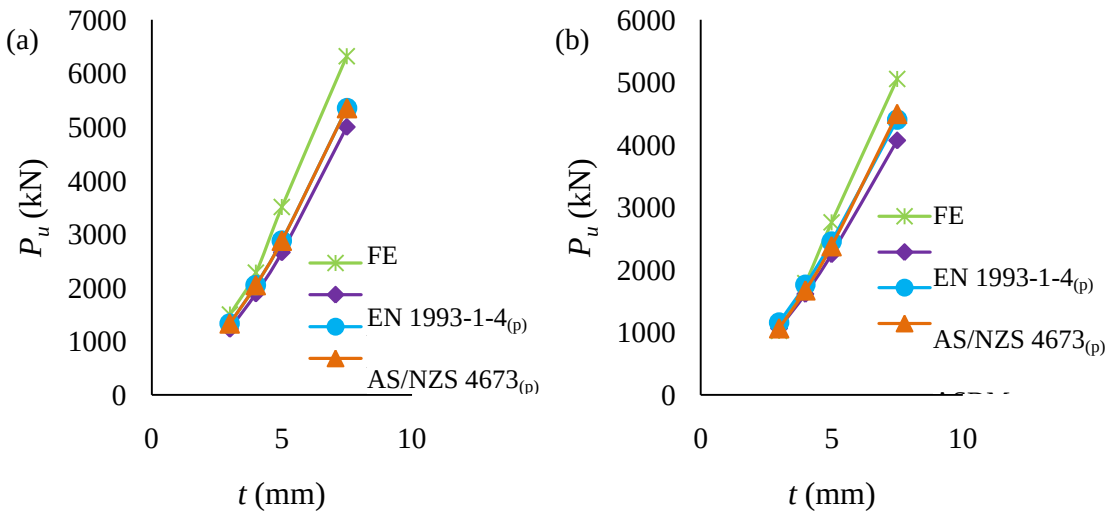

(a) $l300w300r150$ (b) $l300w300r450$

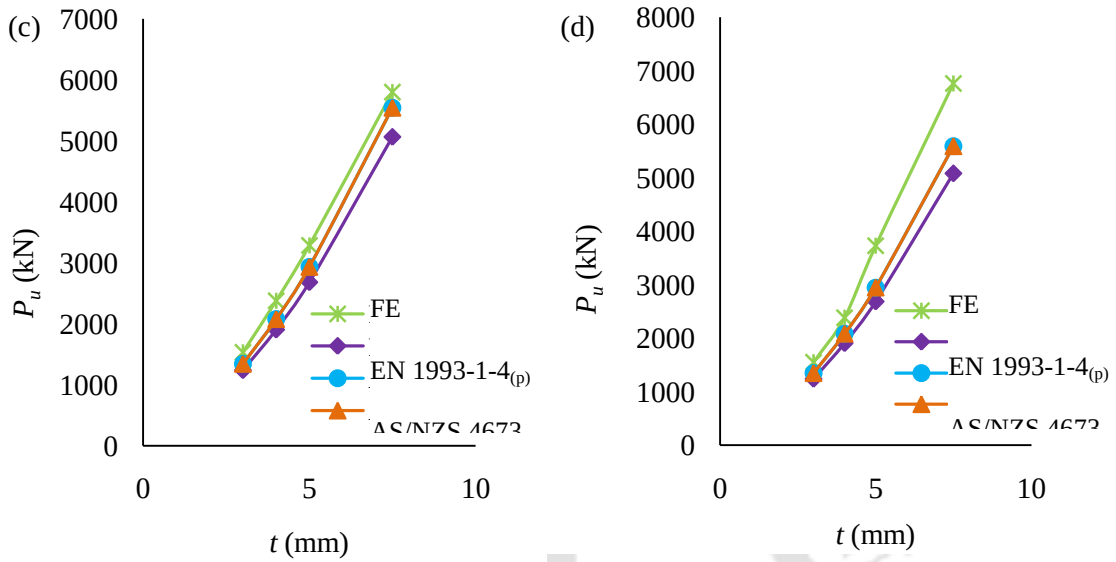

(c) *l*500*w*300*r*150 (d) *l*600*w*300*r*150

Figure 3.27: Comparison of FE and (proposed) modified codes (EN 1993-1-4$_{(P)}$, AS/NZS 4673$_{(P)}$, ASDM$_{(P)}$).

CHAPTER 4

NUMERICAL STUDY OF FIXED ENDED LEAN DUPLEX STAINLESS STEEL (LDSS) FLAT OVAL HOLLOW SLENDER COLUMNS UNDER PURE AXIAL COMPRESSION

4.1 INTRODUCTION

In the previous chapter, investigations on the load capacity and deformation characteristics of fixed ended flat oval LDSS stub columns under axial compression were presented, for Class 2, 3 and 4 sections. In similar lines, in this chapter, the previous study (Chapter 3) is extended for slender sections for both thin (or slender; Class 4) and thick (stocky; Class 1-3 sections), using FE analyses. The effect of the various cross-sectional parameters *viz*., curve element radius (r), flat element length, l_f), thickness (t), width between flat elements (w), on the ultimate compressive resistance (or ultimate load capacity, P_u) are assessed as a function of column height or length (h). In addition, the deformation failure modes are also studied for possible identification of various failure mechanisms (e.g. coupled instabilities), for both the slender and stocky cross-sections. As mentioned in the literature review

(Chapter 2), such identification of failure mechanisms were reported by Silvestre *et al.* (2013) for Class 4 sections, for semi-elliptical sections with assumed two types of yield stresses (f_y = 355 MPa and 750 MPa; elastic-perfectly plastic constitute model) using FE analysis. The results from the present study are then compared with those predicted by available design codes for stainless steel such as EN 1993-1-4 (2015), AS/NZS 4673 (2001) and design method such as DSM (e.g. Schafer and Pekoz, 1998). It may be noted that these codes are not specifically developed for LDSS, and hence as mentioned in the literature review (Chapter 2), the FE results are further compared with those modified versions of AS/NZS 4673 (2001) and DSM (1998) reported by Huang and Young (2014b) Reliability of both the original and modified i.e. EN 1993-1-4 (2015), AS/NZS 4673 (2001) and DSM (1998), AS/NZS* and DSM* were assessed against the present FE results, to check their efficiency.

4.2 FINITE ELEMENT MODELLING

4.2.1 General

The FE modelling approach followed here for the analyses of fixed-ended slender hollow LDSS columns is similar to the modelling of LDSS stub columns presented in the previous chapter (see Section 3.2). LDSS material constitutive material model proposed by Gardner and Ashraf (2006) along with similar fixed ended boundary conditions and shell finite elements (S4R) available in Abaqus (2009) were employed. The initial geometry was perturbed by both local and global imperfection magnitudes, necessary for modelling slender columns, using the imperfection magnitudes proposed by Theofanous *et al.*, 2009a, Chan and Gardner, 2008 etc. (for local imperfection magnitude) and Theofanous and Gardner (2009), Patton and Singh (2013), Zhu and Young (2012) etc. (for global imperfection magnitude). The FE modelling approach was initially validated against experimental studies on slender LDSS hollow tubular columns reported by Theofanous and Gardner (2009). The following sections briefly describe the FE modelling approach adopted.

4.2.2 Geometry and boundary conditions

Similar flat-oval cross sections and boundary conditions shown in Figure 3.2 (in Chapter 3) are considered for FE analysis of LDSS flat-oval hollow tubular columns. Typically, the bottom part was fixed while the axial compressive displacement was applied on the top through displacement control, with the top end being allowed to translate freely only in the axial direction. These boundary conditions were achieved through reference points RF1 and RF2, which are kinematically coupled, as detailed in Section 3.2.2. Such approaches were adopted in the literature e.g. Lui and Young (2003), Ellobody and Young (2005), Ellobody (2007), Theofanous and Gardner (2009), Patton and Singh (2013), Gardner and Ministro (2004) etc. The various geometrical dimensions used for the parametric study are r (radius of curve element) = 25, 50, 75 and 100 mm, w (distance between flat elements) = 50, 100, 150 and 200 mm and l_f (flat element length) = 50, 75, 100 and 150 mm. Two types of cross-sections viz., slender (Class 4) and stocky (Class 1 and 2) sections with t = 2 mm and t = 10, 15, 20 mm, respectively were considered for the study. The height (h) of the column was varied from 1000-15000 mm and 1000-3500 mm for the slender and stocky columns respectively. A higher value of h (~ ≥ 12000 mm) was adopted to achieve flexural type mechanism (to be discussed in Section 4.7.1.4). As compared to the stub columns presented in the previous chapter, the cross sectional sizes of the slender columns are made smaller, so that higher column slenderness values can be obtained, without significantly increasing the lengths, thus, making the FE mesh economical.

4.2.3 Finite element mesh

The slender hollow flat oval LDSS columns were discretised using the same S4R elements (mentioned in Section 3.2.3). The size of the S4R elements were maintained at ~ 10 x 10 mm (and hence with an aspect ratio ~ 1.0) for all the specimens analysed. This element size is considered to be optimum, considering both accuracy and speed of FE analyses, and was arrived at by performing mesh

convergence study through linear elastic eigen value analyses. In all, ~2,600-30,000 S4R elements were used, to model slender columns.

4.2.4 Initial geometric imperfections

In order to impose the initial geometric imperfections (both local and global/flexural imperfections), linear elastic eigen analyses was first carried out (using the Lanczos method) to extract both the local and global mode shapes (it may be noted that only local imperfection was used for the analysis of stub columns in the previous chapter). The local and global buckling mode shapes were found to occur in the first few eigen modes. Both the mode shapes were superimposed on the initial perfect geometry to create the final shape of the slender hollow column for the analyses (see Ellobody and Young, 2005, Ellobody, 2007, Theofanous and Gardner, 2009, Zhu and Young, 2012, Patton and Singh, 2013). Following the reports in the literature, both the local and global mode shapes were scales with imperfection magnitudes of t/100 (see e.g. Theofanous *et al*., 2009a, Chan and Gardner, 2008) and h/1500 (see e.g. Theofanous and Gardner, 2009, Patton and Singh, 2013) respectively.

4.3 VALIDATION OF FE MODELS

Before proceeding with the FE analyses, it is necessary to validate the FE modelling approach adopted herein with some benchmark experimental results, in order to convince its validity. Thus, the current FE modelling approach is validated with comparable experimental results reported by Theofanous and Gardner (2009) on pinned-ended LDSS slender SHC (Square Hollow Column-80x80x4 and 60x60x3) of lengths, h = 800, 1200, 1600 and 2000 mm. The key material parameters (Young's modulus, E, 0.2% proof stress, $\sigma_{0.2}$, 1% proof stress, $\sigma_{1.0}$, strain hardening coefficients, n and $n'_{0.2,1.0}$) used in the Gardner and Ashraf (2006) model are shown in Table 4.1. The LDSS material stress-strain curve for the 60x60x3 specimen is shown in Figure 4.1 (See Figure 3.3 for the material stress strain curve of 80x80x4

specimen). It may be mentioned that in the subsequent parametric study (following this validation), LDSS material properties corresponding to specimen 80x80x4 is used (see Figure 3.3), as in the case of Chapter 3, to have a consistent approach. The geometric details of the validated experimental columns under axial compression are given in Table 4.2. The size and number of elements used for the validation are ~8x8 mm, and 6000 and 10,000 S4R elements respectively. The validation is presented in the form of load (P) vs lateral mid-length deflection (δ_{lat}) in Figure 4.2. It can be seen that both the ultimate and post-ultimate curve profiles are well matched, thus indicating that the current FE modelling approach can provide reasonably accurate results for the modelling of LDSS hollow columns under axial compression.

4.4 PARAMETRIC STUDY OF LDSS FLAT OVAL HOLLOW SLENDER COLUMNS

FE analyses of LDSS flat oval hollow sender columns were carried out by varying the geometrical parameters like flat element length (l_f = 50-150 mm), radius of the curve element (r = 25-100 mm), distance between the flat elements (w = 50-200 mm), length/height of the columns (h = 1000-15000 mm), and thickness (t = 2-20 mm). The entire analyses matrix results in three types of cross-sections i.e. Class 1 (i.e. $l_f/t\varepsilon \leq 33$), Class 2 ($l_f/t\varepsilon \leq 35$) and Class 4 ($l_f/t\varepsilon > 37$) following EN 1993-1-4 (2015). The results of the FE analyses were grouped under two headings i.e. slender cross-sections (i.e. Class 4 sections; t = 2 mm) and stocky cross-sections (i.e. Class 1 and 2; t = 10-20 mm). In all, a total of 200 FE flat oval hollow slender column models were analysed. The labelling convention followed the pattern flat length (l_f), distance between flat lengths (w), radius of curve element (r), thickness (t) and height (h). For example, $l50w50r25t2h1000$ would represent a column with l_f = 50 mm, w = 50 mm, r = 25 mm, t = 2 mm and h = 1000 mm. Based on the FE analyses, structural performance of the columns under axial compression were assessed, with attention towards load capacity and deformation modes. Special observations are

also made on the failure modes or mechanism both at ultimate (i.e. δ_u) and post-ultimate (e.g. ~1.5 δ_u) deformations, for both the slender and stocky cross sections. Later, the FE results were compared with the predictions made by stainless steel design codes such as EN 1993-1-4 (2015) and AS/NZS 4673 (2001), to check their applicability for LDSS flat oval hollow columns. Further, the FE results are also compared with proposed modified AS/NZS 4673 (2001) specifications made by Huang and Young 2014b (based on their experimental studies on LDSS hollow square and rectangular sections). Before, proceeding with the presentation of results and discussions (Section 4.6), the codal and modified codal, and design method considerations are presented in the following sub-sections.

4.5 CODAL AND MODIFIED DESIGN CONSIDERATIONS

In this section, the EN 1993-1-4 (2015) and AS/NZS 4673 (2001), modified AS/NZS 4673 (2001), modified DSM procedures for calculating the design strengths are briefly described below. The DSM procedure presented in Section 3 (see Chapter 3) remains applicable for the case of slender column also. Sample calculations following the above mentioned design procedures are provided in the Annexure.

4.5.1 EN 1993-1-4 (2015)

The column design strength of EN 1993-1-4 (2015) i.e. (P_{EN}) as per Clause 5.4.2 of EN 1993-1-4 (2015) are given in Equation 4.1

$$P_{EN} = \chi f_y A \tag{4.1}$$

where the buckling reduction factor, χ (to account for flexural buckling) is defined as ;

$$\chi = \frac{1}{\varphi + \left[\varphi^2 - \overline{\lambda^2}\right]^{0.5}} \leq 1.0 \text{ ; where } \varphi = 0.5\left(1 + \alpha\left(\overline{\lambda} - \overline{\lambda_0}\right) + \overline{\lambda^2}\right) \tag{4.2}$$

The non-dimensional slenderness ratio, $\bar{\lambda}$, is given by Equation 4.3;

$$\bar{\lambda} = \sqrt{\frac{Af_y}{P_{cre}}} \tag{4.3}$$

where, A is the cross-sectional area. As per EN 1993-1-4 (2015), *A* is taken as the gross cross-sectional area (A_g) for Class 1 and 2 sections, and effective cross-sectional area (A_e) for Class 4 sections (see Equation 3.5 for A_e). P_{cre} is the elastic critical force for the relevant buckling mode based on gross cross sectional properties given by Equation 4.4.

$$P_{cre} = \frac{\pi^2 EI}{h^2} \tag{4.4}$$

where, *E*, *I* and *h* are the Young's modulus, moment of inertia and effective height of the column taking into consideration of the boundary conditions respectively. The values of α (imperfection factor) and $\bar{\lambda}_o$ (limiting slenderness) considered in this study are 0.49 and 0.40, respectively (see Table 5.3 of the EN 1993-1-4, 2015).

4.5.2 AS/NZS 4673 (2001)

The column design strength based on AS/NZS 4673 (2001) i.e. ($P_{AS/NZS}$) is given in Equation 4.1

$$P_{AS/NZS} = Af_n \tag{4.5}$$

where f_n is the stress in the column member i.e. the least of the flexural, torsional and flexural-torsional buckling stress and is given by Equation 4.6

$$f_n = \frac{f_y}{\phi + \sqrt{\phi^2 - \lambda_f{}^2}} \leq f_y \tag{4.6}$$

The expression for ϕ and λ_f are given in Equations 4.7 and 4.8

$$\phi = \frac{1}{2}\left(1 + \eta + \lambda_f{}^2\right) \tag{4.7}$$

$$\lambda_f = \left(\frac{jh}{r}\right)\sqrt{\frac{f_y}{\pi^2 E}} \tag{4.8}$$

where *j*, *r*, *h* are the effective length factor, radius of gyration, and unbraced total length of column respectively, and

$$\eta = \alpha\left(\left(\lambda_f - \lambda_1\right)^\beta - \lambda_0\right) \tag{4.9}$$

In the above expression (Equation 4.9), α, β, λ_o and λ_l denote the buckling stress coefficients. As the current AS/NZS 4673 (2001) does not provide the values of these coefficients, the values corresponding to S31803 (EN 1.4462, duplex) i.e. 1.16, 0.13, 0.65 and 0.42 for α, β, λ_o and λ_l, respectively (see Table 5 of AS/NZS 4673, 2001), have been used in deriving the column strength.

4.5.3 Proposed modified AS/NZS 4673 (Huang and Young, 2014b)

As mentioned before, LDSS material particularly EN 1.4162 is not covered in the current AS/NZS 4673 (2001). Thus, based on their study, Huang and Young (2014b) on LDSS square and rectangular hollow members, new bucking stress coefficient values i.e. 0.86, 0.14, 0.67 and 0.45 for α, β, λ_o and λ_l, respectively, were suggested for members made of LDSS in Table 4.3. Further, resistance factor of 0.85 has been used as recommended by Huang and Young (2014b). With the new buckling coefficient values, modified AS/NZS 4673 design strength ($P^*_{AS/NZS}$) are estimated for LDSS columns.

4.5.4 Proposed modified DSM (Huang and Young, 2014b)

The direct strength method (DSM), originally, developed by Schafer and Pekoz (1998) for the design of cold formed steel members has been presented in Section 3.3.2. A modification to the original DSM was reported by Huang and Young

(2014b) based on their studies on square and rectangular LDSS hollow columns. The modified nominal axial strength, P^*_{DSM} (for LDSS columns) is given in Equation 4.10.

$$p^*_{DSM} = \min(P_{ne}, P_{nl}) \quad (4.10)$$

where,

$$P_{ne} = \begin{cases} (0.87^{\lambda_c^2})P_y & \text{for } \lambda_c \le 1 \\ \left(\frac{0.877}{\lambda_c^2}\right)P_y & \text{for } \lambda_c \le 1 \end{cases} \quad (4.11)$$

$$P_{nl} = \begin{cases} P_{ne} & \text{for } \lambda_l \le 0.769 \\ \left[1 - 0.16\left(\frac{P_{crl}}{P_{ne}}\right)^{0.4}\right]\left(\frac{P_{crl}}{P_{ne}}\right)^{0.4} P_{ne} & \text{for } \lambda_l > 0.769 \end{cases} \quad (4.12)$$

A comparison of DSM (Equations 3.20 and3.21) and modified DSM (Equations 4.11 and 4.12), shows that the difference between the DSM and modified DSM (or DSM*) are in the values of coefficients of P_y and P_{ne}; and on the limits of λ_l and λ_c.

4.6 RELIABILITY ANALYSIS

In order to assess the applicability of the design codes such as EN 1993-1-4 (2015), AS/NZS 4673 (2001), DSM (1998); and modified AS/NZS 4673 (2001), modified DSM (Huang and Young, 2014b) for flat oval hollow slender columns, reliability analyses have been carried out considering their respective resistance factors, and load combinations. The reliability analyses were carried out based on the procedure suggested in the commentary of the ASCE 8-02 (2002) (for cold-formed steel structures), as detailed in Section 3.3.4.

4.7 RESULTS AND DISCUSSION

The non-linear FE analyses results of the flat-oval LDSS hollow slender columns under axial compression, for the parameter range mentioned in Section 4.4 are presented in the following sub-sections. As mentioned in Section 4.4, the results

are presented in two cases viz., a) slender sections (or Class 4 sections) and b) stocky sections (or Class 1 and 2 sections) in Sections 4.7.1 and 4.7.2 respectively. The results are presented in the form of different deformation or failure mechanisms, followed by the effect of cross-sectional parameters like r, l_f, w, and h, on the load capacity (P_u). Afterwards, the FE results are compared with predictions from EN 1993-1-4 (2015), AS/NZS 4673 (2001), DSM (Schafer and Pekoz, 1998); and modified AS/NZS 4673 (2001), modified DSM (Huang and Young, 2014b), to check their efficiency for flat-oval LDSS hollow slender columns.

4.7.1 Slender sections (Class 4)

4.7.1.1 *Deformation mechanisms*

Based on the FE analyses of flat oval hollow slender columns of slender sections (Class 4), considering non-dimensional slenderness value ($\overline{\lambda}$) up to ~7 (or h = 1000-15000 mm), three key failure or deformation mechanism have been identified observing their deformation modes at δ_u (i.e. deformation corresponding to P_u) and 1.5 δ_u, *viz.*, a) Local to local yielding (Mechanism SL1A), b) Local to local yielding flexural (Mechanism SL1B), and c) Flexural to flexural yielding (Mechanism SL2). The three deformation mechanisms are described below:

a) Local to local yielded buckling (Mechanism SL1A)

The SL1A mechanism is generally classified based on the deformation mode of local buckling at δ_u and locally yielded buckling at post ultimate load (i.e. 1.5δ_u). Figure 4.3 shows the typical variation of normalised loads i.e. P/P_{cr} and P/P_y (where P_{cr} is the critical elastic buckling load obtained through Abaqus; $P_y = Af_y$ is the gross yield load) with axial deformation / shortening (δ) and von-Mises contour plots superimposed on deformed shapes (at δ_u and 1.5 δ_u). The results are presented for the specimen *l*50*w*50*r*75*t*2*h*1000. It can be seen from Figure 4.3b and 4.3c that, P_u/P_{cr} = ~0.4 (which is much lesser than 1) and P_u/P_y < 1.0 (although by a small margin). This behaviour may be related to the relatively lower value of $\overline{\lambda}$ (~ 0.5)

associated with the specimen; lower value of $\overline{\lambda}$, results in higher values of P_{cr}, and the section can sustain improve strength because of the relatively slenderness. From Figure 4.3a, it can be seen that at P_u (or δ_u), there is an initiation of local bucking in both the flat and curve elements for ~ 75% of the middle length (see inset figure E1). Also it can be observed that alternate buckled half wavelengths are also stressed to yield (shown by grey colour), while almost the rest of the specimens are highly stressed closed to yield, with the yielded area getting larger towards the mid length. This may be because, the value of r (= 75 mm) is relatively larger, resulting in a flatter curve (r = 25 mm would result in a semi-circular curve), with comparable dimensions with that of flat length (l_f = 50 mm), and this coupled with a relatively less slender length (i.e. h/l_f = 20), has possibly provided local buckling patterns on both the flat and curve elements. Further, because of the less slender length, flexural type of buckling is also prevented. As the deformation increases beyond δ_u (say 1.5 δ_u), it is seen that the local buckling gets localised around the mid length, resulting in a significantly larger single local buckling (approaching localised crushing) at the mid-length (see inset figure E2). With this formation of a single localised buckling zone, the local buckling occurring elsewhere (i.e. away from the mid height) appears to have reduced their magnitudes with significant distressing due to redistribution of the stress to the weaker mid length zone. As a result, at 1.5 δ_u, most region of the column are in elastic range, with the buckled middle zone (~ 12.5% length of the column length) stressing beyond the yield. Further, it may also be observed that the column axis remains more or less in the original straight form, with no signs of global or flexural (or lateral) deformation. Further, it can be seen from Figure 4.3b, at much later post-ultimate deformation e.g. ~3 δ_u, there appears to be a flattening (or near horizontal) of the load-deformation curve, suggesting a compression plastic/yield deformation, with a non-linear pre-P_u curve (indicative of strain hardening). This may be due to the localised gross section yielding at the midspan (see inset figure E2). Further, the closeness of P_u/P_y value to 1.0, indicates that the column is able to resists nearly the

gross section yield load at ultimate load. This may be related to the formation of a number of distributed local buckling on both the curve and flat elements for an extended length (~75% of the column length) at P_u, resulting in a higher load resistance, as evident from the alternate buckling half wavelength stressing beyond yield stress. Also, the observation that P_u/P_y or $P_u / A_g f_y$ = ~1.0, the behaviour of such columns are close to stocky stub behaviour. The additional strength of such slender columns may have come from the improved interaction or coupling of the curve and flat elements, resulting in better stress mobilisation, which is characteristic of low value of $\overline{\lambda}$ (say ~<1.0). Such kind of failure/deformation mode characterised by formation of i) distributed local buckling for most of the column length at P_u, and ii) localised gross section yielded buckling/crushing around the mid length, at post-P_u, can be termed as Local to local yielded buckling (or Mechanism SL1A). Mechanism SL1A was found to occur in ~ 22 specimens (see Table 4.4). Such similar type of mechanism was also reported by Silvestre *et al*., (2013) in their study on semi-elliptical hollow section columns of carbon steel, although because of the unsymmetrical geometry i.e. semi-elliptical (with semi-circular curve element), the formation of local buckling was seen mostly in the flat elements at P_u. Similar observation of occurrence of local buckling at only the flat plate was observed in flat oval section i.e, section comprising of flat and plate elements as reported by Zhu and Young (2012).

b) Local to local yielded flexural (Mechanism SL1B)

Typical variation of P/P_{cr} and P/P_y vs δ and plot of von-Mises stress contour superimposed on deformed shape are shown in Figure 4.4, for the failure mechanism, Local to local yielded flexural (Mechanism SL1B). The plots in the figure correspond to the specimen *l*75*w*50*r*25*t*2*h*2500. This column member corresponds to $\overline{\lambda}$ value of ~1.1, hence relatively larger and close to the intermediate range of length, as compared to the specimen with Mechanism SL1A (discussed above). From the load-deformation plots (Figure 4.4b and 4.4c), the pre-

P_u curve is nearly linear, suggestive of the elastic behaviour, whilst in the post-P_u, a sharp decrease/decay in the load curve can be seen, with no sign of being near horizontal for comparable large axial deformation, unlike the case of Mechanism SL1A (see Figure 4.3b). The values of P_u/P_{cr} and P_u/P_y are found to be of the order of ~0.6 and ~0.5 respectively. From Figure 4.4a, it can be observed that, at δ_u, occurrence of distributed local buckling can be seen on the flat elements, with stresses much below the yield stress, indicating elastic behaviour (see the pre-P_u ascending linear curve in Figure 4.4b). The stress in the ~24% of the mid length portion appears to be slightly higher than the rest. This may be because, the length of the flat element is now relatively longer (l_f = 75 mm) compared to the other cross-sectional dimensions, also the curve element is of semi-circular shape, which is known to have better buckling resistance than flat elements (Silvestre *et al*., 2013, Zhu and Young, 2011, 2012). At the post-P_u i.e. at 1.5 δ_u a global or flexural type of deformation is seen along the weaker principle plane (see inset figure F2). At three zones viz., around mid-length and at the two supports, yielding can be seen, characteristic of flexural bending of fixed ended column. The size of the yielded zones are about ~12% and ~6% of the column length for the mid-length and end zones respectively, although at the support ends, the formation of the yielded zone is towards the compression sides (at least at 1.5 δ_u). At 1.5 δ_u, it can also be seen that local buckling is not totally eliminated (as in the Mechanism SL1A), although they (with possibly reduced lateral deflection magnitudes) are mostly visible around the mid length portion (~50% of the column length). Further, it is also seen that as a result of the flexural buckling, reduction in stress distribution elsewhere than the yielded zones. The occurrence of flexural buckling has significantly reduced the load capacity, as indicated by a lower value of P_u/P_y (~0.5).

c) Flexural to flexural yielding (Mechanism SL2)

Figure 4.5 shows typical variation of P/P_{cr} and P/P_y with δ and plot of von-Mises stress contour superimposed on deformed shapes (corresponding to δ_u and 1.5 δ_u),

for the specimen *l*50*w*50*r*50*t*2*h*3500, depicting the flexural to flexural yielding (Mechanism SL2) mechanism. This type of mechanism occurs when the length of the specimen is sufficiently long, or when $\bar{\lambda}$ is large enough. For the specimen considered, $\bar{\lambda}$ = ~1.75. From Figure 4.5b and 4.5c, it can be observed that P_u/P_{cr} = ~1.17 and P_u/P_y = 0.4. The pre-P_u curve is found to be linear indicating the elastic nature and the post-P_u curve showed a relatively gradual drop in load. The value of P_u/P_{cr} > 1.0, may be related to the contribution from the interaction of curve and flat elements, and due to post-critical strength of the constituent elements. In this mechanism also, the P_u/P_y is much lower than 1, suggesting that the overall failure mechanism is flexural or elastic. At δ_u, the column has shown signs of initiation of flexural buckling with a relatively uniform higher stress around a major portion in the mid-length together with a much reduced stress at the ends (see inset G1 in Figure 4.5a). At 1.5 δ_u, a distinct flexural deformation mode is seen with yielded zone being formed at mid-length, and supports ends, for ~25% and 7% of the column length respectively. It is interesting to note that, for this particular example, the axis of flexural bending is perpendicular to the flat element, and hence the yielding is mostly seen on the curve surface. This kind of behaviour may have been influenced by the imperfection mode shape seeded in FE.

Variation of P_u/A_ef_y (where, A_e is the effective area as defined in Equation 3.5) with $\bar{\lambda}$ is shown in Figure 4.6 considering ~100 FE models. In the plot, data points with $\bar{\lambda}$ in the range ~0.89-6.7 have been considered. In the Figure 4.6, the locations of the typical specimens considered in Section 4.7.1.1 in describing the failure mechanisms are also indicated. It may be seen that, two distinct regions may be roughly demarcated with $\bar{\lambda}$ =~1.25, based on the deformation pattern initiated at P_u, *viz.*, 1) local buckling initiated region ($\bar{\lambda}$ <~1.25,) where Mechanisms SL1A and SL1B are the dominant governing failure mechanisms, and 2) flexure buckling initiated region ($\bar{\lambda}$ >~1.25,) where Mechanisms SL2 is the governing failure mechanism. It may be noticed from the plot that, flexure buckling initiated region

can be conservatively separated with $\bar{\lambda}$ >~1.25, it is not distinctly possible (at least based on the available current result and way of plotting with $\bar{\lambda}$), to separate regions dominated with Mechanisms SL1A and SL1B (or SL1 Mechanism), further some points with Mechanism SL2 are also associated with $\bar{\lambda}$ <~1.25. Also, it is possible to get different values of P_u/A_ef_y for similar values of $\bar{\lambda}$, indicating that although widely accepted, $\bar{\lambda}$ may not be the best variable to consider.

4.7.1.2 *Effect of curvature radius (r)*

The effect of curve element radius (r) on P_u is presented in Figure 4.7 in the form of variation of P_u with r/w and P_u/A_ef_y (l_f = 50 mm, w = 50 mm, t = 2 mm) for r = 25-100 mm. It can be seen from Figure 4.7a, that as h increases from 1000-15000 mm, the load capacity (P_u) decreases in general for the range of r/w considered. It is also observed that P_u is highest for r/w = 0.5 (or when the curve element is semi-circular in shape) and decreases till r/w = 1. For r/w > 1.0, there is not much change in the value of P_u. At first, this behaviour may be related to the higher buckling resistance of the semi circular curve elements as compared to that of flatter (or higher radii) curve elements, also the area contribution to the load resistance is highest for semi-circular section (or r/w = 0.5). Variation of effective area (A_e) with r/w (see Figure 4.7b) shows that A_e is highest for semi-circular section, dropping to a minimum around r/w =1 (drop = ~19 % for h = 1000 mm), and thereafter remaining near constant (as mentioned before it may be noted that curve element is considered to be fully effective, whereas the effective areas are calculated for the flat length, as per relevant code). However, a normalised plot of P_u/A_ef_y with r/w (Figure 4.7c) shows that, apparently, the variation of A_e seems to agree with the variation of P_u with r/w for the shortest height considered i.e. h = 1000 mm, as can be seen from the horizontality of the P_u/A_ef_y (suggesting of a stub type behaviour; see inset figure L1 and L2). A value of $P_u/A_ef_y \geq 1.0$, corresponding to h = 1000 mm, suggest that the column is able to sustain at least the yield load. This agrees with the failure mode associated with Mechanism SL1 for h = 1000 mm, where the main dominant

failure mode is distributed local buckling at P_u. In contrast, for larger values of h i.e. $h \geq 2000$ mm, the behaviour of $P_u/A_e f_y$ i.e. after normalisation with $A_e f_y$, remains more or less unchanged (i.e. it does not become near horizontal). This agrees with the observation that almost all (expect for the date corresponding to $r/w = 0.5$ and $h = 2000$ mm) the data points for ≥ 2000 mm are associated with the flexure initiated failure mechanism i.e. Mechanism SL2 (see inset figure L3 and L4). The SL2 mechanism is found to occur for $P_u/A_e f_y \leq \sim 0.78$. Higher values of P_u associated with semi-circular sections, even for flexure initiated member (i.e. for $h \geq 2000$ mm), may then be related to the resistance/strength enhancement from the curved semicircular element.

4.7.1.3 *Effect of flat length (l_f)*

The effect of flat length (l_f) on the load capacity (P_u) is presented in Figure 4.8 (w = 50 mm, r = 25 mm, t = 2 mm, and l_f = 50-150 mm), for h = 1000-15000 mm, considering semi-circular curve section. It can be seen that for the shortest column considered (h = 1000 mm), there is a slight drop (~ 8%) in P_u for l_f increases from 50 to 75 mm, then remains near constant for $l_f \geq 75$ mm. Although it is expected that as A_e would be increased (as a result of increasing in l_f), hence an increasing trend was expected, the initial drop in P_u, then may be related to the increased buckling half wavelength due to increased in l_f, which may have offsetted the associated increase in strength as result of increasing in A_e (see inset figures L1 and L2; Figure 4.8b). For h = 2000 mm, P_u, however remains near unchanged, and this may be related to the transitional stage wherein the increased in P_u at $r/w = 0.5$ (e.g. the case of L1) may again have been influenced by the possibility of flexure type failure associated with slender length. For 2000 mm $\leq h \leq$ 5000 mm, an initiate increase in P_u can be seen which then plateaus at l_f = 75-150 mm, whilst for $h \geq$ 5000 mm, there appears to be a near linear increase in P_u with l_f. A normalised plot $P_u/A_e f_y$ with l_f is shown in Figure 4.8c. It thus can be seen that for l_f = 50 mm the $P_u/A_e f_y$ = ~1.0, for both h = 1000 and 2000 mm columns, whilst the other data

points showed $P_u/A_ef_y \leq$ ~1.0. It may be noted that all the data points corresponding to $h \geq 5000$ mm, and data points corresponding to l_f = 50 and 75 mm for h = 3500 mm and l_f = 50 mm for h = 2500 mm, showed Mechanism SL2 (i.e. flexure initiated), and hence agrees with the relative lower value of P_u/A_ef_y i.e. $P_u/A_ef_y <$ ~ 0.7.

4.7.1.4 *Effect of distance between flat elements* (*w*)

The effect of the distance between flat elements (w) is presented in the form of variation of P_u and P_u/A_ef_y with w, for h = 1000-15000 mm in Figure 4.9 (l_f = 50 mm, r/w = 0.5, t = 2 mm, w = 50-200 mm). It can be seen that P_u increases near linear with increase in w, although the rate of increase appears to be non-linear for $h \geq$ 9000 mm. An increase of about 300 % in w (from 50 mm), showed an increase of ~165% and ~230% for h = 1000 and 15000 mm respectively, indicating that the increase of w is more effective in slender columns. Increase of w results in linear increase of A_e, as shown in Figure 4.9b. In Figure 4.9c, variation of P_u/A_ef_y with w is shown. From Figure 4.9c, It can be seen that, for h = 1000-2500 mm, it appears that the increase in A_e (with w) may be the dominant factor for increase in P_u (as shown by the near horizontal variation). Similar behaviour are also seen for h = 2500 and 3500 mm, for $w \geq$ 100. This may be because, as w increases A_e also increases, resulting in an increase in the curve semi-circular area, further in this case, as l_f is constant, there appears to be a shift in the failure mechanism from SL2 to SL1, i.e. a local buckling initiated mechanism (with stub type response), dominant A_e dependent load resistance. It is also observed that for $P_u/A_ef_y \leq$ ~0.65, the corresponding data points are associated with SL2 mechanism. Furthermore, in slender columns it is observed that for those data points which underwent SL2 mechanism (i.e. flexure initiated failure mode), an ascending P_u/A_ef_y can be observed with increasing w. This may be related to the increase in stiffness or resistance to flexural bending, due to increase cross-sectional area.

4.7.1.5 Effect of height (*h*)

Figures 4.10(a, b and c) show the effect on P_u, due to change in column height (h) for t = 2 mm. Variation of P_u with h for l_f = 50-150 mm (w = 50 mm, r = 25 mm) is shown in Figure 4.10a. It can be seen from Figure 4.10a, that for shorter length (h = 1000-2000 mm), the effect of variation in l_f on P_u is not very significant (see also Figure 4.7). However, as h increases, there appears to be a near parallel non-linear drop in P_u with decreasing l_f. As discussed in Section 4.7.1.2, although longer or slender members follow flexure initiated Mechanism SL2, effective cross sectional area (A_e) increases with increasing l_f, and hence the increase in P_u with increasing l_f. Howver, at very large length (say 15000 mm), such beneficial effect of increasing l_f appears to diminish. Figure 4.10b shows the effect of h on P_u for for r = 25-100 mm (l_f = 50 mm, w = 50 mm). Clearly, it is observed that for r = 50-100 mm, there appears to have no significant effect on P_u, although r = 25 showed much higher value of P_u. This is because, at r = 25 mm (or r/w = 0.5), the curve elements correspond to semi-circular section, which enhances the load capacity (as discussed in Section 4.7.1.2). Effect of changes in w = 50-200 mm (l_f = 50, r/w = 0.5 or semicircular curve section) is shown in Figure 4.10b. It can be seen that except for w = 50 mm, a near linear drop in P_u with h, can be seen for higher values of w, with increasing trend of P_u for increasing w (as discussed in Section 4.7.1.3). Essentially, with increasing w, in order to maintain r/w = 0.5 (or semi-circular curve ends), r increases, leading to increased A_e, and hence P_u. For the smallest w considered (i.e. w = 50 mm), a non-linear trend is observed, predominantly because of the enhanced member slenderness (or higher $\bar{\lambda}$). In Figures 4.10 (d-f), effect of l_f, r and w on P_u are also plotted again, as a function of $\bar{\lambda}$ (considering the same data set). It is readily seen that, the normalised plot is able to capture the effect of l_f, r and w relatively well.

4.7.1.6 *Comparison with design strengths*

Comparison of the FE results with those predicted by EN 1993-1-4 (2015), AS-NZS 4673 (2001), modified AS/NZS 4673; DSM and modified DSM are presented in the form of variation of $P_u/A_e f_y$ with $\overline{\lambda}$, $P_u/A_e f_y$ with λ and P_u/P_y with λ_C in Figures 4.11a, 4.12a and 4.13a respectively., whilst the corresponding variation of P_{FE}/P_{EN}, $P_{FE}/P_{AS/NZS}$ and P_{FE}/P_{DSM} are presented in Figures 4.11b, 4.12b and 4.13b respectively. Note that P_{FE} corresponds ultimate load (P_u) generated through FE analyses. The values of P_{FE}/P_{EN}, $P_{FE}/P_{AS/NZS}$, $P_{FE}/P^*_{AS/NZS}$, P_{FE}/P_{DSM}, P_{FE}/P^*_{DSM} for all the 100 specimens, along with corresponding β (reliability index) values are given in Table 4.4. It can be seen from Table 4.4, that the values of β, for EN 1993-1-4 (2015), AS-NZS 4673 (2001), modified AS/NZS 4673, DSM (2002) and modified DSM are 2.51, 2.31, 1.76, 2.68 and 2.45 respectively, suggesting that EN 1993-1-4 (2015) and DSM (2002) have $\beta \geq 2.5$, whilst AS/NZS 4673 (2001), modified AS-NZS 4673 and modified DSM (Huang and Young, 2014b) provided $\beta < 2.5$. If the lower limit of β as suggested by ASCE 8-02 (2002) are considered as critical limit, it may be noted that the current EN 1993-1-4 (2015), DSM (which was designed for stainless steel in general), are applicable for the design of LDSS flat oval hollow column sections, however AS/NZS 4673 (2001), modified versions of AS/NZS 4673 and DSM (Huang and Young, 2014b) are not applicable. Also it can be noted that the predictions made by DSM are found to be the most reliable with $\beta = 2.68$, amongst the comparison made. Comparison of Figures 4.11b, 4.12b, and 4.13b, shows that, P_{FE}/P_{EN} and P_{FE}/P_{DSM} are in the range 1-2 for $\overline{\lambda} \geq$ ~2.0 and $\lambda_c \geq$ ~2.0, whilst their value decreases as $\overline{\lambda}$ and λ_c becomes smaller than 2.0, and with $0 < \overline{\lambda} <$~2.0, $0 < \lambda_c <$~2.0, their values becomes < 1.0. It thus, indicate that, both EN 1993-1-4 (2015) and DSM (both current and modified versions) are mostly conservative for $\overline{\lambda} \geq$ ~2.0, $\lambda_c \geq$~2.0, whilst, they are unconservative for $0 < \overline{\lambda} <$~2.0 and $0 < \lambda_c <$~2.0. However, from Figure 4.12, it appears that $P_{FE}/P_{AS/NZS}$ is in a relatively larger range i.e. ~1-3.5 for $\lambda \geq$ ~2.0 (indicating relatively more

conservativeness), and the values of $P_u/P_{AS/NZS}$, decreased for 0 <λ <~2.0. Further, it may be seen that AS/NZS 4673 (2001) predicted unconservative load values for 0 <λ<~1.0, however, modified AS/NZS 4673 showed some unconservative load prediction for 0 < λ<~2.0. Hence, it can be observed that all the compared design codes / methods, are shown to be unconservative for lower values of slenderness i.e, in terms of $\bar{\lambda}$, λ or λ_c according to the differences of the design codes and method, say $\bar{\lambda}$ or λ or λ_c <~1.0 or most of the data points associated with Mechanism SL1A (mainly due to the occurrence of local buckling at the slender section).

4.7.2 Stocky sections (Class 1 and 2)

4.7.2.1 *Deformation mechanisms*

For the stocky cross-section sections (i.e. Class 1 and 2) considered in this study, based on the FE analyses of ~120 slender models, three failure or deformation mechanisms have been identified viz., 1) Yield to yield with local bucking (Mechanism ST1), 2) Yield to yield with flexural buckling (Mechanism ST2), and 3) Flexural to flexural buckling (Mechanism ST3). These classifications are based on observations of von-Mises contour superimposed in deformed shapes, at ultimate load and post ultimate load i.e. at δ_u and 1.5 δ_u.

a) Yield to yield with local bucking (Mechanism ST1)

Figure 4.14 shows the typical variation of P/P_{cr} and P/P_y (where $P_y = A_g f_y$ is the gross yield load) with δ, for yield to yield with local buckling (or Mechanism ST1). The plots correspond to specimen *l*50*w*150*r*75*t*15*h*1000. From Figures 4.14b and 4.14c, it can be seen that P_u/P_{cr} = ~0.08 and P_u/P_y = ~1.32. The lower value of P_u/P_{cr} may be related to the high value of elastic buckling load associated with relatively short column with stocky cross-section (h/l_f = 20 and $\bar{\lambda}$ =`0.17). A high value of P_u/P_y or $P_u/A_g f_y$ > 1.0, indicates that the column is able to withstand load more than the gross yield, the additional strength may then be related to the strain hardening of high strength LDSS steel. Due to this high load capacity (beyond the

gross yield load), a gradual drop (P_u/P_y = 1 at δ/h = ~ 7%) and rounded load deformation curve around the peak can be seen. At δ_u, almost the column has yielded without any signs of bucking (inset figure P1), and however, at 1.5δ_u, three outward local buckling (with half buckling wavelength ~11% of column length) can be observed both at mid-length and the two end spots. It can be noticed that even at 1.5δ_u, most region are still yielded with small region in the flat elements near the buckled portion being distressed.

b) Yield to yield with flexural buckling (Mechanism ST2)

Typical plots of variation of P/P_{cr} and P/P_y with δ, and von-Mises contour plots are shown in Figure 4.15, for yield to yield with flexural bucking mechanism (Mechanism ST2). The plots to specimen *l*50*w*150*r*75*t*15*h*2000. It can be seen from Figure 4.15, that P/P_{cr} = 0.17 and P/P_y = ~1.18. Now compared to the previous example for Mechanism ST1, the cross-sectional parameters are same, except for the increase (~100%) in *h* to 2000 from 1000 mm, with $\overline{\lambda}$ =~ 0.35.The effect of this can be seen in increase (~112%) of P/P_{cr} and decrease (~10%) in P/P_y as compared to the specimen considered for Mechanism ST1 (see Figure 4.14). At the ultimate load (or δ_u), the specimen is almost yielded (with no instance seen for local buckling), whereas, at 1.5 δ_u, flexural buckling can observed with most region still being yielded (distressed at the ends for ~29% column can be seen at the flat element side). The post-ultimate load-deformation curve (see Figure 4.15b) appears to be relatively sharper, with P/P_y = 1.0 occurring at ~1.3% of the column length, this again is relatively shorter as compared to the specimen discussed in the previous section (Figure 4.14).

c) Flexural to flexural buckling (Mechanism ST3)

Figure 4.16 shows the plots (variation of P/P_{cr} and P/P_y with δ, and von-Mises contour plot) illustrating the flexural to flexural buckling mechanism (or Mechanism ST3). The behaviour shown in Figure 4.16 relates with the specimen

*l*50*w*50*r*75*t*15*h*2000, resulting in much larger $\overline{\lambda}$ value (~1.1), as compared to the specimens discussed previously. As compared to the specimens with the above mentioned ST1 and ST2 mechanisms, in this specimen, the value of P_u/P_{cr} is much larger (~1.0) however, the value of P_u/P_y has dropped to 0.67, suggesting that global behaviour is in the elastic range (the pre-P_u load-deformation curve is again near linear). At P_u, the curvature of the load-deformation curve is now relatively sharper with a faster drop in post-P_u load. In Figure 4.16a, it is seen that at δ_u, there is an initiation of flexural buckling with compression yielded regions at the mid-length and the two end supports (characteristic of fixed ended boundary conditions). At $1.5\delta_u$, enhanced flexural type continue to happen with the compression yielded region covering ~28% of the column length (inset figure R1); the yielded region at the ends are also increased (~12.5 % of column length), however, it now shifted towards the tension side.

Variation of P_u/A_gf_y with $\overline{\lambda}$, for all the 120 data points are shown in Figure 4.17, with data points corresponding to the above mentioned three Mechanisms i.e. ST1, ST2 and ST3 being marked. The data points corresponding to the three typical specimens considered for illustrating the three failure/deformation mechanisms are also highlighted. From the figure, roughly, it is now possible to demarcate the limits of the three failure mechanisms e.g. $\overline{\lambda} < 0.32$; $0.32 \leq \overline{\lambda} \leq 1.0$; and $\overline{\lambda} > 1.0$ corresponds to ST1, ST2 and ST3 mechanisms respectively. It may also be noted that both ST1 and ST2 (or combinely ST) corresponds to yield initiated failure mechanism at P_u, whilst ST3, corresponds to flexure buckling initiated mechanism.

4.7.2.2 *Effect of curvature radius* (*r*)

The effect of curvature radius (r) of the curve elements on the load capacity of slender columns with stocky sections is presented in Figure 4.18 (l_f=50 mm, w = 50 mm, t = 15 mm, r = 25-100 mm, for h = 1000-3500 mm. It can be seen that semi-circular curve section (r/w = 0.5) showed the highest load capacity, with P_u remaining almost flat for $r/w \geq 1.0$; with the drop in P_u when r/w is increased from

0.5 to 1, is ~18-20% for all the values of h considered. It may be noted that as r tends to zero (or $r/w \rightarrow 0$, in this case), the section would approach to flat plate of thickness $2t$ and width w, as also noted by Ruiz-Teran and Gardner (2008) for the elastic analysis of elliptical sections. The results corresponding to such flat plates are also plotted in Figure 4.18a. Clearly, P_u values corresponding to r = 0.0 (or r/w = 0) are relatively much lower, owing to the absence of curve elements, when compared to flat oval hollow sections.

Figure 4.18(c) shows the variation of $P_u/A_g f_y$ with r/w (variation of A_g with r/w is given in Figure 4.18(b). It can be seen that $P_u/A_g f_y > 1.0$ for h = 1000 mm, whereas for $h \geq 2000$ mm, $P_u/A_g f_y < 1.0$. $P_u/A_g f_y > 1.0$ is due to strain hardening. It is also observed that the data points corresponding to $P_u/A_g f_y < 1.0$, falls under Mechanism ST3 (from h = 2000-3500 mm), whilst the data points belonging to h = 1000 mm, corresponds to Mechanism ST2. It may be observed that the rise in $P_u/A_g f_y$ may be related to the decrease in A_g as r/w increases (or as r become flatter), although the drop in A_g for $1 \leq r/w$ is very marginal.

4.7.2.3 *Effect of flat length* (l_f)

Figure 4.19 shows the effect of flat length element (l_f) on P_u and $P_u/A_g f_y$ with increasing columns height from 1000-3500 mm (w = 50 mm, r = 25 mm, t = 15 mm, l_f = 50-150 mm). From Figure 4.19a, it appears that there is near linear increase in P_u with l_f ; the average increase is found to be ~94-110% for 200% increase in l_f (from l_f =50 mm). This is also consistent with the linear increase in A_g with increase in l_f in Figure 4.19(b). Further, as, $l_f \rightarrow 0$, the section approaches circular hollow section, similar to the argument put forward by Ruiz-Teran and Gardner (2008) wherein the behaviour of elliptical section would tend towards circular as the aspect ratio $\rightarrow$ 1. In Figure 4.19(a), results for corresponding circular sections (by making l_f = 0) are presented. The reduction in P_u values for the circular sections (or l_f = 0) are consistent with the absence of stiffening contribution of the two flat elements.

The variation of P_u/A_gf_y with l_f in Figure 4.19(c), is seen to be near horizontal for all the values of h, although the shortest height column (h = 1000 mm) resulted in P_u/A_gf_y > 1.0, whereas for $h \geq 2000$, P_u/A_gf_y < 1.0. Further, data points corresponding to P_u/A_gf_y < 1.0, resulted in ST3 mechanism, whilst those corresponding to P_u/A_gf_y > 1, resulted in ST2 mechanism.

4.7.2.4 *Effect of distance between flat elements* (*w*)

Effect of distance between flat elements (w) is presented in the form of variation of P_u and P_u/A_gf_y with w, in Figure 4.20, (l_f = 50 mm, w/r = 2, t = 15 mm, w = 50-200 mm), for h = 1000 – 3500 mm. In Figure 4.20, it can be seen that $P_u/A_gf_y \geq 1.0$ and remains near flat, for $w \geq 100$ mm. However, for w < 100 mm and $h \geq 2000$ mm, P_u/A_gf_y < 1.0. At lower values of w, e.g. w close to 50 mm, the columns become relatively slender so as to initiate the failure by flexure at P_u, especially for $h \geq 2000$ mm, as can be seen from the inset Figures L3 and L4 (Figure 4.20a). These behaviour is in agreement with the association of Mechanism ST3 (i.e. flexure initiated deformation) for $w \leq 100$ mm and $h \geq 2000$ mm. For $w \geq 100$ mm and h = 2000-3500 mm, P_u/A_gf_y > 1, due to the failure Mechanism ST2 (i.e. yield to yield with flexural buckling).

4.7.2.5 *Effect of thickness* (*t*)

Figure 4.21 shows the effect of thickness (t) on P_u and P_u/A_gf_y for l_f = 50 mm, w = 50 mm, and r = 100 mm, for variation of t from 10-20 mm. From Figure 4.21a, there appears to show a near linear increase in P_u, with the rate of increase of t for all height of columns but decreases with increase in h. The increase in P_u with increased in thickness correlate well with the linear increase in gross-area of cross-section as shown in Figure 4.21(b).

For 200% increase in t (from 10 mm), the increase in P_u for h = 1000 and 3500 mm are ~ 88% and ~ 46 % respectively. In Figure 4.21(c), it is seen that for P_u/A_gf_y < 1.0 which occurred for $h \geq 2000$ mm, the curves are almost flat, however for P_u/A_gf_y >

1.0 (associated for h = 1000 mm), the variation showed a slight increase. It may be related to the associated failure mechanisms: h = 1000 mm showed ST2 mechanism whilst $h \geq$ 2000 mm, showed ST3 mechanism. For the columns with ST2 mechanism, the increasing trend in $P_u/A_g f_y$, the role of strain hardening may have become load enhancing role with increasing A_g. However, for the longer sections, the decreasing effect of P_u with increasing h, may have been neutralised by the opposite effect (increase of P_u) of increasing A_g, and hence have resulted in near flat behaviour of $P_u/A_g f_y$.

4.7.2.6 *Effect of height (h)*

Effect of LDSS flat oval hollow column height (h) on P_u is presented in Figures 4.22(a, b and c); for t = 15 mm. Figure 4.22(a) shows the variation of P_u with h for l_f = 50-150 mm (w = 50 mm, r = 25 mm). It can be seen from Figure 4.22(a) that P_u decreases with increasing h in a near-non-linear trend; the decrease being nearly constant ~ 77% for the range of l_f considered. However the values of P_u are found to be higher for longer lf. The effect of h on P_u, for r = 25-100 mm (l_f = 50 mm, w = 50 mm) is shown in Figure 4.22(b). Although, a near-non-linear drop in P_u with h (~77% and ~74% for r = 25mm and 50-100 mm respectively) is observed in Figure 4.22(b), it is seen that P_u values corresponding to r = 25 mm (i.e. when the curve element is semi-circular or r/w = 0.5) are the highest. For r = 50-100 mm, the P_u results are found to be similar. Variation of P_u with h for w = 50-200 mm (l_f = 50, r/w = 0.5 or semicircular curve section) is shown in Figure 4.22(c). It can be observed that a near-linear decrease in P_u can be seen in Figure 4.22(c), with the decrease being lowest (~ 8%) for w = 200 mm and highest (~ 77%) for w = 50 mm. Thus, it can be observed that, although the decrease in P_u with h is quite expected (due to increase in global/member slenderness), the rate of decrease is relatively less sensitive (~74-77%) to variations in l_f and r; however, it is quite sensitive (~8-77%) to variation in w. This may be because, increasing w (maintaining r/w at 0.5) can relatively lower the member slenderness as compared to increasing lf or r.

Variation of P_u/A_gf_y with $\overline{\lambda}$ for changes in l_f, r and w are also plotted for the same date set considered in Figures 4.22(d-f). It is interesting to note the normalised plots are able to capture well the effects of r and l_f (see the near convergence of the plots in Figures 4.22 (d) and (e)). However, such well behaved plots are not seen when w is varied (see Figure 4.22 (f)). This is essentially because, for the case of w = 50 mm, most of the slender ($\overline{\lambda}$ > ~1) specimens failed by flexure-flexure or ST3 mechanism (see Table 4.5), whilst the other specimens failed by either mechanism ST1 or ST2 (note P_u/A_gf_y > 1.0).

4.7.2.7 *Comparison with design strengths*

Comparison of the prediction from design codes (EN-1993-1-4, AS/NZS 4673) and method (DSM) and their proposed modified versions (Huang and Young, 2014b) with the results from FE analyses are shown in Figure 4.23-4.25, for stocky LDSS flat oval hollow columns. Unlike the thin section, full cross-section is taken as effective section in case of thick section and so the design curve of EN 1993-1-4 has been shown in Figure 4.23(a).

The comparisons are shown in the form of variation of P_u/A_gf_y vs $\overline{\lambda}$ for EN 1993-1-4 (2015), P_u/A_gf_y vs λ for AS/NZS 4673 (2001), P_u/P_y vs λ_c for DSM (2002). The FE results are based on 120 models with slenderness ($\overline{\lambda}$ or λ or λ_c) ratio in ranges of ~0.12-2.25. The ratio of P_u from FE analyses (i.e. P_u) and those of design predictions are shown in Figures 4.23b, 4.24b and 4.25b to show the scattering of the compared results. It can be seen that EN-1993-1-4 (2015), AS/NZS (2001), and the modified version of AS/NZS (Huang and Young, 2014b) are conservative. However, although DSM and modified DSM is able to provide conservative values of P_u, it is seen that some of their predictions are found to be underconsevative (specially for 0.63 < $\overline{\lambda}$ <1.2), as indicated by P_u/P_{DSM} < 1.0 in Figure 4.24(b). The results of the reliability analyses are presented in Table 4.5. based on the reliability and analyses and considering the minimum requirement value of the target

reliability index (β_o) as 2.5 (ASCE specification), it can be inferred that all the compared design codes, method and their modified versions are reliable and applicable, with β value of 3.28, 3.52, 3.90 for EN-1993-1-4 (2006), AS/NZS 4673(2001) and DSM (2002); and 3.38, 3.50 for modified AS/NZS and modified DSM (Huang and Young, 2014b) respectively. However, in case the reliability resistance factor (Ø) and load combination has been made same with values of 0.85 and 1.25DL+1.5LL, the reliability index values for the current EN 1993-1-4 (2015), AS/NZS 4673 (2001) and DSM (2002) are 3.49, 3.52, 3.46; while the proposed modified AS/NZS 4673 and DSM (Huang and Young, 2014b) gives the values of 3.38 and 3.07 respectively. It has been noticed that β values for the modified versions are found to be lower and hence, their use are expected to be more economical.

4.8 CONCLUSIONS

A parametric investigation on the structural behaviour (e.g. deformation modes, load capacity etc.) of fixed ended stocky (Class 1-3) and slender (Class 4) LDSS flat oval hollow slender columns under axial compression has been presented using finite element analyses, considering variations on curve element radius, flat element length, flat element separation distance, thickness and columns heights or lengths. Conclusions drawn from the parametric analyses are presented in two sub-headings *viz*., a) slender cross-section columns and b) stocky cross-section columns.

a) Slender cross-section column

1) Observing stress contours and deformed shapes corresponding to ultimate and post-ultimate loads, three primary failure or deformation mechanisms have been identified *viz*., 1) Local to local yielded buckling (Mechanism SL1A), 2) Local to local yielded flexural buckling (Mechanism SL1B), and 3) Flexural to flexural yielded buckling (Mechanism SL2). Mechanisms SL1A and SL1B are associated with $\overline{\lambda} < 1.25$; whilst Mechanism SL2 corresponds to $\overline{\lambda} > 1.25$ respectively. It is

seen that, Mechanisms SL1A and SL1B correspond to local initiated failure mechanism at P_u, whilst Mechanism SL2, is associated with flexure buckling initiated mechanism.

2) It is observed that P_u is highest for r/w = 0.5 (or when the curve element is semi-circular in shape) and decreases till r/w = 1. For r/w > 1.0, there is no significant change in the value of P_u.

3) For the shortest column considered (h = 1000 mm), a slight drop (~ 8%) in P_u for l_f increases from 50 to 75 mm can be observed, which then remains near constant for $l_f \geq$ 75 mm. However, for intermediate column length i.e. 2000 mm $\leq h \leq$ 5000 mm, an initial increase in P_u can be seen which then plateaus (with a lower rate of increase) at l_f = 75-100 mm, whilst for larger column lengths e.g. $h \geq$ 5000 mm, there appears to be a near linear increase in P_u with l_f.

4) In general, P_u is found to increase in a near linear trend with increase in w, although, for $h \geq$ 9000 mm, the rate of increase follows a non-linear patter (with the rate of increase getting higher for larger w). Further, the role of increasing w in increasing P_u, is found to be more effective in slender columns.

5) In general it is seen that, P_u decreases with increasing h, although it appears that the rate of decrease with relatively more less sensitive for changes in l_f and r, as compared to changes in w. Moreover, it is observed that the normalised plot (i.e. $P_u/A_g f_y$ vs $\overline{\lambda}$) is able to capture the effect of l_f, r and w relatively well.

6) The current EN 1993-1-4 (2015), DSM, are found to be applicable for the design of LDSS flat oval hollow slender cross-section column, however AS/NZS 4673 (2001) and modified versions of AS/NZS 4673 and DSM (Huang and Young, 2014b) are observed to be not reliable.

b) Stocky cross-section columns

1) For the stocky sections (Class 1 and 2), based on the stress contours and deformed shapes at the ultimate load and post-ultimate loads, three failure or deformation mechanisms have been identified *viz*., 1) Yield to yield with local bucking (Mechanism ST1), 2) Yield to yield with flexural buckling (Mechanism ST2), and 3) Flexural to flexural buckling (Mechanism ST3). ST1, ST2 and ST3 mechanisms corresponds to $\overline{\lambda} < 0.32$; $0.32 \leq \overline{\lambda} \leq 1.0$; and $\overline{\lambda} > 1.0$ respectively. Both ST1 and ST2 corresponds to yield initiated failure mechanism at P_u, whilst ST3, corresponds to flexure buckling initiated mechanism.

2) It is seen that semi-circular curve section (r/w = 0.5) showed the highest load capacity, with P_u remaining almost flat for $r/w \geq 1.0$, with the drop in P_u when r/w is increased from 0.5-1.0, is ~18-20% for all the lengths of columns analysed.

3) A near linear increase in P_u with l_f is observed; the average increase is found to be ~94-110% for 200% increase in l_f (from l_f =50 mm).

4) In general, P_u increases with increase in w, however the rate of increase seems to be relatively higher for $w \leq 100$ mm, especially for $h \geq 2000$ mm.

5) A near linear increase in P_u with increase in thickness is observed, with the rate of increase of t for all heights of column but decreases with increase in h.

6) It can be observed that, although the decrease in P_u with h is quite expected (due to increase in global/member slenderness), the rate of decrease is relatively less sensitive (~74-77%) to variations in l_f and r; however, it is quite sensitive (~8-77%) to variation in w. Further, it is noted the normalised plots ($P_u/A_g f_y$ vs $\overline{\lambda}$) are able to capture well the effects of r and l_f, however, such well behaved plots are not seen when w is varied, specially for $\overline{\lambda} <$ ~1.

7) All the compared design codes, method and their modified versions are reliable and applicable, with β values of 3.28, 3.52, 3.90 for EN-1993-1-4 (2015), AS/NZS 4673 (2001) and DSM (2002); and 3.38, 3.50 for modified AS/NZS and modified DSM (Huang and Young, 2014b) respectively. It has been noticed that β values for the modified versions are found to be lower and hence, their use are expected to be more economical.

Table 4.1

Compressive LDSS flat material properties (Theofanous and Gardner, 2009).

Cross-section	E (MPa)	$\sigma_{0.2}$ (MPa)	$\sigma_{1.0}$ (MPa)	Compound R-O coefficients	
				n	$n'_{0.2,1.0}$
80x80x4	197200	657	770	4.7	2.6
60x60x3	206400	711	845	5.0	2.7

Table 4.2

Slender column dimensions (Theofanous and Gardner, 2009).

Specimen	D (mm)	B (mm)	t (mm)	r_i (mm)	Buckling length , l_{cr} (mm)
80x80x4-1200	79.3	79.6	3.72	3.8	1199.5
80x80x4-2000	79.6	79.5	3.80	3.4	1999.0
60x60x3-2000	60	60	3.13	2.7	1999.0
60x60x3-1600	59.6	60	3.15	2.4	1599.0
60x60x3-1200	60	60	3.13	2.4	1199.0
60x60x3-800	60	60	3.13	2.4	799.0

l_{cr} = Buckling length, D = Depth, B = Width, t = thickness, r_i = internal corner radius.

Table 4.3

Existing and proposed new coefficients of buckling stress in AS/NZS standard (Huang and Young, 2014b).

Coefficients	a	b	λ_o	λ_l
Existing Coefficients for EN 1.4462 (Duplex)	1.16	0.13	0.65	0.42
Proposed Coefficients for EN 1.4162 (Lean duplex)	0.86	0.14	0.67	0.45

Table 4.4

Comparison of FE strength with design strengths for slender section (t = 2 mm; Class 4).

Specimen	P_u / P_y	Failure mode at δ_u	Failure mode at $1.5\delta_u$	$\frac{P_{FE}}{P_{EN}}$	$\frac{P_{FE}}{P_{AS/NZS}}$	$\frac{P_{FE}}{P^*_{AS/NZS}}$	$\frac{P_{FE}}{P_{DSM}}$	$\frac{P_{FE}}{P^*_{DSM}}$
*l*50*w*50*r*25*t*2*h*1000	0.94	L	L+F	1.05	0.97	0.97	1.03	0.97
*l*50*w*50*r*25*t*2*h*2000	0.88	L	L+F	1.41	1.46	1.31	1.24	0.98
*l*50*w*50*r*25*t*2*h*2500	0.71	F	F	1.49	1.48	1.35	1.24	1.07
*l*50*w*50*r*25*t*2*h*3500	0.50	F	F	1.74	1.65	1.56	1.48	1.48
*l*50*w*50*r*25*t*2*h*5000	0.30	F	F	1.94	1.82	1.77	1.81	1.81
*l*50*w*50*r*25*t*2*h*7000	0.18	F	F	2.08	1.96	1.93	2.06	2.06
*l*50*w*50*r*25*t*2*h*9000	0.11	F	F	2.02	1.93	1.91	2.06	2.06
*l*50*w*50*r*25*t*2 *h*10000	0.09	F	F	2.03	1.94	1.92	2.09	2.09
*l*50*w*50*r*25*t*2*h*12000	0.06	F	F	2.03	1.96	1.94	2.12	2.12
*l*50*w*50*r*25*t*2*h*15000	0.04	F	F	2.02	1.97	1.96	2.15	2.15
*l*75*w*50*r*25*t*2*h*1000	0.75	L	L+F	0.94	0.87	0.87	0.90	0.88
*l*75*w*50*r*25*t*2*h*2000	0.74	L	L+F	1.26	1.37	1.23	1.05	0.92
*l*75*w*50*r*25*t*2*h*2500	0.69	L	L+F	1.47	1.57	1.43	1.15	1.00

*l*75*w*50*r*25*t*2*h*3500	0.50	F	F	1.69	1.78	1.68	1.37	1.37
*l*75*w*50*r*25*t*2*h*5000	0.32	F	F	1.93	2.03	1.96	1.76	1.76
*l*75*w*50*r*25*t*2*h*7000	0.18	F	F	2.05	2.18	2.14	1.99	1.99
*l*75*w*50*r*25*t*2*h*9000	0.12	F	F	2.10	2.26	2.23	2.11	2.11
*l*75*w*50*r*25*t*2*h*10000	0.09	F	F	2.05	2.22	2.20	2.09	2.09
*l*75*w*50*r*25*t*2*h*12000	0.07	F	F	2.05	2.24	2.22	2.13	2.13
*l*75*w*50*r*25*t*2*h*15000	0.04	F	F	2.04	2.25	2.14	2.15	2.15
*l*100*w*50*r*25*t*2*h*1000	0.65	L	L+F	0.94	0.86	0.86	0.89	0.87
*l*100*w*50*r*25*t*2*h*2000	0.63	L	L+F	1.16	1.31	1.17	1.02	0.89
*l*100*w*50*r*25*t*2*h*2500	0.61	L	L+F	1.33	1.53	1.38	1.10	0.97
*l*100*w*50*r*25*t*2*h*3500	0.49	L	L+F	1.69	1.96	1.83	1.31	1.31
*l*100*w*50*r*25*t*2*h*5000	0.32	F	F	1.92	2.25	2.18	1.71	1.71
*l*100*w*50*r*25*t*2*h*7000	0.19	F	F	2.06	2.46	2.42	1.97	1.97
*l*100*w*50*r*25*t*2*h*9000	0.12	F	F	2.07	2.51	2.48	2.06	2.06
*l*100*w*50*r*25*t*2*h*10000	0.10	F	F	2.07	2.52	2.50	2.09	2.09
*l*100*w*50*r*25*t*2*h*12000	0.07	F	F	2.06	2.54	2.38	2.12	2.12
*l*100*w*50*r*25*t*2*h*15000	0.04	F	F	2.01	2.51	2.36	2.11	2.11
*l*150*w*50*r*25*t*2*h*1000	0.49	L	L	0.89	0.81	0.81	0.88	0.86
*l*150*w*50*r*25*t*2*h*2000	0.49	L	L	1.04	1.24	1.11	1.01	0.90
*l*150*w*50*r*25*t*2*h*2500	0.48	L	L	1.19	1.49	1.34	1.13	0.97
*l*150*w*50*r*25*t*2*h*3500	0.41	L	L	1.40	1.89	1.76	1.26	1.27
*l*150*w*50*r*25*t*2*h*5000	0.20	F	F	1.59	2.26	2.18	1.36	1.38
*l*150*w*50*r*25*t*2*h*7000	0.18	F	F	1.91	2.80	2.74	1.78	1.78
*l*150*w*50*r*25*t*2*h*9000	0.12	F	F	1.98	2.96	2.92	1.93	1.93
*l*150*w*50*r*25*t*2*h*10000	0.11	F	F	2.17	3.27	4.01	2.15	2.15
*l*150*w*50*r*25*t*2*h*12000	0.07	F	F	2.00	3.04	3.75	2.02	2.02
*l*150*w*50*r*25*t*2*h*15000	0.05	F	F	2.02	3.12	3.85	2.09	2.09
*l*50*w*50*r*50*t*2*h*1000	1.00	L	L	1.12	1.07	1.03	1.09	1.03
*l*50*w*50*r*50*t*2*h*2000	0.72	F	F	1.19	1.23	1.10	1.04	0.81
*l*50*w*50*r*50*t*2*h*2500	0.61	F	F	1.30	1.30	1.18	1.07	0.95
*l*50*w*50*r*50*t*2*h*3500	0.41	F	F	1.46	1.39	1.32	1.24	1.24
*l*50*w*50*r*50*t*2*h*5000	0.19	F	F	1.26	1.20	1.16	1.19	1.19
*l*50*w*50*r*50*t*2*h*7000	0.12	F	F	1.49	1.42	1.40	1.48	1.48

*l*50*w*50*r*50*t*2*h*9000	0.06	F	F	1.15	1.10	1.09	1.17	1.17
*l*50*w*50*r*50*t*2*h*10000	0.05	F	F	1.13	1.09	1.08	1.17	1.17
*l*50*w*50*r*50*t*2*h*12000	0.04	F	F	1.45	1.41	1.40	1.52	1.52
*l*50*w*50*r*50*t*2*h*15000	0.03	F	F	1.44	1.41	1.40	1.53	1.53
*l*50*w*50*r*75*t*2*h*1000	0.94	L	L	1.06	1.01	0.98	1.03	0.97
*l*50*w*50*r*75*t*2*h*2000	0.72	F	F	1.19	1.23	1.10	1.04	0.81
*l*50*w*50*r*75*t*2*h*2500	0.57	F	F	1.21	1.21	1.10	1.00	0.88
*l*50*w*50*r*75*t*2*h*3500	0.38	F	F	1.36	1.30	1.23	1.16	1.16
*l*50*w*50*r*75*t*2*h*5000	0.19	F	F	1.27	1.20	1.16	1.19	1.19
*l*50*w*50*r*75*t*2*h*7000	0.11	F	F	1.36	1.30	1.28	1.35	1.35
*l*50*w*50*r*75*t*2*h*9000	0.06	F	F	1.15	1.11	1.10	1.18	1.18
*l*50*w*50*r*75*t*2*h*10000	0.05	F	F	1.14	1.10	1.09	1.18	1.18
*l*50*w*50*r*75*t*2*h*12000	0.04	F	F	1.32	1.28	1.28	1.38	1.38
*l*50*w*50*r*75*t*2*h*15000	0.02	F	F	1.30	1.28	1.27	1.39	1.39
*l*50*w*50*r*100*t*2*h*1000	0.91	L	L	1.02	0.98	0.94	1.00	0.94
*l*50*w*50*r*100*t*2*h*2000	0.71	F	F	1.18	1.23	1.10	1.03	0.81
*l*50*w*50*r*100*t*2*h*2500	0.56	F	F	1.20	1.20	1.09	0.99	0.87
*l*50*w*50*r*100*t*2*h*3500	0.36	F	F	1.30	1.24	1.17	1.11	1.11
*l*50*w*50*r*100*t*2*h*5000	0.19	F	F	1.26	1.19	1.16	1.19	1.19
*l*50*w*50*r*100*t*2*h*7000	0.10	F	F	1.19	1.14	1.12	1.18	1.18
*l*50*w*50*r*100*t*2*h*9000	0.07	F	F	1.29	1.24	1.22	1.32	1.32
*l*50*w*50*r*100*t*2*h*10000	0.05	F	F	1.28	1.23	0.33	1.32	1.32
*l*50*w*50*r*100*t*2*h*12000	0.04	F	F	1.27	1.23	0.33	1.33	1.33
*l*50*w*50*r*100*t*2*h*15000	0.02	F	F	1.25	1.23	0.32	1.33	1.33
*l*50*w*100*r*50*t*2*h*1000	0.86	L	L	0.90	0.87	0.87	0.88	0.87
*l*50*w*100*r*50*t*2*h*2000	0.84	L	L	0.92	0.90	0.85	0.92	0.87
*l*50*w*100*r*50*t*2*h*2500	0.83	L	L	0.98	1.04	0.94	0.96	0.87
*l*50*w*100*r*50*t*2*h*3500	0.79	L	L	1.16	1.22	1.10	1.06	0.87
*l*50*w*100*r*50*t*2*h*5000	0.69	F	F	1.50	1.48	1.36	1.25	1.11
*l*50*w*100*r*50*t*2*h*7000	0.51	F	F	1.86	1.76	1.66	1.61	1.61
*l*50*w*100*r*50*t*2*h*9000	0.34	F	F	1.91	1.78	1.72	1.77	1.77
*l*50*w*100*r*50*t*2*h*10000	0.29	F	F	1.97	1.83	0.90	1.86	1.86
*l*50*w*100*r*50*t*2*h*12000	0.21	F	F	1.97	1.84	0.88	1.92	1.92

*l*50*w*100*r*50*t*2*h*15000	0.14	F	F	2.01	1.89	0.90	2.02	2.02
*l*50*w*150*r*75*t*2*h*1000	0.86	L	L	0.89	0.87	0.87	0.91	0.91
*l*50*w*150*r*75*t*2*h*2000	0.84	L	L	0.87	0.85	0.85	0.91	0.90
*l*50*w*150*r*75*t*2*h*2500	0.83	L	L	0.86	0.84	0.84	0.91	0.90
*l*50*w*150*r*75*t*2*h*3500	0.81	L	L	0.93	0.99	0.89	0.93	0.89
*l*50*w*150*r*75*t*2*h*5000	0.78	L	L	1.10	1.17	1.05	1.02	0.88
*l*50*w*150*r*75*t*2*h*7000	0.57	F	F	1.16	1.16	1.05	0.98	0.84
*l*50*w*150*r*75*t*2*h*9000	0.49	F	F	1.44	1.38	1.29	1.20	1.19
*l*50*w*150*r*75*t*2*h*10000	0.43	F	F	1.50	1.42	0.88	1.29	1.29
*l*50*w*150*r*75*t*2*h*12000	0.33	F	F	1.58	1.47	0.89	1.43	1.43
*l*50*w*150*r*75*t*2*h*15000	0.23	F	F	1.62	1.50	0.89	1.54	1.54
*l*50*w*200*r*100*t*2*h*1000	0.87	L	L	0.89	0.87	0.87	0.94	0.95
*l*50*w*200*r*100*t*2*h*2000	0.80	L	L	0.83	0.81	0.81	0.89	0.89
*l*50*w*200*r*100*t*2*h*2500	0.78	L	L	0.81	0.79	0.79	0.87	0.87
*l*50*w*200*r*100*t*2*h*3500	0.77	L	L	0.81	0.78	0.78	0.89	0.87
*l*50*w*200*r*100*t*2*h*5000	0.77	L	L	0.91	0.98	0.88	0.93	0.88
*l*50*w*200*r*100*t*2*h*7000	0.73	L	L	1.08	1.14	1.02	0.99	0.86
*l*50*w*200*r*100*t*2*h*9000	0.61	F	F	1.20	1.20	1.09	1.02	0.85
*l*50*w*200*r*100*t*2*h*10000	0.56	F	F	1.28	1.25	1.13	1.06	0.97
*l*50*w*200*r*100*t*2*h*12000	0.46	F	F	1.36	1.30	1.16	1.13	1.13
*l*50*w*200*r*100*t*2*h*15000	0.34	F	F	1.46	1.36	1.21	1.30	1.30
Number of data				100	100	100	100	100
Mean (P_m)				1.44	1.53	1.42	1.38	1.34
COV (V_p)				0.28	0.38	0.49	0.31	0.34
Resistance factor (Φ)				0.91	0.85	0.85	0.80	0.80
Reliability index (β)				2.51	2.31	1.76	2.68	2.45

L = local failure ; F = Flexure failure; L+F = local-flexural failure

Table 4.5

Comparison of FE strength with design strengths for slender stocky section (t = 10-20 mm; Class 1 and 2).

Specimen	P_u / P_y	Failure mode at δ_u	Failure mode at $1.5\delta_u$	$\frac{P_{FE}}{P_{EN}}$	$\frac{P_{FE}}{P_{AS/NZS}}$	$\frac{P_{FE}}{P^*_{AS/NZ}}$	$\frac{P_{FE}}{P_{DSM}}$	$\frac{P_{FE}}{P^*_{DSM}}$
*l*50*w*50*r*25*t*10*h*1000	1.16	Y	F	1.27	1.35	1.21	1.31	1.21
*l*50*w*50*r*25*t*10*h*2000	0.83	F	F	1.53	1.55	1.40	1.33	1.07
*l*50*w*50*r*25*t*10*h*2500	0.67	F	F	1.69	1.63	1.51	1.41	1.35
*l*50*w*50*r*25*t*10*h*3500	0.30	F	F	1.32	1.22	1.17	1.19	1.19
*l*75*w*50*r*25*t*10*h*1000	1.13	Y	F	1.22	1.28	1.15	1.27	1.18
*l*75*w*50*r*25*t*10*h*2000	0.83	F	F	1.47	1.50	1.35	1.30	1.00
*l*75*w*50*r*25*t*10*h*2500	0.52	F	F	1.24	1.20	1.11	1.03	0.97
*l*75*w*50*r*25*t*10*h*3500	0.32	F	F	1.31	1.22	1.16	1.17	1.17
*l*100w50*r*25*t*10*h*1000	1.09	Y	F	1.16	1.21	1.09	1.21	1.13
*l*100w50*r*25*t*10*h*2000	0.83	F	F	1.78	1.48	1.33	1.28	0.97
*l*100*w*50*r*25*t*10*h*2500	0.69	F	F	1.59	1.55	1.43	1.33	1.24
*l*100*w*50*r*25*t*10*h*3500	0.32	F	F	1.30	1.21	1.15	1.15	1.15
*l*150*w*50*r*25*t*10*h*1000	1.04	Y	F	1.09	1.13	1.04	1.15	1.07
*l*150*w*50*r*25*t*10*h*2000	0.83	F	F	1.39	1.44	1.29	1.24	0.95
*l*150*w*50*r*25*t*10*h*2500	0.68	F	F	1.52	1.49	1.36	1.28	1.17
*l*150*w*50*r*25*t*10*h*3500	0.34	F	F	1.28	1.20	1.14	1.13	1.13
*l*50*w*50*r*50*t*10*h*1000	1.18	Y	F	1.30	1.39	1.25	1.34	1.23
*l*50*w*50*r*50*t*10*h*2000	0.80	F	F	1.51	1.52	1.38	1.31	1.07
*l*50*w*50*r*50*t*10*h*2500	0.62	F	F	1.61	1.55	1.44	1.34	1.30
*l*50*w*50*r*50*t*10*h*3500	0.30	F	F	1.36	1.26	1.21	1.23	1.23
*l*50*w*50*r*75*t*10*h*1000	1.00	Y	F	1.33	1.43	1.29	1.38	1.26
*l*50*w*50*r*75*t*10*h*2000	0.59	F	F	1.36	1.37	1.24	1.18	0.90
*l*50*w*50*r*75*t*10*h*2500	0.46	F	F	1.45	1.40	1.29	1.21	0.97
*l*50*w*50*r*75*t*10*h*3500	0.25	F	F	1.40	1.30	1.25	1.27	1.05
*l*50*w*50*r*100*t*10*h*1000	1.20	Y	F	1.31	1.40	1.26	1.35	1.25
*l*50*w*50*r*100*t*10*h*2000	0.72	F	F	1.37	1.38	1.25	1.19	0.98
*l*50*w*50*r*100*t*10*h*2500	0.56	F	F	1.47	1.41	1.31	1.22	1.18
*l*50*w*50*r*100*t*10*h*3500	0.31	F	F	1.43	1.33	1.27	1.29	1.29
*l*50*w*100*r*50*t*10*h*1000	1.31	Y	Y	1.21	1.31	1.31	1.35	1.32
*l*50*w*100*r*50*t*10*h*2000	1.16	Y	F	1.25	1.31	1.17	1.30	1.20
*l*50*w*100*r*50*t*10*h*2500	1.12	Y	F	1.32	1.45	1.30	1.33	1.19

*l*50*w*100*r*50*t*10*h*3500	1.00	Y	F	1.52	1.60	1.44	1.40	1.12
*l*50*w*150*r*75*t*10*h*1000	1.28	Y	Y	1.13	1.28	1.28	1.29	1.28
*l*50*w*150*r*75*t*10*h*2000	1.16	Y	F	1.12	1.16	1.16	1.22	1.18
*l*50*w*150*r*75*t*10*h*2500	1.13	Y	F	1.15	1.13	1.13	1.22	1.16
*l*50*w*150*r*75*t*10*h*3500	1.03	Y	F	1.17	1.28	1.15	1.19	1.08
*l*50*w*200*r*100*t*10*h*1000	1.25	Y	Y	1.08	1.25	1.25	1.26	1.25
*l*50*w*200*r*100*t*10*h*2000	1.25	Y	Y	1.15	1.25	1.25	1.28	1.26
*l*50*w*200*r*100*t*10*h*2500	1.24	Y	Y	1.19	1.24	1.24	1.30	1.26
*l*50*w*200*r*100*t*10*h*3500	1.07	Y	F	1.10	1.07	1.07	1.17	1.10
*l*50*w*50*r*25*t*15*h*1000	1.14	Y	F	1.29	1.40	1.26	1.32	1.20
*l*50*w*50*r*25*t*15*h*2000	0.62	F	F	1.28	1.27	1.16	1.09	0.95
*l*50*w*50*r*25*t*15*h*2500	0.47	F	F	1.36	1.29	1.20	1.13	1.13
*l*50*w*50*r*25*t*15*h*3500	0.26	F	F	1.32	1.22	1.17	1.21	1.21
*l*75*w*50*r*25*t*15*h*1000	1.19	Y	F	1.35	1.47	1.33	1.38	1.25
*l*75*w*50*r*25*t*15*h*2000	0.61	F	F	1.29	1.28	1.17	1.09	0.97
*l*75*w*50*r*25*t*15*h*2500	0.47	F	F	1.40	1.33	1.25	1.18	1.17
*l*75*w*50*r*25*t*15*h*3500	0.27	F	F	1.40	1.30	1.25	1.29	1.29
*l*100*w*50*r*25*t*15*h*1000	1.11	Y	F	1.26	1.37	1.23	1.28	1.17
*l*100*w*50*r*25*t*15*h*2000	0.61	F	F	1.29	1.47	1.34	1.26	1.12
*l*100*w*50*r*25*t*15*h*2500	0.47	F	F	1.40	1.33	1.24	1.17	1.17
*l*100*w*50*r*25*t*15*h*3500	0.27	F	F	1.43	1.32	1.27	1.32	1.32
*l*150*w*50*r*25*t*15*h*1000	1.14	Y	F	1.29	1.40	1.27	1.32	1.19
*l*150*w*50*r*25*t*15*h*2000	0.60	F	F	1.28	1.27	1.16	1.08	0.96
*l*150*w*50*r*25*t*15*h*2500	0.49	F	F	1.45	1.37	1.28	1.21	1.21
*l*150*w*50*r*25*t*15*h*3500	0.28	F	F	1.46	1.35	1.30	1.35	1.35
*l*50*w*50*r*50*t*15*h*1000	1.28	Y	F	1.43	1.54	1.39	1.47	1.34
*l*50*w*50*r*50*t*15*h*2000	0.69	F	F	1.38	1.38	1.25	1.18	1.01
*l*50*w*50*r*50*t*15*h*2500	0.54	F	F	1.50	1.43	1.33	1.24	1.23
*l*50*w*50*r*50*t*15*h*3500	0.28	F	F	1.36	1.26	1.21	1.24	1.24
*l*50*w*50*r*75*t*15*h*1000	1.32	Y	F	1.45	1.56	1.41	1.50	1.37
*l*50*w*50*r*75*t*15*h*2000	0.72	F	F	1.41	1.41	1.28	1.21	1.02
*l*50*w*50*r*75*t*15*h*2500	0.55	F	F	1.47	1.41	1.31	1.22	1.20
*l*50*w*50*r*75*t*15*h*3500	0.29	F	F	1.39	1.29	1.24	1.26	1.26
*l*50*w*50*r*100*t*15*h*1000	1.33	Y	F	1.46	1.56	1.41	1.51	1.39
*l*50*w*50*r*100*t*15*h*2000	0.75	F	F	1.42	1.43	1.29	1.23	1.01
*l*50*w*50*r*100*t*15*h*2500	0.56	F	F	1.47	1.41	1.31	1.22	1.18
*l*50*w*50*r*100*t*15*h*3500	0.30	F	F	1.37	1.27	1.22	1.24	1.24

*l*50*w*100*r*50*t*15*h*1000	1.32	Y	F	1.22	1.32	1.32	1.36	1.33
*l*50*w*100*r*50*t*15*h*2000	1.25	Y	F	1.37	1.46	1.31	1.41	1.31
*l*50*w*100*r*50*t*15*h*2500	1.16	Y	F	1.40	1.54	1.38	1.40	1.23
*l*50*w*100*r*50*t*15*h*3500	1.06	Y	F	1.69	1.76	1.58	1.53	1.20
*l*50*w*150*r*75*t*15*h*1000	1.33	Y	Y	1.18	1.33	1.33	1.35	1.34
*l*50*w*150*r*75*t*15*h*2000	1.19	Y	F	1.16	1.19	1.19	1.26	1.21
*l*50*w*150*r*75*t*15*h*2500	1.16	Y	F	1.19	1.16	1.16	1.26	1.19
*l*50*w*150*r*75*t*15*h*3500	1.03	Y	F	1.19	1.30	1.17	1.20	1.08
*l*50*w*200*r*100*t*15*h*1000	1.30	Y	Y	1.12	1.30	1.30	1.31	1.30
*l*50*w*200*r*100*t*15*h*2000	1.22	Y	F	1.11	1.22	1.22	1.25	1.23
*l*50*w*200*r*100*t*15*h*2500	1.19	Y	F	1.12	1.19	1.19	1.23	1.20
*l*50*w*200*r*100*t*15*h*3500	1.09	Y	F	1.10	1.09	1.09	1.17	1.12
*l*50*w*50*r*25*t*20*h*1000	0.92	Y	F	1.08	1.18	1.06	1.09	0.97
*l*50*w*50*r*25*t*20*h*2000	0.57	F	F	1.32	1.29	1.18	1.10	1.03
*l*50*w*50*r*25*t*20*h*2500	0.41	F	F	1.37	1.29	1.22	1.17	1.17
*l*50*w*50*r*25*t*20*h*3500	0.22	F	F	1.31	1.20	1.17	1.22	1.22
*l*75*w*50*r*25*t*20*h*1000	1.09	Y	F	1.28	1.40	1.26	1.29	1.16
*l*75*w*50*r*25*t*20*h*2000	0.76	F	F	1.77	1.72	1.58	1.47	1.38
*l*75*w*50*r*25*t*20*h*2500	0.42	F	F	1.38	1.30	1.23	1.18	1.18
*l*75*w*50*r*25*t*20*h*3500	0.22	F	F	1.33	1.23	1.19	1.25	1.25
*l*100*w*50*r*25*t*20*h*1000	1.08	Y	F	1.27	1.38	1.25	1.28	1.14
*l*100*w*50*r*25*t*20*h*2000	0.56	F	F	1.29	1.26	1.15	1.08	1.00
*l*100*w*50*r*25*t*20*h*2500	0.42	F	F	1.38	1.29	1.22	1.18	1.18
*l*100*w*50*r*25*t*20*h*3500	0.23	F	F	1.34	1.23	1.19	1.25	1.25
*l*150*w*50*r*25*t*20*h*1000	1.05	Y	F	1.22	1.33	1.20	1.23	1.10
*l*150*w*50*r*25*t*20*h*2000	0.54	F	F	1.26	1.23	1.13	1.05	0.98
*l*150*w*50*r*25*t*20*h*2500	0.41	F	F	1.36	1.28	1.21	1.16	1.16
*l*150*w*50*r*25*t*20*h*3500	0.23	F	F	1.34	1.24	1.20	1.26	1.26
*l*50*w*50*r*50*t*20*h*1000	1.35	Y	F	1.56	1.71	1.54	1.58	1.42
*l*50*w*50*r*50*t*20*h*2000	0.70	F	F	1.57	1.54	1.41	1.32	1.21
*l*50*w*50*r*50*t*20*h*2500	0.53	F	F	1.68	1.59	1.49	1.43	1.43
*l*50*w*50*r*50*t*20*h*3500	0.26	F	F	1.50	1.38	1.34	1.39	1.39
*l*50*w*50*r*75*t*20*h*1000	1.41	Y	F	1.63	1.78	1.60	1.65	1.49

*l*50*w*50*r*75*t*20*h*2000	0.74	F	F	1.64	1.61	1.47	1.38	1.25
*l*50*w*50*r*75*t*20*h*2500	0.56	F	F	1.75	1.65	1.55	1.48	1.48
*l*50*w*50*r*75*t*20*h*3500	0.28	F	F	1.58	1.46	1.41	1.47	1.47
*l*50*w*50*r*100*t*20*h*1000	1.45	Y	F	1.66	1.81	1.63	1.69	1.53
*l*50*w*50*r*100*t*20*h*2000	0.76	F	F	1.65	1.63	1.49	1.39	1.25
*l*50*w*50*r*100*t*20*h*2500	0.57	F	F	1.75	1.65	1.55	1.47	1.47
*l*50*w*50*r*100*t*20*h*3500	0.30	F	F	1.60	1.48	1.43	1.48	1.48
*l*50*w*100*r*50*t*20*h*1000	1.33	Y	Y	1.24	1.33	1.33	1.37	1.34
*l*50*w*100*r*50*t*20*h*2000	1.28	Y	F	1.42	1.53	1.38	1.46	1.33
*l*50*w*100*r*50*t*20*h*2500	1.22	Y	F	1.52	1.66	1.49	1.50	1.31
*l*50*w*100*r*50*t*20*h*3500	0.97	F	F	1.62	1.68	1.51	1.45	1.11
*l*50*w*150*r*75*t*20*h*1000	1.34	Y	Y	1.19	1.34	1.34	1.36	1.35
*l*50*w*150*r*75*t*20*h*2000	1.28	Y	F	1.25	1.28	1.28	1.35	1.30
*l*50*w*150*r*75*t*20*h*2500	1.17	Y	F	1.21	1.17	1.17	1.28	1.21
*l*50*w*150*r*75*t*20*h*3500	1.07	Y	F	1.26	1.38	1.24	1.27	1.14
*l*50*w*200*r*100*t*20*h*1000	1.34	Y	Y	1.16	1.34	1.34	1.35	1.34
*l*50*w*200*r*100*t*20*h*2000	1.24	Y	F	1.15	1.24	1.24	1.27	1.25
*l*50*w*200*r*100*t*20*h*2500	1.21	Y	F	1.16	1.21	1.21	1.27	1.23
*l*50*w*200*r*100*t*20*h*3500	1.11	Y	F	1.16	1.15	1.11	1.22	1.14
Number of data				120	120	120	120	120
Mean (P_m)				1.36	1.37	1.28	1.29	1.20
COV (V_p)				0.12	0.12	0.10	0.09	0.11
Resistance factor (Φ)				0.91	0.85	0.85	0.80	0.80
Reliability index (β)				3.28	3.52	3.38	3.90	3.50

Y= Yielded failure ; F = Flexure failure

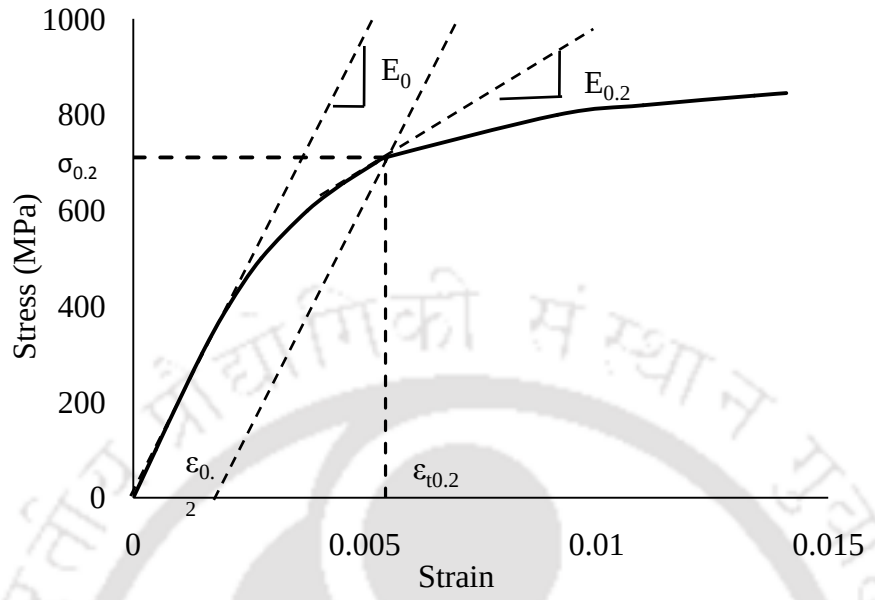

Figure 4.1: Experimental stress-strain curve of LDSS material Grade EN 1.4162 for 60x60x3 (Theofanous & Gardner, 2009).

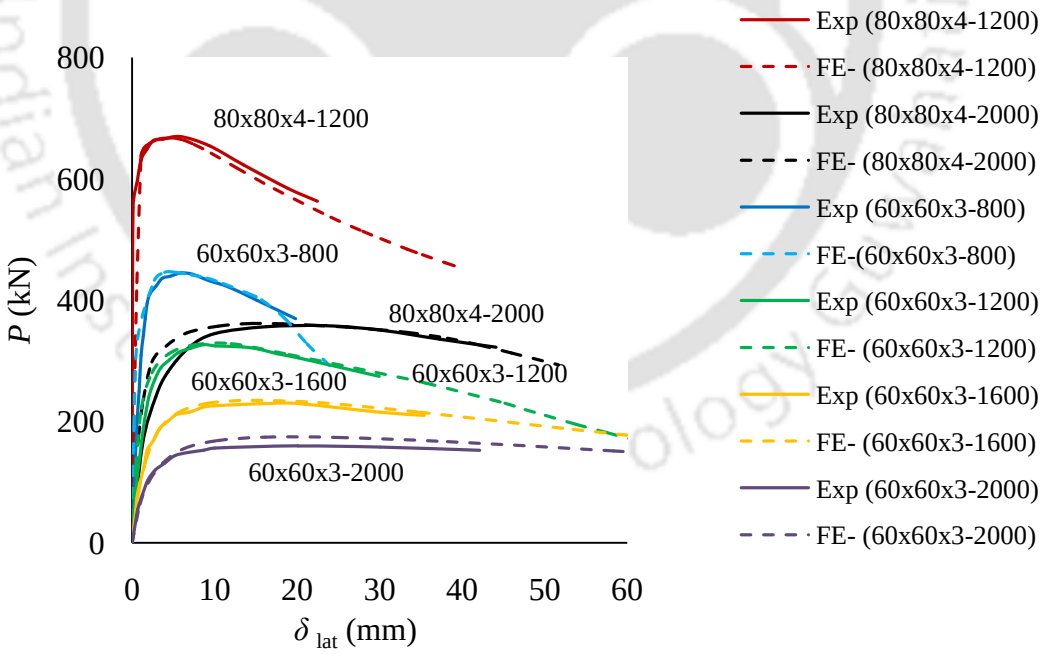

Figure 4.2: Validation of P (load) vs δ_{lat} (lateral displacement) for SHC 80x80x4 (h =1200 and 2000 mm) and SHC 60x60x3 (h = 800, 1200, 1600, 2000 mm) (Theofanous & Gardner, 2009).

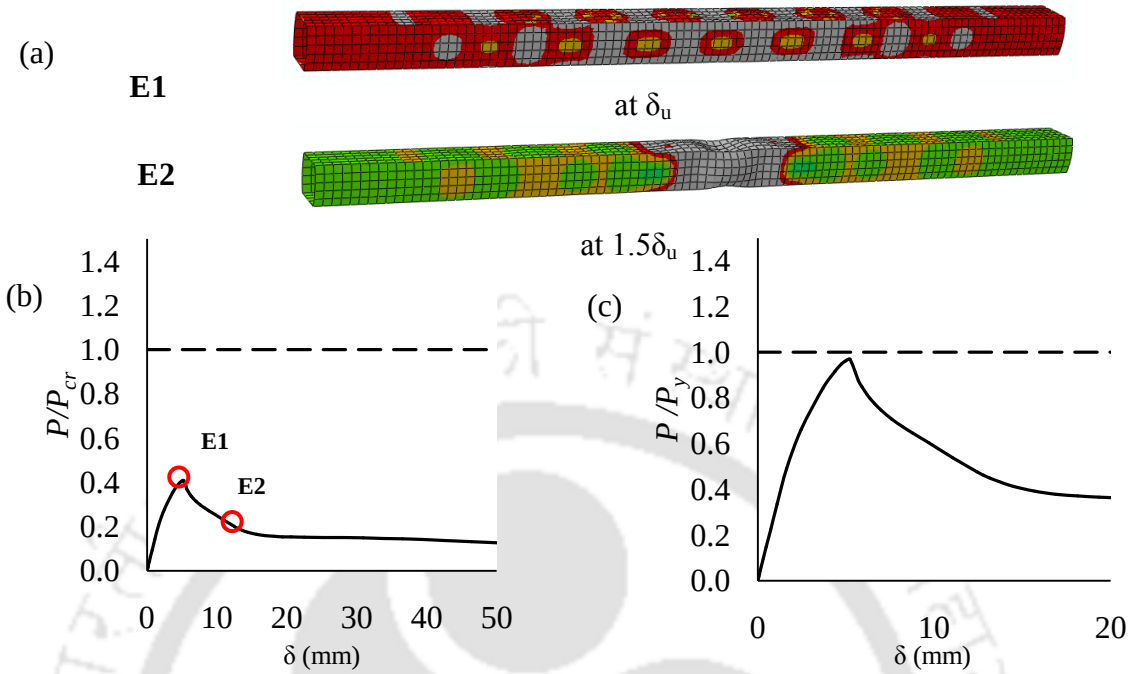

Figure 4.3: Typical Mechanism SL1A (local to local buckling) failure mode: a) von-Misses contour plot of E1 (at δ_u) and E2 (at 1.5δ_u); b) variation of P/P_{cr} with δ (axial deformation) and c) variation of P/P_y with δ (l50w50r75t2h1000).

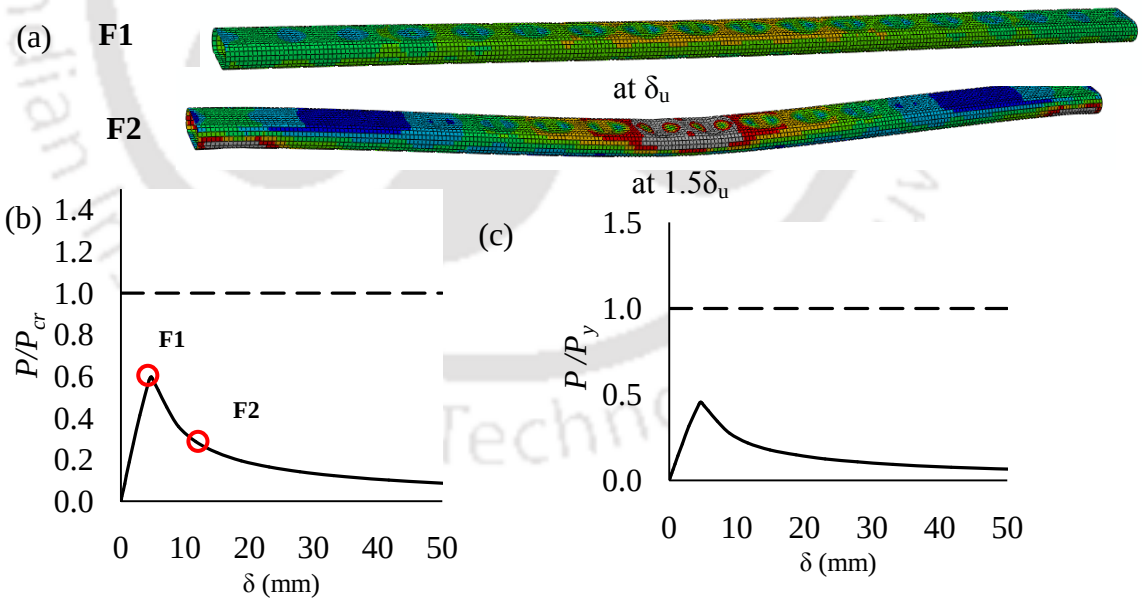

Figure 4.4: Typical Mechanism SL1B (local to local-flexural buckling) failure mode: a) von-Misses contour plot of F1 (at δ_u) and F2 (at 1.5δ_u); b) variation of P/P_{cr} with δ (axial deformation), and c) variation of P/P_y with δ (l75w50r25t2h2500).

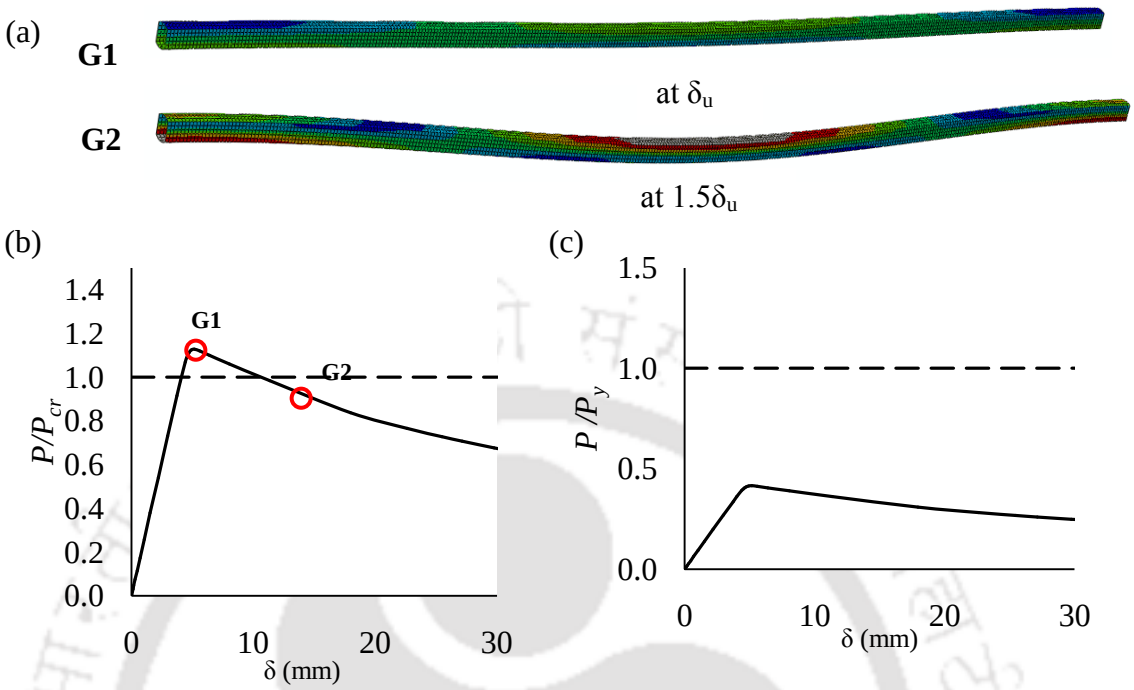

Figure 4.5: Typical Mechanism SL2 (flexural to flexural buckling) failure mode: a) von-Misses contour plot of G1 (at δ_u) and G2 (at $1.5\delta_u$); b) variation of P/P_{cr} with δ (axial deformation), and c) variation of P/P_y with δ ($l50w50r50t2h3500$).

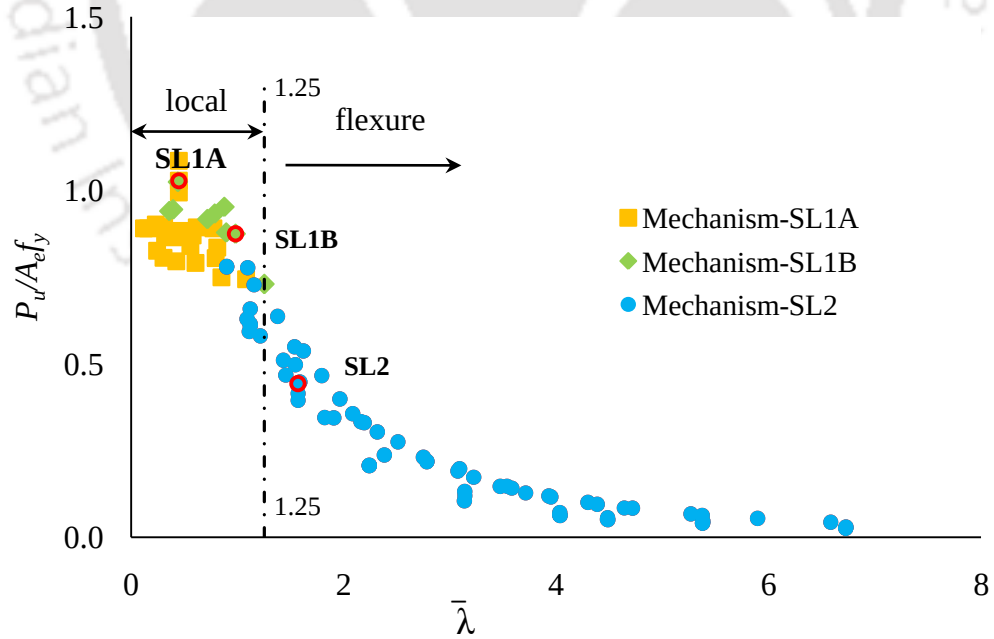

Figure 4.6: Variation of P_u/A_ef_y with $\bar{\lambda}$ showing Mechanisms SL1A, SL1B and SL2 regions.

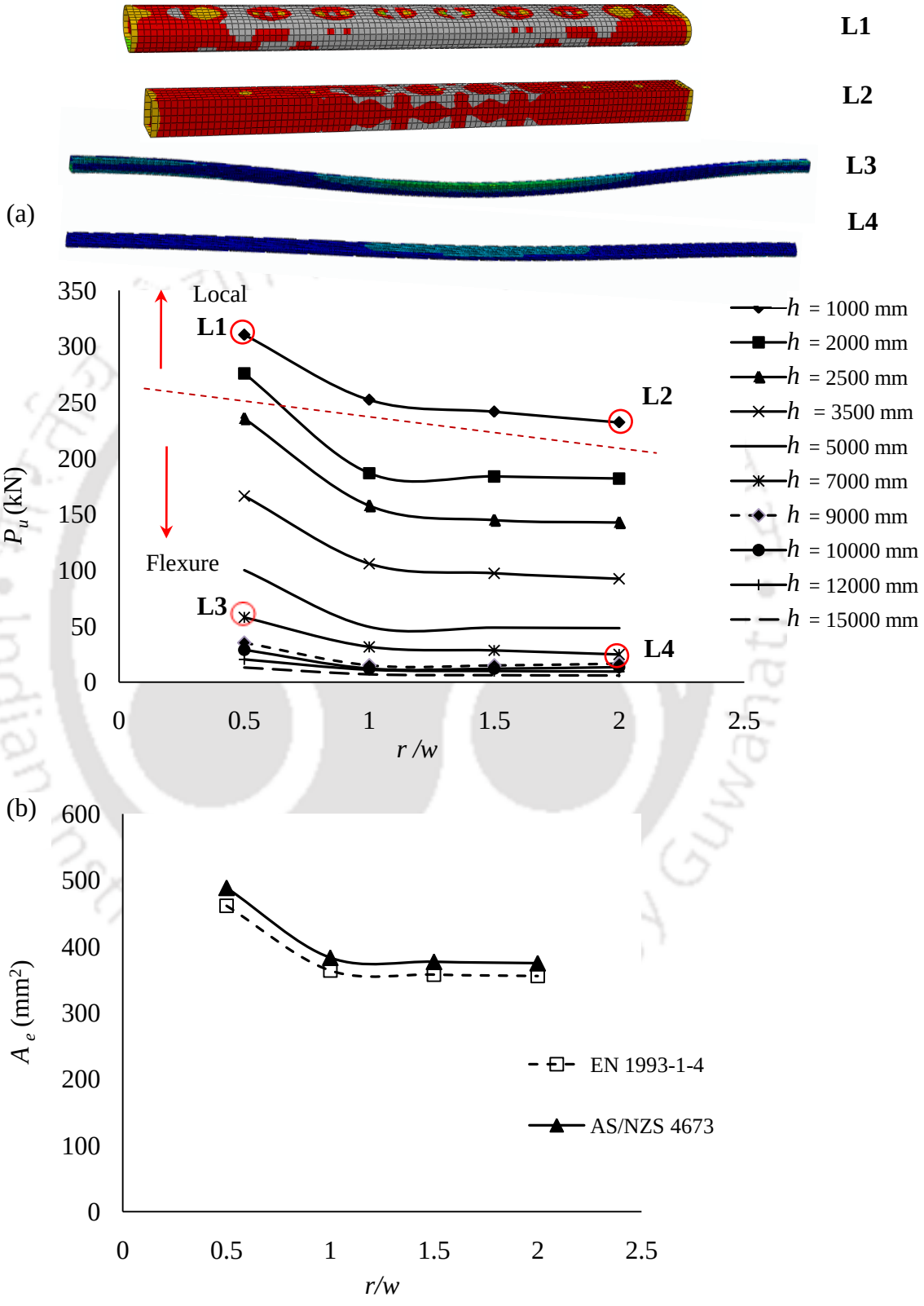

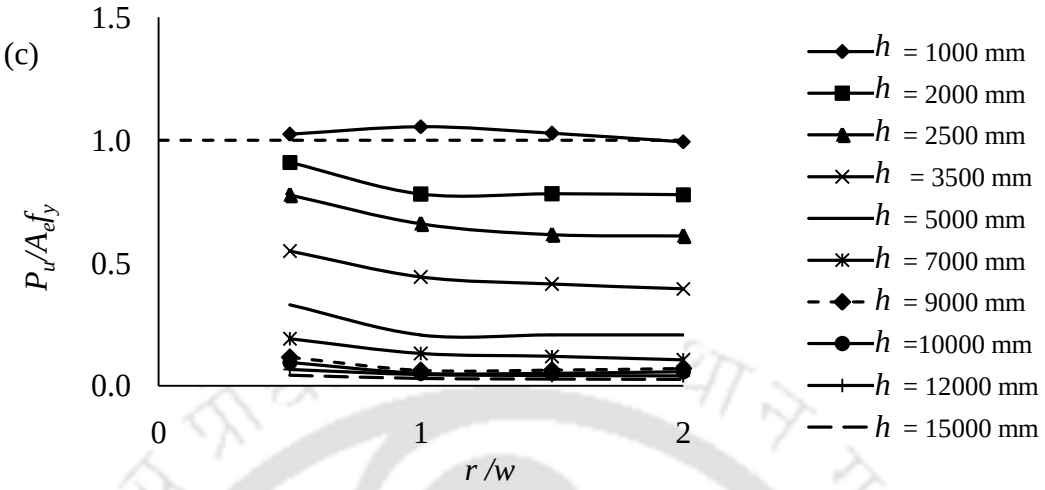

Figure 4.7: Variation of (a) P_u vs r/w, (b) A_e vs. r/w and (c) P_u/A_ef_y vs r/w (l_f = 50 mm, w = 50 mm, t = 2 mm, r = 25 – 100 mm).

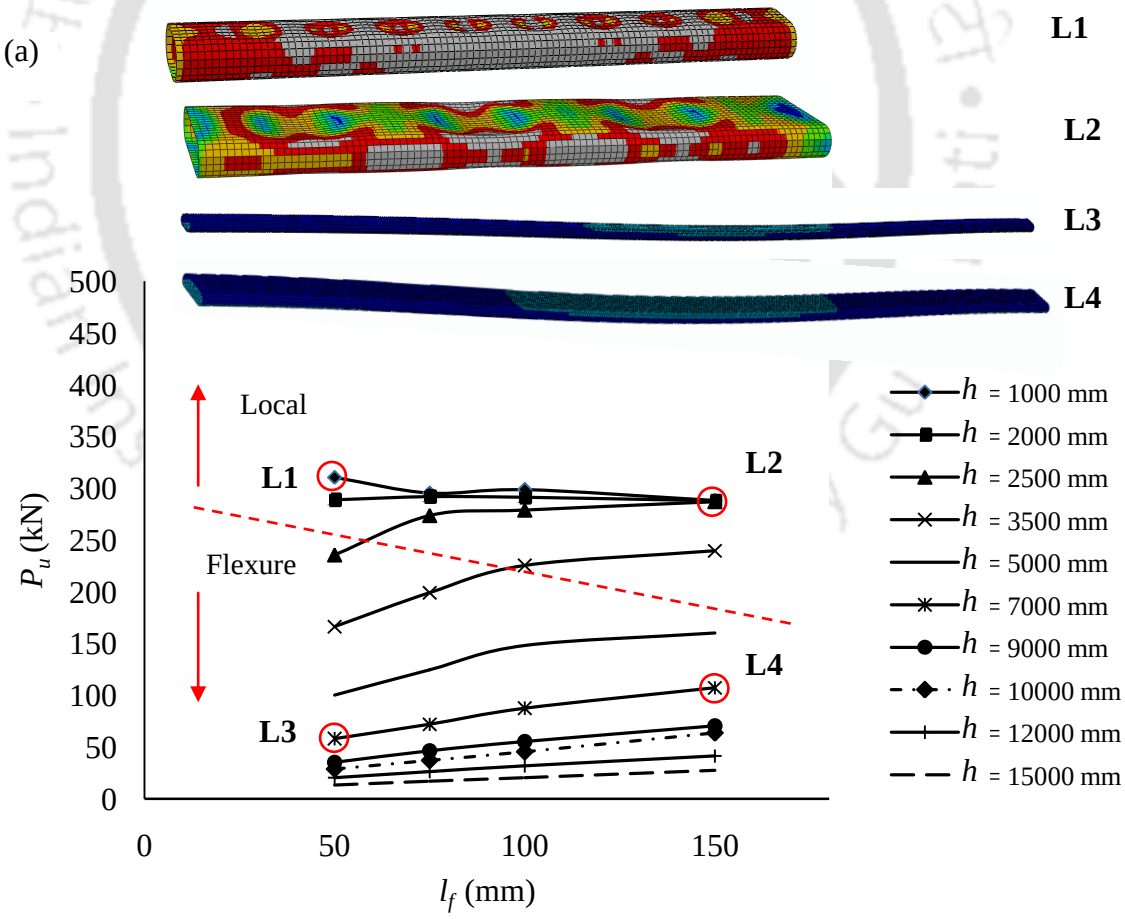

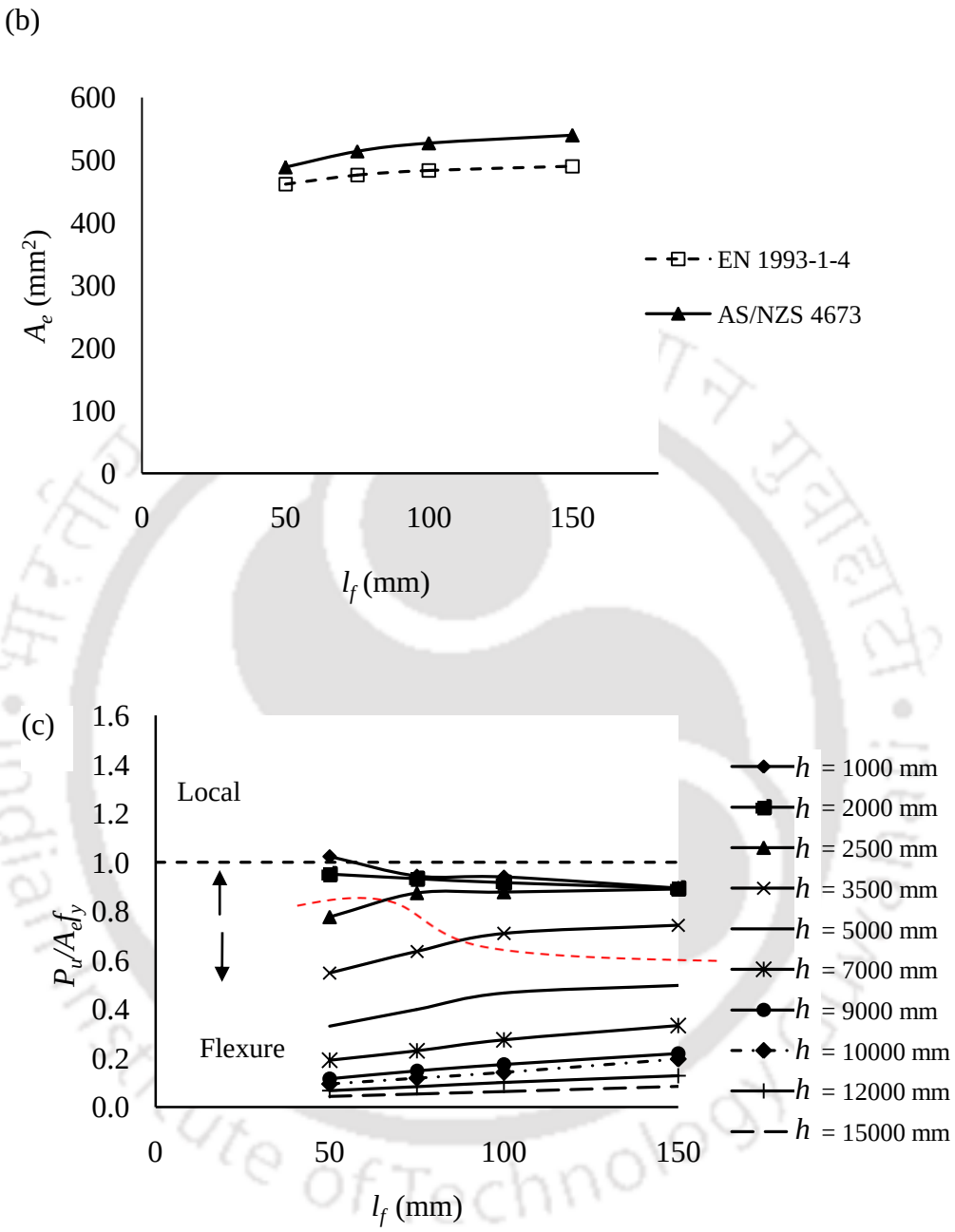

Figure 4.8: Variation of (a) P_u vs l_f, (b) A_e vs. l_f and (c) P_u/A_ef_y vs l_f, (w = 50 mm, r = 25 mm, t = 2 mm, l_f = 50 – 150 mm).

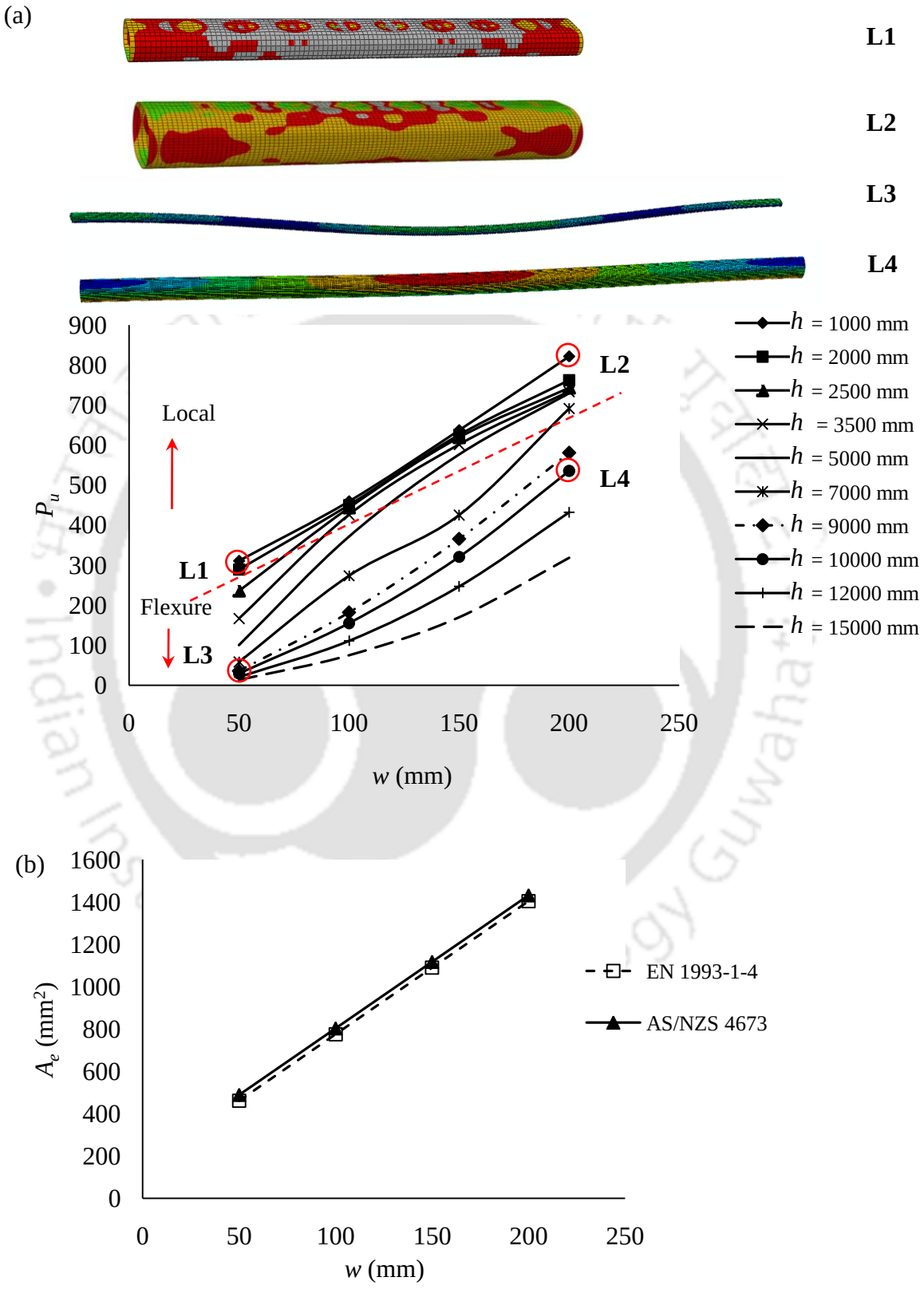

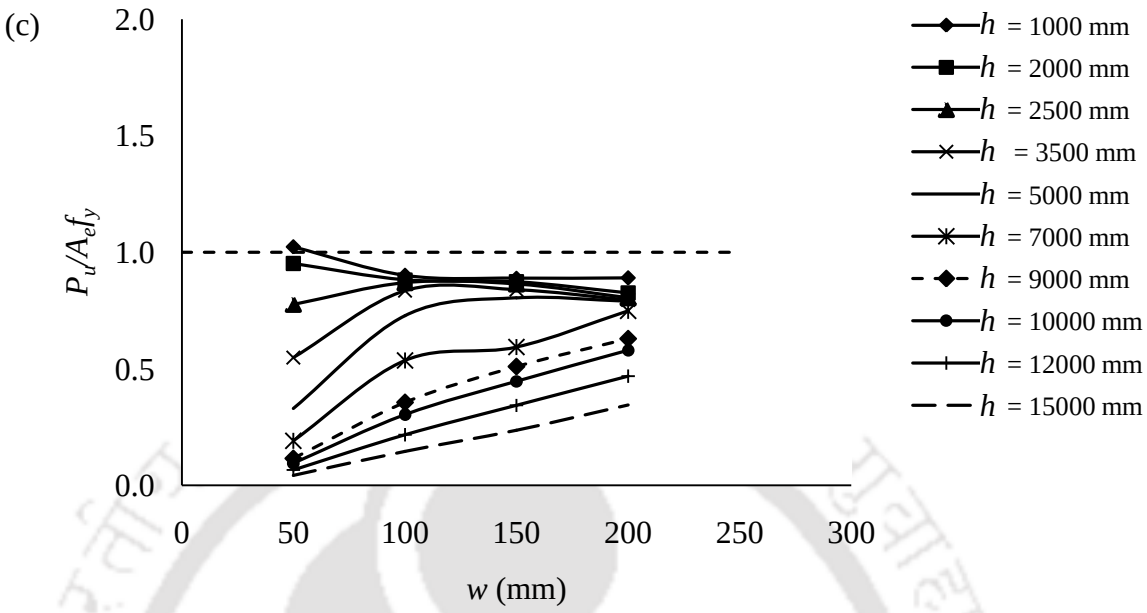

Figure 4.9: Variation of (a) P_u vs w, (b) A_e vs w and (c) P_u/A_ef_y vs w, (l_f = 50 mm, r/w = 0.5, t = 2 mm, w = 50 – 200 mm).

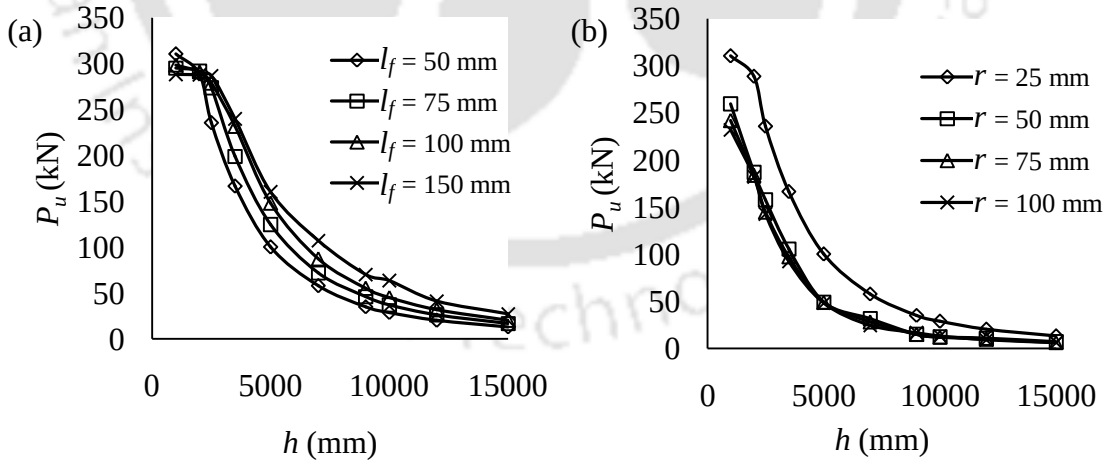

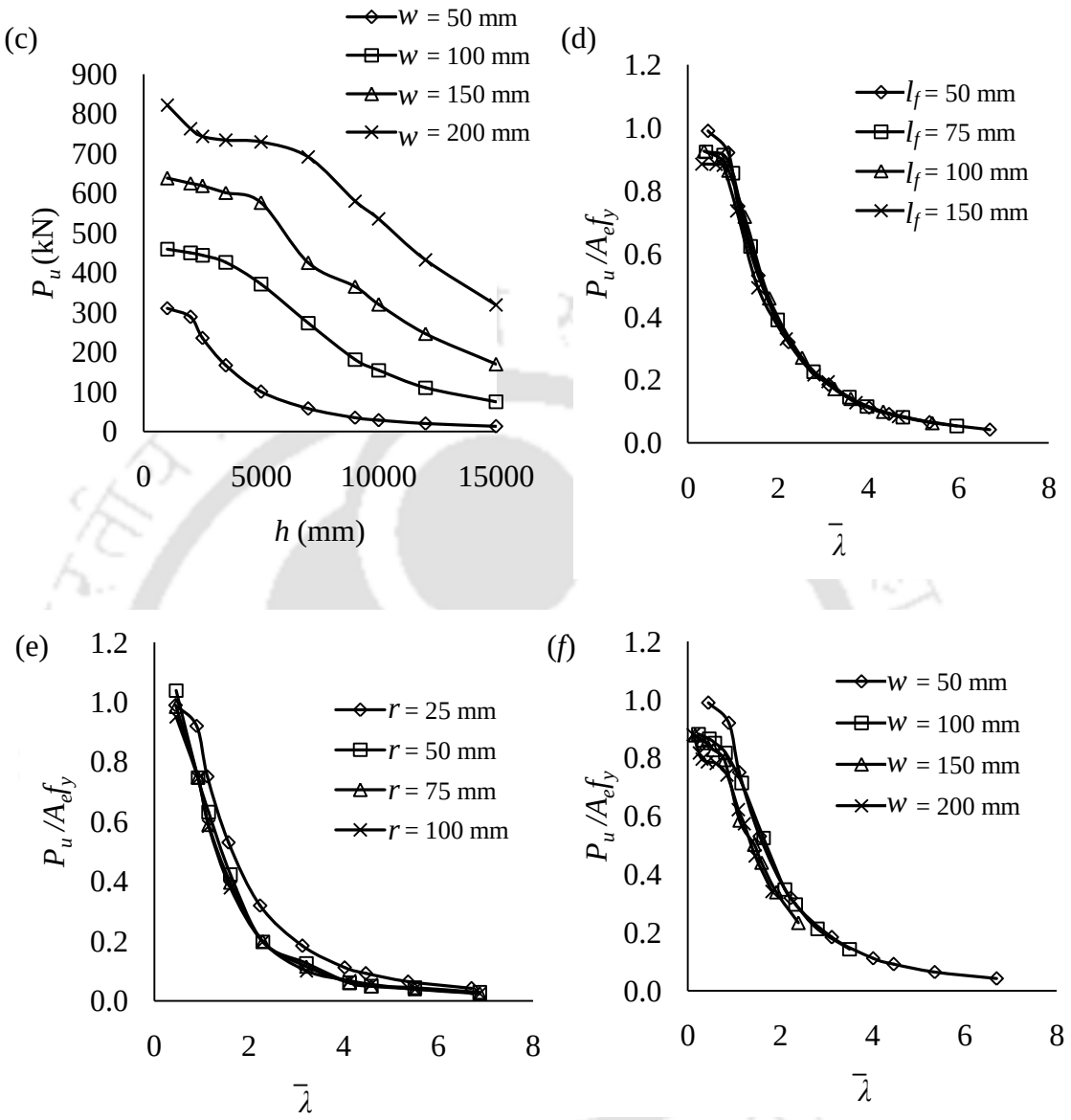

Figure 4.10: P_u vs h (a,b,c) and $P_u/A_e f_y$ vs $\bar{\lambda}$ (d,e,f) of h = 1000-15000 mm at t = 2 mm for w = 50 mm, r = 25 mm, l_f = 50-150 mm (a,d); l_f = 50 mm, w = 50 mm, r = 25-100 mm (b,e); l_f = 50 mm, r/w = 0.2, w = 50 – 200 mm (c,f).

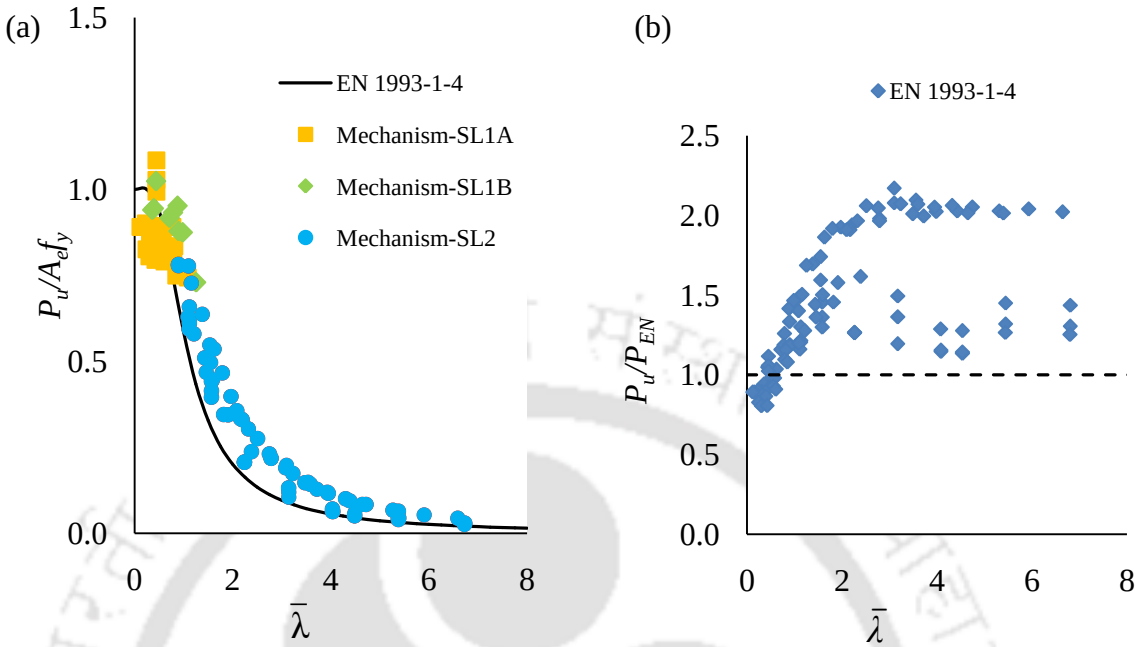

Figure 4.11: Comparison of EN 1993-1-4 (2015) and FE results for t = 2 mm.

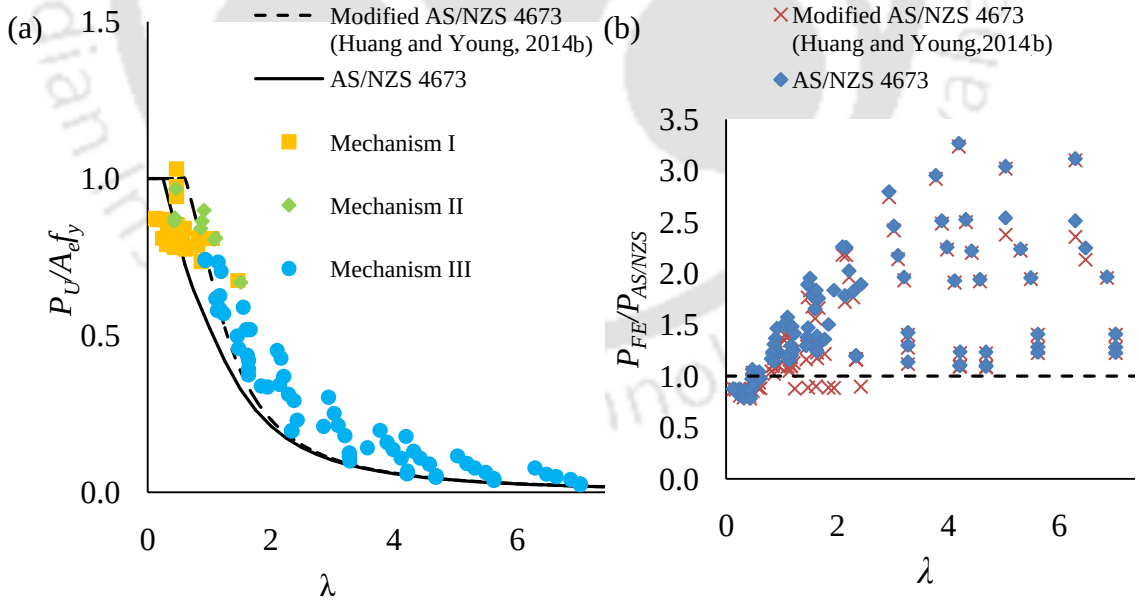

Figure 4.12: Comparison of AS/NZS 4673, modified AS/NZS 4673 (Huang and Young, 2014b) and FE results for t = 2 mm.

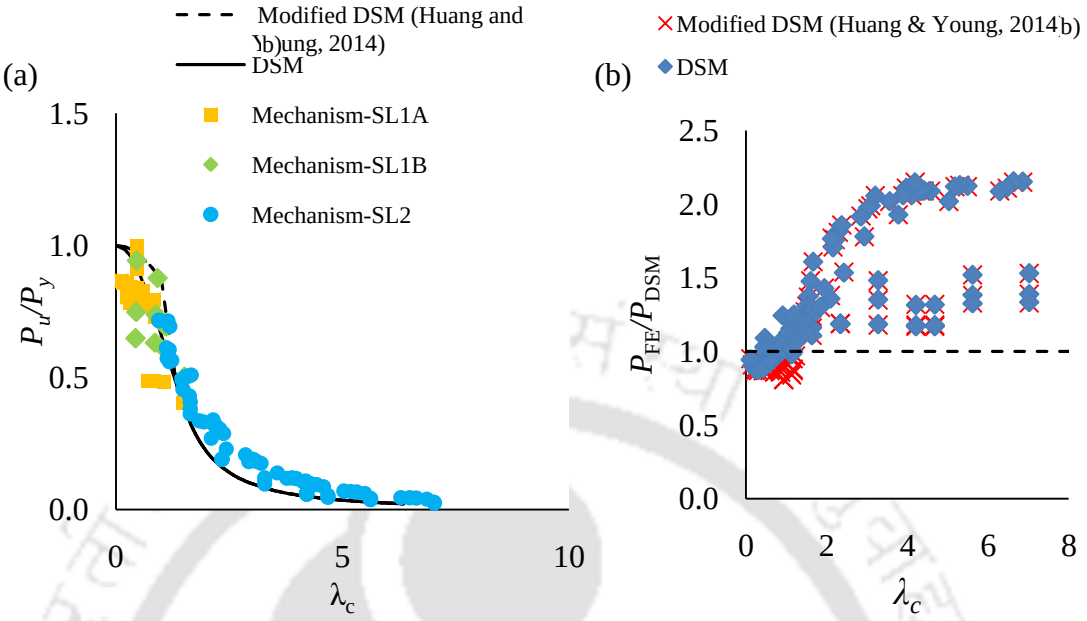

Figure 4.13: Comparison of DSM, modified DSM (Huang and Young, 2014b) and FE results for t = 2 mm.

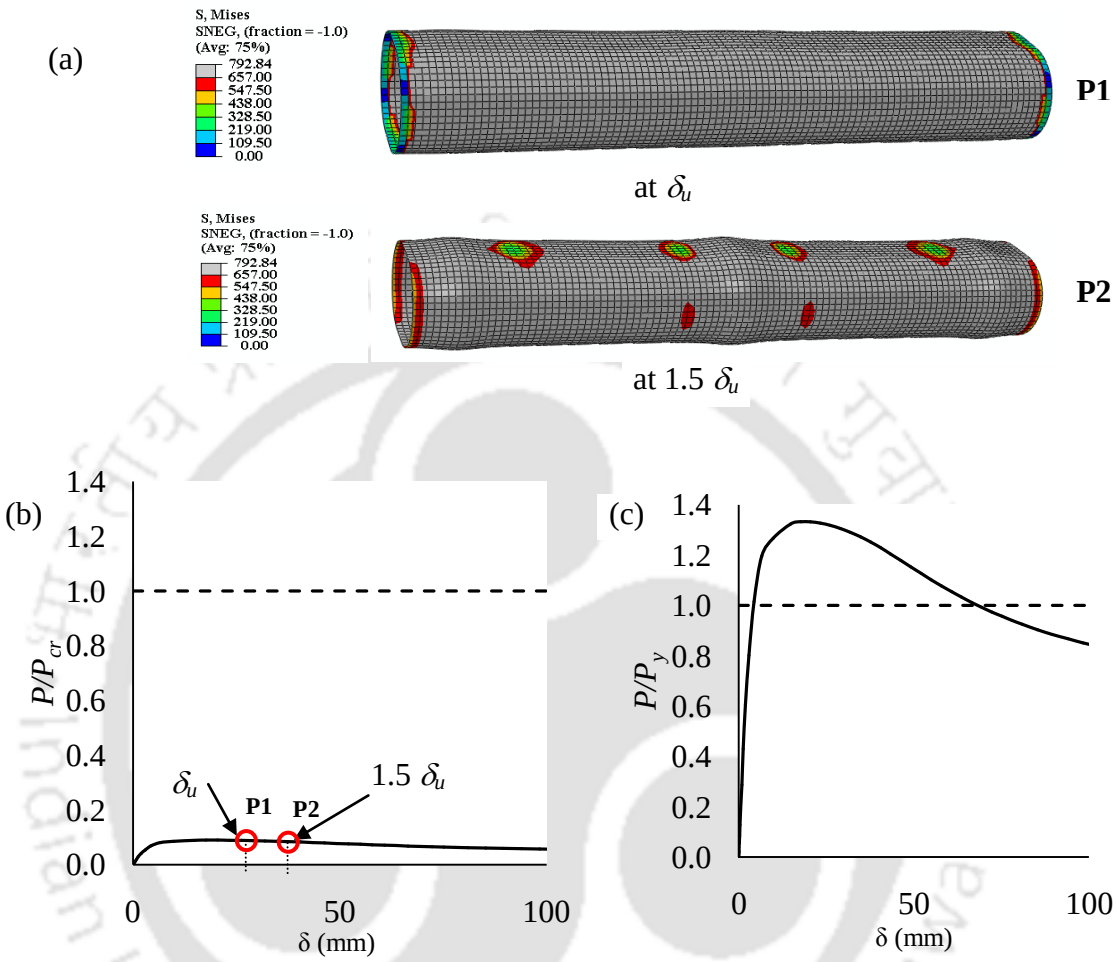

Figure 4.14: Typical Mechanism ST1 (yielding to yielding buckling) failure mode: a) von-Misses contour plot of P1 (at δ_u) and P2 (at 1.5δ_u); b) variation of P/P_{cr} with δ (axial deformation) and c) variation of P/P_y with δ (l50w150r75t15h1000).

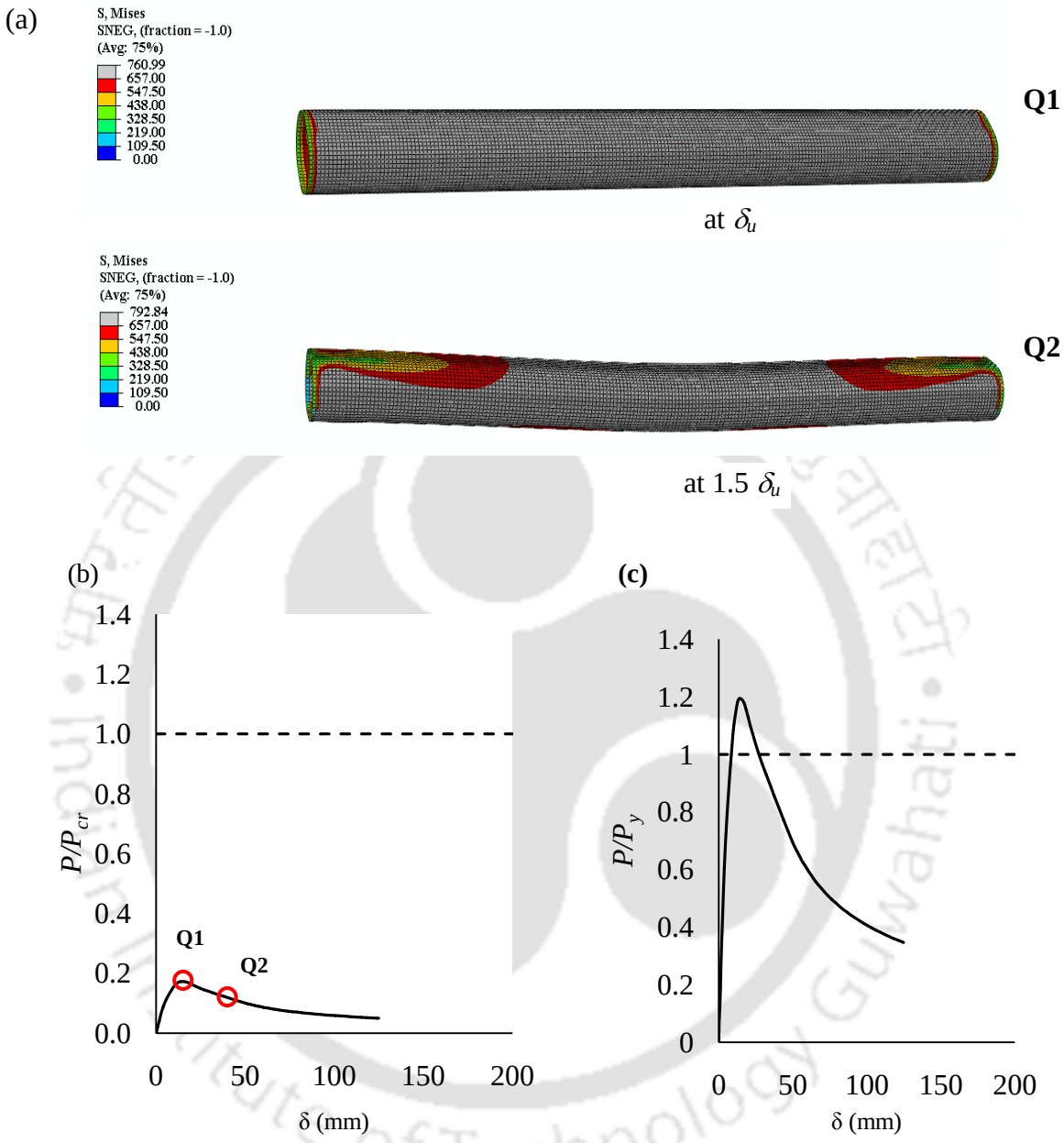

Figure 4.15: Typical Mechanism ST2 (yielding to flexural buckling) failure mode: a) von-Misses contour plot of Q1 (at δ_u) and Q2 (at 1.5δ_u); b) variation of P/P_{cr} with δ (axial deformation), and c) variation of P/P_y with δ (l50w150r75t15h2000).

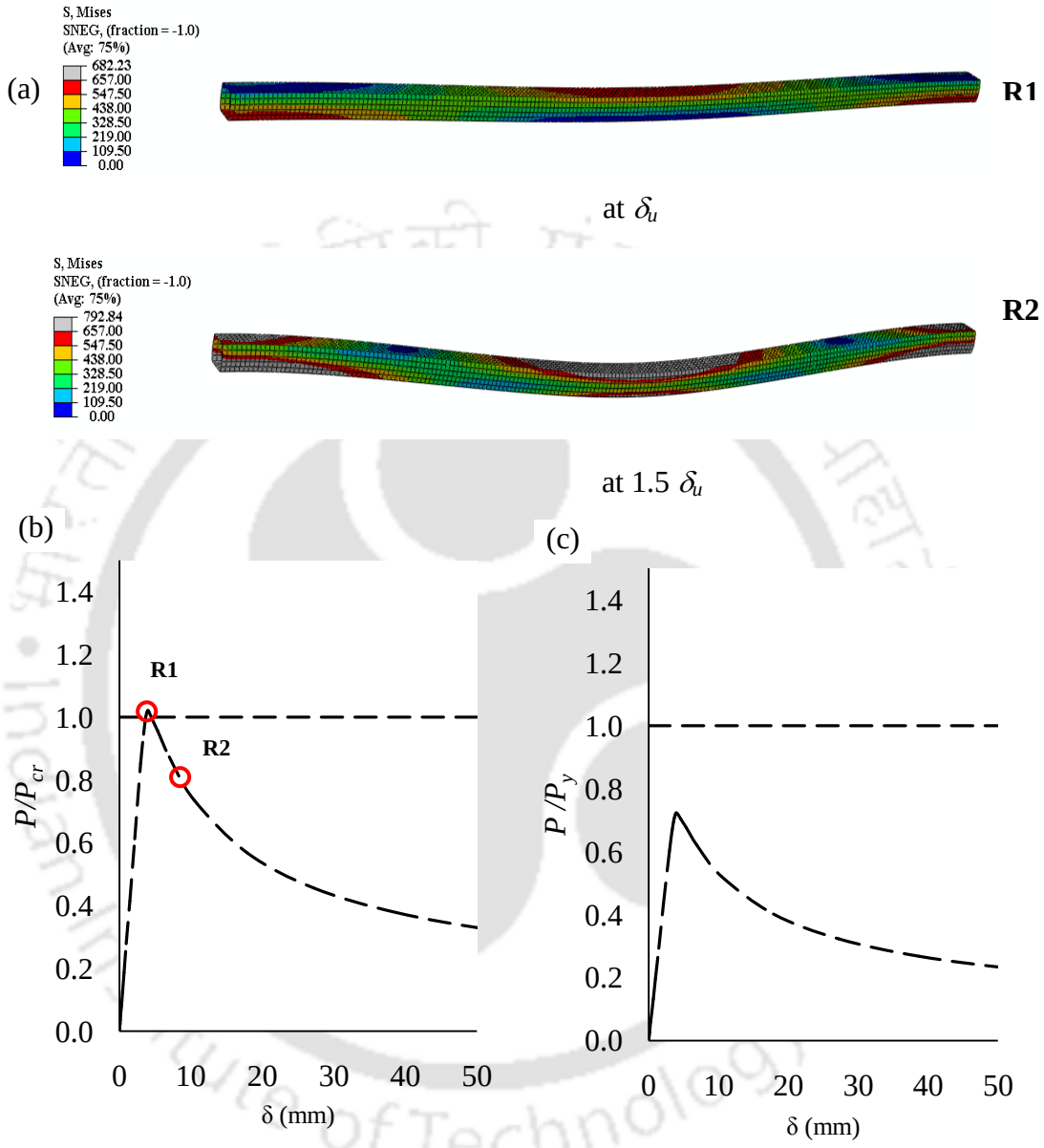

Figure 4.16: Typical Mechanism ST3 (flexural to flexural buckling) failure mode: a) von-Misses contour plot of R1 (at δ_u) and R2 (at 1.5 δ_u); b) variation of P/P_{cr} with δ (axial deformation), and c) variation of P/P_y with δ (l50w50r75t15h2000).

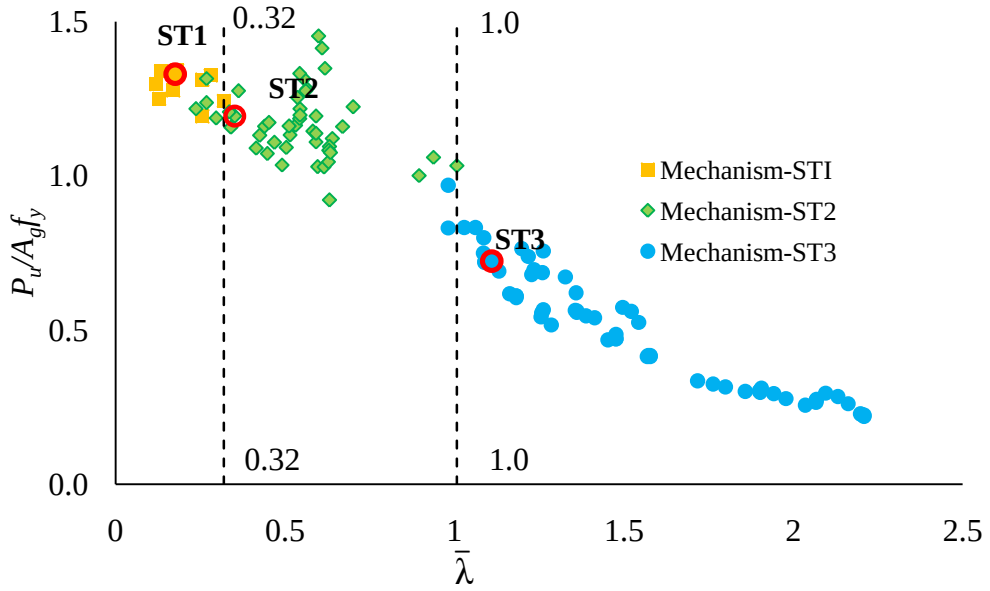

Figure 4.17: Variation of P_u/A_gf_y with $\bar{\lambda}$ showing Mechanisms ST1, ST2 and ST3 regions with t = 10-20 mm.

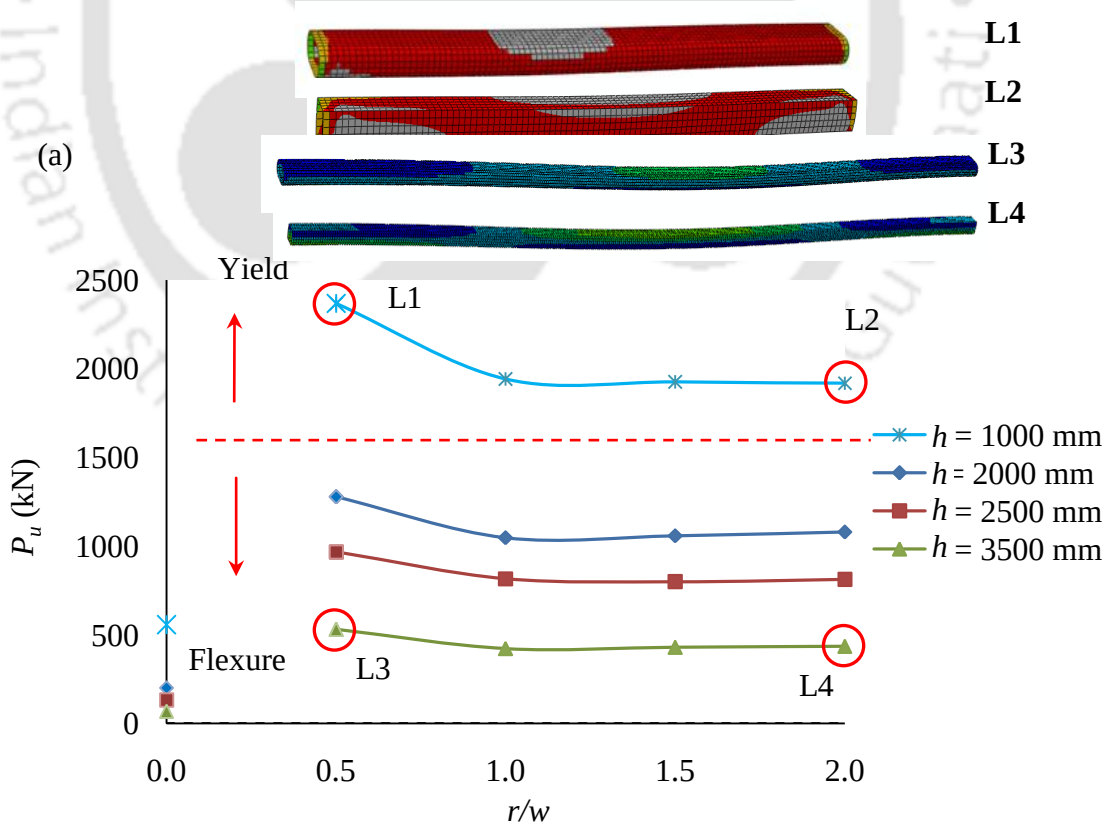

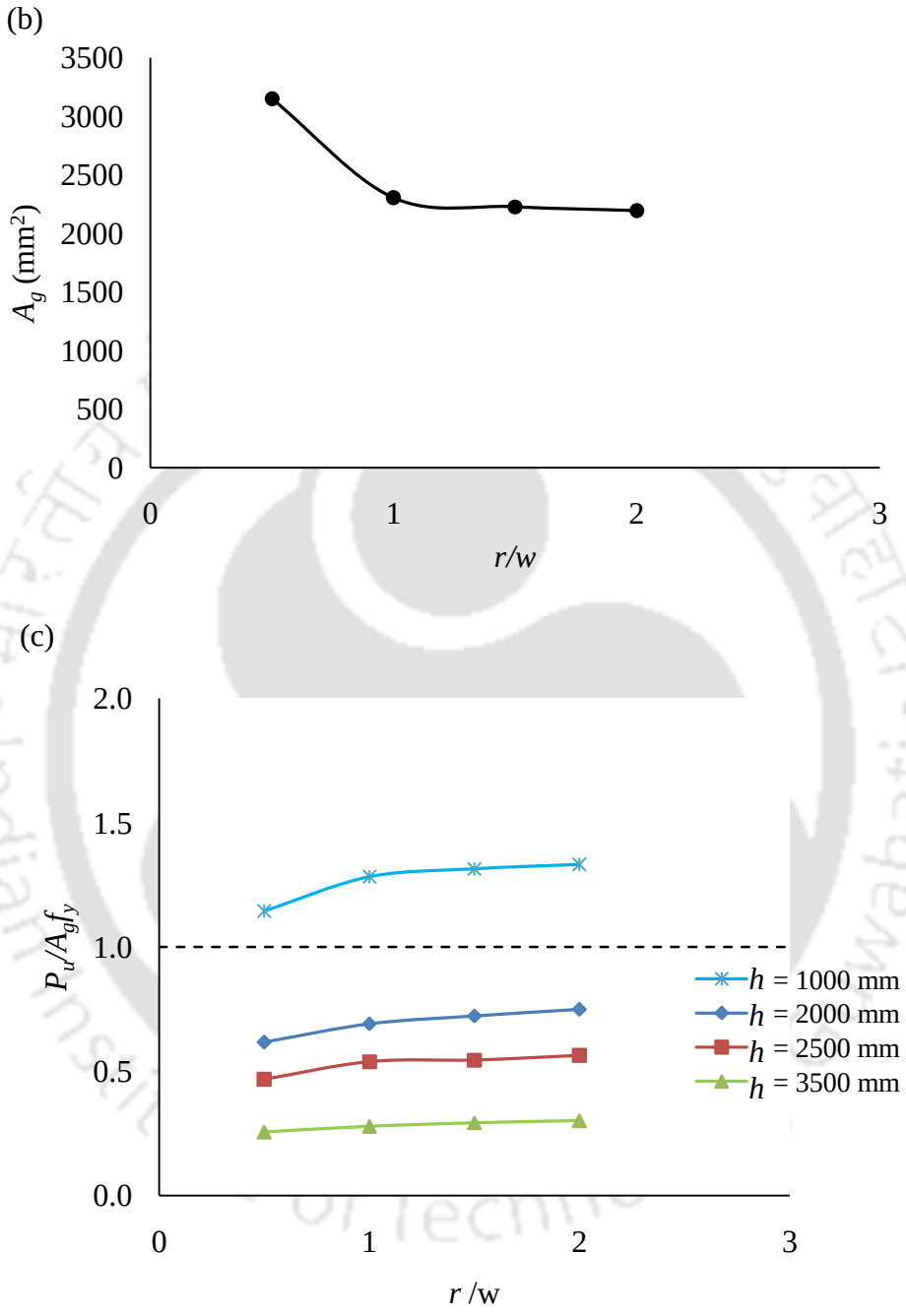

Figure 4.18: Variation of (a) P_u vs r/w, (b) A_g vs r/w and (c) P_u/A_gf_y vs r/w (l_f = 50 mm, w = 50 mm, t = 15 mm, r = 25 – 100 mm).

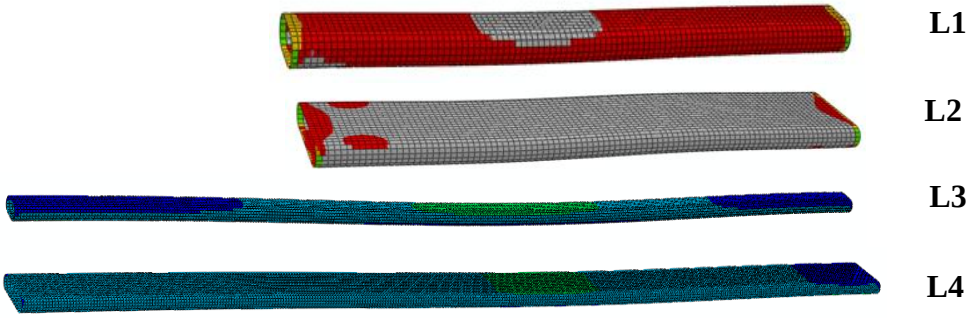

(a)

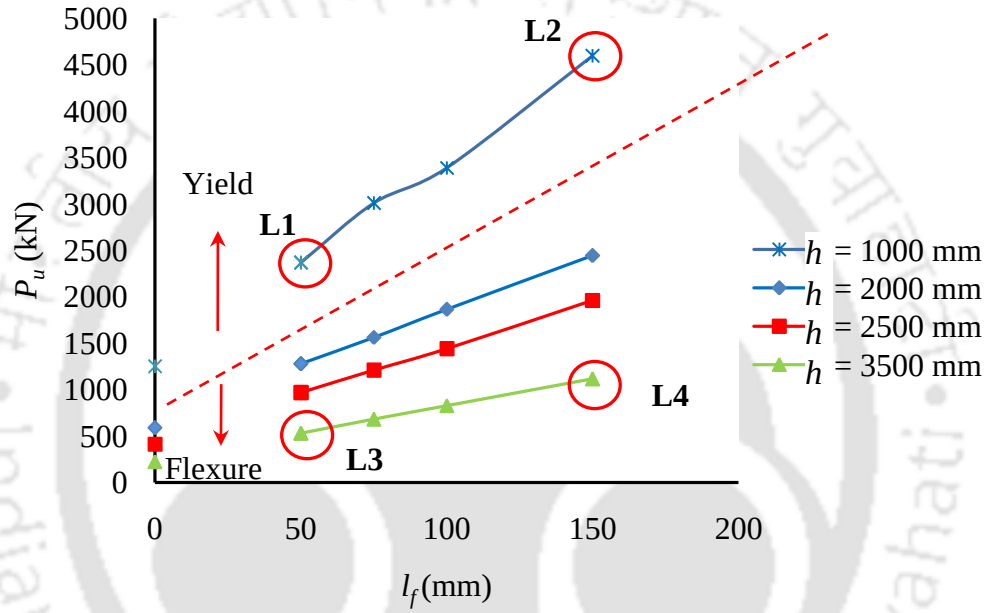

(b)

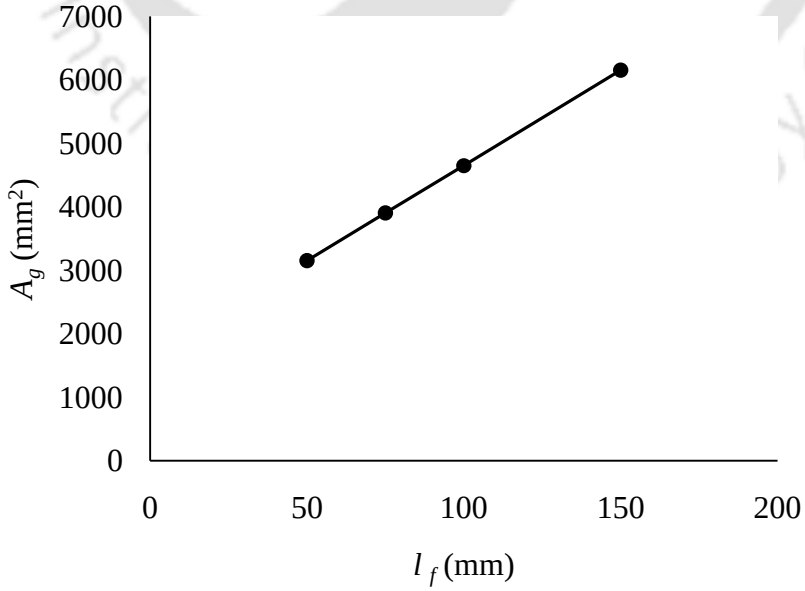

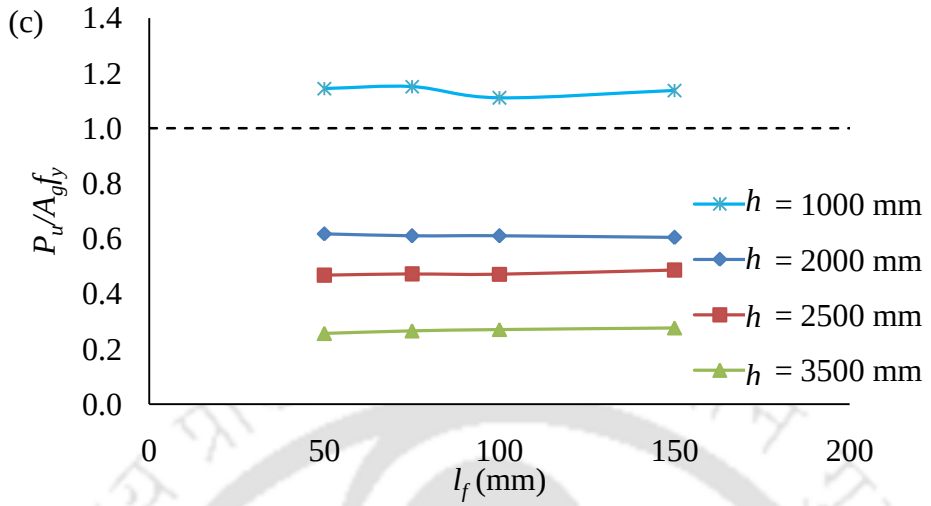

Figure 4.19: Variation of (a) P_u vs l_f, (b) A_e vs l_f and (b) $P_u/A_g f_y$ vs l_f (w = 50 mm, r = 25 mm, t = 15 mm, l_f = 50 – 150 mm).

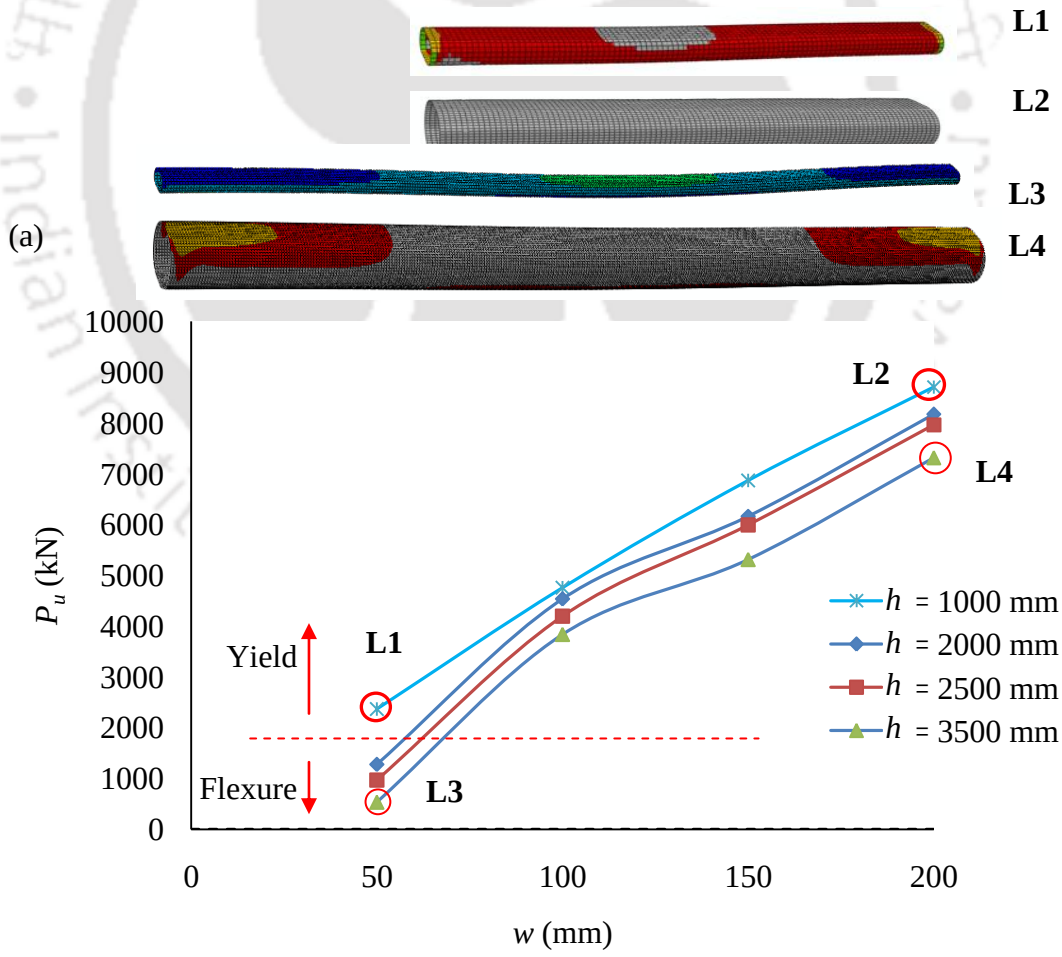

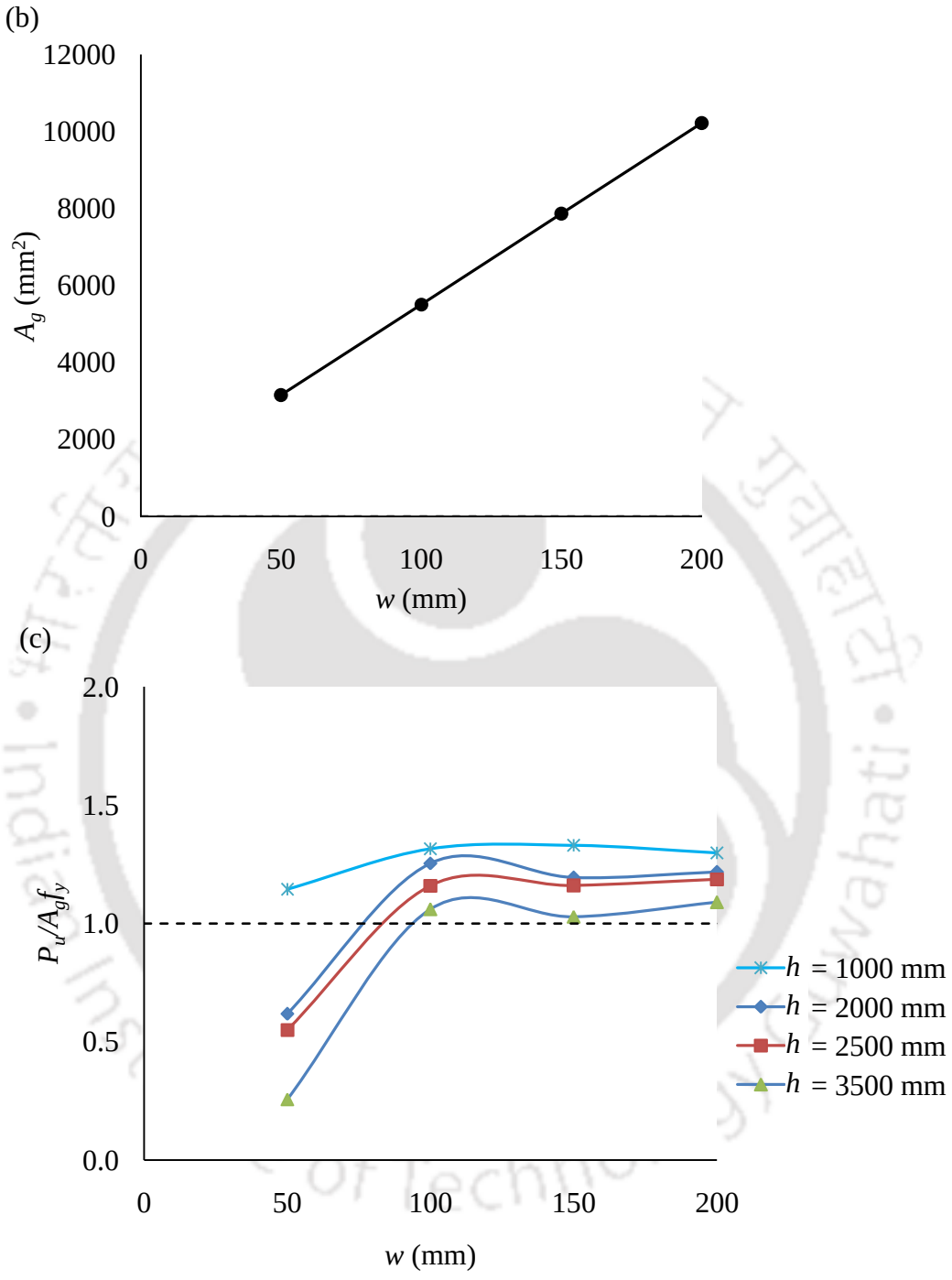

Figure 4.20: Variation of (a) P_u vs w, (b) A_g vs w and (b) P_u/A_gf_y vs w (l_f = 50 mm, w/r = 2, t = 15 mm, w = 50 – 200 mm).

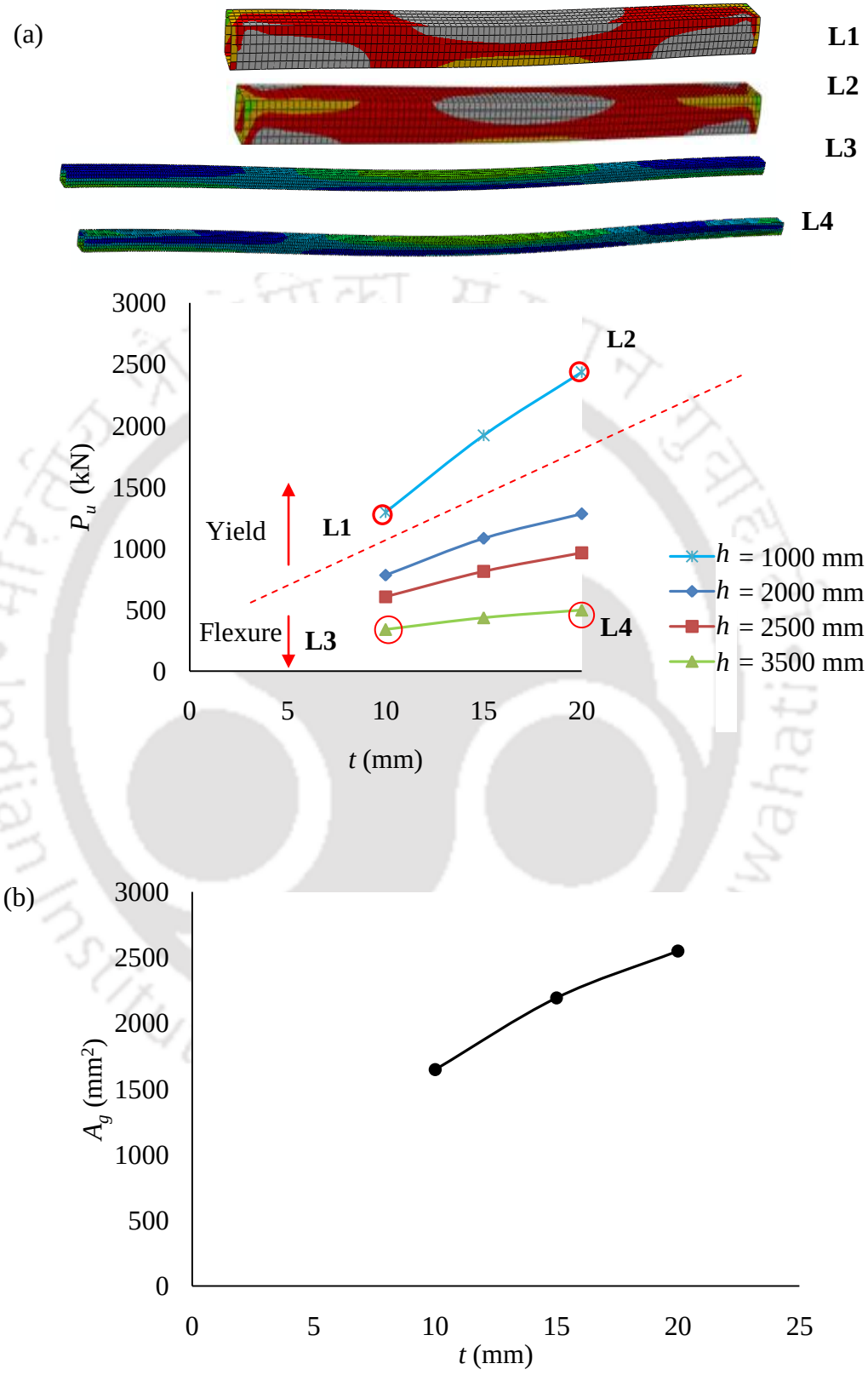

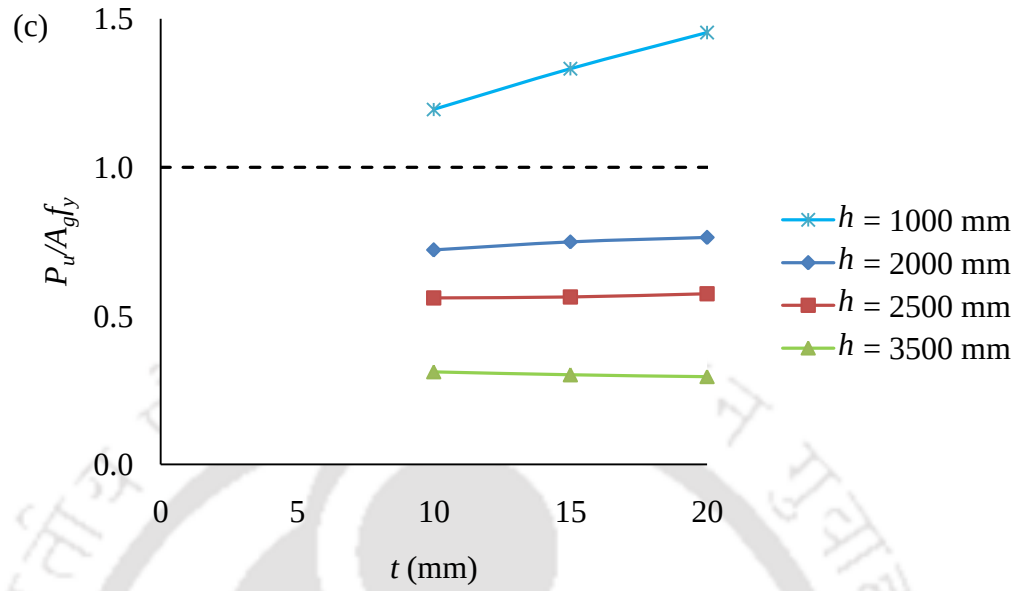

Figure 4.21: Variation of (a) P_u vs t , (b) A_g vs t and (b) P_u/A_gf_y vs t (l_f = 50 mm, w = 50 mm, r = 100 mm).

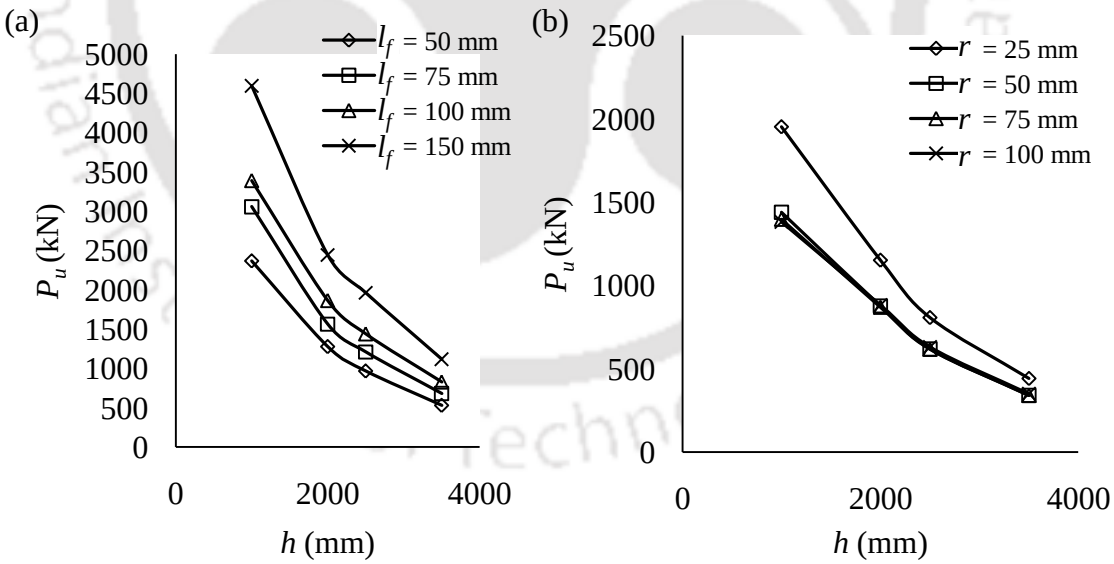

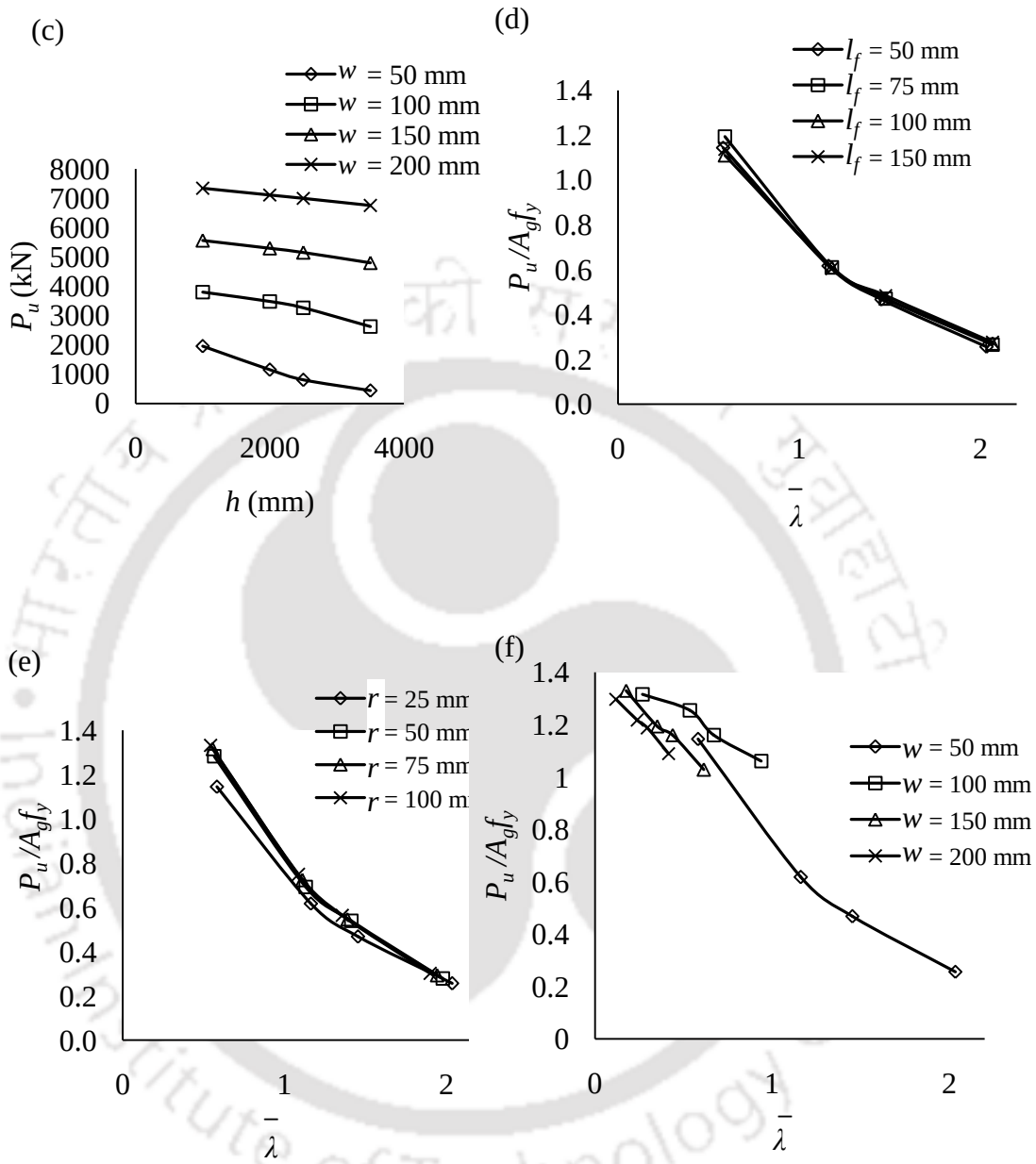

Figure 4.22: P_u vs h (a,b,c) and P_u/A_gf_y vs $\bar{\lambda}$ (d,e,f) at t = 15 mm for w = 50 mm, r = 25 mm, l_f = 50-150 mm (a,d); l_f = 50 mm, w = 50 mm, r = 25-100 mm (b,e); l_f = 50 mm, r/w = 0.2, w = 50 – 200 mm (c,f).

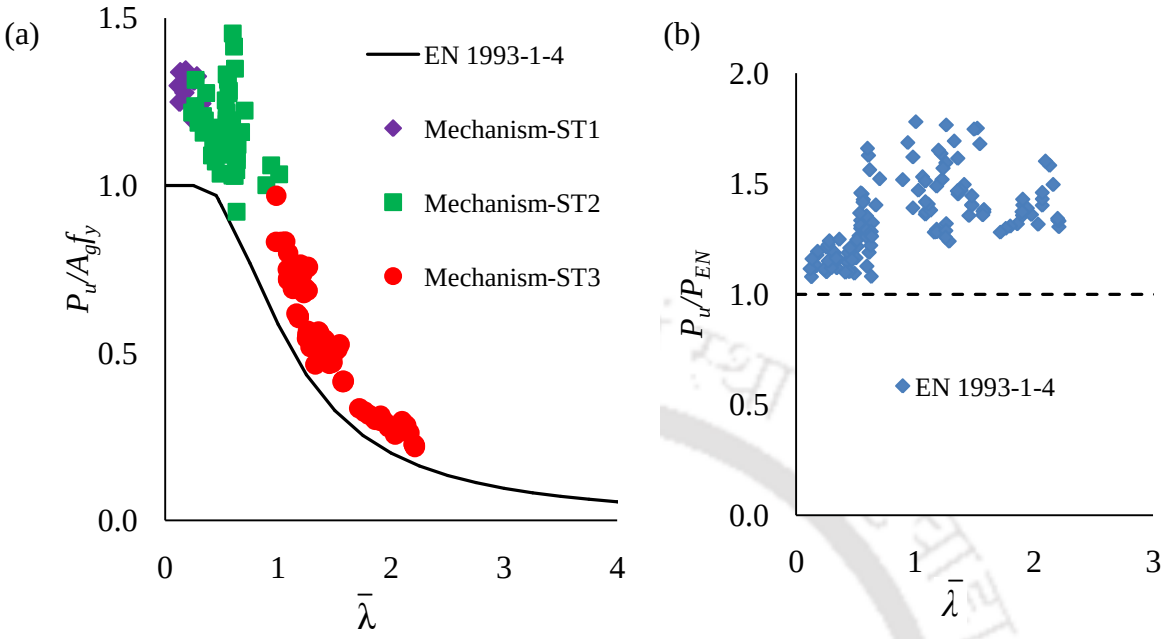

Figure 4.23: Comparison of EN 1993-1-4 (2015) and FE results for t = 10-20 mm.

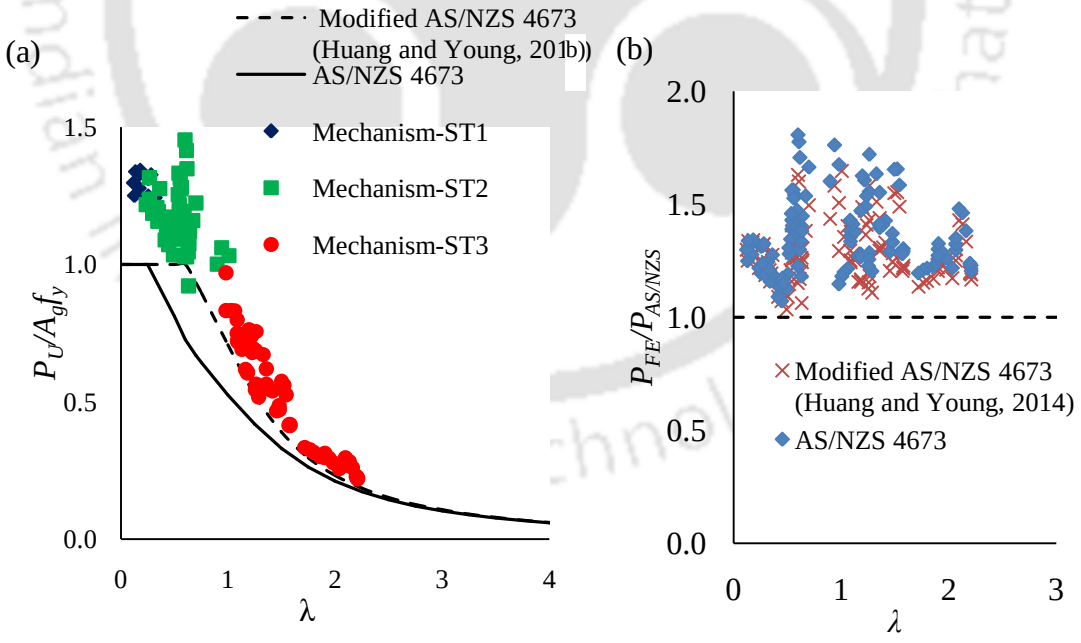

Figure 4.24: Comparison of AS/NZS 4673, modified AS/NZS 4673 (Huang and Young, 2014b) and FE results for t = 10-20 mm.

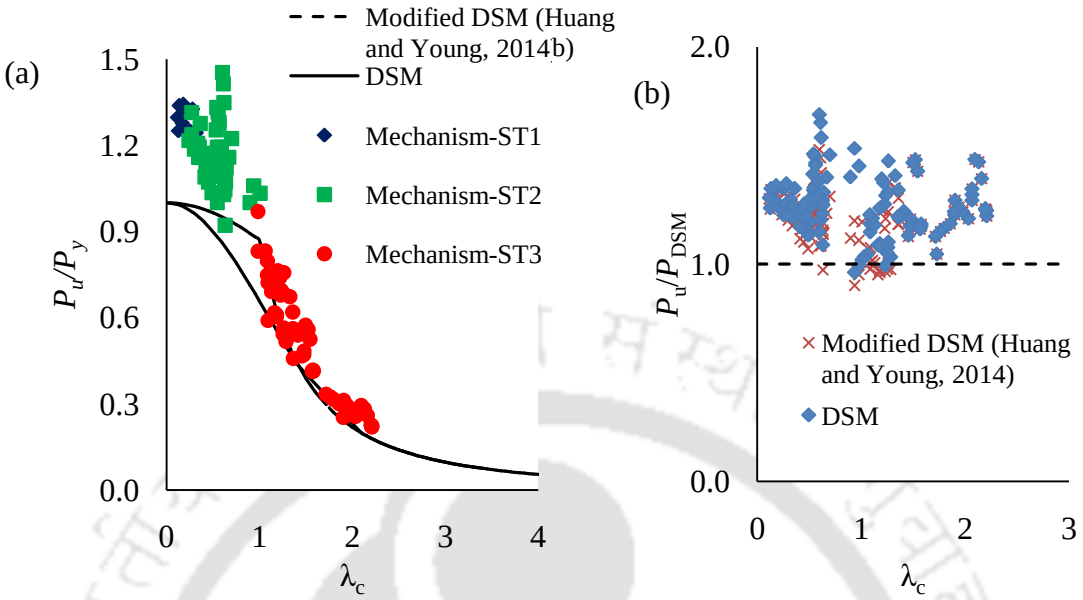

Figure 4.25: Comparison of DSM, modified DSM (Huang and Young, 2014b) and FE results for t = 10- 20 mm.

CHAPTER 5

NUMERICAL STUDY OF FIXED ENDED LDSS FLAT OVAL HOLLOW STUB COLUMNS WITH SQUARE PERFORATION UNDER PURE AXIAL COMPRESSION

5.1 INTRODUCTION

The numerical study of fixed ended flat oval LDSS stub columns under axial compression, presented in Chapter 3, has been extended in this chapter, by considering square perforations. As mentioned in the literature review (Chapter 2), very often it become inevitable to provide cut-outs / opening or perforations in structural steel members, in order to facilitate inspection, piping, wiring, ducts etc (e.g. Yu and Davis, 1971; Davis, 1972, Pennington, 1971; Yu, 2000; Ortiz-Colberg, 1981; Shanmugan, 1997; Han *et al.*, 2006; Shariati and Rokhi, 2008; Umbarkar *et al*., 2013; Kulatunga and Macdonald, 2013). Previous work were seen concentrate mainly on plates (e.g. Pennington, 1971; Vann, 1971; Narayanan and Chow, 1984), stiffened plates (Yu and Davis, 1971), circular column (e.g. Jullien and Liman, 1998; Murakami *et al*., 1998; Yeh *et al*., 1999; Han *et al*. (2006)) , etc.; perforated

with circular (e.g. Yu and Davis, 1971; Sivakumaran, and Abdel-Rahman, 1998; Umbarkar *et al.*,2013), square (e.g. Sivakumaran, and Abdel-Rahman, 1998; Han *et al*., 2006), elliptical perforations (e.g. Shariati and Rokhi, 2008, 2010), etc. To the best of author's knowledge, only Umbarkar *et al*., (2013), attempted to study the effect on LDSS circular hollow stub columns with circular perforation using FE analyses. Hence, in this work, a parametric study has been carried out to investigate the effects of square perforation with regard to size and location (i.e. along transverse and longitudinal directions, on both the flat and curve elements) on the structural behaviour (load capacity and deformation modes or shapes) of fixed ended flat oval LDSS stub hollow columns of stocky ($l_f/t\varepsilon \leq 37$ i.e. t = 15-20 mm) and slender ($l_f/t\varepsilon > 37$ i.e. t = 5-10 mm) cross-sections based on EN 1993-1-4 (2015).

As discussed in the literature review (Chapter 2), EN 1993-1-4 (2015) is not very specific on the design for perforated columns; whilst AISI provided some guidelines (AISI, 1996) for perforated plates, further, the design codes (EN 1993-1-4 (2015), AS/NZS 4673 (2001) and AISI (1996) are silent on the design of even unperforated hollow columns of combined flat and curve oval sections as mentioned in the preceding chapters (e.g. Zhu and Young, 2011; 2012). However, it may be mentioned that, ASDM (2002) provides guidelines for the design of unperforated combined flat and curved sections (through the consideration of effective areas of both flat and curve sections), although the design of flat-oval section is not exclusively detailed. For flat oval cross-section, the curve section has been considered as fully effective i.e. compact/stocky curve section for $w/t < 40$ and slender curve section for $w/t \geq 40$ (See Section 3.3.1 and Zhu and Young, 2012). It may be noted that, the original ASDM (2002) has been able to provide reliable predictions for stub columns of sections with $w/t < 40$ (Compact/ stocky curve section) ; however, it was found to be unreliable for sections with $w/t \geq 40$ (slender curve section) (see Chapter 3). Hence a new ASDM approach considering modified effective thickness of the curve elements has been proposed (referred to as $ASDM_{(p)}$

for sections with $w/t \geq 40$, in Chapter 3). Thus, the present FE analyses of perforated LDSS flat oval stub columns are compared with those predicted by ASDM (for sections with $w/t < 40$) and ASDM(p) (for sections with $w/t \geq 40$), with suitable modifications made further for perforations (here after referred to as the modified proposed $ASDM_m$ or $ASDM_{m(p)}$) in cross sectional area (to discuss later).

5.2 FINITE ELEMENT MODELLING

5.2.1 General

The FE modelling procedure adopted for the analyses of perforated fixed-ended stub hollow LDSS column, in this chapter, is similar to those detailed in Section 3.2, of the previous chapter. Similar material constitutive modelling, fixed-end boundary conditions, S4R shell elements, initial local geometric imperfection etc. as mentioned in Section 3.2 were adopted to model perforated columns. The key difference in the present FE modelling is the incorporation of square perforation in the FE modelling, which is highlighted in the following sub-section.

5.2.2 Geometry, boundary conditions and FE mesh

Typical geometry of the perforated LDSS hollow column is shown in Figure 5.1, along with the boundary conditions. In order to minimise the parameters, certain geometrical dimensions such as flat element length (l_f), radius of curve element (r), distance between flat elements (w) and height (h) were maintained fixed, at 300 mm, 150 mm, 300 mm and 900 mm respectively. Semi-circular curve elements were considered (r/w = 0.5). Two types of sections were analysed based on flat element : 1) stocky and 2) slender sections as per EN 1993-1-4 (2015) respectively. The size of square perforation (l_s = length of perforation side) were varied from 50-300 mm. The perforation positions were varied both on transverse and longitudinal directions i.e. five perforation locations along the transverse direction and three perforation along longitudinal direction (Positions T_1-T_5 transverse and L1-L3 longitudinal as indicated in Figure 5.2). Positions T_1 and T_5 are located at the mid of

the flat and curve elements respectively, while Positions T_2 and T_4 are located at $l_f/4$ and $l_c/4$ from mid of flat and curve elements respectively. Positions T_1 and T_5 are also referred in the thesis as *c-m* (i.e perforation located at mid of curve element or *curve-mid*) and *f-m* (i.e perforation located at mid of flat element or *flat-mid*) respectively. Position T_3 is located at the junction of the curve and flat elements. For the longitudinal perforation, three locations were considered *viz*., Positions L_1, L_2 and L_3. Positions L_1, L_2 and L_3 are located at $h/4$, $h/3$ and $h/2$ (or $h_p = h/4$, $h/3$, $h/2$; where h_p is the location of the perforation center measured from the nearest support end) respectively (Figure 5.2). As in Section 3.2, S4R shell elements with an aspect ratio of ~1 were used for the FE meshing of the columns. In order to capture the stress gradient in the vicinity of the square perforation, the mesh density around the perforation (for a size b x b; b/l_s = 1.6-2.0; see Figure 5.3-5.4) was made finer (mesh convergence study is presented in the following sub-section 5.2.3). Except for the zone surrounding the perforation where finer mesh is implemented, other areas of the column were meshed using S4R elements of size 8x8 – 10x10 mm, thus resulting in ~12,000-20,000 elements, depending on the perforation size. Like the case of unperforated stub columns, based on the lowest/first buckling mode shapes (see Figure 5.2), the geometry of the column was perturbed using an imperfection amplitude scaling factor of $t/100$, as reported in the literature (e.g. Theofanous and Gardner, 2009; Theofanous *et al.* 2009a; Chan and Gardner, 2008). Typical specimen nomenclature followed the pattern: flat length, distance between flat elements, radius of curve element, thickness, side length of the perforation; e.g. specimen $l300w300r150t5l_s50$ corresponds to l_f = 300 mm, w = 300 mm, r = 150 mm, t = 5 mm and l_s = 50 mm.

5.2.3 Mesh convergence study

As it is essential to provide sufficiently fine mesh around the perforation, for capturing the stress gradient (and hence the structural response) reasonably accurate, mesh convergence study was investigated. The results of the mesh

convergence study are presented in Figures 5.5 and 5.6 for perforation located at the curve element and flat element. The results are presented in the form of variation of critical elastic buckling stress (σ_{cr}) with number of elements along the perforation side/edge (N_e), and variation of load (P) with axial deformation (δ), for $l300w300r150t5l_s50$ specimen (i.e., b/l_s = 1.6, b represent the length of the outer mesh and l_s represent the square perforated length) . It can be seen from Figures 5.5 and 5.6 that reasonably stable values of both σ_{cr} and P have been obtained at N_e = 12. For $N_e \geq 12$, the change in σ_{cr} and P is not very significant. Further, a similar value of N_e has been found, for increasing zone size of fine mesh around the perforation e.g. b/l_s = ~2.0 (similar refinement zone size have also been reported in the literature (e.g. Moen and Schafer, 2009; Yao and Rasmussen, 2014). Hence, for all the subsequent analyses, the number of elements along the perforation side/edge is maintained ~12 with b/l_s = ~1.6-2. It may also be mentioned that, such strict mesh sizing may not be possible when the perforation is located very close to the column edge.

5.3 PARAMETRIC STUDY OF LDSS FLAT OVAL PERFORATED STUB COLUMN

In the parametric study, the effect of size and location of square single perforation on the structural behaviour (e.g. load capacity, P_u and failure modes) of flat oval LDSS stub columns are assessed, for both stocky and slender column cross sections. In all ~200 FE models have been constructed based by varying parameters such as, t = 5-20 mm, l_s = 50-300 mm and perforation positions (T_1-T_5; L_1-L_3). The results of the study are presented in the form of load-axial deformation curve, P_u, and percentage reduction in load capacity, ψ_r (=(P_u– $P_{u(p)}$/P_u x 100%); where $P_{u(p)}$ is the value of P_u for perforated columns) etc.

5.4 COMPARISON WITH PROPOSED ASDM PREDICTIONS

As mentioned in Chapter 3 and Section 5.1, in contrast to design codes such as EN-1993-1-4, AS/NZS and AISI; ASDM (2002) has provision to consider strength assessment for sections which are made of combined curve and flat elements (through consideration of effective sections for both the curve and flat elements), and thus serves as an attractive candidate for assessing the strength of LDSS flat oval hollow columns. However, it has been observed in Chapter 3 (Section 3.3.1) that the prediction based on the original expression for A_e (*via* t_e; see Figure 3.5) with sections $w/t \geq 40$ in ASDM (2002) resulted in $\beta < 2.5$, for unperforated stub columns (see Table 3.6). Although the original ASDM (2002) approach was found to be valid for stocky curve sections (i.e. $w/t \leq 40$) (see Table 3.5), for slender curve sections, it was observed to be unreliable (i.e. $\beta < 2.5$). Hence, a modified version (*via* modified effective thickness, t_{ep}) of ASDM has been proposed (i.e. $P_{ASDM(p)}$) in Section 3.4.6, that resulted in improving the reliability (or $\beta > 2.5$) of prediction for slender sections. Hence, in this chapter, the FE results are compared with the original ASDM for stocky curve sections and modified ASDM for slender curve sections (see, Section 3.4.6) to check their applicability for perforated LDSS hollow stub columns. Again, it may be mentioned that ASDM (2002) was not primarily developed to assess structural strength for 'perforated' sections, hence, in this work, for comparison with the FE results, the strength predictions are made based on net cross-sectional area where 'perforated' cross-sectional area (i.e. A_p; expression of A_p follows) is subtracted from the effective area (A_e). Thus the member capacity as per modified ASDM (i.e. $P_{ASDMm(p)}$ for slender sections and P_{ASDMm} for stocky sections) are given by

$$P_{ASDMm} = f_y A_{e(p)} \text{ or } P_{ASDMm(p)} = f_y A_{e(p)} \tag{5.1}$$

where, $A_{e(p)}$ is the effective area of the perforated section (subscript p is indicative of perforated section), and is given by

$$A_{e(p)} = A_e - A_p \tag{5.2}$$

In the procedure adopted herein, it is inherently assumed that, the ineffective area (or neglected area; see Figure 3.5) is located in the middle of the flat or curve elements. The effective thickness of the curve portion is taken by using the modified effective thickness (t_{ep}) for section with $w/t \geq 40$ in $ASDM_{m(p)}$ and t_e (see Equation 3.11) for section with $w/t > 40$ in $ASDM_m$. Also, for centrally located perforations, it is assumed that if $l_s \leq l_{if}$, where l_{if} is the ineffective length in flat element member (and perforation is located in the flat element, no deduction (i.e. $A_p = 0$) in cross-sectional area due to perforation is made; however for $l_s > l_{if}$, $A_p = t(l_s - l_{if})$. Likewise, when the perforation is located centrally, in the curve element, $A_p = l_{sc}t_e$ for $l_{sc} \leq l_{ic}$ (where l_{ic} is the length of effective thickness portion of curve member, l_{sc} is the arc length of perforation with size l_s), and $A_p = (l_{sc} - l_{ic})t + l_{ic}t_e$ for $l_{sc} > l_{ic}$. Further, for perforation which are not located centrally in the flat or curve elements, corresponding appropriate deductions are suggested, consistent with the effective (or ineffective) area representation as shown in Figure 3.5. Reliability of the modified ASDM predictions has been computed using a similar method as outlined in Section 3.3.5, based on ASCE 8-02 (2002) and Zhu and Young (2011) by taking the resistance factor (Φ) of 0.85.

5.5 RESULTS AND DISCUSSION

The results of the FE analyses of single perforated flat oval LDSS hollow stub columns under axial compression are presented in sub sections 5.5.1-5.5.3. The effect of perforation size (l_s) and perforation position are presented in Section 5.5.1 and 5.5.3 respectively, whilst the effect of section thickness (t) is discussed in Section 5.5.2. The effect of perforation size is grouped into two parts on the basis of flat element viz., 1) slender and 2) stocky section based on EN 1993-1-4 (2015). The FE results for the slender and stocky sections pertains to typical thickness, t = 5 mm and t = 20 mm respectively. For both slender and stocky sections, the perforation size effect is presented for perforation located at the mid-height of

column (i.e. $h_p = h/2$, where h_p = location of the perforation along the longitudinal direction) and mid of curve (i.e. Position *c-m* or T_5) and flat (i.e. Position *f-m* or T_1) elements corresponding $h_p = h/2$. The effects of transverse and longitudinal variation of perforation location are presented in Sections 5.5.3.1 and 5.5.3.2 respectively.

5.5.1 Effect of square perforation size (l_s)

5.5.1.1 Slender section

a) Perforation at flat element

The effect of perforation size is presented for LDSS flat-oval hollow columns with centrally located (T_1, L_3; see Figure 5.2) square perforation on flat element face. In Figure 5.7, Figures 5.7a and 5.7b show the variation of P with δ and P/A_gf_y with δ, for l_s = 50, 150 and 300 mm, respectively. The FE result of corresponding unperforated column is also shown for comparison. In addition von-Mises contour plot corresponding to δ_u (i.e. deformation corresponding to P_u) and 1.5 δ_u (i.e. at post-P_u deformation) is also plotted (see Figure 5.7a). It can be seen from Figure 5.7a that, as the perforation size increases, P_u drops; an increase of l_s by 500% (from 50 mm) led to a fall of ~7.8% in P_u. In comparison to the unperforated case, a drop of ~ 12% can be seen in P_u for the column with l_s = 50 mm. In Figure 5.7b, it is seen that $P_u/A_gf_y < 1.0$, indicating that the sections are unable to reach the global yield load (i.e. A_gf_y), as expected of slender cross sections. At P_u, for the smallest perforation considered (i.e. l_s = 50 mm), yielded region (shown in grey colour) is observed to spread in the transverse direction from the perforation side towards the curve element, with significant relaxation/redistribution of stress on either side of the perforation, in the longitudinal direction of the flat element (see inset figure L3). This observation is in contrast to the case of unperforated case, wherein the stress around the centre of the flat element is seen to be relatively lower, and considerable portion of the flat element being yielded (see inset figure L1). This may be related

to the high stress concentration near the periphery (in the transverse direction) of the perforation. At the post-P_u, the yielded region is relatively reduced, with the stress in the curved element dropping below the yield stress (see inset figure L4). As the perforation size increases to 300 mm (= flat element width), similar behaviour is also seen (inset figure L5), although in comparison to the case of l_s = 50 mm, the stress in curve element is relatively reduced below yield stress, with relatively larger region (indicated by blue colour) of flat element showing lower stress. It may also be noted that, particularly for this case with l_s = 300 mm, at the mid height of the column, major portion of the compressive load is resisted by the curve element (as the flat element is devoid of any material). That may be the reason for lower P_u for larger values of perforation size.

b) Perforation at curve element

The effect of square perforation size, located centrally on the curve element is presented in the form of P vs δ and $P/A_g f_y$ vs δ along with von-Mises contour variation, for l_s = 50, 150 and 300 mm in Figure 5.8. Von-Mises contours are plotted both at δ_u and 1.5 δ_u as inset figures in Figure 5.8a. The results from unperforated column is also shown for comparison. It can be seen that the value P_u decreases with increase in perforation size, with a decrease of ~ 17% in P_u obtained for 500% increase in l_s. Hence, it is seen that increase of perforation size in curve element results in higher reduction of P_u as compared to that in flat elements (~ 7.8%; see Figure 5.7a), for similar increase in l_s. This may be because, in the case of unperforated column (see inset figure L1), at P_u, most of the curve surface have yielded in comparison to the flat surface, indicating that curve part resisted significant portion of the compressive load. When perforations are made in the curve part, the resistance capacity of perforated curve part in the total compressive load resistance is reduced, thereby decreasing P_u. In the inset figures L3 and L5, it can be readily seen that von-Mises stress is reduced, with most of the curve part being stress below yield stress. At the post-P_u, for the smallest perforation i.e. l_s =

50 mm (see inset figures L4), the failure mode consists of horizontal local buckling in the flat part at mid column height, with the yielded region confined in the central zone, but extending towards the perforation. For the largest perforation considered (i.e. l_s = 300 mm), the post-P_u failure mode involves formation of transverse local buckling near the junction of the flat and curve (near the perforation edge), with the spread of intermittent yielded region from the perforation edge towards the unperforated curve part. It may be noted that for the largest perforation (l_s = 300 mm), the portion of the curve part above and below the perforation behave like cantilevers. So when loaded, the build up stress in the cantilever portions are relatively lesser. Again, $P_u/A_g f_y$ < 1.0, as expected of slender sections (see Figure 5.8b).

5.5.1.2 Stocky section

a) Perforation at flat element

In Figure 5.9, the results of centrally located square perforation on the flat part of stocky section are shown. Figures 5.9a and 5.9b present variation of P with δ and $P/A_g f_y$ with δ, respectively, along with von-Mises contour variation, for l_s = 50, 150 and 300 mm. Plots for unperforated column are also shown for comparison. It can be seen from Figure 5.9a, for the stocky section considered herein, the whole column has been stressed beyond yield, P_u, with a small region being relaxed of von-Mises stress in the post-P_u (i.e. at 1.5 δ_u). Although, a decrease of ~ 17% in P_u has been observed, for 500% increase in l_s, there appears to have no significant effect on P_u and variation of P with δ, for the smallest perforation i.e. l_s of 50 mm, when compared with the unperforated column. This may be because, as the column is stocky enough, the influence of small perforation on load resistance is negligible. At P_u, both unperforated and perforated columns (with l_s = 50 mm) showed similar von-Mises stress distribution (see inset figures L1 and L3), indicating the minimal effect of the small perforation size. However, as l_s increases e.g. at 300 mm, significant portion of the perforated flat part radiating from the top and bottom

transverse edges of perforation, are now seen to be subjected to reduced stress levels, indicative of decreased load resistance; resulting in much lower P_u. Post-P_u von-Mises contour plot corresponding to axial deformation of 1.5 δ_u , suggest that the failure mode (see inset figures L4 and L6) is gross cross-section yielding along mid height region, followed by, local buckling along the transverse direction at column height, with slight stress relaxation in the region above and below the perforation. This observation also agrees with the observation of $P_u/A_g f_y \sim \geq 1.0$ for l_s = 50-300 mm (Figure 5.9b).

b) Perforation at curve element

The effect of centrally located square perforation at the curve portion of the flat oval column is shown in Figure 5.10, for l_s = 50, 150 and 300 mm, for stocky sections. Variation of P with δ and $P/A_g f_y$ with δ, are shown respectively in Figures 5.10a and 5.10b. From Figure 5.10a, it can be seen that as compared to the unperforated case, a reduction of ~ 4.3% in P_u can be seen for the column with the smallest perforation i.e. l_s = 50 mm. It may be noted that this is contrast to the case of perforation in flat portion, where almost no reduction has been seen, as discussed above. This is consistent with the reduction of stress (below σ_y) in the curve portion (see inset figure L3). With increase in perforation size, by 500% (from l_s = 50 mm), a drop of ~ 37% in P_u is observed. Again, the drop in P_u is much higher in this case, as compared to the case of perforation in flat portion (see Figure 5.9). This may be because, even though the section is stocky, curve section has relatively enhanced load resistance capability (due to their curve geometry) and hence, has more contribution to the total load resistance, and thus, any removal of material from the curve portion, is likely to have more impact on the overall load resistance. The failure mode for l_s = 50 mm, is seen to be yielding followed by transverse local buckling at mid column height (inset figures L3 and L4). When the perforation gets larger (e.g. l_s = 300 mm), at P_u, a significant drop in stress in the perforated curve portion can be seen, with major portion of the load being resisted by the

unperforated curve and a trapezoidal portion of the flat portions (indicated by the yielded region; see inset figure L5). At Post-P_u, a slight relaxation of stress at mid height transverse direction can be seen, subsequent to initiation of location buckling at P_u. Again, $P_u/A_gf_y \sim \geq 1.0$ for l_s = 50-150 mm (Figure 5.10b), however $P_u/A_gf_y \sim$ 0.6 for l_s = 300 mm, agreeing with the large reduction in load capacity for l_s = 300 mm. Thus, it is seen that, presence of relatively large perforation in the curve portions have more load reduction effect as compared to the case of perforation in flat panels, for both slender and stocky sections (see Figures 5.9 and 5.10)

The effect of square perforation size (l_s) on P_u, for thicknesses ranging from t = 5-20 mm are presented in Figures 5.11a and 5.11b for perforations located in flat and curve portions respectively. For the perforation located in flat portion (Figure 5.11a), it can be observed that there appears to have near linear reduction in P_u with l_s. The reduction is found to be higher (~ 17.2%) for the stockier cross-section considered (i.e. t = 20 mm), whilst it is ~ 7.8% for the slender cross-section i.e. t = 5 mm; for 500% increase in l_s from 50 mm. This may be because, for the thin cross-section (t = 5 mm), the contribution of the flat plate on the load carrying capacity is relatively much lower (as can be observed in the inset figure L1; with a small portion of the flat portion being yielded), as compared to the thicker section (see inset figure L2). Hence, an increase in perforation size to 300 mm produced much higher drop in P_u, for the thickest section, as compared to that of the thinnest section. This agrees with the significant reduction in stress below the yield stress for a large part of the flat portion for t = 20 mm (see inset figures L4 vis-a-vis L2). When the perforation is located at the curve element (Figure 5.11b), the reduction in P_u with l_s (for 500% increase in l_s from 50 mm) found to be near linear with a reduction in P_u of ~17.1%, for the thinnest section considered, however, for the thicker sections (e.g. $t \geq 10$ mm), the near-linearity appears to exist till l_s = 250 mm (or ~ 83% of w); for $l_s \geq 250$ mm, there appears to be a slight increase (suggested by the increase in slope) in reduction of P_u. For instance, in the case for t = 20 mm, for l_s = 50-250 mm, the decrease is seen to be ~ 22.7%; whereas for l_s = 50-300

mm, it is ~ 37.4%. This behaviour may be because, when the size of perforation increases enough to get closer to the width between flat plates (i.e. w) e.g. say $l_s \geq$ ~80 % of w (in this study), the contribution of the perforated curve portion on the load resistance appears to have degraded rapidly; and when such a scenario happens, major portion of the load resistance would be borne by the flat elements that are not as efficient as the curve elements. For the thinnest section (t = 5 mm), such transition in the behaviour of P_u (e.g. at l_s = 80%w), is absent, apparently owing to gradual loss in the load resistance (or stiffness) of the perforated curve portion, as a result of relatively smaller thickness.

The effect of perforation size is further presented in Figure 5.12. In Figures 5.12a and 5.12b, variation of ψ_r (=(P_u-P_{up})/P_u x100 %) vs l_s are plotted for perforation located at the flat and curve element portions respectively (where P_u and P_{up} are the ultimate loads of the unperforated and perforated columns respectively). Thus, ψ_r represents a measure of the reduction in the ultimate load due to as compared to the unperforated case.

In the case of perforations located at flat element (Figure 5.12a), a near-linear increase in ψ_r with l_s is seen for t = 10-20 mm. However, for t = 5 mm (i.e. the thinnest section), ψ_r is found to be relatively higher as compared to those of t = 10-20 mm, and remains near constant (ψ_r = ~ 12%) for l_s = 50-200 mm; after which it increases in a linear manner, and merges with the behaviour shown by columns with t = 10-20 mm for $l_s \geq$ 250 mm. Thus, it indicates that the percentage drop in ultimate load (when compared to unperforated sections) due to perforation, remains relatively unaffected for $l_s \leq$ ~80% of l_f, when the section is slender (i.e. for t = 5 mm). This may be because, when the perforation size is relatively smaller and a major portion (or all) of the perforation may lie within the (central) ineffective portion of flat element (the ineffective region is estimated to be about ~60% of l_f, for t = 5 mm), and hence its contribution on the load capacity may not be that

significant. However, as the perforation size gets larger, effective region would get affected by the perforation, leading to drop in load capacity.

From Figure 5.12b, there is a near-linear variation of ψ_r with l_s, for perforation located at the curve element. It may be seen that variation of ψ_r are similar on an average, for t = 10-20 mm i.e. for the thicker sections, however the values of ψ_r are found to be distinctly (and parallel) higher for the thinnest sections considered (i.e. for t = 5 mm). Thus, indicating that the reduction in ultimate load (with respect to unperforated case) is relatively much more pronounce for slender section (e.g. t = 5 mm, in this case) and the curve sections are shown to be effective for all thickness i.e. both thin (t = 5 mm) and thick (t = 10-20 mm) sections.

5.5.2 Effect of thickness (*t*)

The effect of thickness (t) on P_u, for perforations located at flat and curve elements are presented in Figures 5.13a and 5.13b, respectively, for various normalised perforation sizes i.e. l_s/l_f = 0.16-1.0 and l_s/w = 0.16-1.0 (Note l_f = 300 mm, and w = 300 mm). It can be seen that, P_u increases with increasing t, and the rate of average increase being ~ 643% and ~567% for l_s/l_f = 0.16 and 1.0 respectively (see Figure 5.13a), ~ 620% and 633% for l_s/w = 0.16 and 1.0 respectively (see Figure 5.13b), for 300% increase in thickness (from t = 5 mm). Thus it can be observed that, in general, the rate of increase is relatively higher for the smallest perforation (i.e. l_s/l_f = 0.16) in the flat portion, however, in the case of perforation located in the curve portion, the rate of increase is found to be slightly higher when the perforation is largest i.e. at l_s/w = 1.0. Hence, it appears that, increasing thickness has relatively more beneficial effect for hollow columns perforated with smaller perforations in the flat element, whereas it is *vice versa* in the case of perforations located at the curve element. This may be because, for lower thicknesses (say t = 5 mm) when the perforation is located at the curve element, a relatively higher difference in P_u is observed when ls/w is varied from 0.16-1.00 (see figure 5.13b). However, for a

comparable change in perforation size, at lower thicknesses, for perforation located at the flat elements, a relatively closer values of P_u are seen (see figure 5.13a).

Variation of ψ_r vs t are plotted for perforation located at the flat and curved elements in Figure 5.14a and 5.14b respectively, for three perforation sizes *viz.*, l_s/w = 0.16, 0.50 and 1.0 . It is seen from Figure 5.14 that, ψ_r values increases with increasing perforation sizes for all the values of t; with relatively higher values (~+135% higher for l_s/w = 1.0) of ψ_r being associated for columns with perforation located at the curve element, as compared to those with perforation in the flat element. It is also observed that, in general, columns with the largest perforations (l_s/w = 1.0 and l_s/l_f = 1.0) appears to have relatively less influence (<~ 5% and 0.4% for columns with curve and flat perforations respectively) on ψ_r, to the variation in thickness. However, for the columns with smaller perforations (l_s/w = 0.50 and 0.16), such effect is seen for $t \geq$ ~10 mm; whereas, for $t <$ ~ 10 mm, an increase in ψ_r, can be observed for decreasing t. This may be because, although P_u increases with increasing t in a near linear fashion (see Figure 5.13) for the perforated columns, the rate of increase for unperforated columns is smaller for smaller thickness e.g. t < ~12 mm (see Figures 3.18b and 5.13).

5.5.3 Effect of perforation location

Effect of perforations located at flat and curve elements of LDSS flat oval hollow columns are presented in the following sub sections for variation of perforations along transverse (i.e. circumferentially) and longitudinally (i.e. axially) in Sections 5.5.3.1 and 5.5.3.2 respectively. The results are presented for two thicknesses *viz.*, t = 5 mm and 20 mm, thus representing slender (Class 4) and stocky (Class 1) sections respectively. Schematic locations of the perforations are shown in Figure 5.2 and also described in Section 5.2.2. The effect of perforation location is presented for the flat oval section with semi-circular (r/w = 0.5) curve elements.

5.5.3.1 Along transverse direction

Variation of P_u with circumferential perforation positions *viz*., T_1-T_3 are shown in Figure 5.15, for l_s = 50 mm (or l_s/w = 0.16) and 150 mm (or l_s/w = 0.5); with the perforations being located at mid-height of the columns, for a slender section (t = 5 mm). The corresponding plot of P_u for the perforated columns normalised with respect to the P_u corresponding to T5 location, ω_5 (= $P_u/P_{u(T5)}$ x 100%; $P_{u(T5)}$ is the P_u corresponding to T5 location or mid-center of the curve element) as presented in Figure 5.16. It can be seen from Figure 5.15 and 5.16 that, for the large perforation (i.e. l_s/w = 0.5), a drop (~ 8%) in P_u can be seen as the perforation location is changed from T_1 to T_3 (i.e. junction of flat and curve elements); but it remained without significant changes in the curve region (T_3-T_5). However, for the small perforation i.e. l_s/w = 0.16, the variation in P_u appears to be less significant. This may be because, as the curve element provides a stiffening effect, a relatively larger perforation size can significantly decrease the stiffening role, thus producing a decrease in P_u; however, away from T3 location, the variation in position may have little effect on the stress distribution (and hence P_u).

Similar plots for a stocky section (t = 20 mm) are shown in Figures 5.17 and 5.18. In comparison to the slender section (see Figures 5.15), in general, both the small and large perforations showed a mild drop (~2-6%) in P_u, as the perforations are located towards T_5 from T_1 (the drop in P_u ~ 6%, being slightly higher in the case of larger perforation). Again, this may be related to the decrease in sensitivity of the stocky sections to perforations, in comparison to slender section, as discussed in the preceding sections.

5.5.3.2 Along longitudinal direction

Effect of perforation location in the longitudinal direction is shown as variation of ψ_r (=(P_u-P_{up})/P_u x100 %) with $h_{(ph)}$ (= h_p/h x100%) in Figures 5.19a and 5.19b, for perforations located in the flat and curve elements respectively, for a slender section

(t = 5 mm). It can be seen from Figure 5.19a that, for perforations located in the flat element, there is no apparent change in ψ_r for perforation located near the support i.e. $0.25 \leq h_{(ph)} \leq 0.33$; however, an increase in ψ_r (i.e. an indication of larger drop in P_u with perforation) can be observed for $h_{(ph)} \geq 0.33$, for small to relatively large perforations (i.e. l_s/w = 0.16 and 0.5). But, for the largest perforation permissible (l_s/w = 1) in the flat element, an increase in ψ_r is seen for $h_{(ph)}$ = 0.25-0.33, after which it flattens. This may be because, when the perforation is located at mid height (or $h_{(ph)}$ = 0.5), local buckling can be seen to have initiated around mid height (with signs of stress relaxation on both the top and bottom of perforation) (see inset L2 and L4 in Figure 5.19a). On the other hand, von-Mises stress distribution remains more or less the same for $0.25 \leq h_{(ph)} \leq 0.33$ (for ls/l_f = 0.16 and 0.5), but for l_s/l_f = 1 (i.e. the largest perforation), significant change in the stress distribution can be observed when $h_{(ph)}$ is increased from 0.25 to 0.33. The stress distribution corresponding to $h_{(ph)}$ = 0.33 is now seen to be similar to that at 0.50, producing a flatten ψ_r. Again, the drop in ψ_r at lower $h_{(ph)}$, may also be related to the fixed support conditions at the column end, which resists plate buckling as compared to mid-height location.

In the case of perforations located at the curve element (for slender column), relatively higher rate of increase in ψ_r is seen for $0.25 \leq h_{(ph)} \leq 0.33$, with flattening effect seen for $h_{(ph)} \geq 0.33$, for all the perforation sizes. This may be because, from the inset figures L1-L4 in Figure 5.19b showing stress contours, it can be observed that as $h_{(ph)}$ is increased from 0.25 to 0.33, signs of increased in local buckling and stress relaxation area can be seen; the stress pattern at $h_{(ph)}$ = 0.33 remains more or less similar till $h_{(ph)}$ = 0.50.

Similar plots are also presented for a stocky section (t = 20 mm) in Figures 5.20a and 5.20b for perforations located at flat and curve elements respectively. In contrast to the observations made for slender columns (see Figure 5.19), ψ_r mildly decreases or remains near-flat for perforations located at flat or curve elements

respectively. Thus in the case of perforation at flat elements, ψ_r is relatively lowest when located at mid-height or $h_{(ph)}$ = 0.5. At $h_{(ph)}$ = 0.5, for the largest perforation, although initiation of buckling can now be seen at mid-height, relatively more region is now stressed beyond yield (see inset L4 in comparison to L3, in Figure 5.20a) and hence the drop in ψ_r. Such sign of mid-height buckling is not readily seen for the smallest perforation considered (see inset L2 in Figure 5.20a), although relaxation of stress can be seen near the support ends, for $h_{(ph)}$ = 0.5; then the drop in ψ_r could be due to strain hardening effect in stocky sections. In contrast, when the perforation is located in the curve element, there appears to have little effect on ψ_r, when $h_{(ph)}$ is changed from 0.25 to 0.50, although relatively a more visible sign of local buckling (see L4 in Figure 5.20b) or stress relaxation (see L2 in Figure 5.20b) can be observed at $h_{(ph)}$ = 0.5, as compared to that of $h_{(ph)}$ = 0.25. Again, this may be related to the straining hardening effect characteristic of stocky sections, counteracting the decreasing ψ_r effect expected of local buckling and/or stress relaxation.

5.5.4 Comparison with modified ASDM (i.e. $ASDM_{(P)}$ or $ASDM_{m(p)}$) for perforation

In this section, comparison of the proposed modified ASDM (or $ASDM_m$ or $ASDM_{m(p)}$) (for perforated column; see Section 5.4) and FE predictions are made for flat oval hollow columns. Thickness range from 5-20 mm has been chosen in order to generate normalised cross-sectional slenderness ($\overline{\lambda}_p$) from 0.5-1.8 (see Equation 3.4). Further, in the computation of $\overline{\lambda}_p$, full length of the flat element has been adopted for simplification, without consideration of the effect of perforation. As mentioned in Section 5.4, for perforations located centrally in the curve element, a proposed modified effective thickness (t_{ep}) is now considered. Based on trial and error *via* comparison of FE and ASDM predictions, a value of t_{ep} = 0.5 t_e is arrived (see Section 3.4.5; Equation 3.36). A schematic diagram for the consideration for effective and ineffective thicknesses (or areas) for perforated flat oval column

section is shown in Figure 5.21, for proposed modified ASDM (i.e. $ASDM_m$ for stocky curve section and $ASDM_{m(p)}$ for slender curve section). The comparison of modified ASDM and FE predictions with perforations located at T_5 (i.e. mid of curve element) and T_1 (i.e. mid of flat element), for various longitudinal positions i.e. L_1-L_3, thus considering 120 models, is shown in Table 5.1. It can be seen from Table 5.1 that, mean, COV and reliability index (β) for perforations located at the mid of curve element (Location T_5) are 1.04, 0.11 and 2.74 for $P_{FE}/P_{ASDM(p)}$ (or $P_{FE}/P_{ASDMm(p)}$) respectively; whereas for perforations located at the mid of flat element (Location L_1) are 1.11, 0.09 and 3.09 respectively. Thus, it can be seen that predictions made by modified ASDM are reliable (i.e. $\beta > 2.5$) for the perforation at T_1 and T_5. Further, Figures 5.22 and 5.23 show the comparison of FE and modified ASDM predictions of P_u, for l_s/l_f = 0.16-1.0, for perforations located in the flat (Location T_1) and curve element (i.e. Location T_5) centres respectively. Thus, it can be seen that the proposed approach of ASDM (or modified ASDM) is able to address the inclusion of single square perforation for the estimation of design capacity of single square perforated flat oval LDSS hollow stub columns.

5.6 CONCLUSIONS

A parametric investigation on the structural behaviour (load capacity and deformation modes or shapes) of fixed ended single square perforated LDSS flat oval hollow stub columns (of stocky and slender cross-sections) under axial compression has been presented using finite element analyses, to study the effects of single square perforation in relation to perforation size and location (i.e. along transverse and longitudinal directions, on both the flat and curve elements). Based on the parametric study, the following conclusions have been drawn:

1) For the perforation located in flat portion, it can be observed that there appears to have near linear reduction in ultimate load capacity (P_u) with perforation size (l_s). The reduction is found to be higher (~ 17.2%) for the stockier cross-section considered (i.e. t = 20 mm), whilst it is ~ 7.8% for the slender cross-section i.e. t = 5

mm; for 500% increase in l_s from 50 mm. However, when the perforation is located at the curve element the reduction in P_u with l_s (for similar increase in perforation size) is found to be near linear with a reduction in P_u of ~17.1%, for the most slender section considered (t = 5 mm), however, for the stockier sections (e.g. $t \geq$ 10 mm), the near-linearity appears to exist till l_s = 250 mm (or ~ 83% of w); for $l_s \geq$ 250 mm, there appears to be a slight increase in reduction of P_u.

2) The percentage drop in P_u (when compared to unperforated sections) or ψ_r , due to perforation, remains relatively unaffected for $l_s \leq$ ~80% of l_f, when the section is slender (i.e. for t = 5 mm), when the perforation is located at the flat element. However, when the perforation is located at the curve element, the reduction in P_u (with respect to unperforated case) is relatively much more pronounce for slender section (e.g. t = 5 mm, in this case) and the curve sections are shown to be effective for all both slender and stocky sections.

3) It can be observed that, in general, the rate of increase is relatively higher for the smallest perforation (i.e. l_s/l_f = 0.16) in the flat portion, however, in the case of perforation located in the curve portion, the rate of increase is found to be slightly higher when the perforation is largest i.e. at l_s/w = 1.0. Hence, it appears that, increasing thickness has relatively more beneficial effect for hollow columns perforated with smaller perforations in the flat element, whereas it is *vice versa* in the case of perforations located at the curve element.

4) The ψ_r values increases with increasing perforation sizes for all the values of t; with relatively higher values (~+135% higher for l_s/w = 1.0) of ψ_r being associated for columns with perforation located at the curve element, as compared to those with perforation in the flat element. It is also observed that, in general, columns with the largest perforations (l_s/w = 1.0 and l_s/l_f = 1.0) appears to have relatively less influence (<~ 5% and 0.4% for columns with curve and flat perforations respectively) on ψ_r, to the variation in thickness. However, for the columns with

smaller perforations (l_s/w = 0.50 and 0.16), such effect is seen for $t \geq$ ~10 mm; whereas, for $t <$ ~ 10 mm, an increase in ψ_r, can be observed for decreasing t.

5) In case of slender section (t = 5 mm), for the large perforation (i.e. l_s/w = 0.5), a drop (~ 8%) in P_u can be seen as the perforation location is changed from T_1 (mid of flat element) to T_3 (i.e. junction of flat and curve elements); but it remained without significant changes in the curve region (T_3-T_5) i.e T5 is (mid-curve element). However, for the small perforation i.e. l_s/w = 0.16, the variation in P_u appears to be less significant. However, in comparison to the slender section, for stocky sections, in general, both the small and large perforations showed a mild drop (~2-6%) in P_u, as the perforations are located towards T_5 from T_1 (the drop in P_u ~ 6%, being slightly higher in the case of larger perforation).

7) For the slender section (t = 5 mm), it can be seen that, for perforations located in the flat element, there is no apparent change in ψ_r for perforation located near the support i.e. $0.25 \leq h_{(ph)} \leq 0.33$; however, an increase in ψ_r (i.e. an indication of larger drop in P_u with perforation) can be observed for $h_{(ph)} \geq 0.33$, for small to relatively large perforations (i.e. l_s/w = 0.16 and 0.5). But, for the largest perforation permissible (l_s/w = 1) in the flat element, an increase in ψ_r is seen for $h_{(ph)}$ = 0.25-0.33, after which it flattens.

8) In the case of perforations located at the curve element (for slender column), relatively higher rate of increase in ψ_r is seen for $0.25 \leq h_{(ph)} \leq 0.33$, with flattening effect seen for $h_{(ph)} \geq 0.33$, for all the perforation sizes. However, in contrast to slender columns, for stocky sections, ψ_r mildly decreases or remains near-flat for perforations located at flat or curve elements respectively.

9) A design approach based on ASDM has been proposed (based on modified effective thickness) to address the inclusion of single square perforation for the estimation of design capacity of single square perforated flat oval LDSS hollow columns.

Table 5.1

Comparison between FE with modified ASDM (P_{ASDMm} or $P_{ASDMm(p)}$) results.

Model of PHCs	Position of perforation	P_{FE}/P_{ASDMm} or $P_{FE}/P_{ASDMm(P)}$	Position of perforation	P_{FE}/P_{ASDMm} or $P_{FE}/P_{ASDMm(P)}$
*l*300*w*300*r*150*t*5l_s50	T5L3	1.11	T1L3	1.08
*l*300*w*300*r*150*t*10 l_s50	T5L3	0.95	T1L3	0.95
*l*300*w*300*r*150*t*15 l_s50	T5L3	1.14	T1L3	1.13
*l*300*w*300*r*150*t*20 l_s50	T5L3	1.18	T1L3	1.22
*l*300*w*300*r*150*t*5 l_s100	T5L3	1.08	T1L3	1.07
*l*300*w*300*r*150*t*10 l_s100	T5L3	0.98	T1L3	0.97
*l*300*w*300*r*150*t*15 l_s100	T5L3	1.10	T1L3	1.15
*l*300*w*300*r*150*t*20 l_s100	T5L3	1.17	T1L3	1.23
*l*300*w*300*r*150*t*5 l_s150	T5L3	1.02	T1L3	1.06
*l*300*w*300*r*150*t*10 l_s150	T5L3	0.98	T1L3	0.97
*l*300*w*300*r*150*t*15 l_s150	T5L3	1.08	T1L3	1.13
*l*300*w*300*r*150*t*20 l_s150	T5L3	1.15	T1L3	1.22
*l*300*w*300*r*150*t*5 l_s250	T5L3	0.94	T1L3	1.20
*l*300*w*300*r*150*t*10 l_s250	T5L3	0.89	T1L3	0.98
*l*300*w*300*r*150*t*15 l_s250	T5L3	1.01	T1L3	1.12
*l*300*w*300*r*150*t*20 l_s250	T5L3	1.11	T1L3	1.22
*l*300*w*300*r*150*t*5 l_s300	T5L3	1.00	T1L3	1.21
*l*300*w*300*r*150*t*10 l_s300	T5L3	0.81	T1L3	0.97
*l*300*w*300*r*150*t*15 l_s300	T5L3	0.88	T1L3	1.12
*l*300*w*300*r*150*t*20 l_s300	T5L3	1.05	T1L3	1.22
*l*300*w*300*r*150*t*5l_s50	T5L2	1.36	T1L2	1.09

*l*300*w*300*r*150*t*10 l_s50	T5L2	0.96	T1L2	0.93
*l*300*w*300*r*150*t*15 l_s50	T5L2	1.13	T1L2	1.13
*l*300*w*300*r*150*t*20 l_s50	T5L2	1.19	T1L2	1.20
*l*300*w*300*r*150*t*5 l_s100	T5L2	1.13	T1L2	1.09
*l*300*w*300*r*150*t*10 l_s100	T5L2	0.97	T1L2	0.95
*l*300*w*300*r*150*t*15 l_s100	T5L2	1.10	T1L2	1.15
*l*300*w*300*r*150*t*20 l_s100	T5L2	1.16	T1L2	1.22
*l*300*w*300*r*150*t*5 l_s150	T5L2	1.02	T1L2	1.08
*l*300*w*300*r*150*t*10 l_s150	T5L2	0.98	T1L2	0.98
*l*300*w*300*r*150*t*15 l_s150	T5L2	1.08	T1L2	1.15
*l*300*w*300*r*150*t*20 l_s150	T5L2	1.15	T1L2	1.22
*l*300*w*300*r*150*t*5 l_s250	T5L2	0.94	T1L2	1.22
*l*300*w*300*r*150*t*10 l_s250	T5L2	0.81	T1L2	0.99
*l*300*w*300*r*150*t*15 l_s250	T5L2	1.00	T1L2	1.12
*l*300*w*300*r*150*t*20 l_s250	T5L2	1.10	T1L2	1.22
*l*300*w*300*r*150*t*5 l_s300	T5L2	0.99	T1L2	1.20
*l*300*w*300*r*150*t*10 l_s300	T5L2	0.81	T1L2	0.98
*l*300*w*300*r*150*t*15 l_s300	T5L2	0.89	T1L2	1.11
*l*300*w*300*r*150*t*20 l_s300	T5L2	1.05	T1L2	1.21
*l*300*w*300*r*150*t*5l_s50	T5L1	1.22	T1L1	1.10
*l*300*w*300*r*150*t*10 l_s50	T5L1	0.95	T1L1	0.93
*l*300*w*300*r*150*t*15 l_s50	T5L1	1.12	T1L1	1.13
*l*300*w*300*r*150*t*20 l_s50	T5L1	1.18	T1L1	1.21
*l*300*w*300*r*150*t*5 l_s100	T5L1	1.15	T1L1	1.10
*l*300*w*300*r*150*t*10 l_s100	T5L1	0.95	T1L1	0.96
*l*300*w*300*r*150*t*15 l_s100	T5L1	1.10	T1L1	1.15
*l*300*w*300*r*150*t*20 l_s100	T5L1	1.16	T1L1	1.22
*l*300*w*300*r*150*t*5 l_s150	T5L1	1.05	T1L1	1.08
*l*300*w*300*r*150*t*10 l_s150	T5L1	0.96	T1L1	0.99
*l*300*w*300*r*150*t*15 l_s150	T5L1	1.08	T1L1	1.15

*l*300*w*300*r*150*t*20 l_s150	T5L1	1.15	T1L1	1.21
*l*300*w*300*r*150*t*5 l_s250	T5L1	0.94	T1L1	1.22
*l*300*w*300*r*150*t*10 l_s250	T5L1	0.90	T1L1	1.04
*l*300*w*300*r*150*t*15 l_s250	T5L1	1.01	T1L1	1.13
*l*300*w*300*r*150*t*20 l_s250	T5L1	1.09	T1L1	1.21
*l*300*w*300*r*150*t*5 l_s300	T5L1	1.05	T1L1	1.24
*l*300*w*300*r*150*t*10 l_s300	T5L1	0.82	T1L1	0.99
*l*300*w*300*r*150*t*15 l_s300	T5L1	0.90	T1L1	1.12
*l*300*w*300*r*150*t*20 l_s300	T5L1	1.05	T1L1	1.21
Mean		1.04		1.11
COV		0.11		0.09
Reliability Index (β)		2.74		3.09

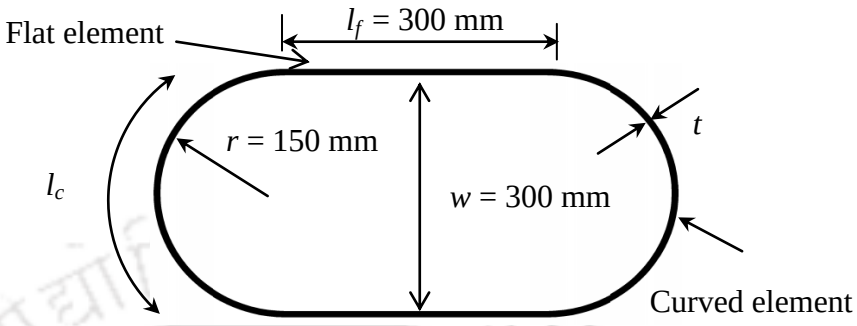

Figure 5.1: Flat oval hollow section.

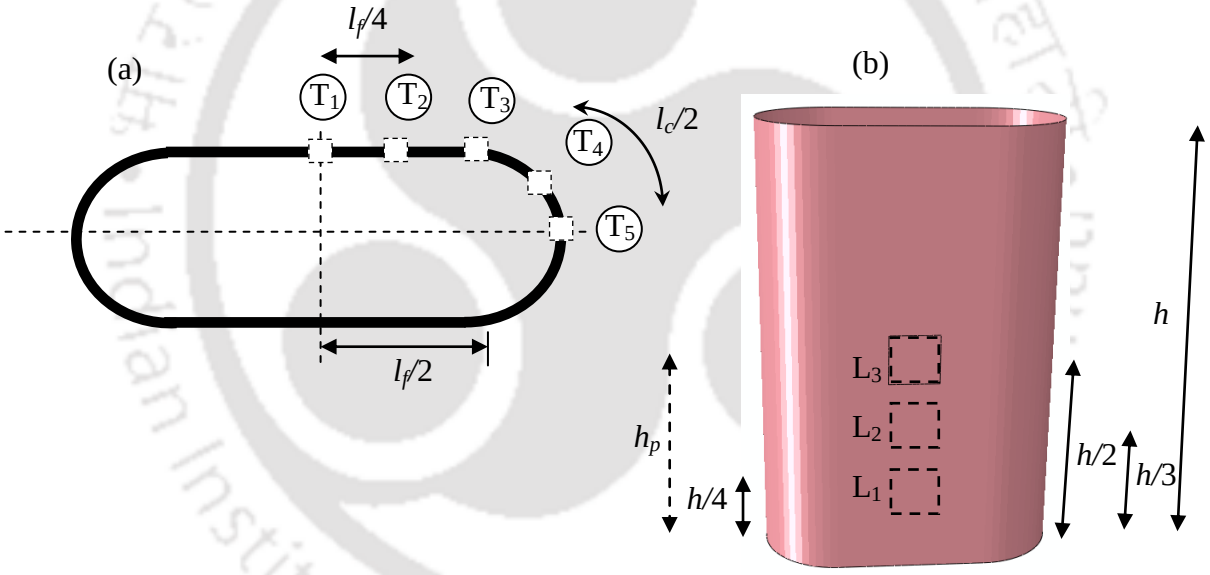

Figure 5.2: Locations of square perforation: a) transverse direction (T_1-T_5) and b) longitudinal direction (L_1-L_3).

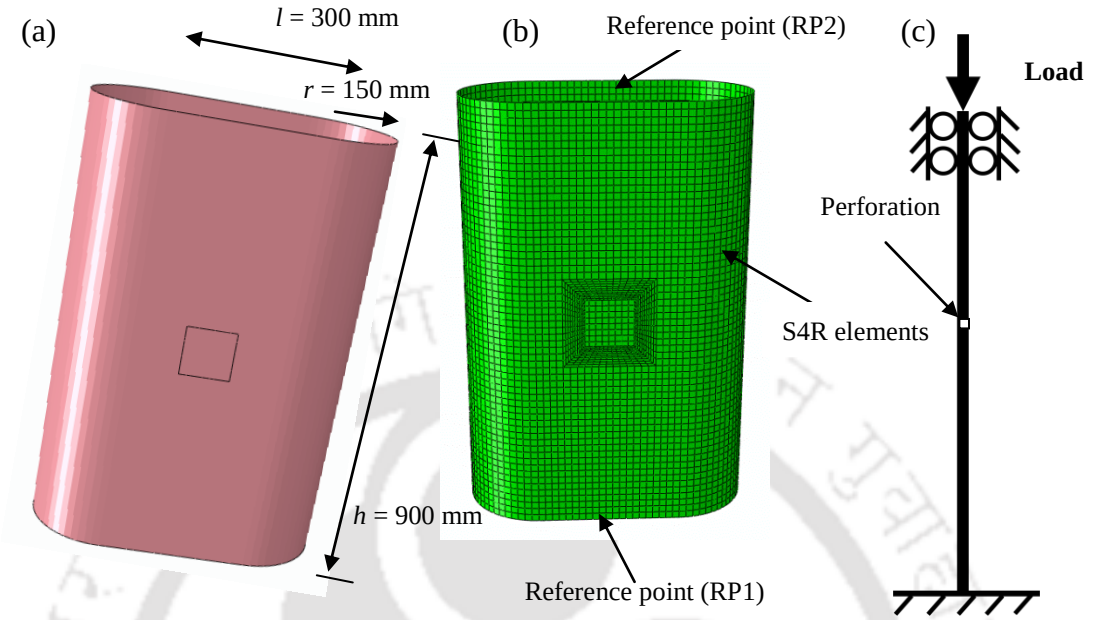

Figure 5.3: Typical FE (a) geometry, (b) FE mesh and (c) boundary conditions of LDSS perforated flat oval hollow column.

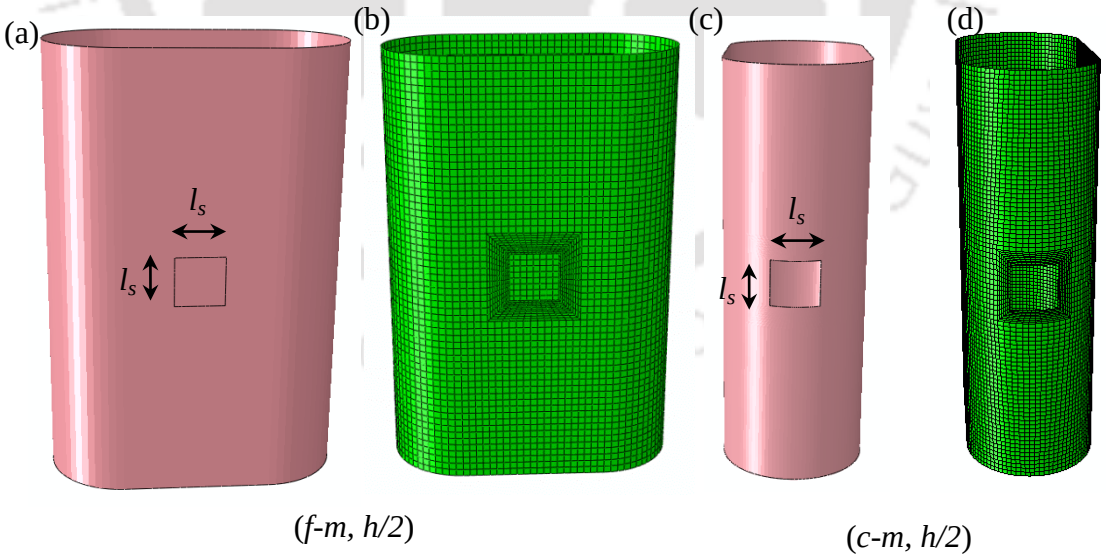

Figure 5.4: Typical location of perforation at the flat element (a, b) and curve element (c, d).

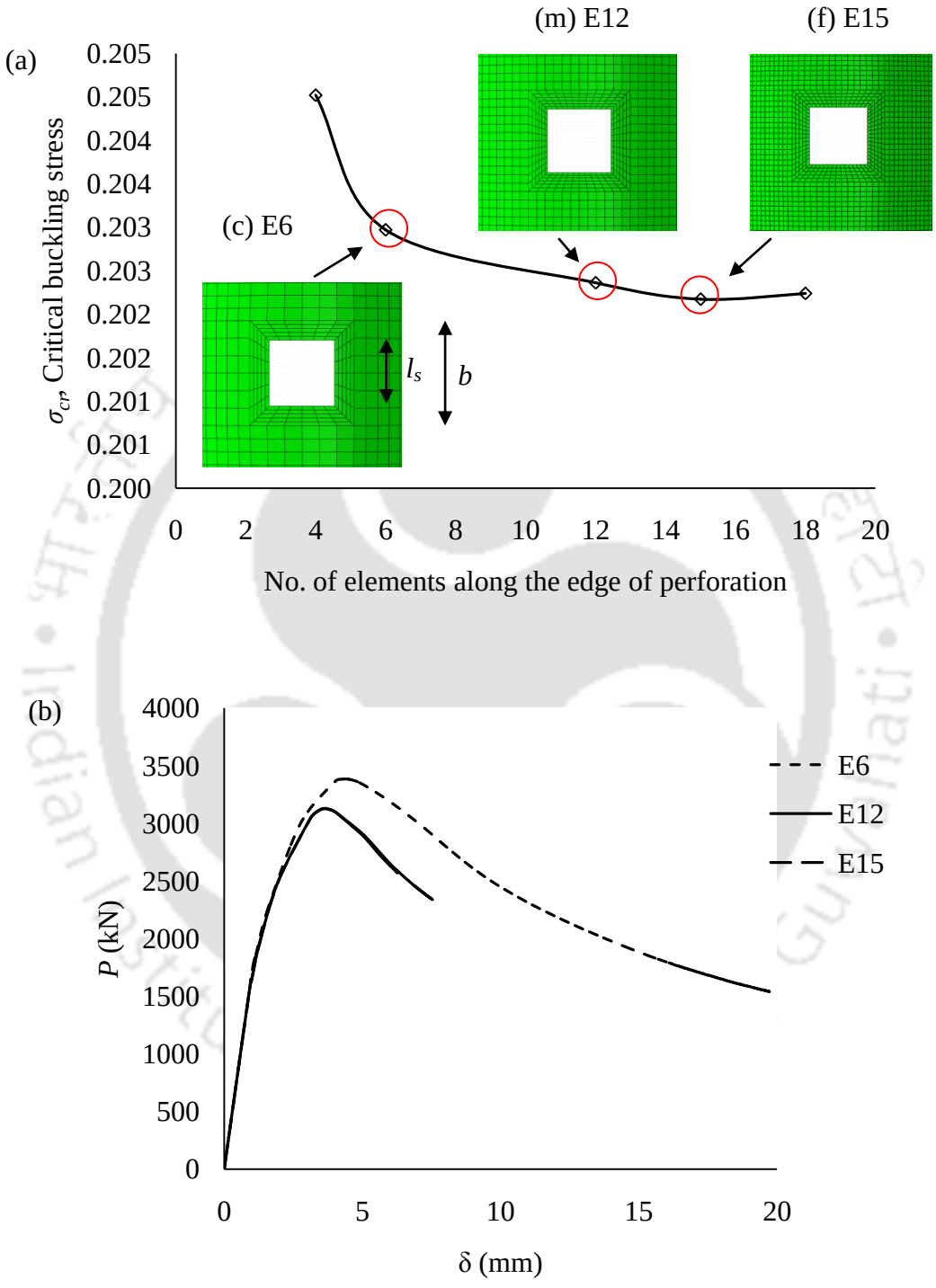

Figure 5.5: a) Variation of σ_{cr} with no. of elements along perforation edge (for T_5L_3) and b) Variation of P vs. δ ($l300w300r150t5l_s50$).

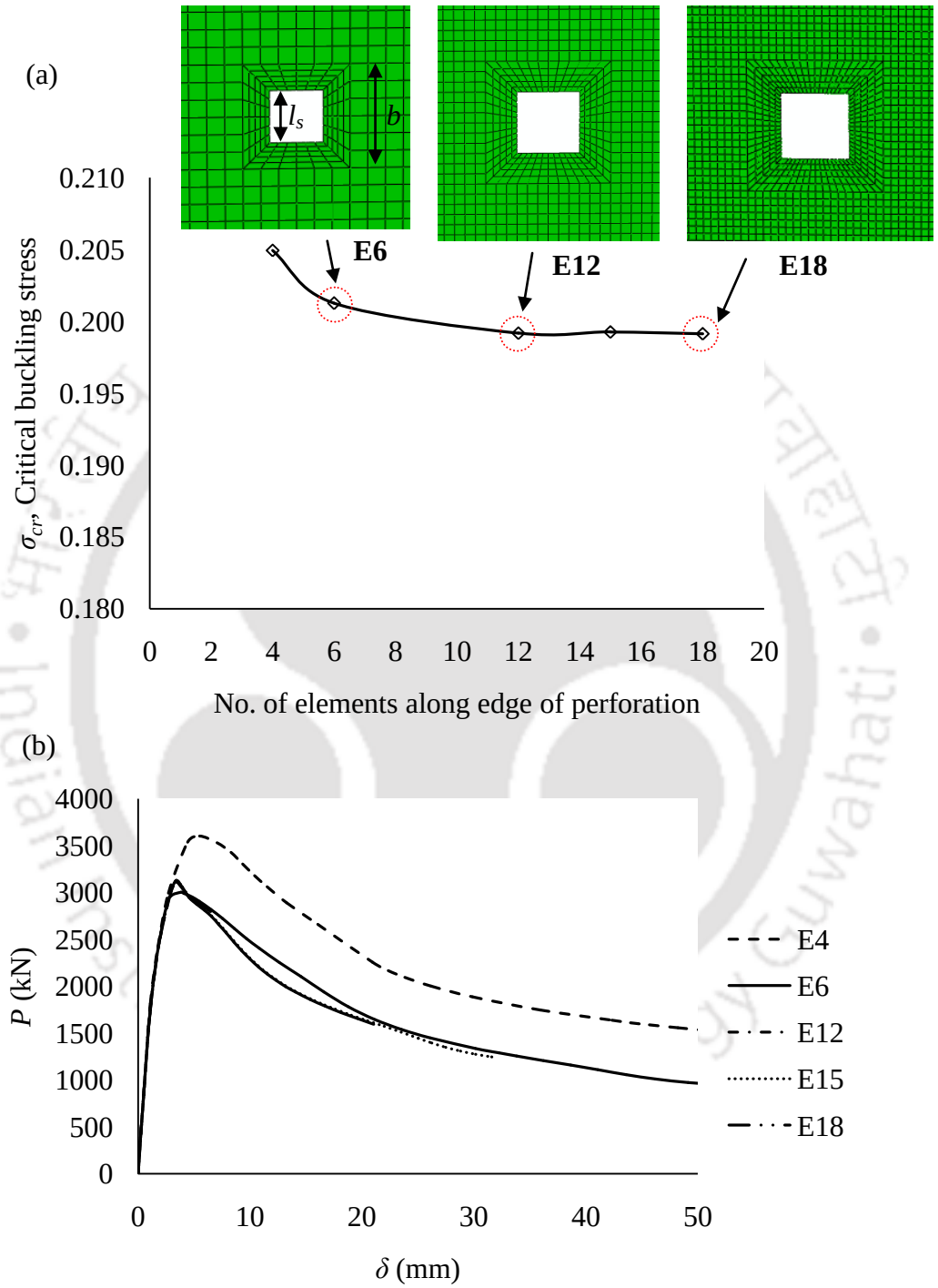

Figure 5.6: a) Variation of σ_{cr} with no. of elements along perforation edge (for T_1L_3) and b) Variation of P vs. δ ($l300w300r150t5l_s50$).

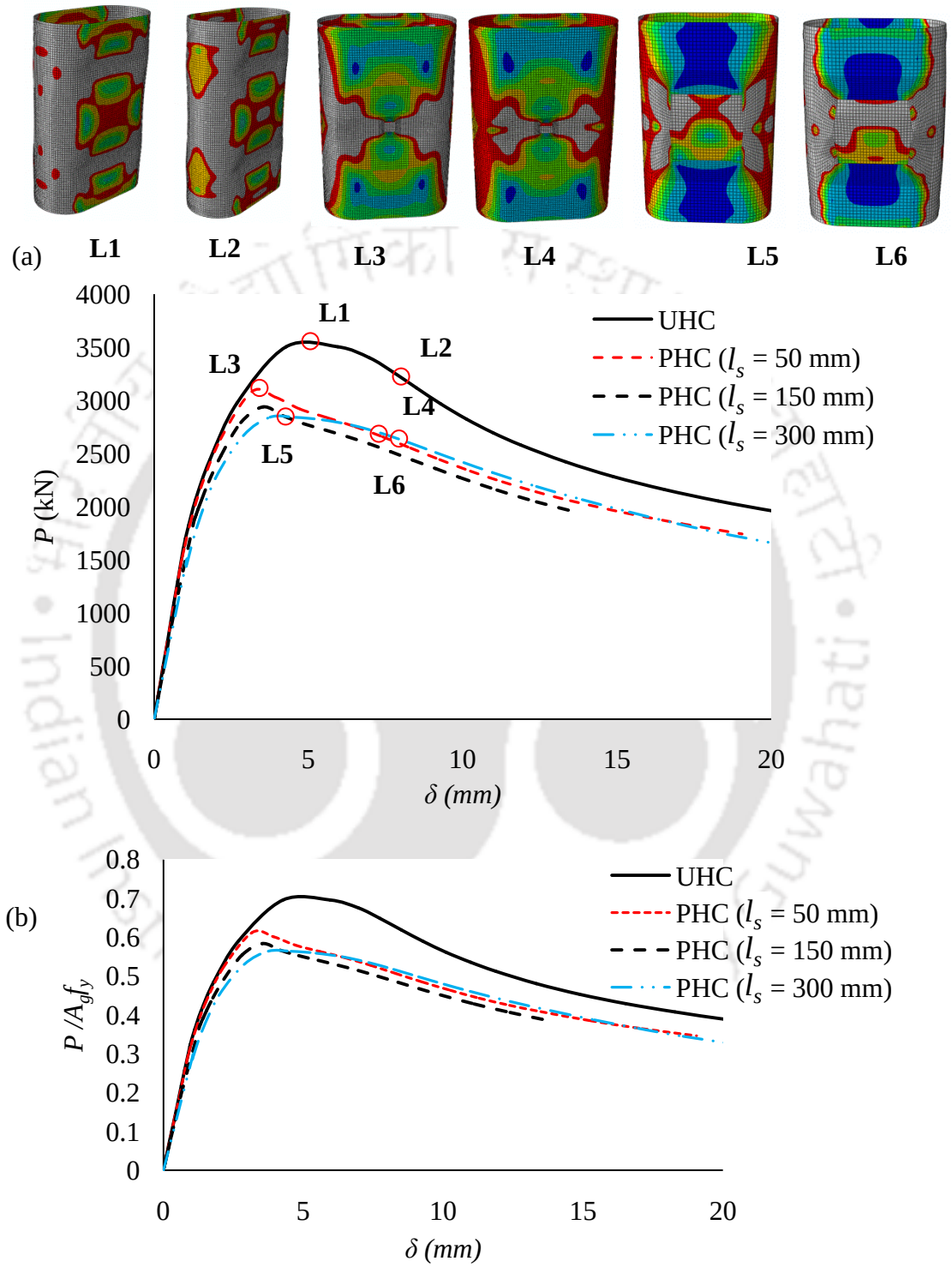

Figure 5.7: (a) P vs δ and (b) $P/A_g f_y$ vs δ (perforation located at flat element centre, t = 5 mm).

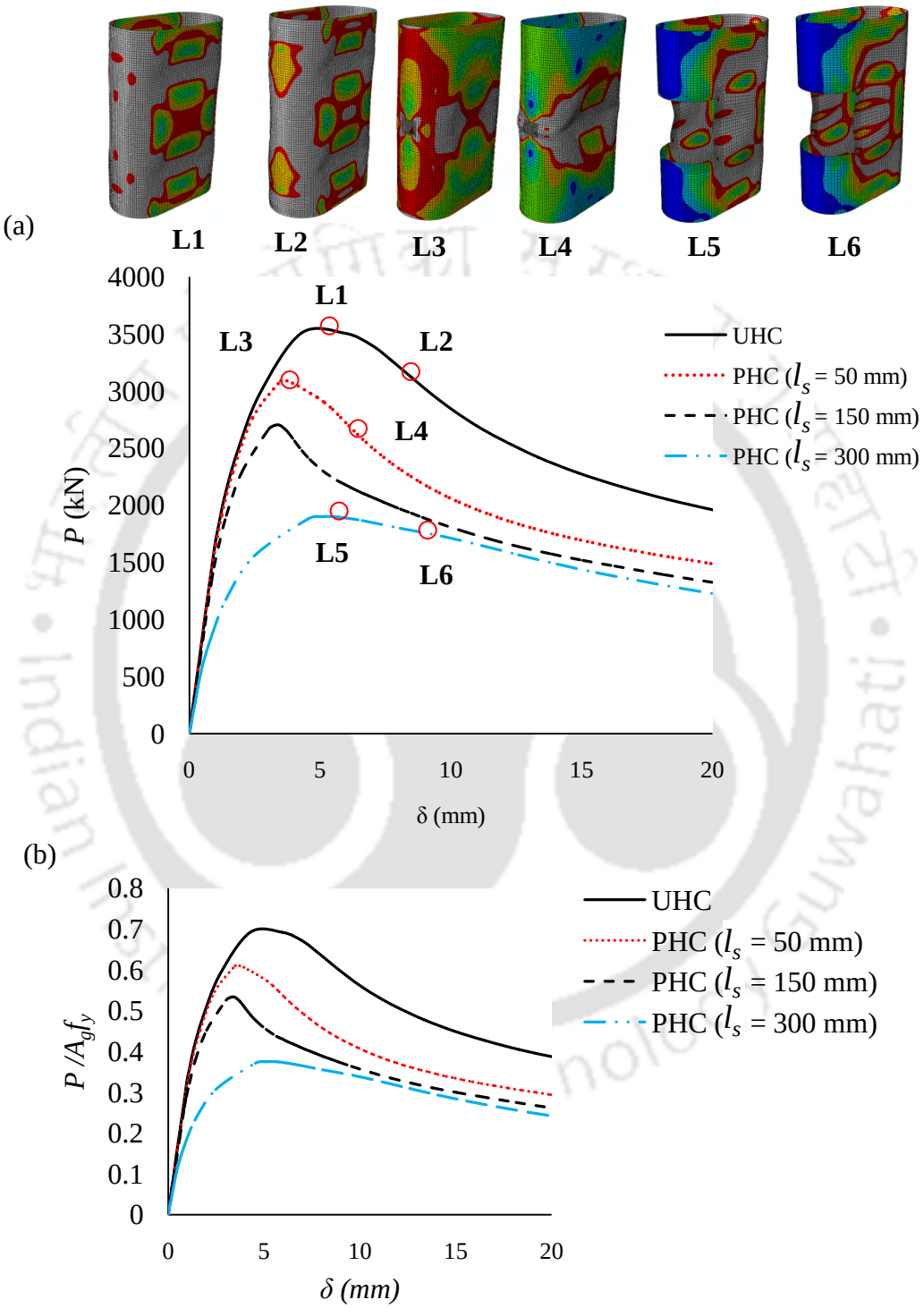

Figure 5.8: (a) P vs δ and (b) $P/A_g f_y$ vs δ (perforation located at curved element centre, t = 5 mm).

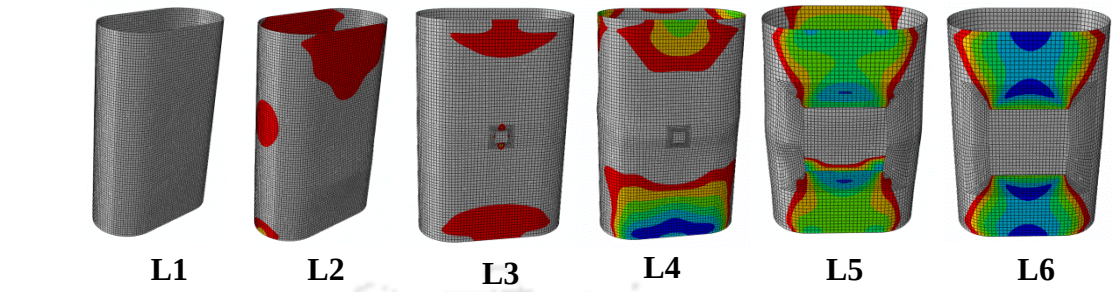

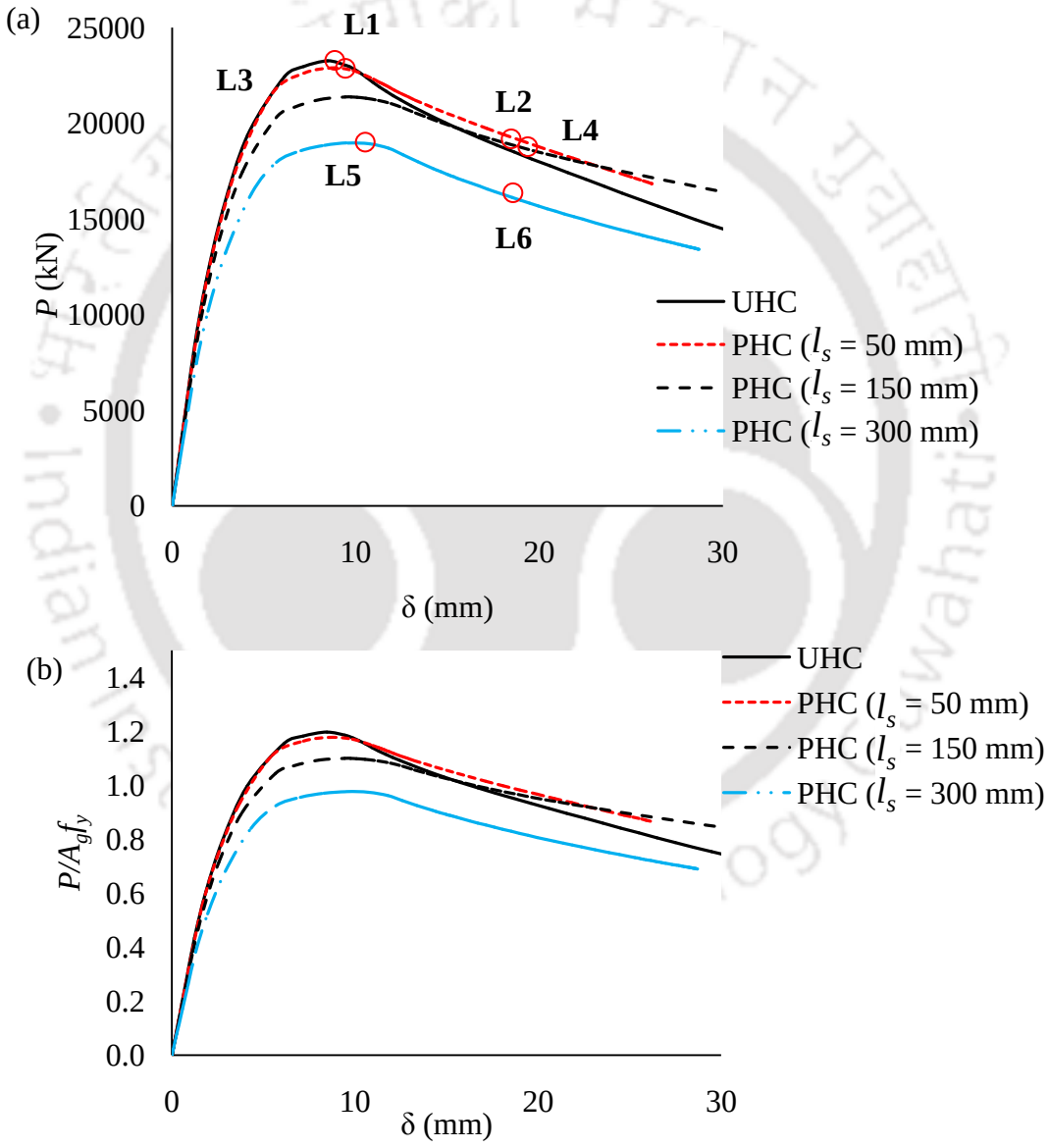

Figure 5.9: (a) P vs δ and (b) $P/A_g f_y$ vs δ (perforation located at flat element centre, t = 20 mm).

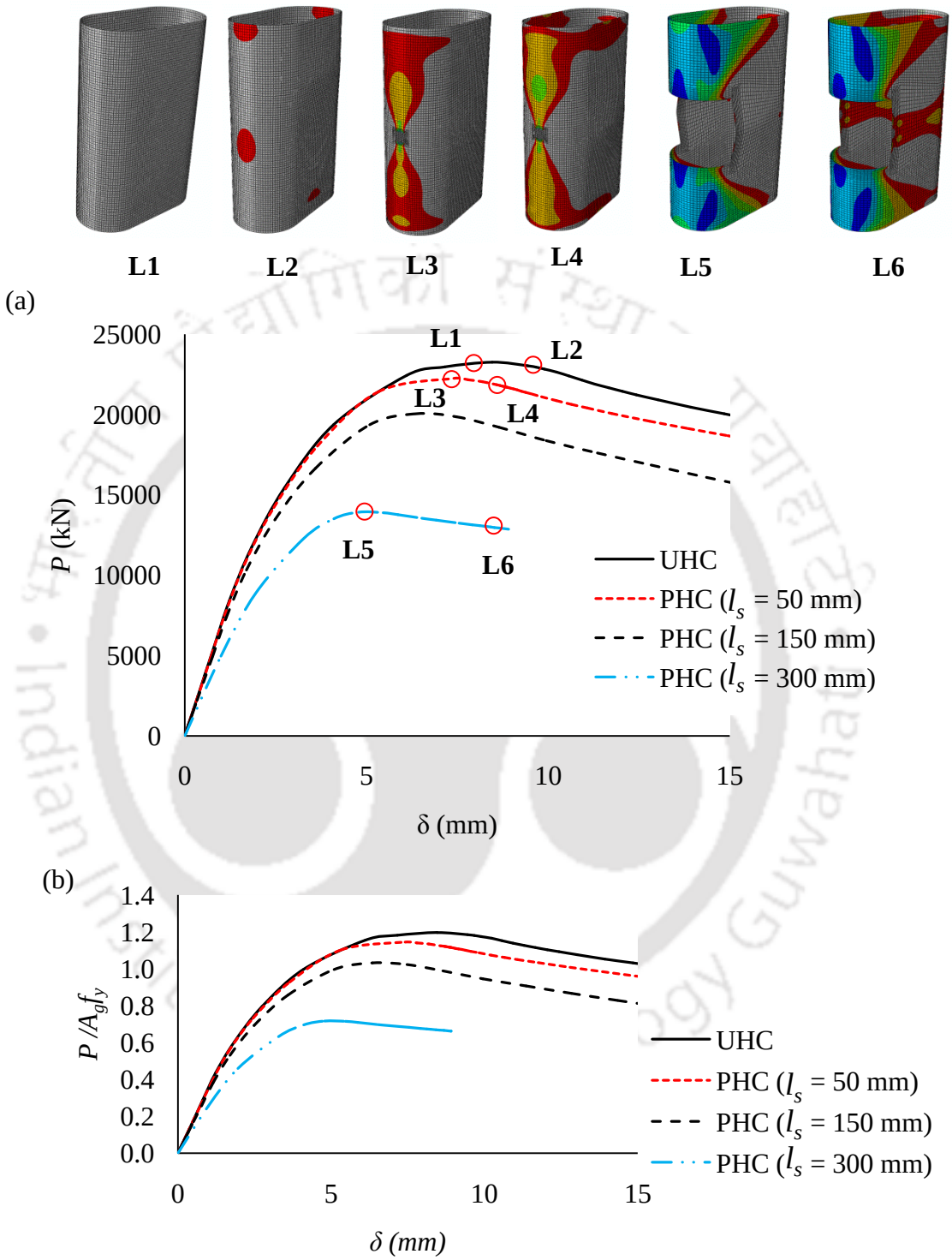

Figure 5.10: a) P vs δ and b) $P/A_g f_y$ vs δ (perforation located at curve element centre, t = 20 mm).

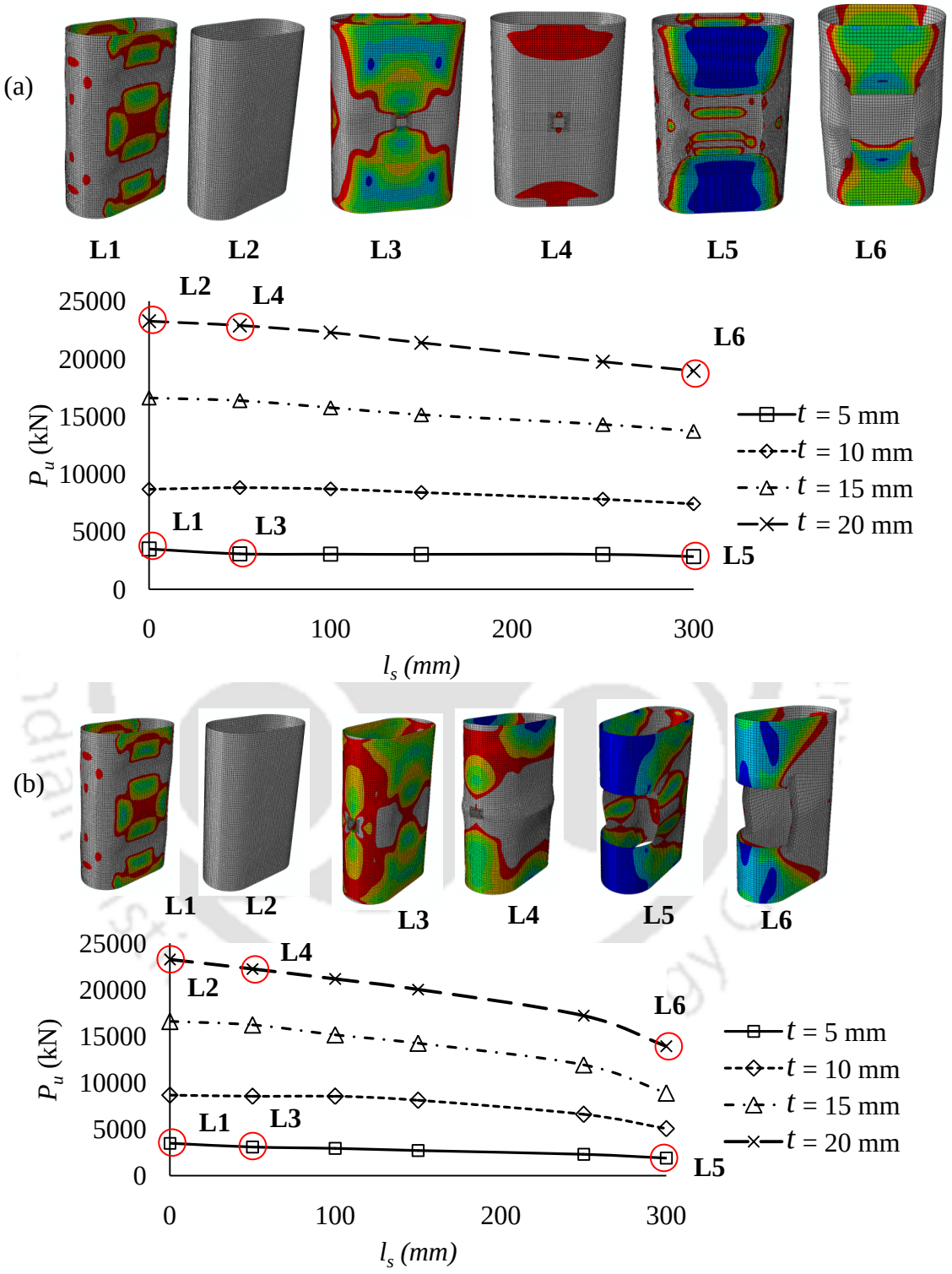

Figure 5.11: P_u vs l_s for perforation located at a) flat element centre, b) curved element centre.

(a)

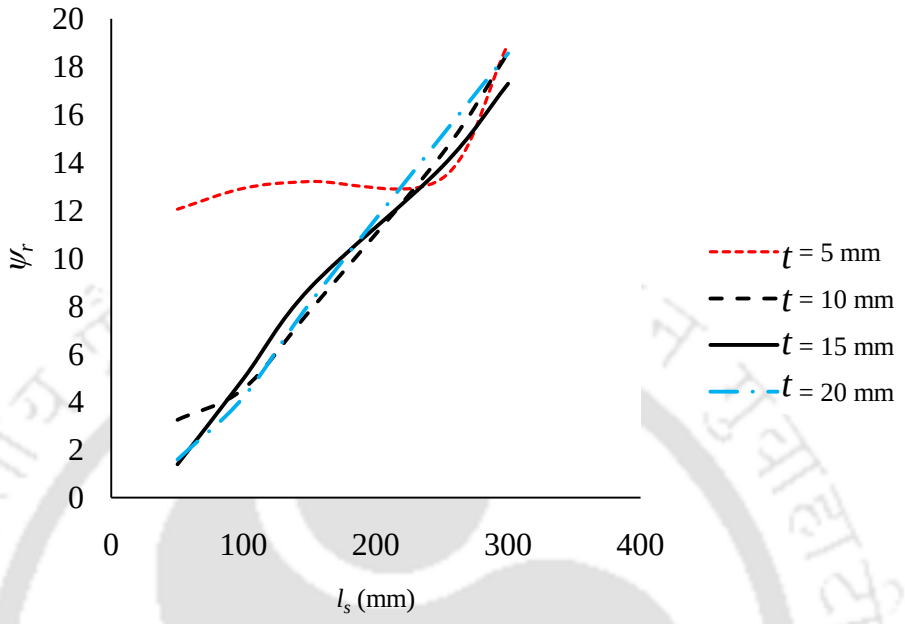

(b)

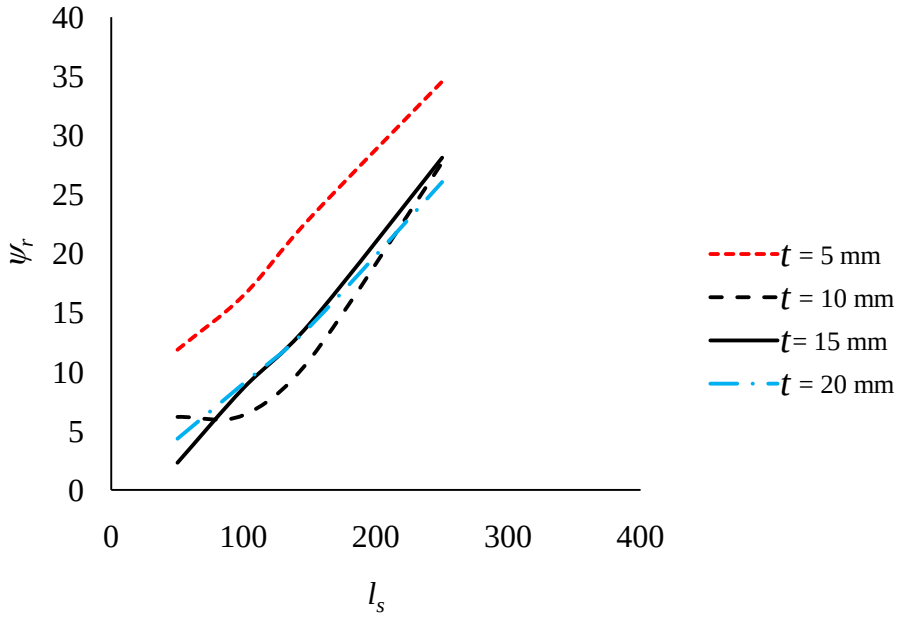

Figure 5.12: ψ_r (=(P_u-P_{up})x100/P_u) % vs l_s for perforation located at a) flat element centre, b) curved element centre.

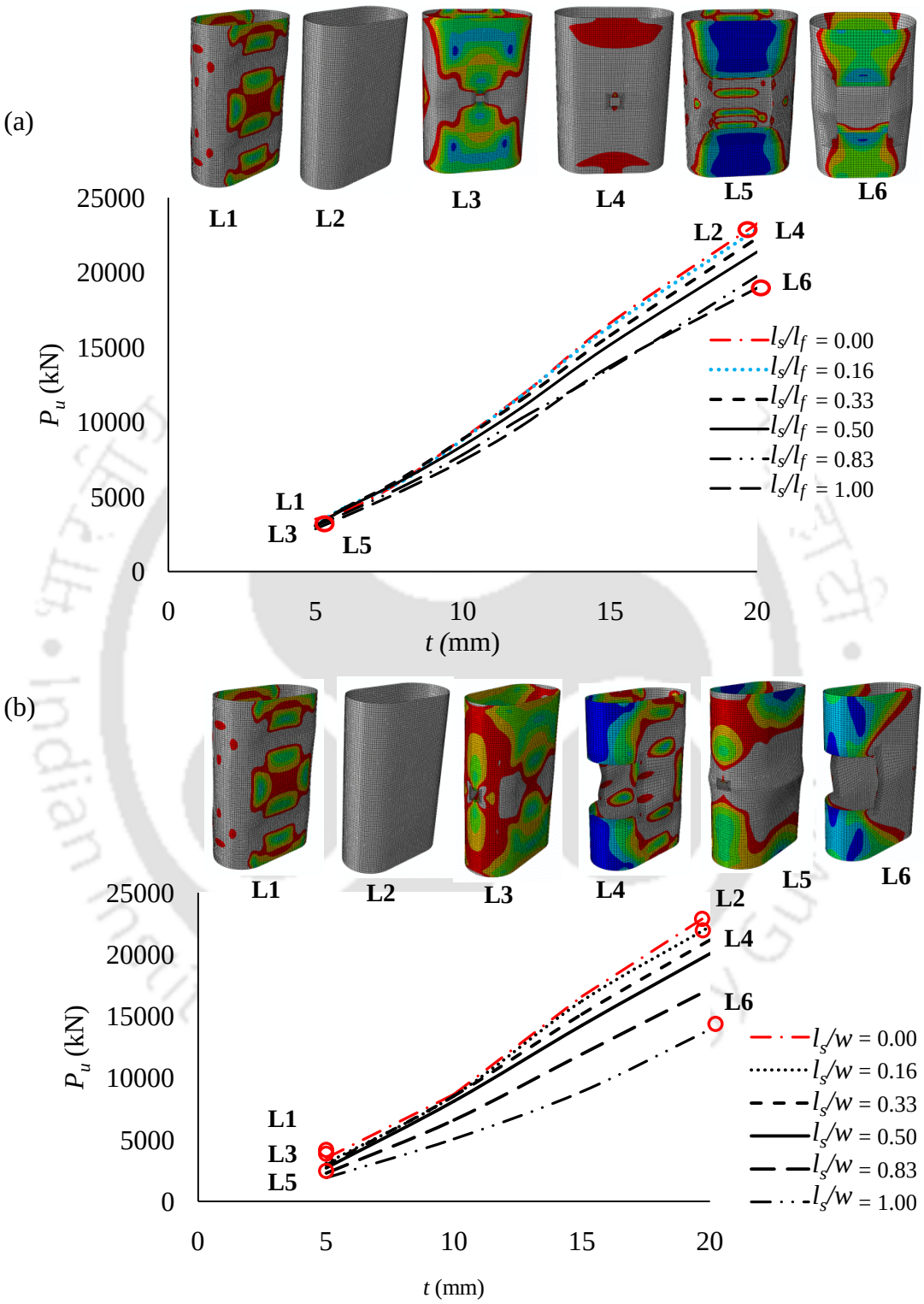

Figure 5.13: P_u vs t for perforation located at a) flat element centre, b) curved element centre.

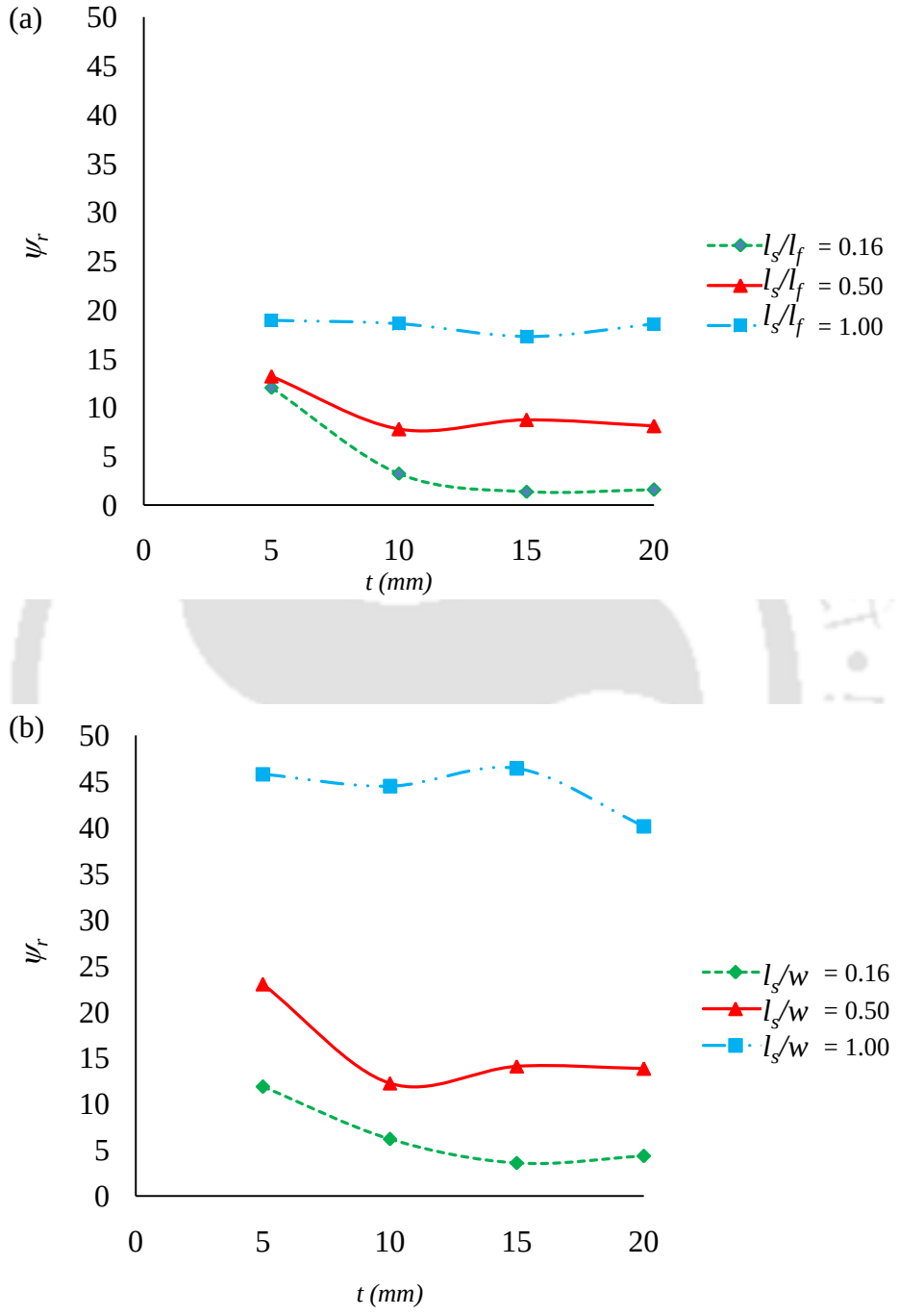

Figure 5.14: ψ_r (=(P_u-P_{up})x100/P_u) % vs t for perforation located at a) flat element centre, b) curved element centre.

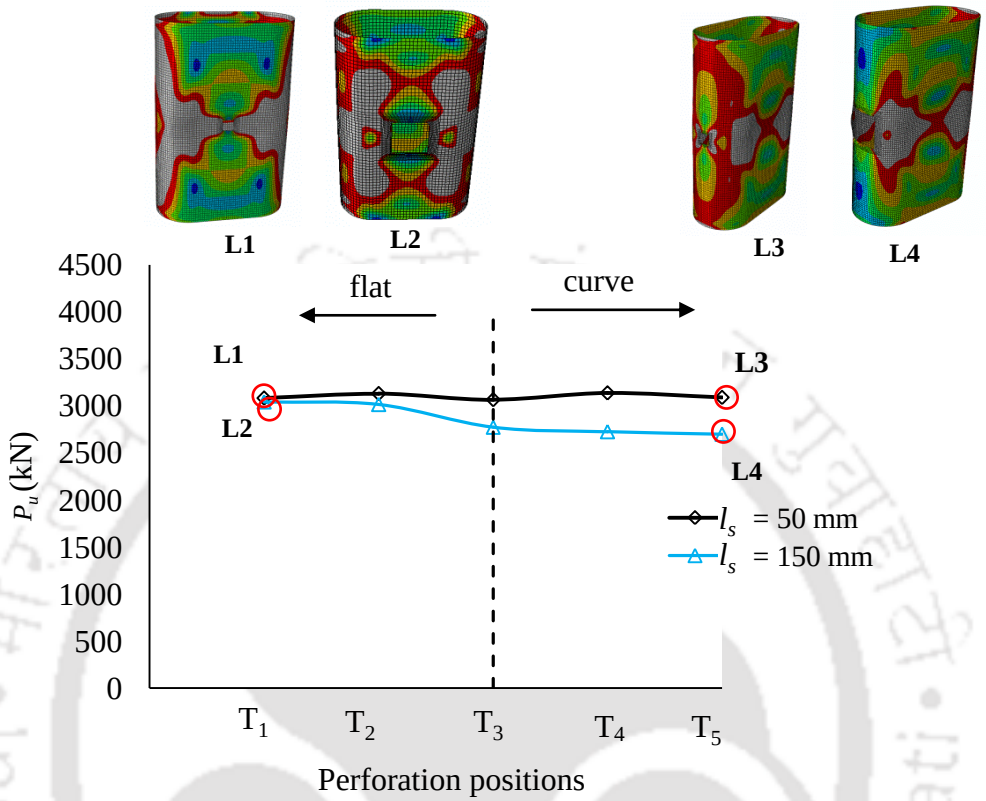

Figure 5.15: P_u vs circumferential perforation positions (t = 5 mm).

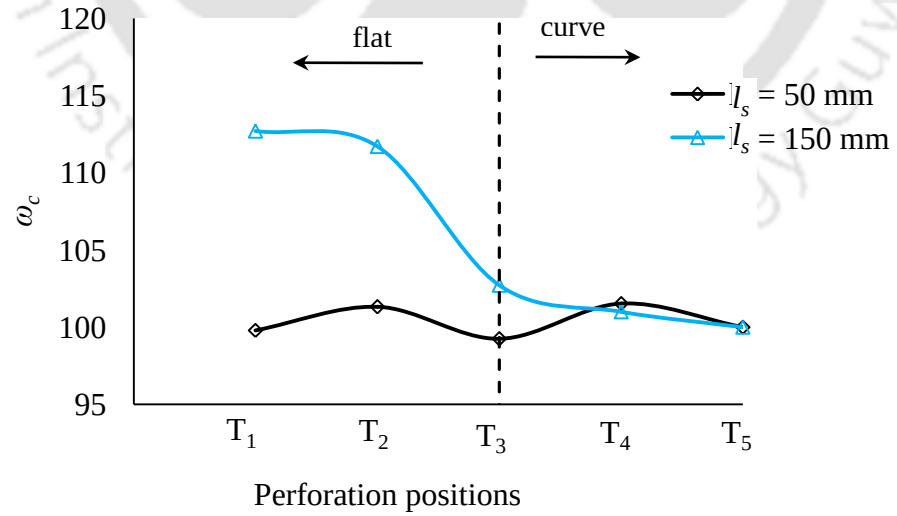

Figure 5.16: ω_c (= $P_u/P_{u(T5)}$ x 100)% vs circumferential perforation positions (t = 5 mm).

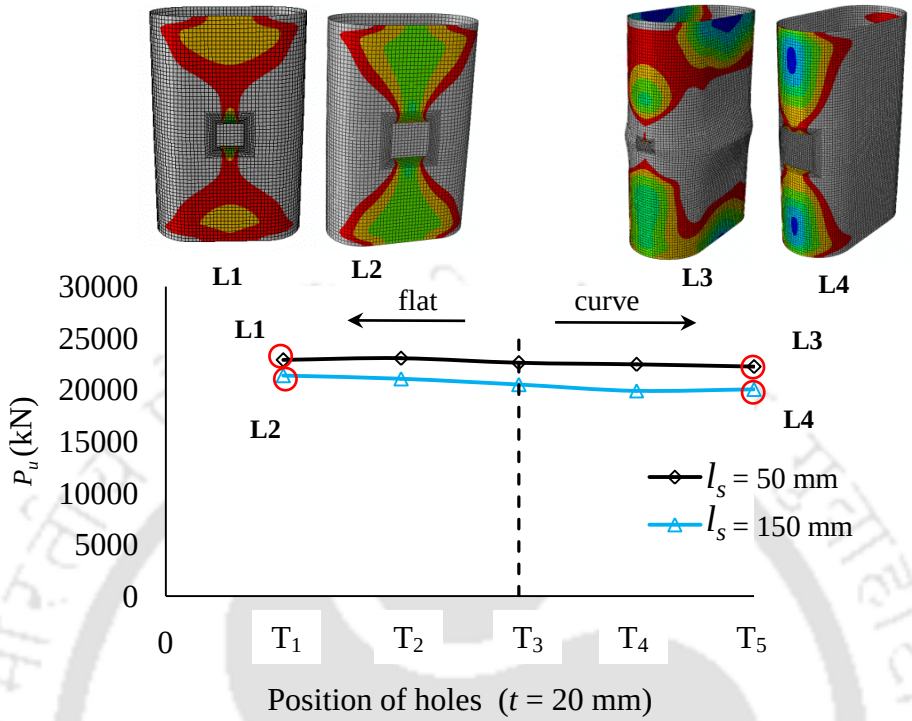

Figure. 5.17: P_u vs circumferential perforation positions (t = 20 mm).

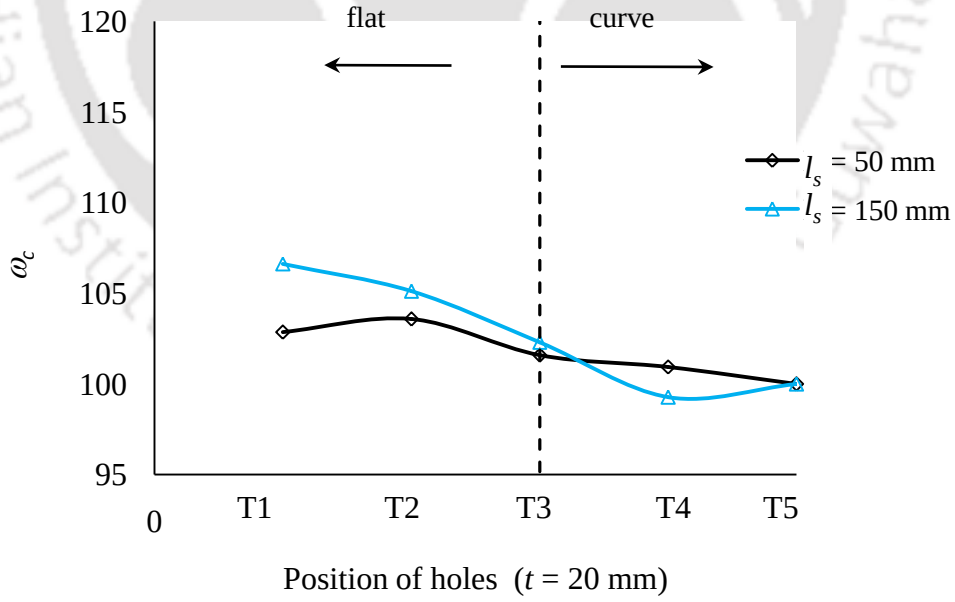

Figure 5.18: ω_c (= $P_u/P_{u(T5)}$ x 100)% vs circumferential perforation positions (t = 20 mm).

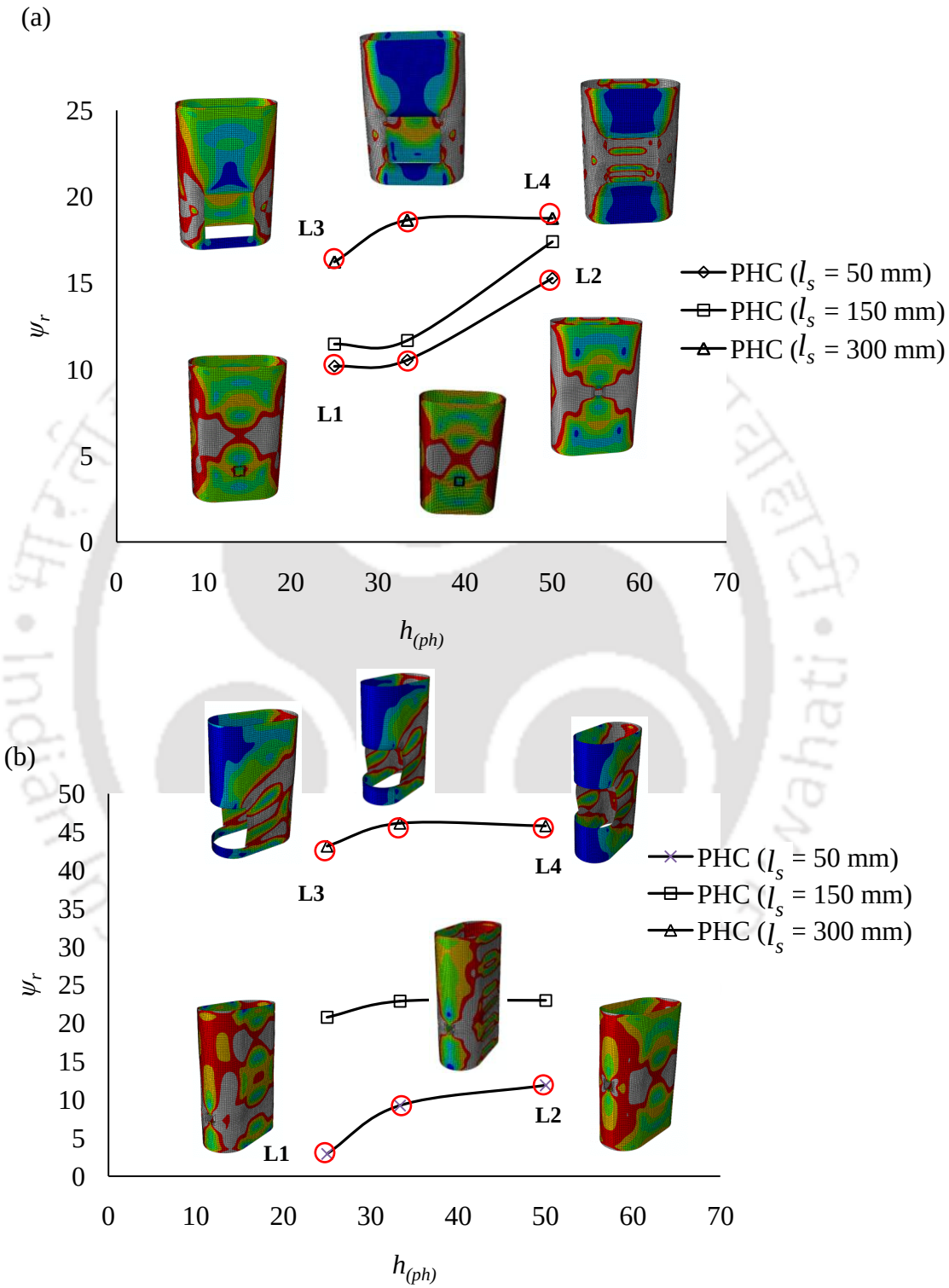

Figure. 5.19: ψ_r (=(P_u-P_{up})/P_u x100%) vs $h_{(ph)}$ (= h_p/h x100%) for perforation located at a) flat element centre, b) curved element centre (t = 5 mm).

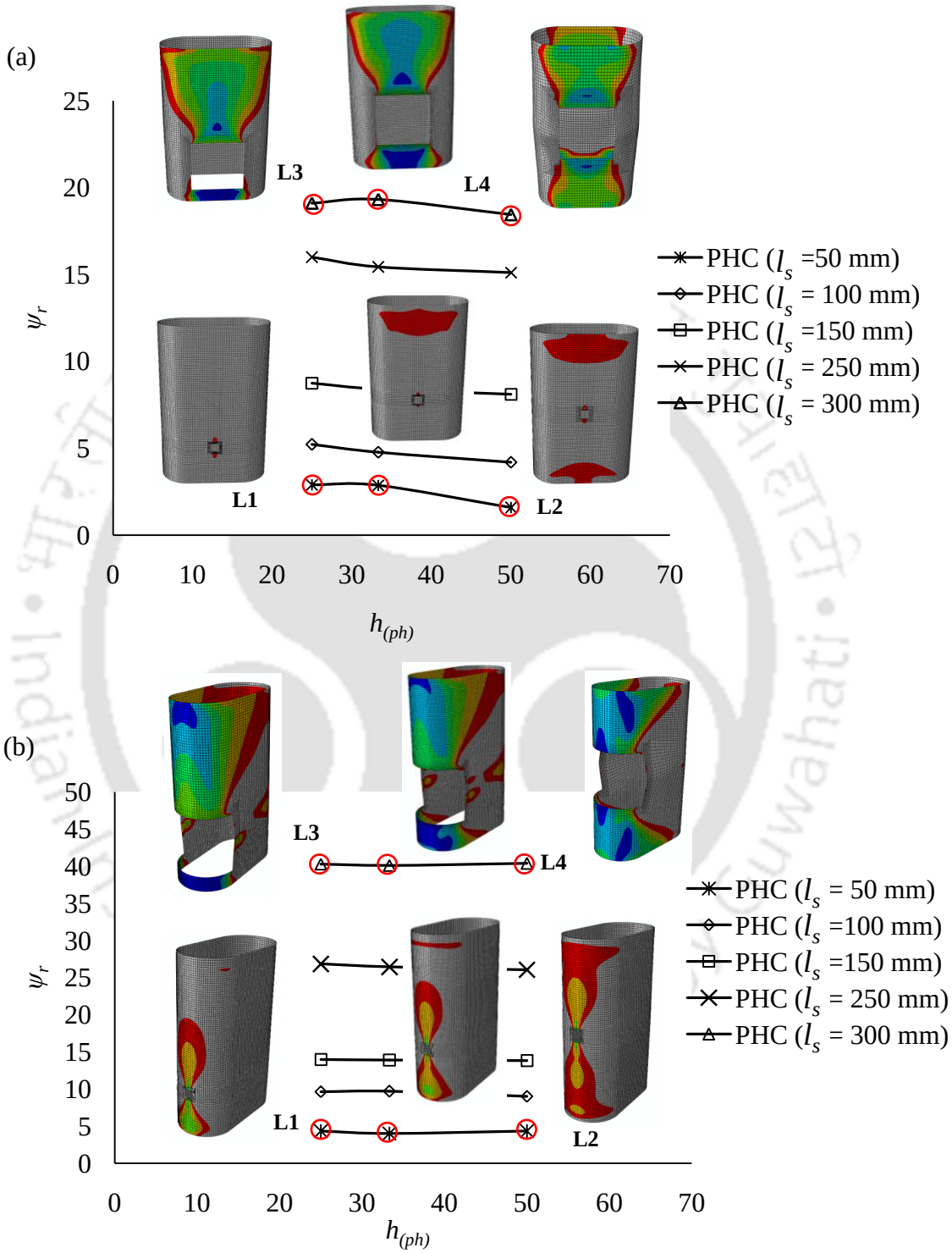

Figure 5.20: ψ_r (=(P_u-P_{up})/P_u x100%) vs $h_{(ph)}$ (=h_p/h x100%) for perforation located at a) flat element centre, b) curved element centre (t = 20 mm).

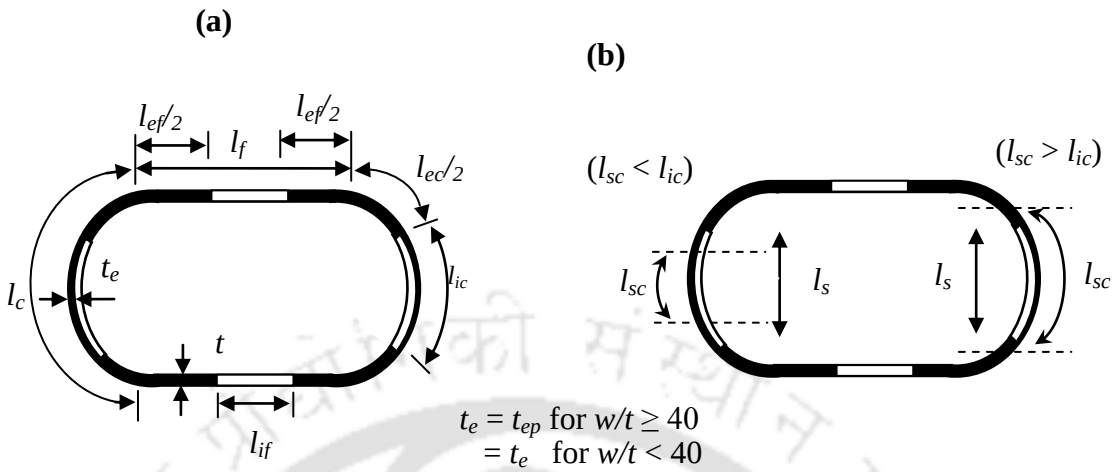

Figure 5.21: Schematic representation of area deductions as per modified ASDM (i.e. ASDM$_m$ or ASDM$m(p)$).

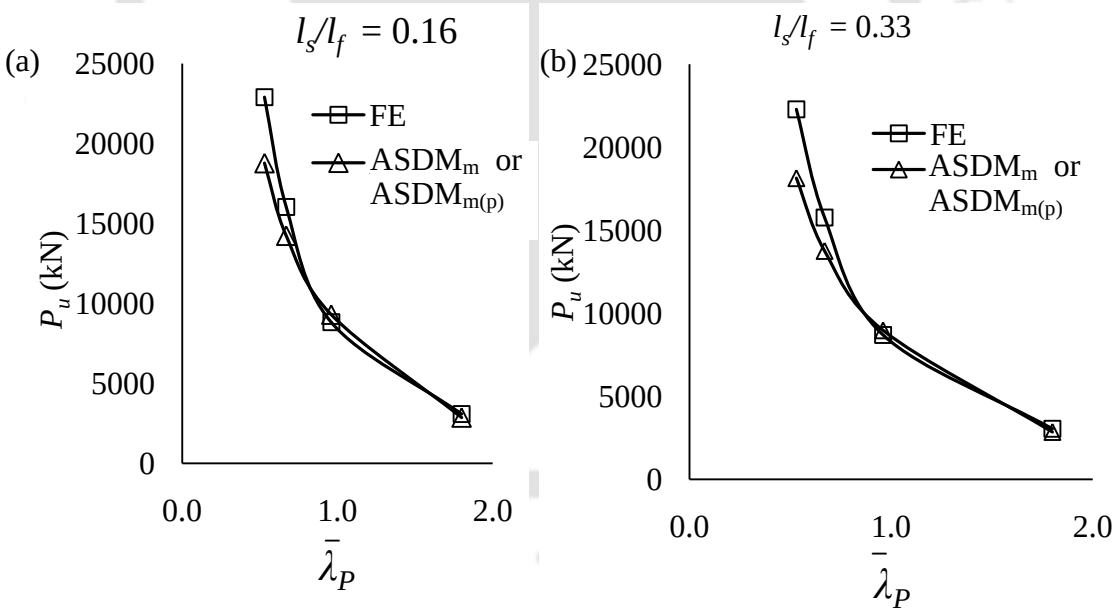

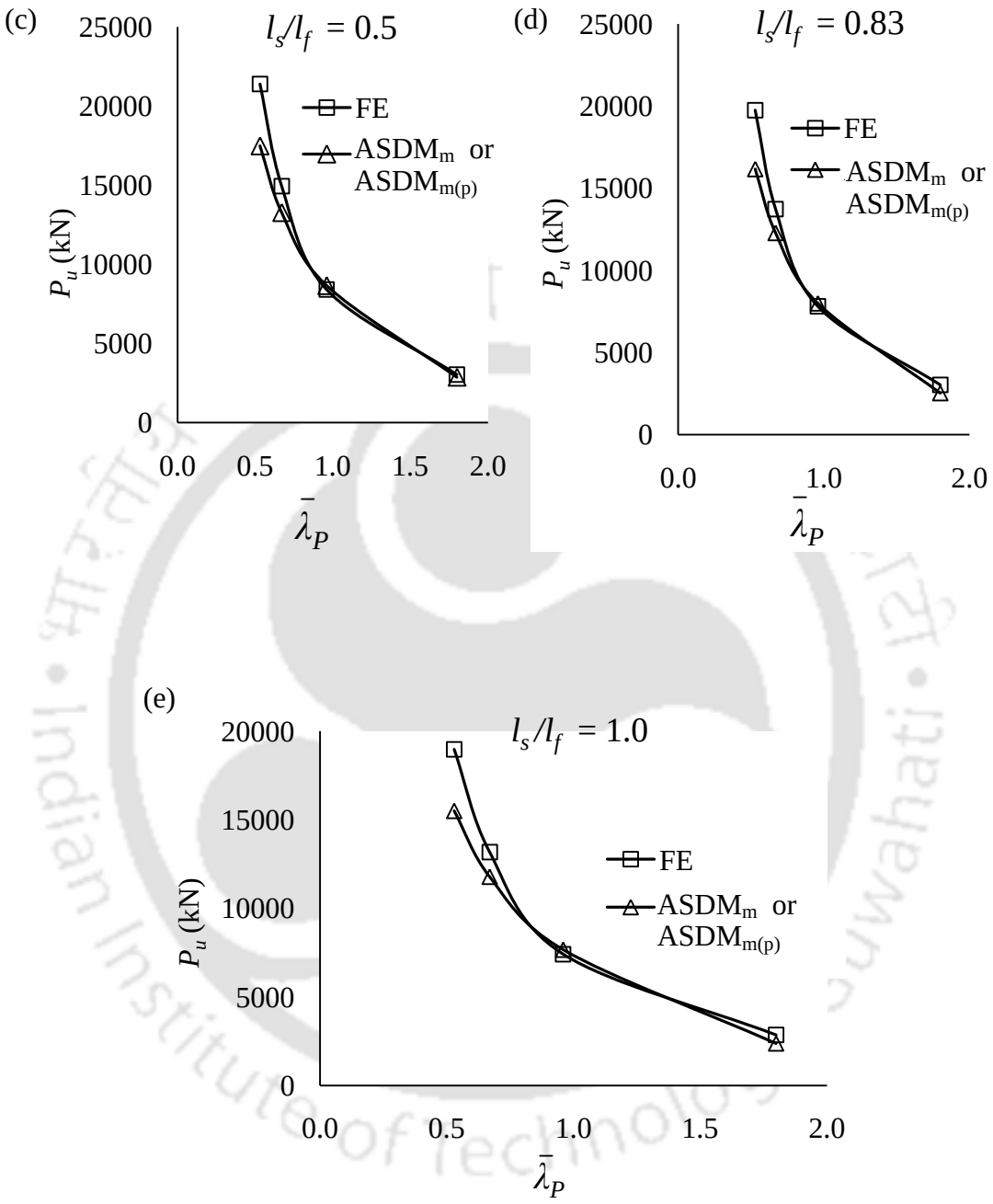

Figure. 5.22: Comparison of FE and ASDM$_m$ for perforations at flat element center (Location T_1).

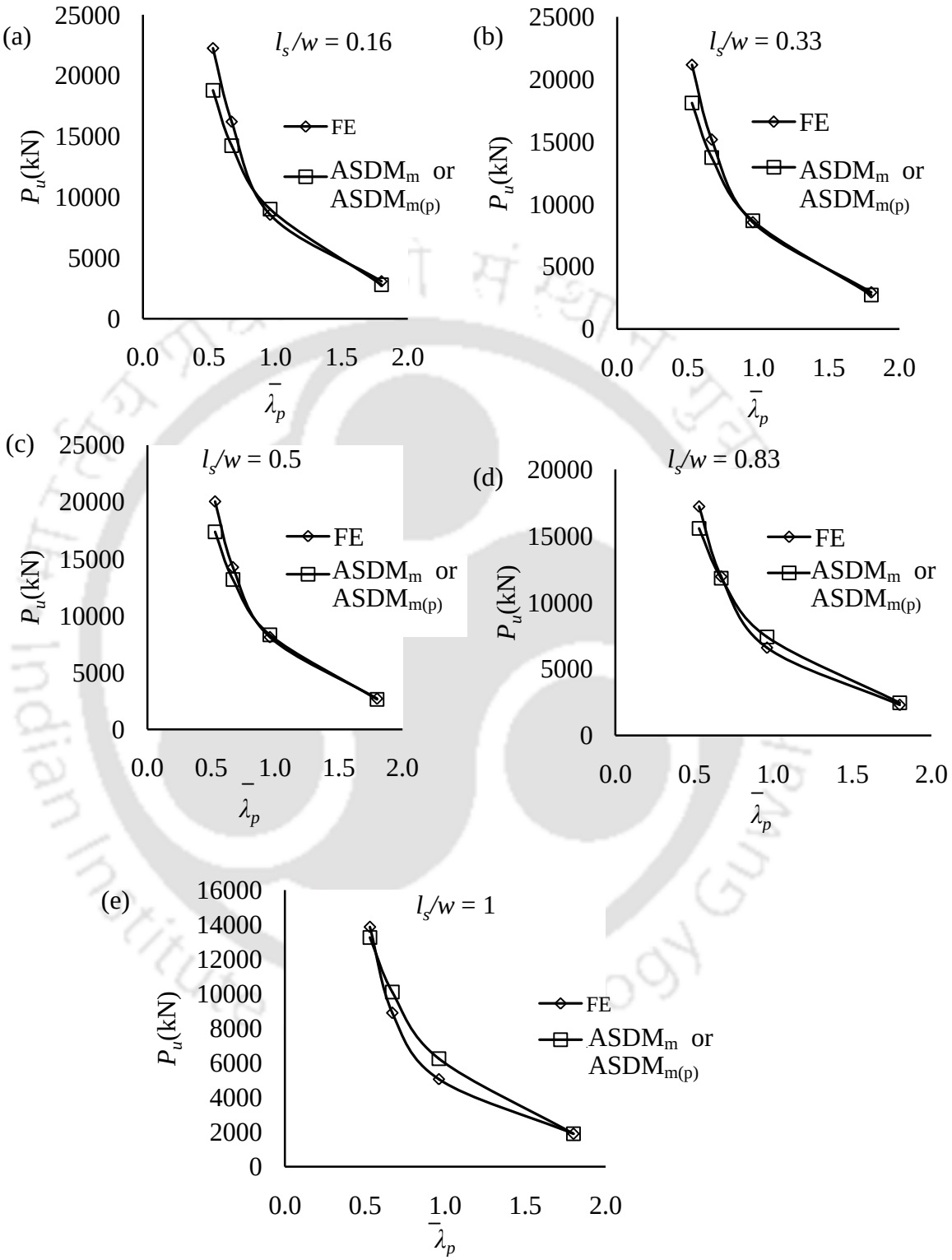

Figure 5.23: Comparison of FE and ASDM$_m$ or ASDM$_{m(p)}$ (modified ASDM for perforations) at curve element center (Location T_5).

CHAPTER 6

CONCLUSIONS AND SUGGESTIONS FOR FURTHER WORK

6.1 INTRODUCTION

Recent advancement in stainless steel alloy development has resulted in a new and promising structural duplex stainless steel variety known as Lean Duplex Stainless Steel (LDSS: UNS 32101, EN 1.4162). In comparison to other breeds of structural stainless steel, LDSS has been reported to offer attractive properties like cheaper cost (in relation to austenitic stainless steel), higher strength, acceptable weldability and fracture toughness properties, improved high temperature properties, etc. (e.g. Theofanous and Gardner, 2009; Saliba and Gardner, 2013a). Very recently, LDSS has been featured in the amended version of Eurocode (EN 1993-1-4, 2006/A1:2015), at the end of 2015. Structural studies on LDSS hollow columns are limited mostly to Square Hollow Section (SHS) (e.g. Theofanous and Gardner, 2009; Huang and Young, 2013, 2014b); Rectangular Hollow Section (RHS) (Theofanous and Gardner, 2009; Huang and Young, 2013, 2014b), L, T, + (Patton and Singh, 2012, 2013), Circular Hollow Section (CHS) Umbarkar *et al.*, (2013). Hence, in this thesis, an attempt has been made to systematically study the structural behavior of aesthetically pleasing LDSS flat oval (a composite section of

flat and curve elements) hollow stub and slender columns under pure compression. The investigation also includes the effect of single square perforation on LDSS hollow stub columns. Important conclusions based on the current study are enumerated below. At the end of this chapter, suggestions for possible extension of the present work are given.

6.2 CONCLUSIONS

6.2.1 LDSS flat oval hollow stub columns

Parametric study on the structural behaviour of fixed ended LDSS flat oval hollow section stub column, is presented, considering variation of l_f (flat length), r (curvature radius), t (thickness), keeping w (flat plate spacing) and h (height of column) constant at 300 mm and 900 mm respectively, using the finite element (FE) analyses. Based on the FE analyses, the following conclusions have been obtained:

1) LDSS flat oval hollow sections with semicircular end elements (i.e. r/w = 0.5) provided the maximum column strength (P_u) of the stub columns, however for $r/w \geq$ 0.5 (or flatter curve end elements) a sharp drop in the values of P_u can be observed, the drop being relatively larger for higher values of t.

2) For thinner sections (e.g. $t \leq 5$ mm), there is no significant variation on the values of P_u, when l_f/w is increased from 0 to 2.33 (i.e. l_f = 700 mm). However, as the thickness is increased, an increase in the value of P_u can be seen with increasing l_f/w, with the slope of increment getting relatively higher as the thickness increases.

3) Strength (load capacity) gain per unit increase in area by 1) increasing t, increases with increasing r and decreases with increasing l_f ; 2) increasing l_f, increases with increasing t; while the decrease in strength per unit decrease in area by increasing r decreases with increasing t.

4) Increase in load capacity per unit material area increment as a result of increase of ~ 566% increase in t (from t = 3 mm) is ~≥ 87% for all radii of curvatures considered, while it is ~≥ 71% for increase in flat length, which shows that the increase in thickness has more positive effect on column strength.

5) It has been found that ASDM, DSM, DSM* and CSM are reliable for the design of flat oval LDSS columns, whilst ASCE 8-02, AS/NZS 4673, and EN 1993-1-4 are not, although, predictions made by ASCE 8-02, AS/NZS 4673, and EN 1993-1-4 are observed to be reliable for compact or stocky curve section with $w/t < 40$.

6) An expression has been proposed for calculating the effective thickness of curve elements of slender ($w/t \geq 40$) flat oval LDSS sections, which can provide reliable load capacity predictions when used with ASCE 8-02, AS/NZS 4673, and EN 1993-1-4 equations.

6.2.2 LDSS flat oval hollow slender columns

A parametric investigation on the structural behaviour (e.g. deformation modes, load capacity etc.) of fixed ended stocky (Class 1-3) and slender (Class 4) LDSS flat oval hollow slender columns under axial compression has been presented using finite element analyses, by varying l_f , r , t , w and h. Conclusions drawn from the parametric analyses are presented in two sub-headings *viz*., a) slender cross-section columns and b) stocky cross-section columns.

a) Slender cross-section column

1) Based on the stress contours and deformed shapes corresponding to P_u and post-P_u, three primary failure or deformation mechanisms have been identified *viz*., 1) Local to local yielded buckling (Mechanism SL1A), 2) Local to local yielded flexural buckling (Mechanism SL1B), and 3) Flexural to flexural yielded buckling (Mechanism SL2). Mechanisms SL1A and SL1B are found to occur for $\overline{\lambda} < 1.25$; whilst Mechanism SL2 corresponds to $\overline{\lambda} > 1.25$ respectively.

2) P_u is found to be highest for r/w = 0.5 (or when the curve element is semi-circular in shape) and decreases till r/w = 1. For r/w > 1.0, there is no significant change in the value of P_u.

3) For the shortest column considered (h = 1000 mm), a slight drop (~ 8%) in P_u for l_f increases from 50 to 75 mm can be observed, which then remains near constant for $l_f \geq$ 75 mm. However, for intermediate column length i.e. 2000 mm $\leq h \leq$ 5000 mm, an initial increase in P_u can be seen which then plateaus (with a lower rate of increase) at l_f = 75-100 mm, whilst for larger column lengths e.g. $h \geq$ 5000 mm, there appears to be a near linear increase in P_u with l_f.

4) In general, P_u is found to increase in a near linear trend with increase in w, although, for $h \geq$ 9000 mm, the rate of increase follows a non-linear pattern (with the rate of increase getting higher for larger w). Further, the role of increasing w in increasing P_u, is found to be more effective in slender columns.

5) In general it is seen that, P_u decreases with increasing h, although it appears that the rate of decrease with relatively more less sensitive for changes in l_f and r, as compared to changes in w. Moreover, it is observed that the normalised plot (i.e. $P_u/A_g f_y$ vs $\overline{\lambda}$) is able to capture the effect of l_f, r and w relatively well.

6) The current EN 1993-1-4 (2015), DSM, are found to be applicable for the design of LDSS flat oval hollow slender cross-section column, however AS/NZS 4673 (2001) and modified versions of AS/NZS 4673 and DSM (Huang and Young, 2014b) are observed to be not reliable.

b) Stocky cross-section columns

1) For the stocky sections (Class 1 and 2), based on the stress contours and deformed shapes at P_u and post-P_u, three failure or deformation mechanisms have been identified *viz*., 1) Yield to yield with local bucking (Mechanism ST1), 2) Yield to yield with flexural buckling (Mechanism ST2), and 3) Flexural to flexural

buckling (Mechanism ST3). ST1, ST2 and ST3 mechanisms corresponds to $\overline{\lambda}$ < 0.32; 0.32 ≤ $\overline{\lambda}$ ≤ 1.0; and $\overline{\lambda}$ > 1.0 respectively.

2) Semi-circular curve section (r/w = 0.5) showed the highest load capacity, with P_u remaining almost flat for $r/w \geq 1.0$, with the drop in P_u when r/w is increased from 0.5-1.0, is ~18-20% for all the lengths of columns analysed.

3) A near linear increase in P_u with l_f is observed; the average increase is found to be ~94-110% for 200% increase in l_f (from l_f = 50 mm).

4) In general, P_u increases with increase in w, however the rate of increase seems to be relatively higher for $w \leq 100$ mm, especially for $h \geq 2000$ mm.

5) A near linear increase in P_u with increase in thickness is observed, with the rate of increase of t for all heights of column but decreases with increase in h.

6) The rate of decrease in P_u with h is relatively less sensitive (~74-77%) to variations in l_f and r; however, it is quite sensitive (~8-77%) to variation in w. Further, it is noted that the normalised plots ($P_u/A_g f_y$ vs $\overline{\lambda}$) are able to capture well the effects of r and l_f, however, such well behaved plots are not seen when w is varied, specially for $\overline{\lambda}$ < ~1.

7) All the compared design codes, method and their modified versions are reliable and applicable, with β values of 3.28, 3.52, 3.90 for EN-1993-1-4 (2015), AS/NZS 4673 (2001) and DSM (2002); and 3.38, 3.50 for modified AS/NZS and modified DSM (Huang and Young, 2014b) respectively. It has been noticed that β values for the modified versions are found to be lower and hence, their use are expected to be more economical.

6.2.3 LDSS flat oval singly square perforated hollow stub columns

A parametric investigation on the structural behaviour (load capacity and deformation modes or shapes of fixed ended single square perforated LDSS flat

oval hollow stub columns (of stocky and slender cross-sections as per EN 1993-1-4, 2015) under axial compression has been presented using finite element analyses. The effects of single square perforation in relation to perforation size and location (i.e. along transverse and longitudinal directions, on both the flat and curve elements) have been investigated. Based on the parametric study, the following conclusions have been drawn:

1) For the perforation located in flat portion, it can be observed that there appears to have near linear reduction in ultimate load capacity (P_u) with perforation size (l_s). The reduction is found to be higher for the stockier cross-section considered, whilst it is lower for the slender cross-section. When the perforation is located at the curve element the reduction in P_u with l_s is found to be near linear, however, for the stockier sections, the near-linearity appears to exist till l_s = ~ 83% of w; for larger l_s, there appears to be a slight increase in the reduction of P_u.

2) The percentage drop in P_u (when compared to unperforated sections) or ψ_r , due to perforation, remains relatively unaffected for $l_s \leq$ ~80% of l_f, when the section is slender, when the perforation is located at the flat element. However, when the perforation is located at the curve element, ψ_r is seen to be relatively much more pronounce for slender section and the curve sections are shown to be effective for all both slender and stocky sections.

3) Increasing thickness is found to have relatively more beneficial effect for hollow columns perforated with smaller perforations in the flat element, whereas it is *vice versa* in the case of perforations located at the curve element.

4) In general, columns with the largest perforations appear to have relatively less influence on ψ_r, to the variation in thickness. However, for the columns with smaller perforations, such effect is seen for relatively stockier section; whereas, for slender sections, an increase in ψ_r, can be observed for decreasing t.

5) In case of slender sections, for larger perforation, a drop in P_u can be seen as the perforation location is changed from T_1 (mid of flat element) to T_3 (i.e. junction of flat and curve elements); but it remained without significant changes in the curve region (T_3-T_5) i.e. T5 is (mid-curve element). However, for smaller perforation, the variation in P_u appears to be less significant. And, in comparison to the slender section, for stocky sections, in general, both the small and large perforations showed a mild drop in P_u, as the perforations are located towards T_5 from T_1.

6) For slender section, it can be seen that, for perforations at the flat element, there is no apparent change in ψ_r when located near the support i.e. $0.25 \leq h_{(ph)} \leq 0.33$; however, an increase in ψ_r can be observed for $h_{(ph)} \geq 0.33$, for small to relatively large perforations. But, for the largest perforation permissible at the flat element, an increase in ψ_r is seen for $h_{(ph)} = 0.25$-0.33, after which it flattens.

7) In the case of perforations located at the curve element (for slender sections), relatively higher rate of increase in ψ_r is seen for $0.25 \leq h_{(ph)} \leq 0.33$, with flattening effect seen for $h_{(ph)} \geq 0.33$, for all the perforation sizes. However, in contrast to slender columns, for stocky sections, ψ_r mildly decreases or remains near-flat for perforations located at flat or curve elements respectively.

8) A design approach based on ASDM has been proposed (based on modified effective thickness) to address the inclusion of single square perforation for the estimation of design capacity of single square perforated flat oval LDSS hollow stub columns.

6.3 SUGGESTION FOR FUTURE WORK

Although it appears that a significant work (close to 500 FE models) has been undertaken on the FE analyses of LDSS flat oval hollow (unperforated and perforated) columns under axial compression, to investigate the effect of various relevant geometric parameters, to assess their structural behavior; ample scopes for its extension can be highlighted. These extensions can be in the form of changing

loading conditions, consideration of infilled materials, variation of perforation types, etc., via both FE and experimental approaches. Based on such studies, enhancements in the design rules may be given attention. Some possible such extensions are presented herein:

6.3.1 Loading conditions

The present study is limited to pure axial compression of column. Hence, the study can be expanded by considering eccentric loading, cyclic loading, torsion, bending, shear, or combinations of such loadings etc. In addition, effect of extreme loadings such as impact and blast may also be investigated. Another area, which can be of considerable importance, can be assessment of the effect of fire.

6.3.2 Filler material

It is widely reported that, addition of filler material like concrete into the hollow tubular members (and hence concrete filled steel tubular columns/members) can enhance the load carrying capacity of the member. Thus the present study on LDSS flat oval hollow columns may be extended by incorporating various filler materials like different grades of plain concrete, reinforced concrete, steel fibre reinforced concrete, ultra light weight concrete, geopolymer concrete, etc. In addition to filler concrete, closed or open section steel members may be inserted in order to enhance the performance (via confinement of the inner concrete and preventing local buckling of outer skin) of the concrete filled flat oval hollow columns.

6.3.3 Types of perforation

The effects of single square perforations on the LDSS flat oval hollow columns have been presented in this thesis. Thus, the study can be extended to include various shapes of perforations such as circular, elliptical, oval, rhombus etc. Additionally, instead of single perforations, double or multiple perforations may be

included to investigate the interaction effects. Perforations of different sizes can also be considered.

6.3.4 Type of stiffeners

The strength of the members may be reduced due to the presence of perforations. To compensate the loss of strength of member, the role of stiffeners (surrounding the perforations) may be studied. Different shapes (e.g. straight, curved, etc.) and cross-sections (e.g. flat, semi-circular etc.) of stiffeners may also be used in the extended study.

6.4 OTHER SUGGESTIONS

Apart from all the suggested topics, the present work can also be extended to include following topics.

1) Perforation effects on LDSS flat oval hollow slender columns.
2) Tapered LDSS flat oval hollow stub and slender columns.
3) LDSS flat oval hollow members as beams, etc.

REFERENCES

AISI, (1974). Stainless steel cold-formed structural design manual. *American Iron and Steel Institute*, Washington.

ANSI/ASCE 8-90 (1991). Specification for the design of cold-formed stainless steel structural members. ANSI/ASCE 8-90. *American Society of Civil Engineers*. New York.

AS/NZS 4673 (2001). Cold-formed stainless steel structures. Australian/New Zealand Standard, Australia.

ASCE 8-02 (2002). Specification for the design of cold-formed stainless steel Structural members. *American Society of Civil Engineers*. New York.

ASDM (2002). Automotive Steel Design Manual – Revision 6.1 (ASDM), *American Iron and Steel Institute*, Automotive Applications Committee, Southfield.

AS/NZS 4600 (2005). Cold-formed steel structures.. Australian/ New Zealand Standard, Australia.

AISC 360 (2005). Specification for structural steel buildings. *American Institute of Steel Construction*, Chicago.

AISI (2007). North American specification for the design of cold-formed steel structural members. AISI S100-2007, *American Iron and Steel Institute*, Washington.

Ashraf, M., Gardner, L. & Nethercot, D.A. (2005). Strength enhancement of the corner regions of stainless steel cross-sections. *Journal of Constructional Steel Research*, 61, 37-52.

Ashraf, M., Gardner, L. & Nethercot, D.A. (2006a). Compression strength of stainless steel cross-sections. *Journal of Constructional Steel Research*, 62, 105-115.

Ashraf, M., Gardner, L. & Nethercot, D.A. (2006b). Finite element modelling of structural stainless steel cross-sections. *Thin-Walled Structures*, 44, 1048-1062.

Ashraf, M., Gardner, L. & Nethercot, D. A. (2008). Resistance of stainless steel CHS columns based on cross-section deformation capacity. *Journal of Constructional Steel Research*, 64, 962-970.

ABAQUS (2009). Abaqus/Standard user's manual volumes I–III and ABAQUS CAE manual. Version 6.9-EF1, Dassault Systemes Corporation, USA.

Afshan, S. & Gardner, L. (2013). The Continuous strength method for structural stainless steel design. *Thin-Walled Structures*, 68, 42-49.

Ahmed, S., Ashraf, M. & Anwar-Us-Saadat, M. (2016). The Continuous Strength Method for slender stainless steel cross-sections. *Thin-Walled Structures*, 107, 362-376.

Ancon (2017). https://www.ancon.co.uk. Retrieved on 13 March 2017.

Anbarasu, M. & Ashraf, M. (2017). Interaction of local-flexural buckling for cold-formed lean duplex stainless steel hollow columns. *Thin-Walled Structures*, 112, 20–30.

Baddoo, N.R. (2003). A comparison of structural stainless steel design standards, Review. Stainless Steel in Structures, *International Experts Seminar*, Ascot.

Bambach, M.R. & Rasmussen, K.J.R. (2004). Effective widths of unstiffened elements with stress gradient. *Journal of Structural Engineering*, 130, 1611-1619.

Bardi, F.C. & Kyriakides, S. (2006). Plastic buckling of circular tubes under axial compression — Part I: Experiments. *International Journal of Mechanical Sciences*, 48, 830–841.

Becque, J., Lecce, M. & Rasmussen, K.J.R. (2008). The direct strength method for stainless steel compression members. *Journal of Constructional Steel Research*, 64, 1231-1238.

Becque, J. & Rasmussen, K.J.R. (2009). A numerical investigation of local-overall interaction buckling of stainless steel lipped channel columns. *Journal of Constructional Steel Research*, 65, 1685-1693.

Juliaworld (2017). http://juliaworld.net/cloud-gate-chicago-usa. Retrieved on 18 March 2017.

Chan, T.M. & Gardner, L. (2008). Compressive resistance of hot-rolled elliptical hollow sections. *Engineering Structures*, 30, 522-532.

Chan, T.M. & Gardner, L. (2009a). Flexural buckling of elliptical hollow section columns. *Journal of Structural Engineering*, 135, 546-557.

Chan, T.M., & Gardner, L. (2009b). Structural performance of stainless steel oval hollow sections. *Proceeding of Tubular Structures* XII, Shanghai, 535-543.

Chan, T.M., Gardner, L. & Law, K.H. (2010). Structural design of elliptical hollow sections: a review. *Proceedings of the Institution of Civil Engineers: Structures and Buildings*, 163, 391-402.

Cardoso, F.S. & Rasmussen, K.J. (2013). The behaviour and design of concentrically loaded T-section steel columns. Research report R933, School of civil Engineering, The University of Sydney, Australia.

Constructalia (2017). http://www.constructalia.com/ deutsch/ projektgalerie/italien /arco_ di_ malizia_ ponte _piove_di_sacco_brucken_aus_duplexedelstahl #. Retrieved on 18 March 2017.

Dawson, R. G. & Walker, A. C. (1972). Post-buckling of geometrically imperfect plates. *Journal of the Structural Division*, 98, 75-94.

Davis, C.S. (1972). The structural behaviour of cold-formed steel members with perforated elements. Phd Thesis, Department of Civil Engineering, University of Missouri Rolla, Rolla, Missouri.

Dabaon, M.A., El-Boghdadi, M.H. & Hassanein, M.F. (2009). A comparative experimental study between stiffened and unstiffened stainless steel hollow tubular stub columns. *Thin-Walled Structures*, 47, 73-81.

EN 1993-1-4 (1996). Eurocode 3: design of steel structures—part 1.4: general rules—supplementary rules for stainless steel. CEN.

EN 1993-1-1 (2005). Eurocode 3 – Design of steel structures – Part 1-1: General rules and rules for buildings. CEN.

Ellobody, E. & Young, B. (2005). Structural performance of cold-formed high strength stainless steel columns. *Journal of Constructional Steel Research*, 61,1631-1649.

EN 1993-1-3 (2006). Eurocode 3 – Design of steel structures – Part 1-3: General rules – Supplementary rules for cold-formed members and sheeting. CEN.

EN 1993-1-4 (2006). Eurocode 3 – Design of steel structures – Part 1-4: General rules – Supplementary rules for stainless steel. CEN.

Ellobody, E. (2007). Buckling analysis of high strength stainless steel stiffened and unstiffened slender hollow section columns. *Journal of Constructional Steel Research*, 63, 145-155.

Ellobody, E., Feng, R. & Young, B. (2014). Finite element analysis and design of metal structures. Elsevier, Waltham.

EN 1993-1-4 (2015). Eurocode 3 – Design of steel structures – Part 1-4:. General rules – Supplementary rules for stainless steel. EN 1993-1-4: 2006+A1:2015. CEN.

Feinstein, G., Erickson, B. & Kempner, J. (1971). Stability of oval cylindrical shells. *Experimental Mechanics*, 11, 514–520.

Forskitt, M. Moon, J.R. & Brook, P.A. (1991). Elastic properties of plates perforated by elliptical holes. *Applied Mathematical Modelling,* 15,182-190.

Faxing, D., Lei, F., Zhiwu, Y. & Gang, L. (2015). Mechanical performances of concrete- filled steel tubular stub columns with round ends under axial loading. *Thin-Walled Structures*, 97, 22–34.

Gardner, L. (2002). A new approach to structural stainless steel design. Phd Thesis. Structures Section. Department of Civil and Environmental Engineering. Imperial College London.

Gardner, L. & Ministro, A. (2004). Testing and numerical modelling of structural steel oval hollow sections, 04-002-ST. London, Department of civil and environmental engineering, Imperial college.

Gardner, L. & Nethercot, D.A. (2004a). Numerical modeling of stainless steel structural components-A consistent approach. *Journal of Structural Engineering*, 130, 1586-1601.

Gardner, L. & Nethercot, D.A. (2004b). Stainless steel structural design: a new approach. *The Structural Engineer*, 82, 21-28.

Gardner, L. & Nethercot, D.A. (2004c). Experiments on stainless steel hollow sections-part 2: Member behaviour of columns and beams. *Journal of Constructional Steel Research*, 60, 1319-1332.

Gardner, L. (2005). The Use of stainless steel in structures. *Progress in Structural Engineering and Materials*, 7, 45-55.

Gardner, L. & Ashraf, M. (2006). Structural design for non-linear metallic materials. *Engineering Structures*, 28, 926-934.

Gardner, L., Cruise, R.B., Sok, C.P., Krishnan, K. & Santos, J.M.D. (2007). Life-cycle costing of metallic structures. *Proceedings of the Institution of Civil Engineers-Engineering Sustainability*, 160, 167-177.

Gardner, L. (2008). The continuous strength method. *Proceedings of the institution of Civil Engineers-Structures and Buildings*, 161, 127-133.

Gardner, L., Chan, T.M. & Wadee, M.A. (2008). Shear response of elliptical hollow sections. *Proceedings of the Institution of Civil Engineers - Structures and Buildings*, 161, 301–309.

Gardner, L. (2010). Recent research on stainless steel tubular structures. *Proceedings of the Tubular Structures* XIII, Hong Kong. 249-256,

Gardner, L., Chan, T.M. & Abela, J.M. (2011). Structural behavior of elliptical hollow sections under combined compression and uniaxial bending. *Advanced Steel Construction*, 7, 86-113.

Ghazijahani, T.G., Jiao, H. & Holloway, D. (2015). Structural behavior of shells with different cutouts under compression: An experimental study. *Journal of Constructional Steel Research*, 105, 129-137.

Gardner, L. (2016). The continuous strength method for steel, stainless steel and aluminium structural design. *Proceedings of the Eighth International Conference on Steel and Aluminium Structures*, Hong Kong,

Hill, H.N. (1944). Determination of stress-strain relations from "offset" yield strength values. Technical note no 927, National Advisory Committee for Aeronautics, Washington.

Hutchinson, J.W. (1968). Buckling and initial post-buckling behavior of oval cylindrical shells under axial compression. *Journal of Applied Mechanics*, 35, 66-72.

Hancock, G.J., Kwon Y.B. & Bernard, E.S. (1994). Strength design curves for Thin-Walled sections undergoing distortional buckling. *Journal of Constructional Steel Research*, 31, 169-186.

Han, H., Cheng, J., Taheri, F. & Neil, P. (2006). Numerical and experimental investigations of the response of aluminum cylinders with a cutout subject to axial compression. *Thin-Walled Structures*, 44, 254-270.

Haque, T.M. (2011). Elliptical hollow section T and X connections. Masters Thesis. Department of Civil Engineering. University of Toronto, Toronto.

Hassanein, M. (2011). Finite element investigation of shear failure of lean duplex stainless steel plate girders. *Thin-Walled Structures*, 49, 964-973.

Huang. Y. & Young, B. (2012). Material properties of cold-formed lean duplex stainless steel sections. *Thin-Walled Structures*, 54, 72-81.

Huang, Y. & Young, B. (2013). Tests of pin-ended cold-formed lean duplex stainless steel columns. *Journal of Constructional Steel Research*, 82, 203-215.

Huang, Y. & Young, B. (2014a). Experimental investigation of cold-formed lean duplex stainless steel. *Thin Walled Structures*, 76, 105-117.

Huang, Y. &Young, B. (2014b). Structural performance of cold-formed lean duplex stainless steel columns. *Thin-Walled Structures*, 83, 59-69.

Huang, Y. & Young, B. (2015). Design of Cold-Formed Lean Duplex Stainless Steel Members in Combined Compression and Bending. *Journal of Structural Engineering*, 141, 1–10.

Hok (2017). http://www.hok.com/about/news/2016/03/24/skytrax-ranks-hamad-in-terna tional-airport-as-the-worlds-best-in-2016-awards/. Retrieved on 20th March 2017.

Johnson, A.L. & Winter, G. (1966). Behaviour of stainless steel columns and beams. *Journal of the Structural Division*, 92, 97-118.

Jullien, J.F. & Limam, A. (1998). Effect of openings on the buckling of cylindrical shells subjected to axial compression. *Thin-Walled Structures*, 31,187– 202.

Kempner, J. (1962). Some results on buckling and post-buckling of cylindrical shells. Collected papers on Instability of shell structures. *National Aeronautics and Space Administration*, Technical Report TN D-1510, 173-186.

Kempner, J. & Chen, Y. N. (1964). Large deflections of an axially compressed oval cylindrical shell. *Proceedings of the 11th International Congress of Applied Mechanics*, Munich, 299-305.

Kempner, J. & Chen, Y. N. (1966). Buckling and post buckling of an axially compressed oval cylindrical shell. PIBAL Report, 917, Department of Aerospace Engineering and Applied Mechanics, Polytechnic Institute of Brooklyn, Brooklyn.

Kempner, J. & Chen, Y.N. (1969). Postbuckling of an axially compressed oval cylindrical shell. *Proceedings of the 12th International Congress of Applied Mechanics*, Stanford University, Stanford, 246-256.

Kulatunga, M.P. & Macdonald, M. (2013). Investigation of cold-formed steel structural members with perforations of different arrangements subjected to compression loading. *Thin-Walled Structures*, 67, 78-87.

Lind, N.C., Ravindra, M.K. & Power, J. (1971). A review of the effective width formula. *1st International Specialty Conference on Cold-Formed Steel Structures*, Missouri University of Science and Technology, Missouri, 37-42.

Lin, S.H., Yu, W.W. & Galambos, T.V. (1988). Load and resistance factor design of cold-formed stainless steel, statistical analysis of material properties and development of the LRFD provisions, Fourth progress report, Civil Engineering study 88-6, Department of Civil Engineering, University of Missouri-Rolla, Missouri.

Liu, Y. & Young, B. (2003). Buckling of stainless steel square hollow section compression members. *Journal of Constructional Steel Research*, 59, 165-177.

Marguerre, K. (1951). Stability of the cylindrical shell of variable curvature. Technical Memorandum 1302, *National Advisory Committee for Aeronautics*, Washington.

Mann, A.P. (1993). The structural use of stainless steel. *The Structural Engineer*, 71, 60-69.

Murakami, S., Nishimura, Takeuchi, S., Inoguchi, H. & Jikuya, K. (1998). Ultimate strength of cylindrical tubular columns with circular perforation. *Second international conference on Thin-Walled Structures*, Department of civil engineering, National University of Singapore, Singapore, 587-594.

Mirambell, E. & Real, E. (2000). On the calculation of deflections in structural stainless steel beams: an experimental and numerical investigation. *Journal of Constructional Steel Research*, 54, 109-133.

Moen, C.D. & Schafer, B.W. (2011). Direct Strength Method for design of cold-formed steel columns with holes. *Journal of Structural Engineering*, 137, 559-570.

McCann, F., Fang, C., Gardner, L. & Silvestre, N. (2016). Local buckling and ultimate strength of slender elliptical hollow sections in compression. *Engineering Structures*, 111, 104-118.

Metalresources (2017) http://www.metalresources.net/index.php/about/news-press-releas-es /204-stunning-hamad-international-airport-doha-is-largest-stainless-steel-roof. Retrieved on 18 March 2017.

NACA 840 (1942). Tensile and pack compressive tests of some sheets of Aluminium alloy, 1025 carbon steel and chromium-nickel steel. *Technical Note No. 840, National Advisory Committee for Aeronautics,* Washington.

Narayanan, R. & Chow, F.Y. (1983). Effective widths of plates loaded uniaxially. *Thin-Walled Structures*, 1, 165-187.

Narayanan, R. & Chow, F.Y. (1984). Ultimate capacity of uniaxially compressed perforated plates. *Thin-Walled Structures*, 2, 241-264.

NAS (2007). North American Specification for the Design of Cold-Formed Steel Structural Members. Washington, DC: *American Iron and Steel Institute*, Washington.

Nowzartash, F. & Mohared, M. (2011). Column curves for elliptical hollow section members. *Journal of Constructional Steel Research*, 67, 1525-1536.

NCCI (2013). The continuous strength method for structural stainless steel design. http://www.steel-ncci.co.uk/Clauses/List-NCCIs. UK.

Niu, S., Rasmussen, K.J.R. & Fan, F. (2015). Local – Global Interaction Buckling of Stainless Steel I-Beams . II : *Numerical Study and Design*, 141, 1–13.

Ortiz-Colberg, R. (1981). The load carrying capacity of perforated cold-formed steel columns. Masters Thesis. Cornell University, Ithaca.

Pennington-Vann, W. (1971). Compressive buckling of perforated plate elements. *Proceedings of the First Specialty Conference on Cold-Formed Structures*, University of Missouri-Rolla, Missouri, 52-57.

Parks, M.B. & Yu, W.W. (1987). Structural behavior of members consisting of flat and curved elements. SAE Technical Paper Series 870464.

Parks, M.B. & Yu, W.W. (1989). Local buckling behavior of stiffened curved elements. *Thin-Walled Structures*, 7, 1-22.

Pham, C.H. & Hancock, G.J. (2012). Direct strength design of cold-formed C-sections for shear and combined actions. *Journal of structural engineering*, 138, 759-768.

Patton, M.L. & Singh, K.D. (2012). Numerical modelling of lean duplex stainless steel hollow columns of square, L-, T-, and + - shaped sections under pure axial compression. *Thin-Walled Structures*, 53, 1-8.

Patton, M.L. & Singh, K.D. (2013). Buckling of fixed-ended lean duplex stainless steel hollow columns of square , L- , T- , and + -shaped sections under pure axial compression — a finite element study. *Thin-Walled Structures*, 63,106-116.

Pham, S.H., Pham, C.H. & Hancock, G.J. (2014). Direct strength method of design for shear including sections with longitudinal web stiffeners. *Thin-Walled Structures*, 81, 19-28.

Ramberg, W. & Osgood, W.R. (1943). Description of stress-strain curves by three parameters. *Technical Note No. 902, National advisory committee for aeronautics*, Washington.

Riks, E.(1972). The application of Newton's method to the problem of elastic stability. *Journal of Applied mechanics*, 39,1060-1065.

Riks, E. (1979). An incremental approach to the solution of snapping problems. *International Journal of Solids and Structures*, 15, 529-551.

Ridley-Ellis, D.J., Owen, J.S. & Davies. G. (2003). Torsional behavior of rectangular hollow sections. *Journal of Constructional Steel Research*, 59, 641-663.

Rasmussen, K.J.R. (2003). Full-range stress-strain curves for stainless steel alloys. *Journal of Constructional Steel Research*, 59, 47-61.

Ruiz-Teran, A.M. & Gardner, L. (2008). Elastic buckling of elliptical tubes. *Thin-Walled Structures*, 46, 1304–1318.

REF (2014). Research Excellence Framework, Impact case study (REF3b), http:// impact.ref.ac.uk/ casestudies2 /refservice.svc / Get Case Study PDF/ 42181, Imperial college, London.

Ruukki (2017). http://sei.ckcest.cn/ product_img/100001/8408/533557/ Document/ Form% 20220% 20370_TP_12.2008_EN.pdf. Retrieved on 20th March 2017.

Shanmugam, N.E. (1997). Openings in thin-walled steel structures. *Thin-Walled Structures*, 28, 355-372.

Sun, J. & Butterworth, J.W. (1998). Behaviour of steel single angle compression members axially loaded through one leg. *Proceedings of the Australian Structural Engineering Conference*, Auckland. 859 - 866.

Schafer, B. W. & Pekoz, T. (1998). Direct strength prediction of cold formed steel members using numerical elastic buckling solutions. *Proceeding of 14th International Specialty Conference on Cold-Formed Steel Structures*, University of Missouri-Rolla, Missouri, 69–76.

Sivakumaran, K.S. & Abdel-Rahman (1998). A finite element analysis model for the behavior of cold-formed steel members. *Thin-Walled Structures*, 31, 305-324.

Schafer, B.W. (2002). Progress on the direct strength method. *Proceeding of 16th International Specialty Conference on Cold-formed Steel Structures*, Orlando. 647–662.

Schafer, B.W. (2006). Review: The Direct Strength Method of cold-formed steel member design. *Stability and Ductility of Steel Structures*, Lisbon. 6-8.

Schafer, B. & Adany, S. (2006). Buckling analysis of cold-formed steel members using CUFSM: conventional and constrained finite strip methods. *Eighteenth international specialty conference on cold-formed steel structures*, Orlando. 39-54.

Silvestre, N. (2008). Buckling behaviour of elliptical cylindrical shells and tubes under compression. *International Journal of Solids and Structures*, 45, 4427–4447.

Schafer, B. W. (2008). Review: The direct strength method of cold-formed steel member design. *Journal of Constructional Steel Research*, 64, 766–778.

Shariati, M. & Rokhi, M.M. (2008). Numerical and experimental investigations on buckling of steel cylindrical shells with elliptical cutout subject to axial compression. *Thin-Walled Structures*, 46, 1251-1261.

Shariati, M. & Rokhi, M.M. (2010). Buckling of steel cylindrical shells with an elliptical cutout. *International Journal of Steel Structures*, 10, 193-205.

Silvestre, N. & Gardner, L. (2011). Elastic local post-buckling of elliptical tubes. *Journal of Constructional Steel Research*, 67, 281-292.

Silvestre, N., Pires, T. & Duarte, A.P.C. (2013). Numerical analysis of semi-elliptical hollow section columns. *Proceedings of the institution of Civil Engineers, Structures and Buildings*, 166, 424-433.

Saliba, N. & Gardner, L. (2013a). Cross-section stability of lean duplex stainless steel welded I-sections. *Journal of Constructional Steel Research*, 80, 1–14.

Saliba, N. & Gardner, L. (2013b). Experimental study of the shear response of lean duplex stainless steel plate girders. *Engineering Structures*, 46, 375-391.

Structurae (2017). https://structurae.net/structures/cala-galdana-bridge. Retrieved on 20th March 2017.

TataSteelConstruction (2017). https://www.tatasteelconstruction.com/en_GB/Products / structural-buildings-and-bridges. Retrieved on 18 March 2017.

Tennyson, R.C., Booton, M. & Caswell, R.D. (1971). Buckling of imperfect elliptical cylindrical shells under axial compression. *AIAA Journal*, 9, 250–255.

Tvegraard, V. (1976). Buckling of elastic-plastic oval cylindrical shells under axial compression. *International Journal of Solids Structures*, 12, 683-691.

Talja, A. & Salmi, P. (1995). Design of stainless steel RHS beams, columns and beam-columns. Research Note 1619, VTT Building Technology, Finland.

Trahair, N.S., Bradford, M.A., Nethercot, D.A. & Gardner, L.(2008). The behaviour and design of steel structures to EC3,CRC Press.

Theofanous, M., Chan, T.M. & Gardner, L. (2009a). Structural response of stainless steel oval hollow section compression members. *Engineering Structures*, 31, 922-934.

Theofanous, M., Chan, T.M. & Gardner, L. (2009b). Flexural behaviour of stainless steel oval hollow sections. *Thin-Walled Structures*, 47, 776-787.

Theofanous, M. & Gardner, L. (2009). Testing and numerical modelling of lean duplex stainless steel hollow section columns. *Engineering Structures*, 31, 3047-3058.

Theofanous, M. & Gardner, L. (2010). Experimental and numerical studies of lean duplex stainless steel beams. *Journal of Constructional Steel Research*, 66, 816-825.

Theofanous, M. & Gardner, L. (2011). Effect of element interaction and material nonlinearity on the ultimate capacity of stainless steel cross-sections. *Steel and Composite Structures*, 12, 73-92.

Theofanous, M., Liew, A. & Gardner, L. (2012). Ultimate capacity of stainless steel RHS subjected to combined compression and bending. *Proceeding of Tubular Structures* XIV, London, 423-430.

Umbarkar, K.R., Patton, L.M. & Singh, K.D. (2013). Effect of single circular perforation in lean duplex stainless steel (LDSS) hollow circular stub columns under pure axial compression. *Thin-Walled Structures*, 68, 18-25.

Vann, W.P. (1971). Compressive buckling of perforated plate elements. *Proceedin--gs of the First Specialty Conference on Cold-Formed Structures*, University of Missouri-Rolla, Missouri, 52-57.

Virdi, K.S. (1981). Design of circular and rectangular hollow section columns. *Journal of Constructional Steel Research*, 1, 35-45.

Vartdal, B.J., Al-Hassani, S.T.S. & Burley, S.J. (2006). A tube with a rectangular cut-out. Part 2: subject to axial compression. *Proceedings of the Institution of Mechanical Engineers, Part C: Journal of Mechanical Engineering Science*, 220, 652-643.

Winter, G. (1948). Performance of Thin Steel Compression Flanges. International Association for Bridge and Structural Engineering, Congress Report, Liege.

Wang, Z., Chen, J., Xie, E. & Lin, S. (2014). Behavior of concrete-filled round-end steel tubular steel columns under axial compression. *Journal of Building Structures*, 35,123-130. (In Chinese)

Wikimedia (2017a). https: // commons.wikimedia.org/wiki/ Category:Celtic_ Gateway_ Foot bridge. Retrieved on 18 March 2017.

Wikimedia (2017b). https://commons.wikimedia.org/wiki/File:Sant_Fruit%C3% B3s_1 .JPG. Retrieved on 18 March 2017.

Yu, W. W. & Davis, C.S. (1971). Buckling behaviour and post-buckling strength of perforated stiffened compression elements. *Proceedings of the First Specialty Conference on Cold-Formed Structures*, University of Missouri-Rolla, Missouri, 58-64.

Yeh, M.K., Lin, M.C. & Wu, W.T. (1999). Bending buckling of an elastoplastic cylindrical shell with a cutout. *Engineering Structures*, 21, 996–1005.

Yu, W.W. (2000). Cold-formed steel design. John Wiley & Sons, Inc.

Young, B. & Liu, Y. (2002). Experimental investigation of cold-formed stainless steel RHS columns. *Sixteenth International Specialty Conference on Cold-Formed Steel Structures*; Orlando, 398-414.

Young, B. & Hartono, W. (2002). Compression tests of stainless steel tubular members. *Journal of Structural Engineering*, 128, 754–761.

Yang, Z., Kim, C., Cho, C. & Beom, H.G. (2008). The concentration of stress and strain in finite thickness elastic plate containing a circular hole. *International Journal of Solids and Structures*, 45,713-731.

Yuan, H.X., Wang, Y.Q., Shi, Y.J. & Gardner, L. (2014). Stub column tests on stainless steel built-up sections. *Thin-Walled Structures*, 83, 103-114.

Yao, Z. & Rasmussen, K.J. (2014). Finite element modelling and parametric studies of perforated thin-walled steel columns. Research Report R948, ISSN 1833-2781, School of Civil Engineering, University of Sydney, Sydney.

Zhou, F. & Young, B. (2005). Tests of cold-formed stainless steel tubular flexural members. *Thin-Walled Structures*, 43, 1325-1337.

Zhu, Y. & Wilkinson, T. (2007). Finite element analysis of structural steel elliptical hollow sections in pure compression. *Proceeding of the Tubular Structures XI*, Quebec, 179–186.

Zhu, J. & Young, B. (2011). Cold-formed-steel oval hollow sections under axial compression. *Journal of Structural Engineering*, 137,719-727.

Zhu, J. & Young, B. (2012). Design of cold-formed steel oval hollow section columns. *Journal of Constructional Steel Research*, 71, 26-37.

Zhao, O., Afshan, S. & Gardner, L. (2017). Structural response and continuous strength method design of slender stainless steel cross-sections. *Engineering Structures*, 140, 14-25.

APPENDIX A

SAMPLE DESIGN CALCULATION FOR FIXED ENDED LDSS FLAT OVAL HOLLOW STUB COLUMNS UNDER PURE AXIAL COMPRESSION

The calculation of cross-section resistance for flat oval LDSS hollow stub column specimen *l*300*w*300*r*150*h*900 (i.e. l_f = 300 mm, w = 300 mm, r = 150 mm, h = 900 mm) for Class 3 (t = 3 mm) and Class 4 (t = 20 mm) sections with fixed ended column length of 900 mm as per EN 1993-1-4 (2015), ASCE 8-02 (2002), AS/NZS 4673 (2001) and ASDM (2002) are given below. The typical cross-section geometry of flat oval stub column is shown in Figure A.1.

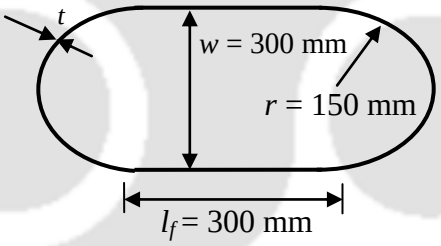

Figure A.1: Schematic diagram for specimen *l*300*w*300*r*150*t*3*h*900.

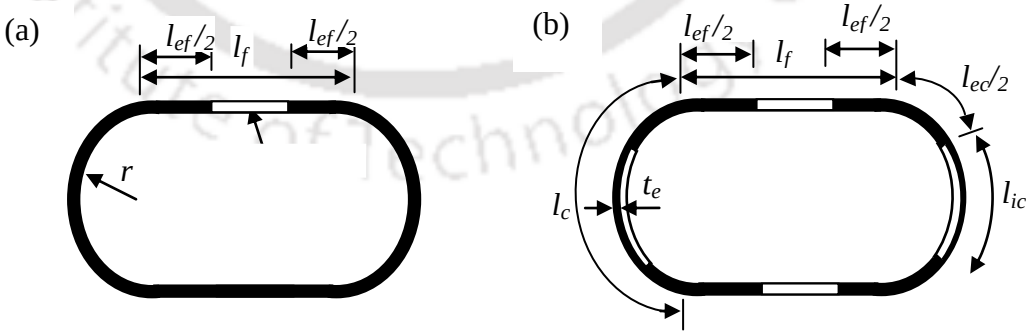

Figure A.2: Effective area representation as per (a) EN 1993-1-4 (2015), ASCE 8-02 (2002) and AS/NZS 4673 (2001), (b) ASDM (2002).

The material properties of LDSS taken from Theofanous and Gardner (2009) are

E = 197200 MPa; f_y or $\sigma_{0.2}$ = 657 MPa

Geometric properties of flat oval section (considering only effective area of flat portion by taking the curve portion as fully effective as per Zhu and Young, 2012) can be calculated as per Equation A.1:

$$A_g = 2(l_f + \pi r)t \quad \text{(A.1)}$$

$A_g = 2(300 + \pi \times 150)3 = 4627.43$ mm^2 (for t = 3 mm)

$A_g = 2(300 + \pi \times 150)20 = 30849.56$ mm^2 (for t = 20 mm)

As per EN 1993-1-4(2015)

Cross-sections are classified as per Class classification (Equations A.2 – A.3).

$l_f/t\varepsilon \leq 37$ => Class 3 sections (A.2)

$l_f/t\varepsilon > 37$ => Class 4 sections (A.3)

where, $\varepsilon = \left(\frac{235}{f_y}\frac{E}{210000}\right)^{0.5} = \left(\frac{235}{657}.\frac{197200}{210000}\right)^{0.5} = 0.58$

For flat oval section, $l300w300r150t3$ i.e. l_f = 300 mm, t = 3 mm

$l_f/t\varepsilon = 300/(3\times0.58) = 172.41 > 37$; Hence, Class 4 section (slender section).

For flat oval section, $l300w300r150t20$ i.e. l_f = 300 mm, t = 20 mm

$l_f/t\varepsilon = 300/(20\times0.58) = 25.86 < 37$; Hence, Class 3 section (stocky section).

Effective area determination for Class 4 section, $l300w300r150t3$ (Equation A.4)

$$A_e = A_g - (2l_f - 2l_{ef})t \quad \text{(A.4)}$$

The effective length, l_{ef} is calculated by following using Equations A.5 - A.7;

$$\bar{\lambda}_p = \frac{\left(\frac{l_f}{t}\right)}{28.4\varepsilon\sqrt{k}} \quad \text{(A.5)}$$

$$\bar{\lambda}_p = \frac{\left(\frac{300}{3}\right)}{28.4 \times 0.58 \times \sqrt{4.0}} = 3.04$$

$$\rho = \frac{0.772}{\bar{\lambda}_p} - \frac{0.079}{\bar{\lambda}_p{}^2} \quad \text{(A.6)}$$

$= 0.25$ but ≤ 1.0

$l_{ef} = \rho l_f = 0.25 \times 300 = 75$ mm (A.7)

Hence, $A_e = 4627.43 - (2 \times 300 - 2 \times 75)\ 3 = 3277.43$ mm^2

The column capacity as per EN 1993-1-4 (2015) is

$P_{EN} = A_e f_y = 3277.43 \times 657 = 2153271.51$ N = 2153.27 kN (for t = 3 mm)

$P_{EN} = A_g f_y = 30849.56 \times 657 = 20268160.92$ N = 20268.16 kN (for t = 20 mm)

As per ASCE 8-02 (2002)

The effective area of the section ($l300w300r150t3$) is calculated by using Equations A.8-A.10

$$\lambda = \left(\frac{1.052}{\sqrt{k}}\right)\left(\frac{l_f}{t}\right)\left(\sqrt{\frac{f}{E}}\right) = \left(\frac{1.052}{\sqrt{4.0}}\right)\left(\frac{300}{3}\right)\left(\sqrt{\frac{657}{197200}}\right) = 3.04 \quad \text{(A.8)}$$

$f = f_y$ if the element is in compression (Section 2.2.1 of ASCE 8-02, 2002).

$$\rho = \frac{1}{\lambda} - \frac{0.22}{\lambda^2} \text{ but} \leq 1.0 = 0.305 \quad \text{(A.9)}$$

Conditions; For $\lambda \leq 0.673$ $l_{ef} = l_f$

For $\lambda > 0.673$ $l_{ef} = \rho l_f$

$l_{ef} = \rho l_f = 0.305 \times 300 = 91.5$ mm (as $\lambda > 0.673$) (A.10)

Hence, $A_e = 4627.43 - (2 \times 300 - 2 \times 91.5)\ 3 = 3376.43$ mm^2

The column capacity as per ASCE 8-02 (2002) is

$P_{ASCE} = A_e f_y = 3376.43 \times 657 = 2218314.51$ N = 2218.31 kN

As per ASDM (2002)

For specimen *l*300*w*300*r*150*t*3*h*900.

Calculate slenderness factor (λ) for flat plate as per Equation A.11,

$$\lambda = \left(\frac{1.052}{\sqrt{k}}\right)\left(\frac{l_f}{t}\right)\left(\sqrt{\frac{f}{E}}\right) \tag{A.11}$$

where, $k = 4$, $l = l_f$ = actual length of one flat portion,

f = stress in element, where $f = f_y$ for materials with yield strengths of $f_y = 552$ MPa

For stiffened compression elements with $f_y > 552$ MPa, a reduced yield strength (f_{yrs}) as given by Equation A.12 be substituted for limiting value of f (see Section 3.1.2.1.1 of ASDM 2002), since the cross-section capacity is determined by flat plates, the reduced stress is also calculated based on flat plate for the whole section.

$$f_{yrs} = \left(1 - 0.2\sqrt{\frac{l_f}{t}}\sqrt{\frac{f_y}{E}}\right) f_y = \left(1 - 0.2\sqrt{\frac{300}{3}}\sqrt{\frac{657}{197200}}\right)657 = 581.16\,\text{MPa} \tag{A.12}$$

$$\lambda = \left(\frac{1.052}{\sqrt{4.0}}\right)\left(\frac{300}{3}\right)\left(\sqrt{\frac{581.16}{197200}}\right) = 2.86$$

Conditions; For $\lambda \le 0.673$ $l_{ef} = l_f$

For $\lambda > 0.673$ $l_{ef} = l_{ef}$, effective width of flat plate

As per AISI specification for flat plate, the effective area is calculated by using Equations A.13-A.15.

$$l_{ef} = l_f\left(\frac{1 - \frac{0.22}{\lambda}}{\lambda}\right) = 300 \times \left(\frac{1}{2.86} - \frac{0.22}{2.86^2}\right) = 96.83 \tag{A.13}$$

For fully stiffened compression element with k = 4 and

$$s = 1.28\sqrt{\frac{E}{f_y}} = 1.28\sqrt{\frac{197200}{657}} = 22.18$$

$$l_{ec} = ts\left(1.486 - \frac{0.486S}{\frac{l_c}{t}}\right) = 3x22.18\left(1.486 - \frac{0.486\times 22.18}{466.53/3}\right) = 94.27 \quad \text{(A.14)}$$

The equivalent area, A_o conditions are (A.15)

$$A_o = A \qquad \text{for } \frac{D}{t} \le 0.114\frac{E}{f_y}$$

$$A_o = \left(\frac{2}{3} + \frac{0.038\frac{E}{f_y}}{\frac{D}{t}}\right)A \qquad \text{for } 0.114\frac{E}{f_y} < \frac{D}{t} \le 0.448\frac{E}{f_y}$$

$$A_o = \left(\frac{0.336\frac{E}{f_y}}{\frac{D}{t}}\right)A \qquad \text{for } \frac{D}{t} \ge 0.448\frac{E}{f_y}$$

where, D = Diameter of the curve element = 300 mm

Relations:

$$\frac{D}{t} = \frac{300}{3} = 100$$

$$0.114\frac{E}{f_y} = 0.114\times\frac{197200}{657} = 34.22$$

$$0.448\frac{E}{f_y} = 0.448\times\frac{197200}{657} = 134.47$$

The satisfied condition for A_o is found out as,

$$A_o = \left(\frac{2}{3} + \frac{0.038\frac{E}{f_y}}{\frac{D}{t}}\right)A = \left(\frac{2}{3} + \frac{0.038\frac{197200}{657}}{\frac{300}{3}}\right)4627.43 = 0.78\times 4627.43 = 3612.75mm^2$$

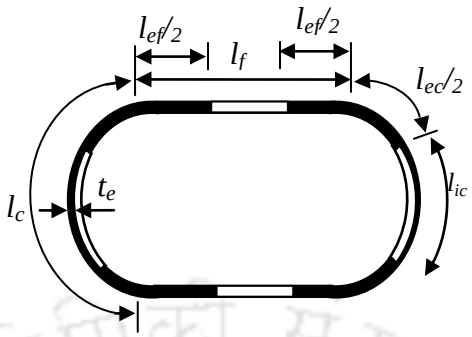

Figure A.3: Effective area calculation of the flat oval section as per ASDM.

The curve portion is stiffer than the flat portion, hence $f = f_y$.

The effective thickness (t_e) for the curve portion is found by using Equation A.16 as shown in Figure A.3,

$$t_e = \left(\frac{A_o}{A}\right)\left(\frac{f_y}{f}\right)t = \left(\frac{3612.75}{4627.43}\right)\left(\frac{657}{581.16}\right)3 = 2.65$$

The effective area is then calculated as using Equations A.17-A.19

Effective area of both side of curve portions, $A_c = 2(l_c - l_{ec})t_e + 2tl_{ec}$ (A.17)

$= 2(466.53 - 94.27)\ 2.65 + 2 \times 3 \times 94.27$

$= 2538.60\ \text{mm}^2$

Effective area of both side of flat portions, $A_f = 2tl_{ef} = 2 \times 3 \times 96.83 = 580.98\ \text{mm}^2$ (A.18)

Total effective area of flat oval section $A_e = A_c + A_f$ (A.19)

$= 2538.60 + 580.98$

$= 3119.58\ \text{mm}^2$

The member capacity of ASDM (2002) is then given by,

$P_{ASDM} = f_y A_e = 657 \times 3119.58 = 2049564.06\ \text{N} = 2049.56\ \text{kN}$

PROPOSED MODIFIED ASDM, EN 1993-1-4 (2015), AS/NZS 4673 (2001)

(for slender section i.e. $w/t \geq 40$)

The modification to ASDM has been suggested only for slender ($w/t \geq 40$) sections column (see Chapter 3), through modified effective thickness (t_{em}) for the curve element (Equation A.20). Substituting appropriate values for $l300w300r150t3$ sample,

$$t_{em} = 0.5\left(\frac{A_o}{A}\right)\left(\frac{f_y}{f}\right)t = 0.5\left(\frac{3612.75}{4627.43}\right)\left(\frac{657}{581.16}\right)3 = 1.325 \quad \text{(A.20)}$$

The effective area of flat oval section is found using Equations A.21-A.23.

Effective area of both side of curve portions,

$$A_c = 2(l_c - 2\times l_{ec})t_{em} + 2tl_{ec} \quad \text{(A.21)}$$
$$= 2(466.53 - 2\times 94.27)\times 1.325 + 2\times 3\times 94.27$$
$$= 1302.29 \text{ mm}^2$$

Effective area of both side of flat portions,

$$A_f = 2tl_{ef} = 2\times 3\times 96.83 = 580.98 \text{ mm}^2 \quad \text{(A.22)}$$

Thus, Total effective area of flat oval section

$$A_e = A_c + A_f \quad \text{(A.23)}$$
$$= 1302.29 + 580.98$$
$$= 1883.27 \text{ mm}^2$$

The member capacity of ASDM (2002) is calculated as

$$P_{ASDM\ (p)} = f_y A_e = 657\times 1883.27 = 1237308.39 \text{ N} = 1237.31 \text{ kN}$$

Similarly, using the modified effective thickness expression (Equation A.20), proposed modified design capacity can be computed for EN 1993-1-4 (2015) and AS/NZS 4673 (2001). Thus,

Total effective area of flat oval section (EN 1993-1-4)
($l_{ef} = \rho l_f = 0.25\times 300 = 75$ mm)

$$A_e = A_c + A_f$$
$$= 1302.29 + 75\times 2\times 3$$
$$= 1752.29 \text{ mm}^2$$

Total effective area of flat oval section	$A_e = A_c + A_f$
(AS/NZS 4673)	$= 1302.29+91.5\times2\times3$
($l_{ef} = \rho l_f = 0.305\times 300 = 91.5$ mm)	$= 1851.29$ mm^2

$P_{EN\ 1993\text{-}1\text{-}4\ (p)} = f_y A_e = 657\times 1752.29 = 1151254.53$ N $= 1151.25$ kN

$P_{AS/NZS\ 4673\ (p)} = f_y A_e = 657\times 1851.29 = 1216297.53$ N $= 1216.30$ kN

As per, DIRECT STRENGTH METHOD (DSM)

The calculation of design strength using DSM are shown below,

A = Gross cross-section area.

A_g or $A = 2(300 + \pi \times 150)3 = 4627.43$ mm^2 for $l300w300r150t3$ ($t = 3$ mm)

A_g or $A = 2(300 + \pi \times 150)25 = 38561.94$ mm^2 for $l300w300r150t25$ ($t = 25$ mm)

h = Column height = 900 mm, h_e = Column effective length = 450 mm

$f_y = 657$ MPa, $E = 197200$ MPa, $h = 900$ mm, $h_e = 450$ mm,

The value of σ_{crl} (critical stress) is found using Abaqus (2009), using Equation A.24,

$$\sigma_{crl} = E\varepsilon = E\lambda\frac{\Delta h}{h} \tag{A.24}$$

where, E is the material Young's modulus, λ is eigen value obtained from FE analysis, Δh is initial displacement at the movable end and h is the height of column.

$\sigma_{crl} = 78.934$ for $l300w300r150t3$ ($t = 3$ mm)

$= 3220.28$ for $l300w300r150t25$ ($t = 25$ mm)

P_{crl} = Critical elastic local buckling load = $\sigma_{crl} \times A$

$= 365261.56$ for $l300w300r150t3$ ($t = 3$ mm)

= 124180089.9 for *l*300*w*300*r*150*t*25 (*t* = 25 mm)

P_y = A × f_y = 3040222 MPa for *t* = 3 mm

= 25335195 MPa for *t* = 25 mm.

Minimum I = 70562426.68 mm^4 for *t* = 3 mm

= 490235221.70 mm^4 for *t* = 25 mm.

r_y = Radius of gyration of gross cross-section about the minor y-axis of buckling

= 123.86 for *t* = 3 mm

= 115.74 for *t* = 25 mm.

Critical elastic buckling load in flexural buckling (P_{cre}) is found using Equation A.25.

$$P_{cre} = \pi^2 EA/(h_e/r_y)^2, \quad \text{(A.25)}$$

P_{cre} = 681673044.50 for *t* = 3 mm

= 4959545484.00 for *t* = 25 mm.

The nominal axial strength for local buckling (P_{nl}) and nominal strength for flexural buckling (P_{ne}) are found out using Equations A.26-A.29.

P_{nl} = nominal axial strength for local buckling as well as interaction of local and overall buckling.

P_{ne} = nominal axial strength for flexural buckling.

$$\lambda_c = \sqrt{P_y / P_{cre}} \quad \text{(A.26)}$$

= 0.067 for *t* = 3 mm

= 0.071 for *t* = 25 mm.

$$p_{ne} = \begin{cases} (0.658^{\lambda_c^2})P_y & \text{for } \lambda_c \le 1.5 \\ \left(\frac{0.877}{\lambda_c^2}\right)P_y & \text{for } \lambda_c \le 1.5 \end{cases} \quad \text{(A.27)}$$

$\lambda_l = \sqrt{P_{ne}/P_{crl}}$ = 2.88 for t = 3 mm and 0.45 for t = 25 mm. (A.28)

$$P_{nl} = \begin{cases} P_{ne} & \text{for } \lambda_l \le 0.776 \\ \left[1 - 0.15\left(\frac{P_{crl}}{P_{ne}}\right)^{0.4}\right]\left(\frac{P_{crl}}{P_{ne}}\right)^{0.4} P_{ne} & \text{for } \lambda_l > 0.776 \end{cases} \quad \text{(A.29)}$$

Using above values, P_{nl} = 1217388.00 N for t = 3 mm and 25281083.00 N for t = 25 mm. Now the design capacity as per DSM is given by,

$$p_{DSM} = \min(P_{ne}, P_{nl}) \quad \text{(A.30)}$$
= 1217.39 kN for t = 3 mm

= 25281.08 kN for t = 25 mm

As per, CONTINUOUS STRENGTH METHOD (CSM)

For specimen *l*300*w*300*r*150*t*15,

f_y = 657 MPa, Ultimate strength, f_u = 840.71 MPa, E = 197200, h = 900 mm, $\sigma_{cr,cs}$ = 1437.76 MPa (elastic buckling stress of full cross-section, from FE) δ_u = 6.44, ε_y = 0.0033 , A = 22430.30 mm^2

$\varepsilon_y = \frac{f_y}{E}$ = 0.0033, ε_u = 0.2185

Cross-section slenderness based on centerline dimensions (NCCI, 2013) is given by Equation A. 31.

$$\bar{\lambda}_p = \sqrt{\frac{f_y}{\sigma_{cr,cs}}} \quad \text{(A.31)}$$

$$\bar{\lambda}_p = \sqrt{\frac{f_y}{\sigma_{cr,cs}}} = \sqrt{\frac{657}{1437.76}} = 0.676 \qquad \text{(i.e. } \leq 0.68\text{, hence CSM is applicable)}$$

Cross-section deformation capacity is given by Equation A.32.,

$$\frac{\varepsilon_{csm}}{\varepsilon_y} = \frac{0.25}{\bar{\lambda}_p^{3.6}} \text{ but } \frac{\varepsilon_{csm}}{\varepsilon_y} \leq \min\left(15, \frac{0.1\varepsilon_u}{\varepsilon_y}\right) \tag{A.32}$$

$$\varepsilon_u = 1 - \frac{f_y}{f_u} = 1 - \frac{657}{840.71} = 0.219$$

$$0.1\frac{\varepsilon_u}{\varepsilon_y} = 0.1\frac{0.219}{0.0033} = 6.562$$

$$\varepsilon_{csm} = \frac{\delta_u}{h} - 0.002 = \frac{6.44}{900} - 0.002 = 0.0052$$

$$\frac{\varepsilon_{csm}}{\varepsilon_y} = \frac{0.25}{\bar{\lambda}_p^{3.6}} = \frac{0.25}{0.68^{3.6}} = 1.002$$

Conditions are satisfied for CSM.

Strain hardening slope is calculated as per Equation A.33.

$$E_{sh} = \frac{f_u - f_y}{0.16\varepsilon_u - \varepsilon_y} \tag{A.33}$$

$$E_{sh} = \frac{f_u - f_y}{0.16\varepsilon_u - \varepsilon_y} = \frac{840.71 - 657}{0.16 \times 0.219 - 0.0033} = 5787.96$$

Cross-section compression resistance is calculated using Equation A.34,

$$f_{csm} = f_y + E_{sh}\varepsilon_y\left(\frac{\varepsilon_{csm}}{\varepsilon_y} - 1\right) \tag{A.34}$$

$$f_{csm} = f_y + E_{sh}\varepsilon_y\left(\frac{\varepsilon_{csm}}{\varepsilon_y} - 1\right) = 657 + 5787.96 \times 0.0033(1.002 - 1) = 657.038 N/mm^2$$

The column capacity as per CSM is given by Eq. A.35.

$$P_{csm} = f_{csm} \times A \tag{A.35}$$

P_{csm} = 657.038 × 22430.30 = 14737559.45 N = 14737.56 kN

APPENDIX B

SAMPLE DESIGN CALCULATION FOR FIXED ENDED LDSS FLAT OVAL HOLLOW SLENDER COLUMNS UNDER PURE AXIAL COMPRESSION

The calculation of cross-section resistance for fixed ended flat oval LDSS hollow slender column specimens *l*50*w*50*r*25*t*2*h*2000 and for Class 4 (t = 2 mm) and Class 3 (t = 15 mm) as per EN 1993-1-4 (2015), and AS/NZS 4673 (2001) are given below. The typical cross-section geometry of flat oval stub column is shown in Figure B.1.

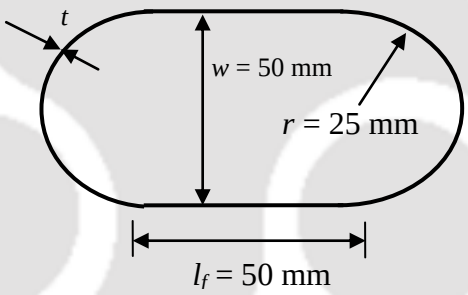

Figure B.1: Schematic diagram for specimen *l*50*w*50*r*25*t*2*h*2000

The material properties of LDSS taken from Theofanous and Gardner (2009) are

E= 197200 MPa;

f_y or $\sigma_{0.2}$ = 657 MPa;

n = 4.7, h = 2000 mm,

k = 4, $\Psi = \sigma_1/\sigma_2 = 1$

Class classification:

As per EN 1993-1-4(2015)

Cross-sections are classified as per Equations A.2 – A.3.

$l_f/t\varepsilon \leq 37$ => Class 3 sections and $l_f/t\varepsilon > 37$ => Class 4 sections

$$\varepsilon = \left(\frac{235E}{f_y \times 210000} \right)^{0.5} = 0.58,$$

h_e(effective height for fixed ends) = (h/2) = 2000/2 = 1000 mm

For l50w50r25t2, $l_f/t\varepsilon$ = 50/(2 × 0.58) = 43.10 > 37 so, Class 4.

For l50w50r25t10, $l_f/t\varepsilon$ = 50/(10 × 0.58) = 8.62 < 37 so, Class 3.

Slenderness value and effective length are calculated as per Equations A.5-A.7,

$$\bar{\lambda}_p = \frac{l_f / t}{28.4\varepsilon\sqrt{k}} = \frac{50/2}{28.4 \times 0.58\sqrt{4}} = 0.759$$, for t = 2 mm (Class 4) and

$$= \frac{50/10}{28.4 \times 0.58\sqrt{4}} = 0.1518,$$ for t = 10 mm (Class 3).

Reduction factor, ρ: for t = 2 mm,

$$\rho = \frac{0.772}{\bar{\lambda}_p} - \frac{0.079}{\bar{\lambda}_p{}^2} = \frac{0.772}{0.759} - \frac{0.079}{0.759^2} = 0.88$$

For t = 10 mm (Class 3 section), ρ = 1 as there is no reduction.

$l_{ef} = \rho l_f$ = 0.88 × 50 = 44.00 mm for t = 2 mm

= 1.00 × 50 = 50 mm for t = 10 mm

Effective area is calculated only for the flat portion as per EN 1993-1-4 (2015) while all curve portions are taken as fully effective.

For Class 3 (t = 10 mm), A_g = 2256.64 mm^2

For Class 4, t = 2 mm, effective area (A_e = 461.59 mm2) is calculated as,

$A = A_g = 501.59$ mm^2 (Class 4, t = 2 mm)

$A_e = A_g - \mathbf{2}(l_f - l_{ef})t = 501.59 - 2(50 - 44)2 = 477.59$ mm^2 (Class 4)

The column capacity as per EN1993-1-4 (P_{EN}) is computed by using Equation B.1.

$$P_{EN} = \chi f_y A \tag{B.1}$$

The required constants are taken as, imperfection factor, $\alpha = 0.49$ and $\bar{\lambda}_0 = 0.40$ (As per EN 1993-1-4 (2015). The value of χ is computed using Equation B.2.

$$\chi = \frac{1}{\phi + \left[\phi^2 - \bar{\lambda}^2\right]^{0.5}} \leq 1 \tag{B.2}$$

,

where, $\phi = 0.5\left(1 + \alpha\left(\bar{\lambda} - \bar{\lambda}_0\right) + \bar{\lambda}^2\right)$ (B.3)

and, $\bar{\lambda} = \sqrt{\frac{Af_y}{N_{cr}}}$; $N_{cr} = \frac{\pi^2 EI}{h^2}$

For Class 3 Section (l50w50r25t10h2000), slenderness ratio ($\bar{\lambda}$) is given by Equation B.4.

$$\bar{\lambda} = \left(\frac{h_e}{R} \times \frac{1}{\lambda_1}\right) \tag{B.4}$$

where, $\lambda_1 = \pi\sqrt{\frac{E}{f_y}} = \pi\sqrt{\frac{197200}{657}} = 54.43$

where, $R = \sqrt{\frac{I}{A}} = \sqrt{\frac{675368.7}{2256.637}} = 17.29$ and

effective length, $h_e = h/2 = 2000/2 = 1000$ mm. thus,

$$\bar{\lambda} = \frac{h_e}{R} \times \frac{1}{\lambda_1} = \frac{1000}{17.29} \times \frac{1}{54.43} = 1.06$$

$$\phi = 0.5\left(1+\alpha\left(\bar{\lambda}-\bar{\lambda}_0\right)+\bar{\lambda}^2\right) = 0.5(1+0.49(1.06-0.40)+1.06^2) = 1.22$$

$$\chi = \frac{1}{\phi+\left[\phi^2-\bar{\lambda}^2\right]^{0.5}} = \frac{1}{1.22+\left[1.22^2-1.06^2\right]^{0.5}} = 0.54$$

$$P_{EN} = \chi f_y A = 0.54\times 657\times 2256.637 = 800609.67N$$

= 800.61 kN

For Class 4 Section (*l*50*w*50*r*25*t*2*h*2000), slenderness ration ($\bar{\lambda}$) is given by Equation B.5.

$$\bar{\lambda} = \frac{h_e}{R}\times\frac{\sqrt{A_e/A}}{\lambda_1} \qquad \text{(B.5)}$$

where,

$$R = \sqrt{\frac{I}{A}} = \sqrt{\frac{202276.20}{501.593}} = 20.082 \quad \text{and}$$

effective length, $h_e = h/2 = 2000/2 = 1000$ mm

$$\bar{\lambda} = \frac{h_e}{R}\times\frac{\sqrt{A_e/A}}{\lambda_1} = \frac{1000}{20.082}\times\frac{\sqrt{477.59/501.593}}{54.43} = 0.892$$

$$\phi = 0.5\left(1+\alpha\left(\bar{\lambda}-\bar{\lambda}_0\right)+\bar{\lambda}^2\right) = 0.5(1+0.49(0.892-0.40)+0.892^2) = 1.02$$

$$\chi = \frac{1}{\phi+\left[\phi^2-\bar{\lambda}^2\right]^{0.5}} = \frac{1}{1.02+\left[1.02^2-0.892^2\right]^{0.5}} = 0.66$$

$$P_{EN} = \chi f_y A_e = 0.66\times 657\times 477.59 = 207092.58N$$

= 207.09 kN

As per AS/NZS 4673 (2001)

The buckling stress coefficients *viz.*, α, β, λ_0, λ_1 values are taken as 1.16, 0.13, 0.65 and 0.42 (corresponding to S31803 (EN 1.4462, duplex); Table 5 of current AS/NZS 4673, 2001) as LDSS material properties are not included in AS/NZS 4673 (2001).

Consider two thicknesses, t = 2 and 10 mm sections i.e. *l*50*w*50*r*25*t*2*h*1000 and *l*50*w*50*r*25*t*10*h*2000 representing Class 4 and Class 3 sections.

Material properties of LDSS taken from Theofanous and Gardner (2009) are,

E = 197200, f_y = 657 MPa, buckling plate coefficient, k = 4,

The values of f_n, Φ, η are given by the following Equations B.6 – B.8.

$$f_n = \frac{fy}{\phi + \sqrt{\phi^2 - \lambda^2}} \leq f_y \tag{B.6}$$

$$\phi = \frac{1}{2}\left(1 + \eta + \lambda^2\right) \tag{B.7}$$

$$\eta = \alpha\left((\lambda - \lambda_1)^\beta - \lambda_0\right) \tag{B.8}$$

For *l*50*w*50*r*25*t*2*h*1000 section,

Gross-area, A = 501.59 mm^2

Slenderness factor λ is given by Equation B.9,

$$\lambda = \left(\frac{1.052}{\sqrt{k}}\right)\left(\frac{l_f}{t}\right)\left(\sqrt{\frac{f_y}{E}}\right) \tag{B.9}$$

$$\lambda = \frac{1.052}{\sqrt{4}} \times \frac{50}{2} \times \sqrt{\frac{657}{197200}} = 0.759$$

$$\rho = \frac{1}{\lambda} - \frac{0.22}{\lambda^2} = \frac{1}{0.759} - \frac{0.22}{0.759^2} = 0.9356 \text{ but } \leq 1.0$$

The effective length is calculated as per Equations B.10-B.11.

For $\lambda \leq 0.673$, $l_{ef} = l_f$ (B.10)

For $\lambda > 0.673$, $l_{ef} = \rho l_f$, (B.11)

So, $l_{ef} = 0.9356 \times 50 = 46.78$ mm

Effective area,

$A_e = A_g - \mathbf{2}(l_f - l_{ef})t = 501.59 - 2(50 - 46.78)2 = 488.71$ mm^2 (Class 4)

$$R = \sqrt{\frac{I}{A}} = \sqrt{\frac{202276.20}{501.593}} = 20.082$$

$$\lambda = \frac{h_e}{R} \times \sqrt{\frac{f_y}{\pi^2 E}} = \frac{500}{20.082} \times \sqrt{\frac{657}{\pi^2 197200}} = 0.4574$$

$$\eta = \alpha\left((\lambda - \lambda_1)^{\beta} - \lambda_0\right) = 1.16((0.4574 - 0.42)^{0.13} - 0.65) = 0.0027$$

$$\phi = \frac{1}{2}\left(1 + \eta + \lambda^2\right) = \frac{1}{2}(1 + 0.0027 + 0.4574^2) = 0.606$$

$$f_n = \frac{fy}{\phi + \sqrt{\phi^2 - \lambda^2}} = \frac{657}{0.606 + \sqrt{0.606^2 - 0.4574^2}} = 654.696 \leq f_y$$

Thus, $P_{AS/NZS} = A_e f_n = 488.71 \times 654.696 = 319956.48$ N $= 319.96$ kN (for $t = 2$ mm)

For *l*50*w*50*r*25*t*10*h*2000 section**:**

Gross area, $A = 2256.6371$ mm^2

Slenderness factor λ is calculated using Equation B.9,

$$\lambda = \left(\frac{1.052}{\sqrt{k}}\right)\left(\frac{l_f}{t}\right)\left(\sqrt{\frac{f_y}{E}}\right) = \frac{1.052}{\sqrt{4}} \times \frac{50}{10} \times \sqrt{\frac{657}{197200}} = 0.1518$$

$$\rho = \frac{1}{\lambda} - \frac{0.22}{\lambda^2} = \frac{1}{0.1518} - \frac{0.22}{0.1518^2} = -2.95 \text{ but} \leq 1.0$$

For $\lambda \leq 0.673$, $l_{ef} = l_f$

For $\lambda > 0.673$, $l_{ef} = \rho l_f$,
So, $l_{ef} = 50$ mm

Effective area,

$A_e = A_g = A = 2256.6371$ mm^2

$$R = \sqrt{\frac{I}{A}} = \sqrt{\frac{675368.70}{2256.6371}} = 17.30$$

$$\lambda = \frac{h_e}{R} \times \sqrt{\frac{f_y}{\pi^2 E}} = \frac{1000}{17.30} \times \sqrt{\frac{657}{\pi^2 197200}} = 1.062$$

$$\eta = \alpha\left(\left(\lambda - \lambda_1\right)^{\beta} - \lambda_0\right) = 1.16((1.062 - 0.42)^{0.13} - 0.65) = 0.341$$

$$\phi = \frac{1}{2}\left(1 + \eta + \lambda^2\right) = \frac{1}{2}(1 + 0.341 + 1.062^2) = 1.234$$

$$f_n = \frac{fy}{\phi + \sqrt{\phi^2 - \lambda^2}} = \frac{657}{1.234 + \sqrt{1.234^2 - 1.062^2}} = 352.767 \le f_y$$

$P_{AS/NZS} = A_e f_n = 2256.6371 \times 352.767 = 796067.099$ N $= 796.07$ kN (for $t = 10$ mm)

MODIFIED AS/NZS 4673 (2001) (Huang and Young, 2014b)

Huang and Young (2014b) proposed that the following values of α, β, λ_o and λ_l for LDSS slender columns for use in AS/NZS 4673 (2001): $\alpha = 0.86$, $\beta = 0.14$, $\lambda_o = 0.67$, $\lambda_l = 0.45$.

For *l*50*w*50*r*25*t*2*h*2000 section,

Gross-area, $A_g = 501.59$ mm^2

Slenderness factor,

$$\lambda = \left(\frac{1.052}{\sqrt{k}}\right)\left(\frac{l_f}{t}\right)\left(\sqrt{\frac{f_y}{E}}\right) = \frac{1.052}{\sqrt{4}} \times \frac{50}{2} \times \sqrt{\frac{657}{197200}} = 0.759$$

$$\rho = \frac{1}{\lambda} - \frac{0.22}{\lambda^2} = \frac{1}{0.759} - \frac{0.22}{0.759^2} = 0.9356 \text{ but} \le 1.0$$

For $\lambda \le 0.673$, $l_{ef} = l_f$

For $\lambda > 0.673$, $l_{ef} = \rho l_f$,
So, $l_{ef} = 0.9356 \times 50 = 46.78$ mm

Effective area,

$A_e = A_g - \mathbf{2}(l_f - l_{ef})t = 501.59 - 2(50 - 46.78)2 = 488.71$ mm^2 (Class 4)

$$R = \sqrt{\frac{I}{A}} = \sqrt{\frac{202276.20}{501.593}} = 20.082$$

$$\lambda = \frac{h_e}{R} \times \sqrt{\frac{f_y}{\pi^2 E}} = \frac{1000}{20.082} \times \sqrt{\frac{657}{\pi^2 197200}} = 0.9149$$

$$\eta = \alpha\left((\lambda - \lambda_1)^{\beta} - \lambda_0\right) = 0.86((0.9149 - 0.45)^{0.14} - 0.67) = 0.196$$

$$\phi = \frac{1}{2}\left(1 + \eta + \lambda^2\right) = \frac{1}{2}(1 + 0.196 + 0.9149^2) = 1.016$$

$$f_n = \frac{fy}{\phi + \sqrt{\phi^2 - \lambda^2}} = \frac{657}{1.016 + \sqrt{1.016^2 - 0.9149^2}} = 450.67 \le f_y$$

$P^*_{AS/NZS} = A_e f_n = 488.71 \times 450.67 = 220246.94$ N $= 220.25$ kN (for $t = 2$ mm)

For *l*50*w*50*r*25*t*10*h*2000 section,

Gross-area, $A = 2256.6371$ mm^2

Slenderness factor,

$$\lambda = \left(\frac{1.052}{\sqrt{k}}\right)\left(\frac{l_f}{t}\right)\left(\sqrt{\frac{f_y}{E}}\right) = \frac{1.052}{\sqrt{4}} \times \frac{50}{10} \times \sqrt{\frac{657}{197200}} = 0.1518$$

$$\rho = \frac{1}{\lambda} - \frac{0.22}{\lambda^2} = \frac{1}{0.1518} - \frac{0.22}{0.1518^2} = -2.95 \text{ but} \le 1.0$$

For $\lambda \le 0.673$, $l_{ef} = l_f$

For $\lambda > 0.673$, $l_{ef} = \rho l_f$,
So, $l_{ef} = 50$ mm

Effective area,

$A_e = A_g = A = 2256.6371$ mm^2

$$R = \sqrt{\frac{I}{A}} = \sqrt{\frac{675368.70}{2256.6371}} = 17.30$$

$$\lambda = \frac{h_e}{R} \times \sqrt{\frac{f_y}{\pi^2 E}} = \frac{1000}{17.30} \times \sqrt{\frac{657}{\pi^2 197200}} = 1.062$$

$$\eta = \alpha\left((\lambda - \lambda_1)^{\beta} - \lambda_0\right) = 0.86((1.062 - 0.45)^{0.14} - 0.67) = 0..227$$

$$\phi = \frac{1}{2}\left(1 + \eta + \lambda^2\right) = \frac{1}{2}(1 + 0.227 + 1.062^2) = 1.177$$

$$f_n = \frac{fy}{\phi + \sqrt{\phi^2 - \lambda^2}} = \frac{657}{1.177 + \sqrt{1.177^2 - 1.062^2}} = 390.04 \le f_y$$

$P^*_{AS/NZS} = A_e f_n = 2256.6371 \times 390.04 = 880178.73$ N $= 880.18$ kN (for $t = 10$ mm)

Considering another section for $l100w50r25t2h2000$ section,

Gross area, $A = 701.593$ mm^2

Slenderness factor,

$$\lambda = \left(\frac{1.052}{\sqrt{k}}\right)\left(\frac{l_f}{t}\right)\left(\sqrt{\frac{f_y}{E}}\right) = \frac{1.052}{\sqrt{4}} \times \frac{100}{2} \times \sqrt{\frac{657}{197200}} = 1.518$$

$$\rho = \frac{1}{\lambda} - \frac{0.22}{\lambda^2} = \frac{1}{1.518} - \frac{0.22}{1.518^2} = 0.563 \text{ but} \le 1.0$$

For $\lambda \le 0.673$, $l_{ef} = l_f$

For $\lambda > 0.673$, $l_{ef} = \rho l_f$,

So, $l_{ef} = 0.563 \times 100 = 56.30$ mm

Effective area,

$A_e = A_g - \mathbf{2}(l_f - l_{ef})t = 701.593 - 2(100 - 56.30)2 = 526.793$ mm^2 (Class 4)

$$R = \sqrt{\frac{I}{A}} = \sqrt{\frac{317542.90}{701.59}} = 21.274$$

$$\lambda = \frac{h_e}{R} \times \sqrt{\frac{f_y}{\pi^2 E}} = \frac{1000}{21.274} \times \sqrt{\frac{657}{\pi^2 197200}} = 0.864$$

$$\eta = \alpha\left((\lambda - \lambda_1)^{\beta} - \lambda_0\right) = 0.86((0.864 - 0.45)^{0.14} - 0.67) = 0.184$$

$$\phi = \frac{1}{2}\left(1 + \eta + \lambda^2\right) = \frac{1}{2}(1 + 0.184 + 0.864^2) = 0.965$$

$$f_n = \frac{fy}{\phi + \sqrt{\phi^2 - \lambda^2}} = \frac{657}{0.965 + \sqrt{0.965^2 - 0.864^2}} = 471.03 \leq f_y$$

$P_{AS/NZS} = A_e f_n$ = 526.793×471.03 = 248135.31 N = 248.14 kN (for t = 2 mm)

DIRECT STRENGTH METHOD (DSM)

σ_{crl} has been obtained from Abaqus (2009) FE following Equation A.24

Consider specimen *l*50*w*50*r*25*t*2*h*2000,

A = Gross cross-section area of flat oval section,

A_g or A = 499.658 mm^2

h = Column height = 2000 mm, h_e = Column effective length = 1000 mm

f_y = 657 MPa, E = 197200 MPa,

r_y = 20.08 mm

Yield load, $P_y = f_y A$

$P_y = A \times f_y$ = 499.658×657 = 328275.31 MPa = 328.28 kN

P_{crl} = 679.53 MPa (From Abaqus, FE analysis by Equation A.21)

$P_{cre} = \pi^2 EA/(h_e/r_y)^2$, critical elastic buckling load in flexural buckling.

= 392.17 kN

$\lambda_c = \sqrt{P_y / P_{cre}}$ = 0.915

$$p_{ne} = \begin{cases} (0.658^{\lambda_c^2})P_y & \text{for } \lambda_c \le 1.5 \\ \left(\frac{0.877}{\lambda_c^2}\right)P_y & \text{for } \lambda_c \le 1.5 \end{cases}$$

$$P_{nl} = \begin{cases} P_{ne} & \text{for } \lambda_l \le 0.776 \\ \left[1 - 0.15\left(\frac{P_{crl}}{P_{ne}}\right)^{0.4}\right]\left(\frac{P_{crl}}{P_{ne}}\right)^{0.4} P_{ne} & \text{for } \lambda_l > 0.776 \end{cases}$$

$$\lambda_l = \sqrt{P_{ne}/P_{crl}} = 0.58$$

Using the above values, P_{ne} = 231.25 kN, P_{nl} = 231.25 kN

Column strength based on DSM:

$$p_{DSM} = \min(P_{ne}, P_{nl})$$

= 231.25 kN

MODIFIED DSM or DSM* (Huang and Young, 2014b)

The modified nominal axial strength, P^*_{DSM} (for LDSS columns; see Huang and Young, 2014b) can be calculated by using Equations B.12-B.14.

$$p^*_{DSM} = \min(P_{ne}, P_{nl}) \quad \text{(B. 12)}$$

$$p_{ne} = \begin{cases} (0.87^{\lambda_c^2})P_y & \text{for } \lambda_c \le 1 \\ \left(\frac{0.877}{\lambda_c^2}\right)P_y & \text{for } \lambda_c \le 1 \end{cases} \quad \text{(B. 13)}$$

$$P_{nl} = \begin{cases} P_{ne} & \text{for } \lambda_l \le 0.769 \\ \left[1 - 0.16\left(\frac{P_{crl}}{P_{ne}}\right)^{0.4}\right]\left(\frac{P_{crl}}{P_{ne}}\right)^{0.4} P_{ne} & \text{for } \lambda_l > 0.769 \end{cases} \quad \text{(B.14)}$$

Thus,

P_{ne} = 292.38 kN, P_{nl} = 292.38 kN

Thus, column strength based on modified DSM is given by,

$$p^*_{DSM} = \min(P_{ne}, P_{nl})$$

$$= 292.38 \text{ kN}$$

APPENDIX C

SAMPLE DESIGN CALCULATION FOR FIXED ENDED LDSS FLAT OVAL HOLLOW STUB COLUMNS WITH SQUARE PERFORATION UNDER PURE AXIAL COMPRESSION

Consider specimen *l*300*w*300*r*150*t*5,

Slenderness factor, λ is computed using Equation A.11,

$$\lambda = \left(\frac{1.052}{\sqrt{4.0}}\right)\left(\frac{300}{5}\right)\left(\sqrt{\frac{598.25}{197200}}\right) = 1.738$$

Reduced yield strength (f_{yrs}) from Equation A.12

$$f_{yrs} = \left(1 - 0.2\sqrt{\frac{l_f}{t}}\sqrt{\frac{f_y}{E}}\right) f_y = \left(1 - 0.2\sqrt{\frac{300}{5}}\sqrt{\frac{657}{197200}}\right)657 = 598.25 \text{ MPa}$$

Effective length, l_{ef} from Equation A.13

$$l_{ef} = l_f\left(\frac{1-\frac{0.22}{\lambda}}{\lambda}\right) = 300 \times \left(\frac{1}{1.738} - \frac{0.22}{1.738^2}\right) = 150.76$$

For fully stiffened compression element with k = 4 and

$$s = 1.28\sqrt{\frac{E}{f_y}} = 1.28\sqrt{\frac{197200}{657}} = 22.18$$

$$l_{ec} = ts\left(1.486 - \frac{0.486S}{\frac{l_c}{t}}\right) = 5x22.18\left(1.486 - \frac{0.486x22.18}{463.38/5}\right) = 151.90$$

The equivalent area, A_o is calculated based on the condition of Equation A.15

$$A_o = \left(\frac{2}{3} + \frac{0.038 \frac{E}{f_y}}{\frac{D}{t}} \right) A = \left(\frac{2}{3} + \frac{0.038 \frac{197200}{657}}{\frac{300}{5}} \right) 7633.85 = 6540.40 mm^2$$

The effective thickness at curve portion is calculated by using the proposed modified ASDM expression (see Equation A.20),

$$t_{em} = 0.5 \times \left(\frac{A_o}{A} \right) \left(\frac{f_y}{f} \right) t = 0.5 \left(\frac{6540.40}{7633.85} \right) \left(\frac{657}{598.25} \right) 5 = 0.5 \times 4.70 = 2.35$$

Effective area of curve portions: $A_c = 2(l_c - l_{ec})t_e + 2tl_{ec}$

$= 2(463.38 - 151.90)\ 2.35 + 2 \times 5 \times 151.90$

$= 2982.96\ \text{mm}^2$

Effective area of flat portions: $A_f = 2tl_{ef} = 2 \times 5 \times 150.76 = 1507.60\ \text{mm}^2$

Total effective area of flat oval section $A_e = A_c + A_f$

$= 2982.96 + 1507.60$

$= 4490.56\ \text{mm}^2$

For perforation of 100 mm size at Location T_5L_3 *r-m* and *h*/2 (see Figure C.1)

(a)

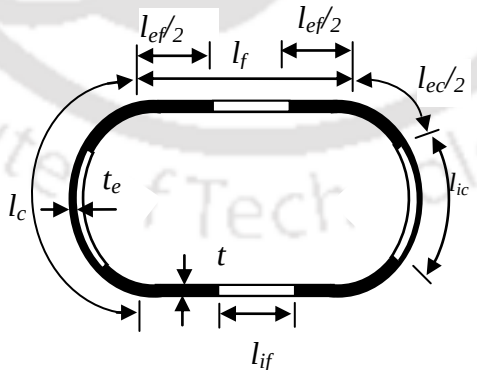

(b)

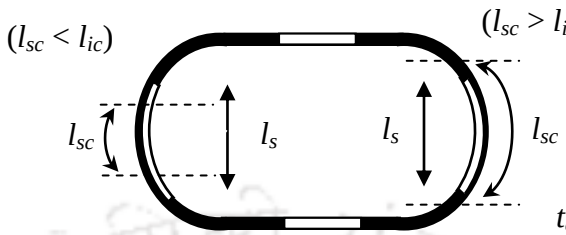

$t_e = t_{em}$ for $w/t \geq 40$

l_s = Perforation

l_{sc} = arc length corresponding to l_s $= t_e$ for $w/t < 40$

Figure C.1: Schematic diagram for effective length estimation as per modified $ASDM_{m(P)}$.

l_{ec} = 151.90 mm,

l_s = 100 mm (perforation size)

l_{sc} = 101.94 mm (arc length corresponding to perforation size, l_s)

Length of curve with reduced thickness i.e. ineffective curve length (l_{ic}),

$l_{ic} = l_c - l_{ec}$ = 463.38 – 151.90 = 311.48 mm

A_p (Area of perforation) calculation:

$A_p = (l_{sc}-l_{ic})t + l_{ic}t_{em}$ for $l_{sc} > l_{ic}$

$A_p = l_{sc}t_{em}$ for $l_{sc} \leq l_{ic}$

Since $l_{sc} < l_{ic}$,

A_p = 101.94 × 2.35 = 239.56 mm2

Effective area for the perforated section, $A_{e(p)} = A_e - A_p$ = 4251.00 mm^2

$P_{ASDMm(P)} = f_y A_{e(p)}$ = 657 × 4251 = 2792907.00 N = 2792.91 kN

LIST OF PUBLICATIONS

A) Journals

1) **Sachidananda, K.** & Singh, K.D. (2015). Numerical study of fixed ended lean duplex stainless steel (LDSS) flat oval hollow stub column under pure axial compression. ***Thin-walled Structures,*** 96,105-119.
2) **Sachidananda, K.** & Singh, K.D. (2017). Structural behaviour of fixed ended stocky lean duplex stainless steel (LDSS) flat oval hollow column under axial compression. ***Thin-walled Structures,*** 113: 47-60.
3) **Sachidananda, K.** & Singh, K.D. (2017). Finite element investigation of fixed ended slender lean duplex stainless steel (LDSS) flat oval hollow column under axial compression (***under preparation***).
4) **Sachidananda, K.** & Singh, K.D. (2017). Perforation effects on the load capacity of fixed ended Lean Duplex Stainless Steel (LDSS) flat oval hollow stub columns under axial compression (***under preparation***).

B) Conferences

1) **Sachidananda, K.** & Singh, K.D. (2013). Structural behaviour of flat oval LDSS stub column under pure axial compression. ***National Conference on Recent Advances in Civil Engineering*** – **NCRACE** 13, Department of Civil Engineering, NERIST, Arunachal Pradesh, India, 15-16 Nov.
2) **Sachidananda, K.** & Singh, K.D. (2015). Design strength of flat oval LDSS stub column under pure axial compression. **15th** ***International Symposium on Tubular Structures***. Rio de Janeiro, Brazil, 27-29 May.
3) **Sachidananda, K.** & Singh, K.D. (2015). Structural behaviour of fixed ended LDSS flat oval slender columns under pure axial compression. **8th** ***International Symposium on Steel Structures,*** Jeju, Korea, 5-7 Nov.
4) **Sachidananda, K.** & Singh K.D. (2016). Numerical study of the effect of boundary conditions on buckling behaviour of flat oval LDSS stub column under axial Compression. In ***10th Structural Engineering Convention*** **(SEC-2016), CSIR-SERC**, India, 21-23 Dec.